Hydrodynamics over Permeable Beds

Fabio Muraro

A thesis submitted in partial fulfilment of the requirements for the degree of
Doctor of Philosophy

The University of Sheffield

Faculty of Engineering

Department of Civil and Structural Engineering

April 2024

Abstract

Free-surface water flows are ubiquitous in nature. As greater river flood risk is expected because of climate change, widespread river monitoring becomes necessary. This could be achieved via remote sensing techniques based on the physical linkage between flow and free surface. Empirical relationships currently describe this linkage, limiting their applicability as changing the scales is not possible.

An experimental campaign aimed at deepening the understanding of the surface-flow linkage was conducted using simulated permeable armoured river deposits. The turbulent flow field was quantified using a 3D Particle Tracking Velocimetry system, whilst the dynamic free surface was studied using a 2D Digital Image Correlation system.
The free surface was found to be dominated by non-dispersive turbulence-induced features and gravity-capillary waves when the free-surface velocity is below the minimum phase velocity of gravity-capillary waves in still water. Conditions with surface velocities above this threshold see the water surface dominated by gravity-capillary waves having the same wavenumber of stationary waves and gravity capillary-waves with different wavenumbers.
In the body of the flow only advective turbulent features were observed below this limit. Above this threshold, most turbulent features advected with the surface velocity, however, features with frequency and scale of the observed gravity-capillary waves were also discovered close to the water surface.

Results for both the free surface and the flow field clearly indicate the existence of two flow regimes where the free-surface velocity represents the discriminating factor: when the free-surface velocity is below the minimum phase velocity of gravity-capillary flow and free surface are dominated by effects of turbulence; when the free-surface velocity is above the minimum phase velocity of gravity-capillary the free surface is governed by gravity-capillary waves and standing waves, while resonance phenomena and turbulence effects occur in the flow field.

Acknowledgements

As the end of this doctorate is approaching, it is time for me to have some thoughts about this journey. Well, truth being told, rather than a journey, it has been a roller coaster of emotions. On the one hand, this has been a fantastic experience as it allowed me to meet many awesome people and to develop as a person; on the other hand, it has also been some sort of odyssey. The challenging objectives of this project, the pandemic and the experimental difficulties met while setting up the systems, they definitely made this experience not that “soft”. Fortunately, I was able to overcome all these troubles, but, I must say, this would not have been possible without the help of many people.

First of all, from the deepest of my heart, I need to thank my supervisors Prof. Simon J. Tait and Dr. Andrew Nichols. I was able to find in them all the support that I needed to overcome all the difficulties I met during these years. Much would not have been accomplished without their help and intuition. I could not have asked for better people to be my supervisors.

A huge thanks to Dr. Giulio Dolcetti for all the advice he gave during this PhD. He was a lighthouse in the dark and vast sea that is data processing.

I must thank all the technicians of the water laboratory, Paul Osborne, Mark Foster, Martin Taylor, Joseph Milner, Chris Green, Alex Cargill and Paul Blackbourn, for all the help they gave me (despite my continuous crazy requests). Without you all, I would still be trying to find a way to have everything working.

I also need to thank the people from the IT service - Paul Bentley and Alan Grundy - and from the administrative section - Lindsay Hopcroft, Lindsey Farnsworth, Inshirah Miladi, Gemma Newsome and Holly Harris.

Last but not least, thank you to my family and friends for their support during this long journey.

Contents

List of Tables

List of Figures

Acronyms

DIC	Digital Image Correlation
PTV	Particle Tracking Velocimetry
PIV	Particle Image Velocimetry
ppm	parts-per-million
ppp	particles-per-pixel
IPCC	Intergovernmental Panel on Climate Change
LSPIV	Large-scale Particle Image Velocimetry
STIV	Space-Time Image Velocimetry
HWA	Hot Wire Anemometry
STB	Shake-The-Box
TKE	Turbulent Kinetic Energy
STI	Space-Time Images
DAQ	Data Acquisition
NI	National Instruments
L-W-H	Length x Width x Height
FOV	Field of View
LED	Light Emitting Diode
POD	Proper Orthogonal Decomposition
CCTV	Closed Circuit Television
GSD	Ground Sample Distance
PDF	Probability Density Function

Publications

Muraro, F., Dolcetti, G., Nichols, A., Tait, S. J., & Horoshenkov, K. V. (2021). Free-surface behaviour of shallow turbulent flows. *Journal of Hydraulic Research*, *59*(1), 1–20. https://doi.org/10.1080/00221686.2020.1870007

Dolcetti, G., Krynkin, A., Alkmim, M., Cuenca, J., De Ryck, L., Sailor, G., Muraro, F., Tait, S. J., & Horoshenkov, K. V. (2024). Reconstruction of the frequency-wavenumber spectrum of water waves with an airborne acoustic doppler array for noncontact river monitoring. *IEEE Transactions on Geoscience and Remote Sensing*, *62*, 1–14. https://doi.org/10.1109/TGRS.2024.3358672

I, the author, confirm that the thesis is my own work. I am aware of the University's Guidance on the Use of Unfair Means (www.sheffield.ac.uk/ssid/unfair-means). This work has not been previously been presented for an award at this, or any other, university.

To my Barkfamily

Alla mia Barkfamiglia

"The world is not to be put in order, the world is order incarnate.
It is for us to put ourselves in unison with this order."

Henry V. Miller

Chapter 1

Introduction

1.1 Background

Since the dawn of civilisation, rivers have always been elements of the natural landscape of paramount importance for humans. Rivers were often chosen as locations for the foundation of cities as they provided a source of fresh water for human, agriculture and commercial consumption, the fertility of land, the possibility to transport goods and so facilitate trade, and cultural exchanges as well. These factors allowed cities to grow and prosper and led to the development of modern day society. However, as technical and scientific skills emerged and developed, the influence of human activities on rivers became more and more invasive, leading to a loss of rivers' natural appearance. If on the one hand, these interventions (e.g. dams, culverts, sand and gravel quarrying, and water abstraction) helped at improving our control on streams and at better managing fluvial resources, on the other hand, the extensive anthropisation enhanced the fragility of fluvial systems causing loss of biodiversity, saltwater intrusions and soil desiccation and loss.

The artificialisation of the stream networks, unfortunately, does not represent the only reason for the change in the behaviour of fluvial systems: since the industrial revolution in the 18th century, there has been a continuous and progressively higher release of greenhouse gases, causing the atmospheric concentration of carbon dioxide (CO_2) to increase from 280 parts-per-million (ppm) in 1750 to over 420 ppm in 2022 (Keeling et al., 2001) as depicted in Figure 1.1, the highest values in 2.5 million years (Foster et al., 2017; Caballero-Gill et al., 2019). This building up of carbon dioxide has induced the phenomenon known as "climate change".

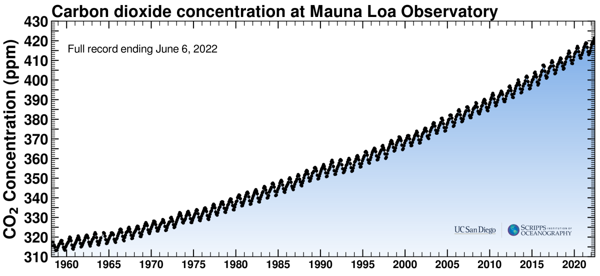

Figure 1.1: Keeling Curve: Carbon Dioxide atmospheric concentration at Manua Loa Observatory (Hawaii, USA) since 1958. Greenhouse emissions over the last 70 years are responsible for over 70% of the total CO_2 concentration increment compared with pre-industrial levels. Reproduced from Keeling et al. (2001).

A new assessment of the impact of human activities on the environment has recently been published by the Intergovernmental Panel on Climate Change (IPCC) (Intergovernmental Panel on Climate Change, 2023). The report does not quantify climate change effects on the current state of the climate, but provides a number of different (though consistent) scenarios according to future plausible greenhouse gas trends. (Fig. 1.2).

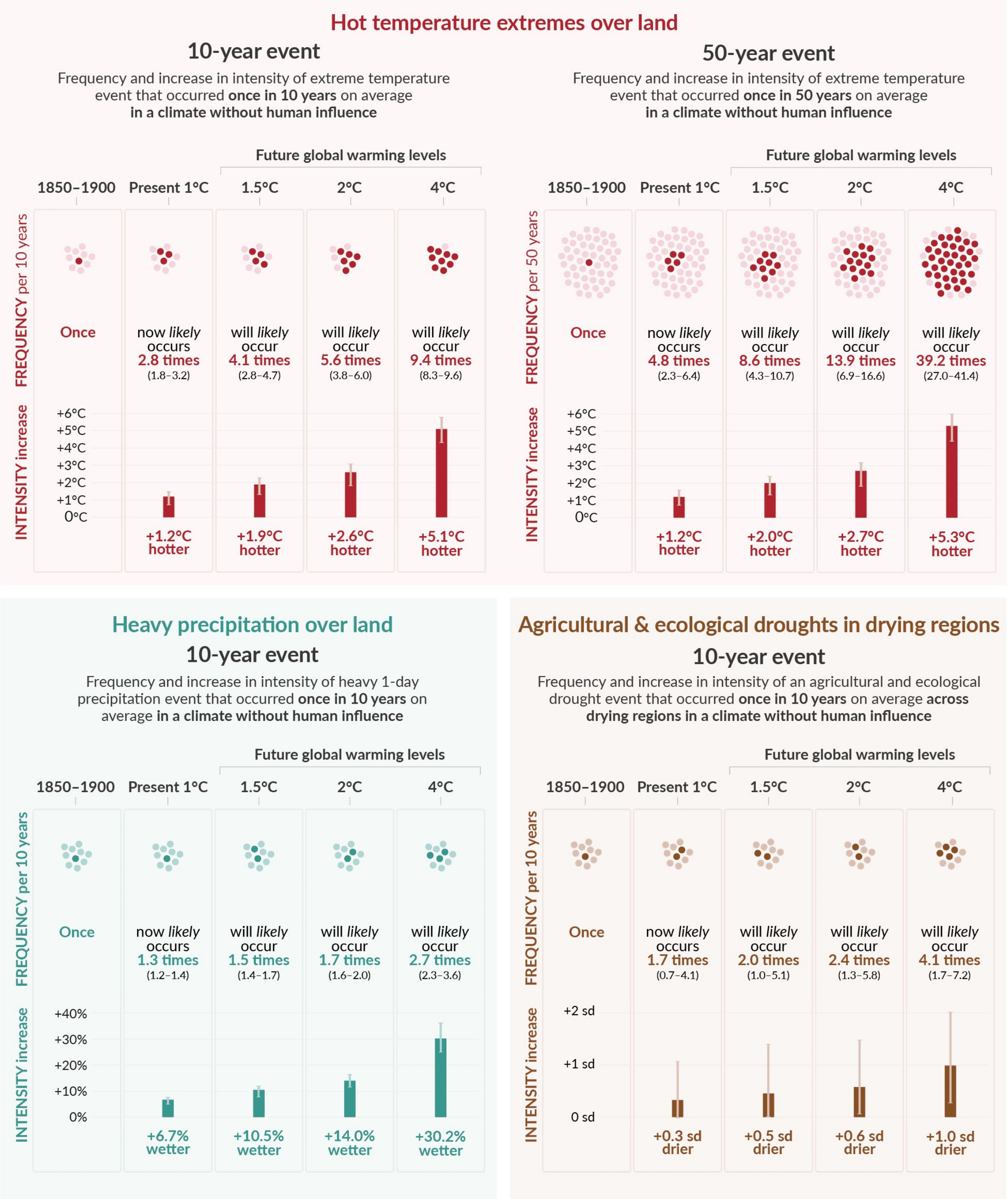

Figure 1.2: IPCC 6th Assessment Report: Projected changes in the frequency and intensity of extremes events according to different earth surface temperature increments. After Intergovernmental Panel on Climate Change (2023).

The IPCC's assessment does not present an estimate of the likelihood of each scenario, however, a commentary of the report by Hausfather and Peters (2020) suggests that an increment of the global surface temperature between 2.1 °C and 3.5 °C by 2100 is most likely. Referring to events that nowadays have a return period of 10 years, extreme heatwaves are expected to be

5.6 times more likely for the 2.6 °C warmer scenario; similarly, 14% more intense precipitation events are suggested and 1.7 times more likely; droughts, on the other hand, are likely to be 2.4 more frequent than currently and drier. These trends represent averages, therefore, greater and more frequent events are likely to occur in some regions. Furthermore, events such as stronger tropical cyclones, reduction of the ice-covered areas, enhanced ocean acidification and faster sea level rise are likely to happen. Unfortunately, these events will create other impacts such as the reduction of agricultural and residential areas, famines, diseases, fresh water scarcity and loss of biodiversity.

Similar conclusions were reached in the latest UK Climate Change Assessment (Betts et al., 2021). The contents of this latter report can be summarised as follows (Slingo, 2021):

- winters will be warmer but wetter as not only more rainy days are expected but also higher rainfall intensities.
- summers are likely to be hotter and drier; nonetheless, rainfall events are expected to be up to 20% more intense.
- more severe and more frequent high temperatures events, as well as worsening of urban heat islands effects, are anticipated; in the scenario of a 4 °C global temperature increase by 2100, by 2080 temperatures exceeding 40 °C are going to be as frequent as today's 32 °C surpasses.
- sub-daily and hourly precipitation rates show pronounced shifts to more intense hourly rainfalls at the expense of lighter rainfalls.

Kovats and Brisley (2021) emphasises a higher risk of flooding and suggests this might be one of the most severe risks due to climate change to the UK population. Considering the risk encompassing all the forms of flooding (fluvial, coastal, pluvial and groundwater), 1.9 millions people across the UK are threatened at the moment (for events with a return period of 75 years), with fluvial flooding responsible for greater potential damage, pluvial (also known as surface water) flooding affecting larger areas and coastal flooding becoming more dangerous as magnitude and suddenness pose a greater risk for life. This is reflected by an expected annual damage of nearly half a billion pounds. Climate change is projected to increase the risk deriving from floods as a larger number of houses and areas that are currently safe are expected to be affected. In the 4 °C global warming by 2100 scenario, the number of people that might be threatened by any form of flooding is expected to be nearly thrice the current number (Fig. 1.3).

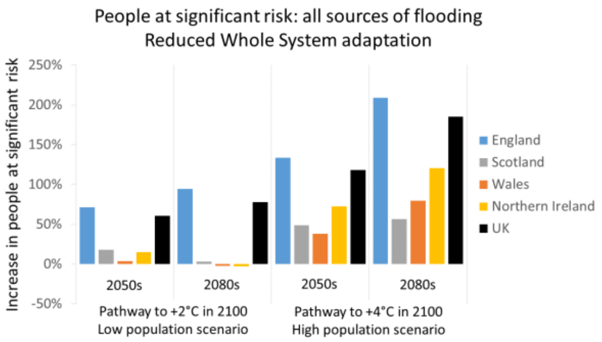

Figure 1.3: Expected trends in the number of people at significant risk of flooding for the UK and Nations. Reproduced from Kovats and Brisley (2021).

The urgency of the flooding problem induced the Environment Agency to define a roadmap for flooding hydrology for the next 25 years (Longfield et al., 2022). This roadmap is aimed at providing knowledge, methods, tools and expertise to improve the UK's resilience to flooding. The development of this agenda was possible thanks to the multitude of feedback (e.g. questionnaires, workshops and surveys) given by experts from the flood hydrology community. The interviews suggested a higher interest in flood estimation (i.e. long-term vision aimed at estimating peak flows) than flood forecasting (i.e. estimation of magnitude, timing and duration of a flood event in a given location) and stressed the importance of fluvial flooding in comparison with other sources of flooding. Furthermore, the interviewees highlighted the interest and importance of having accessible and reliable hydraulic data.

Flood-related data mostly comes from gauging stations where discharge is derived from river stage through empirical relations. The conversion, however, highly relies on the accuracy of the method used to define the water lever (e.g. ultrasound probes and pressure sensors). It follows that any error related to the discharge can be ascribed to uncertainties in the stage and/or in the coefficient of discharge. Also, discharge-stage calibration curves are typically derived from normally observed ranges of depth and rare flood events. Increments in the magnitude of rainfalls and floods are being observed, but there is no guarantee these relationships can hold for such a large scale events.

Generally speaking, an estimate of the error that might arise when defining discharge can be obtained from a simple uniform flow relation such as Gauckler-Manning formula:

$$Q = \frac{A}{n} R_H^{2/3} S^{1/2} \tag{1.1}$$

where Q is discharge, A is the area, n is the Manning coefficient, R_H is the hydraulic radius defined as ratio between the wetted perimeter and the area, and S is the bed slope.
In a hypothetical wide rectangular river (verified when the river width B is much greater than the water depth D, i.e. $B > 10D$), the hydraulic radius can be replaced by the water depth, allowing to calculate straightforward the discharge for unit of width q_D:

$$q_D = \frac{1}{n} D^{5/3} S^{1/2}. \tag{1.2}$$

Differentiating Equation 1.2 and dividing the differential by Equation 1.1 gives:

$$\frac{dq_D}{q_D} = \frac{5}{3}\frac{dD}{D} + \frac{dn}{n} + \frac{1}{2}\frac{dS}{S}. \tag{1.3}$$

Equation 1.3 can be used to weight the error arising from uncertainties in the measurement of the corresponding parameter. It appears clear that the major sources of error come from the stage and the roughness parameters. Considering this estimate is derived using a uniform flow relation, it is implied that the error might be even larger while evaluating a flood event.

River flow rates can of course be evaluated using several other methods, like Large-scale Particle Image Velocimetry (LSPIV) (Fujita et al., 1998; Muste et al., 2008) and Space-Time Image Velocimetry (STIV) (Fujita et al., 2007; Tsubaki et al., 2011). Many of these techniques, however, are based on empirical assumptions linking surface velocity with depth-averaged velocity, require an accurate calibration of the devices (typically cameras) and prior knowledge of the channel shape (Marcus & Fonstad, 2008). It follows that important shortcomings in our ability to measure spatially and temporally varying river flows at high resolutions are currently present. To tackle this deficiency, it is important to improve the accuracy of sensors and sensing techniques (Sayers et al., 2015).

In this optics, the discovery of the existence of a linkage between the free-surface behaviour and the underlying turbulent flow by Horoshenkov et al. (2013), Nichols (2013) and Nichols et al. (2016) can be considered as a major breakthrough as they indicate that all the key bulk flow parameters can be retrieved through the observation of the free-surface wave patterns. Nevertheless, Horoshenkov et al. (2013) did not present clear and conclusive physically-based evidence regarding the origin of surface waves. Welber et al. (2016) suggested this lack of understanding of the surface-flow interactions is responsible for the great uncertainty in flow measurements. At the current stage the comprehension of the free-surface dynamics and governing mechanisms is quite limited, hindering our ability to accurately quantify flow discharge in a non-contact manner at a range of locations and produce reliable estimates about flood propagation and magnitude.

1.2 Aims and Objectives

The purpose of this thesis is to report on investigations regarding the free-surface dynamics and its relation with the underlying flow in order to derive a methodology for rapidly and precisely mapping the hydrodynamics and inferring the morphology of river reaches. Flow and section characteristics (e.g. velocity, shear, depth and bed roughness) may be deduced by simply observing the behaviour of the free surface. To do so, an extensive experimental campaign in a laboratory flume is here presented. Several flow conditions over a permeable rough composite bed made of spheres and sand for different slopes and bed textures were evaluated using Particle Tracking Velocimetry (PTV), Digital Image Correlation (DIC) and wave probes systems. PTV allowed the evaluation of the 3D bulk flow dynamics, while DIC was used to reconstruct the instantaneous free-surface profile and statistically and spectrally characterise it. Time-staggered PTV and DIC measurements, mediated through wave probes, were perform to maximise the level of details on both the regions. Simultaneous evaluations were also conducted to unambiguously derive the linkage between surface and bulk behaviours.

Clear relationships will allow a better definition of the river flow parameters, providing a higher level of accuracy in the evaluation of floods. The knowledge arising from this better comprehension of the flow dynamics might be applied on the field to expand the monitoring network via low cost Closed Circuit Television (CCTV) cameras (Dolcetti et al., 2022) or drones (Woodget et al., 2017), opening to the possibility for real time measurements. This new understanding and monitoring strategy could significantly contribute to improving our resilience against floods via a better planning of interventions and more accurate warnings.

1.3 Research Hypotheses

The objectives of this thesis are going to be pursued through the following research questions:

- Which is (or are) the dominant mechanism(s) that govern(s) the free-surface behaviour?

- Is there a sudden transition from one governing mechanism to another one or do they all simultaneously coexist with different intensity?
- Which bulk flow properties can be inferred from the observation of the air-water interface?
- Can statistically similar beds produce different flow and wave patterns?

1.4 Thesis Structure

This thesis is organised as follows: Chapter 2 provides a review of the currently available literature regarding the free-surface behaviour and flow dynamics of open-channel shallow turbulent flows, and about the instrumentation and techniques used to measure them; Chapter 3 focuses on the experimental design and data processing; Chapter 4 presents the results of the analysis, their critical discussion and comparison against previously discovered findings; Chapter 5 draws the conclusions of this thesis and provides some recommendations for further analysis and future studies.

Chapter 2

Literature Review

2.1 Introduction

The purpose of this investigation is to assess the linkage between the free surface and the underlying flow field using various experimental methods. Knowledge of the free-surface behaviour is firstly presented in Section 2.2; this Section focuses on different theories about the surface dynamics and preliminary observations regarding the water surface interface-flow relationships. Section 2.3 examines existing knowledge of the hydrodynamics over permeable beds as these are the most representative cases for natural streams. Section 2.4 describes theory and experimental practice of the instrumentation used in this research; this Section is further divided in three Subsections, each one focusing on a specific system. Section 2.5 underlines ambiguities and gaps in the present literature and paves the questions that this study aims to answer. Finally, Section 2.6 brings together the key knowledge and outlines an approach for the future experimental investigations.

2.2 Free-surface Behaviour of Shallow Turbulent Flows

Many different factors have an influence on the turbulent flow behaviour in rivers and streams. They can be macroscopic (e.g. flow rate, boundary roughness, section geometry and channel slope) or microscopic (e.g. bedforms, grain size distribution, bed porosity and permeability). The free surface is the dynamic upper boundary of a flow system, therefore, it can be reasonably argued that is affected by the very same parameters. This dependency could be visualised in the dynamically behaviour of the air-water interface, implying that the hydraulic and morphological characteristics might be inferred from the characterisation of the free-surface wave pattern (Cooper et al., 2006; Savelsberg et al., 2006; Fujita et al., 2007; Nichols, 2013; Krynkin et al., 2014; Dolcetti, 2016; Legleiter et al., 2017).

Several remote sensing techniques able to estimate specific flow properties are currently available. These can be based on optics (Muste et al., 2008; Nichols & Rubinato, 2016), acoustics (Fukami et al., 2008; Nichols et al., 2012; Nichols et al., 2013) or radio waves (Plant et al., 2005). Non-contact technologies are constantly improving, nonetheless, the actual knowledge of the hydrodynamic mechanisms responsible for the free-surface behaviour and the ability to measure accurately the key characteristics of the free surface behaviour are still limited (Marcus & Fonstad, 2010). Welber et al. (2016) suggested the cause of great uncertainties in flow measurements can be ascribed to this lacking understanding of the surface-flow interactions.

Over the next pages, a review of the literature regarding the free-surface behaviour is presented. This review is strongly based on the recent review published by Muraro et al. (2021). This Section is organised as follows: Subsection 2.2.1 contains the description and classification of the free-surface state according to the framework originally proposed by Brocchini and Peregrine (2001); Subsection 2.2.2 examines the various possible dominant mechanisms of the water interface, focusing on the effect of coherent structures, gravity-capillary waves and stationary waves.

2.2.1 Classification of the Free-surface State

Brocchini and Peregrine (2001) can be considered a seminal study regarding the description of free-surface dynamics. This work was not limited to shallow water flows in rivers and streams, but covers a broad range of hydrodynamic regimes including some that rarely occur in nature. Different free-surface behaviours arising from various turbulent sub-surface fields were evaluated, ranging from "weak" to "strong", i.e. "sufficiently energetic that it causes the free surface to be strongly distorted", turbulence conditions. This flow categorisation allowed researchers to relate the level of agitation of the free surface to various turbulent length scales and energy quantities.

Brocchini and Peregrine (2001) suggested that the multitude of forms of features that can appear on the free surface are produced by different balances between turbulent velocities and length scales. For this reason, they proposed a two-parameter framework to establish a relation between the free-surface effects, produced by turbulence, and the combination of stabilising forces of gravity and surface tension. To express the influence of the stabilising energy densities, Froude and Weber Numbers could have been used, however, dimensional variables were instead preferred to directly convey the magnitude of the observed surface quantities to different free-surface agitation states. The dimensional parameters were defined through the characteristics of "blobs" described as "moderately coherent and discrete volumes of fluid that move upward to the surface, perhaps through it, sometimes falling back on it, or moving parallel to it and hence disturbing it". Brocchini and Peregrine (2001) therefore based their framework on a fluid volume that has a semblance of a coherent structure. Such structure may possess different levels of momentum, potentially allowing it to break through the free surface similarly to a jet. Hence, a length scale L and a velocity scale q, representative of the turbulent motion, were sought for these "blobs". As it was difficult to properly determine the size of the parameter L, they opted to use either the most energetic turbulent scale or the length scale of dominant surface features. Instead, the norm of the velocity vector was chosen for q. For their analysis, these quantities were assumed to be mutually independent. Brocchini and Peregrine (2001) organised their L-q diagram (Fig. 2.1) into 4 regions according to unique Froude (F_{BP}) and Weber (We_{BP}) Numbers, defined as $F_{BP} = q/(2gL)^{1/2}$ and $We_{BP} = \rho_f q^2 L/(2T)$, respectively. Here g is the gravitational acceleration, ρ_f is the fluid density and T is the surface tension at the free surface.

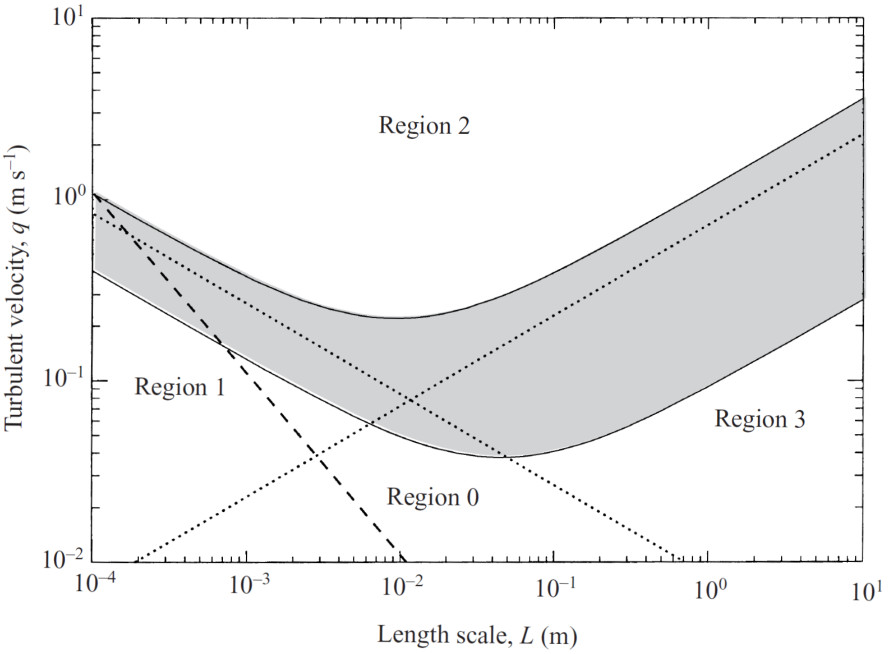

Figure 2.1: L-q diagram for free-surface water flows. Dotted lines represent Equations 2.1, while the dashed line represents the limit corresponding to $Re_{BP} = qL/\nu = 100$ (ν represents the kinematic viscosity of water). Shaded areas represent regions of marginal breaking and are zones where dotted lines could potentially lie. Derived from Brocchini and Peregrine (2001).

From these Numbers, the boundaries of the regions were derived as follows:

$$q = (2F_{BP}^2 gL)^{1/2} \quad \text{and} \quad q = [2We_{BP}T/(\rho_f L)]^{1/2}. \tag{2.1}$$

It has to be noted that these equations are only indicative of threshold values for the Froude and Weber Numbers that separate almost-quiescent water surfaces from highly agitated ones.

Flow regimes following in region 0 in Figure 2.1 present little or no surface disturbances. Nonetheless, even in weak turbulence conditions waves may be generated by small disturbances following the growing mechanism proposed in Teixeira and Belcher (2006). This is the region where most historical experiments can be situated (Muraro et al., 2021).
Region 1 is the area where surface tension effects are greater than gravity. Here, small-scale (order of 10^{-2} m or less) turbulence dominates. Surface tension greatly constrains the perturbation of the free surface, resulting in smooth and rounded features. If the flow conditions fall below the dashed line in Figure 2.1, very little surface deformation can be seen. In the upper part of region 1 surface breakup may occur and lead to air entrainment and turbulence production.
Region 2 presents extremely strong turbulence conditions, where neither gravity nor surface tension effects can maintain the integrity of the interface. As a consequence, a two-phase flow composed of air and water is mostly observed. In this context, turbulent eddies are no longer restrained by the surface boundary. This happens as "blobs" do not slow down enough when approaching the interface: the inertia of the surrounding fluid successfully limits the horizontal component of the turbulent velocity vector but not the vertical. This effect produces violent ejections of liquid.

Region 3 is the part of the graph characterised by the dominance of gravitational effects. This region is probably the most important as the majority of flow conditions in rivers, streams and oceans can be ascribed to this region. Surface waves are typically small, allowing the use of linearised boundary conditions. A wide number of local features can be identified (e.g. waves, dimples and scars). These deformations are due to turbulence with enough energy to perturb the interface, but only at scales smaller than the dimensions of the generating eddies. Small features may evolve and break locally, causing air entrainment.
Shallow flows such as rivers and open channels generally fall in regions 0 or 3. However, in reality a hydrodynamic regime cannot often be associated with a single position on the graph, but is best represented by a trajectory because of the varying level of turbulence.

The analysis presented in Brocchini and Peregrine (2001) was mostly qualitative and could not be properly experimentally tested, nonetheless, it served to identify where further experimental studies were needed.

2.2.2 Governing Mechanisms of the Free-surface Behaviour

The principal physical cause for the free-surface roughness patterns in turbulent flows has not yet been clearly identified. Some processes have been suggested to be responsible for these waves, but sufficient evidence is not available to clearly identify the responsible process. This is because there is a scarcity of high resolution experimental studies where both the flow field and the air-water interface were simultaneously observed. Instead, most of the published works was focused on determining the celerity (speed) of the patterns as this information has a direct implication for non-contact flow velocity measurements.

To better understand the free-surface behaviour, the processes that may cause specific deformations of the air-water interface of a turbulent flow are here examined. Such deformation mechanisms are: interactions between the free surface and coherent turbulent structures, resonance phenomena and effects of bed topography.

Interactions of Coherent Structures with the Free Surface

Nezu et al. (1993) suggests that turbulent components in a flow are not independent from each other or completely random, but demonstrate an organisation in space and time. Such organisation defines a “parcel” of fluid that has its own life cycle and that can be therefore described as “coherent”. This observation leads to the need for the definition of a ”coherent structure”. Several features are suited for this definition, such as eddies, boils, horseshoe vortices and streaks. Two types of coherent structures can be considered generally: bursting phenomena and large-scale vortical motions.

Bursting phenomena, discovered by Kline et al. (1967), Corino and Brodkey (1969) and Grass (1971) take place in the wall region. Over a smooth bed the near-bed sublayer structure is composed of alternating low- and high-speed streaks that are induced by fluid shear. Quasi-streamwise vortices are also present, straddling the low-speed regions. These vortices can occur as single structures or in pairs, appearing as hockey sticks or horseshoes (Fig. 2.2). Once developed, the near-bed streaks and vortices begin to oscillate vertically following the interaction

Figure 2.2: Conceptual model of the creation and development of near-wall bursting phenomena that lead to the formation of boils at the free surface. After Rashidi (1997).

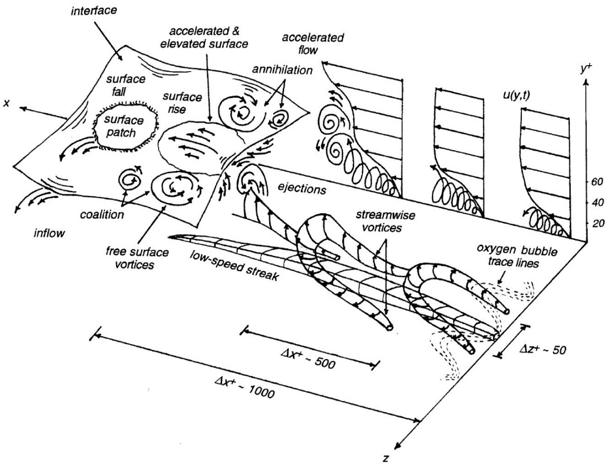

with higher momentum fluid in the overlying flow. Subsequently, these structures go through a complete or partial breaking, forming groups of ejections (Rashidi, 1997). The remaining ejected fluid is later moved away by higher-momentum fluid (Corino & Brodkey, 1969). The entire series of processes forms a "bursting phenomenon". Over a rough bed the roughness disrupts the viscous sublayer, nonetheless, streaks can still form and evolve into bursts. This leaded to the hypothesis that a burst is not triggered by the instability of the viscous sublayer, but by the high-momentum fluid moving from the bulk region towards the bed (Nezu et al., 1993; Rashidi, 1997).

Large-scale motions, described by Matthes (1947), may also exist in the outer region. Six different types of large-scale motions were identified by Nezu et al. (1993). Of these phenomena, five are simple pulsations of the mean flow (i.e. low-frequency motions containing fine turbulence), while just one can be truly considered product of turbulence as it displays sufficient intermittency and randomness in space and size. This turbulent motion, named "kolk" by Matthes (1947), is a strong upward vortex that rises towards the free surface and impinges on it, generating a boil (also known as surface-renewal eddy). A boil represents a localised raising of the free surface where water flows out radially on top of the flowing prism (Matthes, 1947) (Fig. 2.3). Three forms of kolk-boil exist: "boils of the first kind" caused by the flow separation downstream of bedforms (hence they cannot occur over flat beds); "boils of the second kind" linked to secondary motions in the flow; "boils of the third kind" as a result of bursting motions. The first kind of boils was initially studied by Matthes (1947) and Znamenskaya (1963) and later by Jackson (1976). This form of boil develops in the lee area of a bed feature where adverse

Figure 2.3: Boils observed on the Shinano River near Ojyia, Japan, April 2019. The boil can be seen as the flat region clear from waves. This is caused by the strong radial outflow produced by the rising coherent fluid parcel. Reproduced with authorisation from Muraro et al. (2021).

pressure gradients occur. This is suggested by Kline et al. (1967) who observed stronger and more frequent boil phenomena for positive pressure gradients conditions.

Boils of the second kind are associated with secondary currents. Secondary motions are flows that take place along the spanwise direction. As pointed out by Nezu and Rodi (1985), these currents weaken for higher aspect ratios (i.e. the ratio between width of the channel and water depth), therefore are not expected in wide rivers. Nonetheless, secondary flows can appear even in high aspect ratio rivers as turbulent velocity components allow the formation of an unsteady turbulent form of motion. Boils of the second kind were studied by Imamoto and Ishigaki (1985) and by Tamburrino and Gulliver (2007). This form of boil is the result of slow-moving repeating patterns of vertical vortices known as streets, alternated with unperturbed fast moving areas (streaks). Tamburrino and Gulliver (2007) suggested that streets are the manifestation of large streamwise vortices and outer region bursts: as bursts advect, they are trapped and channelled towards the free surface by the streamwise vortices, giving rise to upwellings (rising flows) and streets of vortices. On contrary, fast moving streaks originate in the areas where downwellings (descending flows) occur, hindering bursts from reaching the free surface.

Generation and development of the third kind of boils can be described using the conceptualisation of Rashidi (1997) (Fig. 2.2). Low-momentum near-bed ejections are seen moving fluid upwards towards the free surface and generating spanwise “upsurging vortices” (kolks). These vortices rise towards the free surface and impact on it, causing positive local increases in the instantaneous water height (boils). The vortices then fall back towards the bed and become “downswinging vortices” that produce reduction in the surface elevation (downswings). Quasi two-dimensional surface vortices which resemble whirlpools are then generated in the plane of the surface along the edges of the boils (Kumar et al., 1998). Pan and Banerjee (1995) suggested these vortices originate from surface deformations because of differences in the surface velocity between the boil and downswing areas.

It has to be noted that not all the bursts manage to evolve into a boil. Grass (1971) realised that not all the bursts are able to cross the turbulent boundary layer but only the most energetic ones. Furthermore, a “blockage layer” exists in proximity of the free surface for lesser energetic conditions. This layer constrains the vertical component of turbulence and forces the redistribution of its Turbulent Kinetic Energy (TKE) to the orthogonal directions (Longo, 2010). As a consequence, the free surface is barely perturbed (Smolentsev & Miraghaie, 2005). These two motivations might explain the longer periodicity of boils than bursts (Rao et al., 1971). However, for stronger turbulence situations the blockage layer thins and the transfer of TKE is less efficient. The water surface may be strongly deformed and broken into drops as proposed by Brocchini and Peregrine (2001) for regimes in region 2. Correspondence can be seen with numerical studies by Zhang et al. (1999).

The earliest experiments on the free surface of open-channel flows were given in Freeze et al. (2003) and Smolentsev and Miraghaie (2005) and were focused on supercritical flows. In these studies, the air-water interface behaviour was investigated for regimes varying from almost undisturbed to highly agitated free surface. In their setup, a nozzle continuously injected water from upstream. A honeycomb was later mounted inside the nozzle to reduce the surface agitation that is typical of supercritical flows. As the hydraulic conditions moved towards higher levels of turbulence significant changes in the frequency and amplitude characteristics of the instantaneous depth were observed by both Freeze et al. (2003) and Smolentsev and Miraghaie (2005). Freeze et al. (2003) also observed that the probability density functions of the instantaneous water depth were well approximated by a Gaussian fit. The power spectral density plots of the fluctuating depth revealed large peaks at low frequencies for both studies. Smolentsev and Miraghaie (2005) suggested the peaks were caused by roll waves with wavelength longer than the flow depth, followed by a long tail of low-period features. The high-frequency components were associated with interactions between turbulence and the free surface, and with short gravity and capillary waves. Larger contribution of the shorter scales in the power spectrum and larger standard deviation of the depth, characteristics of rougher water surfaces, were observed with for increasing values of the Froude Number. Freeze et al. (2003) also observed a weak dependence of the depth standard deviation on the flow Reynolds Number. Smolentsev and Miraghaie (2005) inferred the dynamics of the free surface by illuminating the water interface from above and so projecting the wave patterns onto a white sheet placed on the bottom of the flume. The rise and fall of the free surface produced cellular-resembling structures on the flume bottom. The average size at the surface of these cells reduced with the Froude Number and turbulence intensity. Their advection velocity resulted a few percent above the mean flow velocity. This reason suggested that the surface features were associated to the disturbances at the interface produced by turbulent events, i.e. eddies from the near-wall region moving upwards and advecting at the mean flow velocity. Assuming a connection between the characteristics of cells and the size of turbulent eddies, different paths of evolution for the turbulent eddies while approaching the free surface were proposed. For weak levels of turbulence the free surface acts like a rigid boundary and forces eddies to evolve into 2D structures similar to pancakes. In case of strong turbulence eddies maintain the original 3D form and produce larger surface deformations with a different more elongated plan shape.

Fujita et al. (2011) represents one of the few experiments where both the water surface and velocity field were simultaneously measured. Profiles of the free surface along the centreline of a channel were imaged at different instants in time and then cross-correlated. By using the time-lag that produced the maximum in the corresponding correlation function and the spacing between the observed positions Fujita et al. (2011) derived the mean velocity of the free-surface pattern. Free-surface velocity was also measured by using floating tracers. Comparisons between the instantaneous free-surface elevation and turbulent vertical velocity (obtained from PTV) showed a correspondence between the local increases in the water depth and local peaks of the vertical velocity fluctuation. The surface features was seen advecting downstream with a speed similar to the near-surface velocity (within an error of less than 10%). This led to the idea that the free-surface velocity could be recovered by observing the surface pattern. The correlation between surface fluctuations and depthwise vertical velocity fields had positive values near the surface and negative towards the bottom, although the coefficients were always smaller than 0.15. The trend of correlation function suggested the existence of a structure rotating in a clockwise direction at the intermediate depth. This vortex was seen moving towards the surface, interacting with it and inducing a local increment of the water elevation and a counter-clockwise whirl near the interface. The vortex structure travelled with a speed comparable to the flow

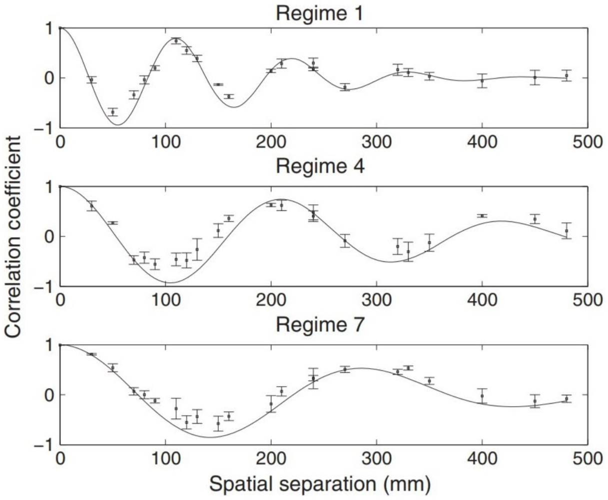

Figure 2.4: Measured and fitted spatial correlation function for progressively higher Froude Numbers ($Fr = 0.29$, $Fr = 0.54$, $Fr = 0.58$ for regimes 1, 4 and 7 in Horoshenkov et al. (2013), respectively). Derived from Horoshenkov et al. (2013).

velocity at the surface, similarly to the surface disturbances.

Laboratory experiments over a rough bed channel are described by Horoshenkov et al. (2013). By means of a non-equidistant array of wave probes the speed of the wave pattern was compared with that of gravity-capillary waves generated artificially either in the presence or absence of flow. Results showed that the surface features, independently of the wave frequency, did not follow the dispersion relation of gravity-capillary waves but rather had a propagation speed ranging between the surface velocity and the mean flow velocity. This suggested a linkage between the advecting wave pattern and the underlying turbulent field. As the free-surface pattern varied continuously in time and space, a spatial correlation function was employed to describe the statistical and spectral characteristics of the dynamic boundary. This function was found to change sign as the spatial lag ρ increased. An analytical form combing a periodic function with an exponentially decaying term was found to well approximate the behaviour of the observed spatial correlation function, $W(\rho)$:

$$W(\rho) = \exp(-\rho^2/\sigma_w^2)\cos(2\pi\rho/L_0) \tag{2.2}$$

where σ_w is the correlation radius, a measure of the correlation length of the surface pattern (i.e. it defines the length within which the free-surface patterns can be considered correlated), and L_0 is the characteristic spatial period of the wave pattern at the free surface.

By adjusting the two parameters σ_w and L_0 with an optimisation process, Equation 2.2 was able to follow well the measured spatial correlation function for different hydraulic regimes (Fig. 2.4). Horoshenkov et al. (2013) also demonstrated that the correlation radius, nondimensionalised with the equivalent hydraulic roughness (i.e. capacity of the flow in dissipating energy), had a linear relationship with the bulk Reynolds Number, $Re = \bar{U}D/\nu$, being $\bar{U}$ the depth- and time-averaged flow velocity. This suggested that the wave dissipation was linked to the energy dissipation within the turbulent flow. By non-dimensionalising the spatial correlation period with the bed roughness height a clear nonlinear relation with the ratio of depth-averaged flow velocity to shear velocity was seen. Therefore, L_0 was reckoned to carry information on the shape of the vertical velocity profile. As last, the characteristic spatial period resulted increasing with the Froude Number.

Nichols et al. (2016) further examined the oscillatory behaviour of the free surface and suggested a model for the surface response to the disturbances induced by turbulence. The characteristic spatial period L_0 in Equation 2.2 and the surface velocity, U_S, were used to define the characteristic frequency of oscillation of a surface feature, f_{shm}:

$$f_{shm} = U_S/L_0. \tag{2.3}$$

It was found that the free surface, excited by underlying turbulence, behaved like an under-damped simple harmonic motion in which where the surface pattern inverts periodically in time while advecting. Nichols et al. (2016) hypothesised that each single surface disturbance, once generated, continuously fluctuate around the water mean level while gravity and surface tension attempt to restore the equilibrium, acting like a spring and mass system. Meanwhile, gravity waves travelling in all directions may be generated. The complex surface wave pattern was then suggested to be as an ensemble of oscillating features named “oscillons” overlapping in space and time, maybe out of phase. Assuming no surface tension, the characteristic frequency of a simple harmonic motion of a water surface feature, f_{shm}, was related to the root-mean-square of the water surface wave height, σ_{RMS}:

$$f_{shm} = (2\pi)^{-1}\{g/[(1.5N + 1)\sigma_{RMS}]\}^{1/2} \tag{2.4}$$

where N is a factor that represents the depth of influence, i.e., the relative vertical extent of the flow field which is affected by a surface deformation.

Validation of the model was performed against the data presented by Horoshenkov et al. (2013) for a range of experimental values of L_0 and U_S (Fig. 2.5). The depth of influence factor, N, calculated by fitting the measured correlation functions, was found to be relatively constant to the value of 28 for a wide range of hydraulic conditions, meaning that the displacements of the free surface could affect the underlying flow down to a depth equal to 28 times the surface height standard deviation. The proposed model could also explain the different responses of the interface to the effects of the sub-surface turbulent field as various kinds of features may be related to the phase of the oscillatory process of the free surface. It was further hypothesised that the production of coherent structures in the near-bed region could be influenced by pressure fluctuations associated with the surface oscillations. For this reason, the simple harmonic frequency was compared to the frequency of near-bed burst event generation, f_B, which was derived from Nezu et al. (1993) as:

$$f_B = U_S/(N_B D) \tag{2.5}$$

where N_B is the normalised bursting period which Nikora and Goring (2000) suggested varying between 1.5-3.0. The two functions f_{shm} and f_B were observed to collapse well for an intermediate value of 2.25, implying that the oscillation period could be directly linked to the near-bed bursting period. It was then suggested that oscillatory behaviour of the free surface could trigger near-bed bursts events through induced pressure fluctuations.

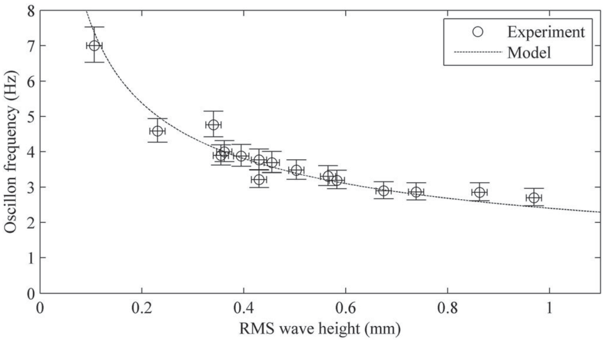

Figure 2.5: Comparison between the measured values (markers) of the surface oscillation frequency for different conditions and the modelled data (dashed line). Derived from Nichols et al. (2016).

Validation attempts of the findings of rather Horoshenkov et al. (2013) and of rather Nichols et al. (2016) were proposed by Legleiter et al. (2017) and by Noss et al. (2020).
Legleiter et al. (2017) defined a model for the surface shape based on the correlation function of Equation 2.2 and rescaled it to simulate the spatial distribution of light shimmering intensities observed from the surface of a river. The modelled river surfaces, however, showed features with wavelengths two orders of magnitude greater than the expected values. Legleiter et al. (2017) indicated that this discrepancy might be because Equation 2.2 does not properly represent the free-surface spatial correlation in a given moment but rather the persistence of advecting features. In Horoshenkov et al. (2013) waves shorter than 30 mm could not be measured due to technical limitations, therefore, Equation 2.2 might not fit well the smaller scales. The water surfaces were also found smoother compared to field observations. A possible explanation was found in the isotropic nature of Equation 2.2 as a single value for L_0 and σ_w was assumed for both the streamwise and spanwise directions. These motivations suggested that Equation 2.2, derived from laboratory investigations, can not be applied directly to large-scale streams.
Noss et al. (2020) created a buoyant device able to keep track of its vertical acceleration while being advecting by a river. The surface elevation in a Lagrangian frame was first derived from the acceleration and then the statistics were compared to the flow parameters observed in a series of experiments in a laboratory flume and in a river. The Lagrangian elevation was characterised by a strong quasi-sinusoidal fluctuating behaviour as predicted by the theory of Nichols et al. (2016). The measured oscillating frequency and amplitude were then fitted with Equation 2.4 but anomalous values of the depth of influence parameter were found. Approximately linear relations between the standard deviation of the drifter elevation and the flow velocity, bulk Froude Number, and bulk Reynolds Number were observed. Data revealed also a strong correlation between the surface statistical moments and the shear velocity, suggesting a connection between the free-surface dynamics and hydraulic resistance.

A similar hypothesis was also proposed by Cooper et al. (2006). In a series of laboratory experiments where the free-surface statistics were derived by means of an ultrasonic sensor higher levels of hydraulic resistance and lower water depths were seen to produce many small laterally elongated boils on the surface, while smaller hydraulic resistances and higher water depths generated rougher water surfaces with fewer but larger surface renewal eddies. The water surface around these boils appeared also much flatter.

Excitation of Gravity-capillary Waves through Resonance

The theory of gravity-capillary waves describes the behaviour of the free surface of an incompressible fluid without viscosity under the stabilising effects of gravity and surface tension. For this theory, a weakly deformed surface can be seen as a linear combination of mutually independent sinusoids (waves). For each wave it is possible to identify a frequency, f, and a wavenumber vector $\boldsymbol{k}$ with modulus $k = 2\pi/\lambda$, where λ is the wavelength. The wavenumber vector defines the direction of propagation of the wave, while the wave celerity, c, derives from the ratio between the frequency and wavenumber modulus, $c = 2\pi f/k$. The celerity of gravity-capillary waves depends on the wavenumber, the flow depth and the mean flow velocity distribution. The relationship between frequency and wavenumber is named the dispersion relation. Assuming a constant depth (therefore neglecting the bed roughness) and a purely gravity-driven flow, the dispersion relation of gravity-capillary waves can be derived either analytically or numerically for a variety of average velocity vertical profiles, e.g.linear (Biesel, 1950), power-function (Fenton, 1973) or more generic (Ellingsen & Li, 2017). When the shear-rate is small (Shrira, 1993), the wave frequency can be simplified as:

$$2\pi f(k) = \boldsymbol{k} \cdot \boldsymbol{U_S} \pm kc_i(k) = \boldsymbol{k} \cdot \boldsymbol{U_S} \pm k[(g/k + Tk/\rho_f)\tanh(kD)]^{1/2} \tag{2.6}$$

where $\boldsymbol{U_S}$ is the flow velocity vector at the surface, $c_i(k)$ is the intrinsic celerity and D is the water depth.

Two solutions with opposite signs are available, each one representing waves propagating in opposite directions. The intrinsic celerity $c_i(k)$ in Equation 2.6 defines the speed of propagation of the waves relative to the mean flow. For depths larger than $2(T/\rho_f g)^{1/2} = 5.5$ mm, it happens for a given wavelength that the dispersion governed by gravity equals the dispersion caused by capillarity, resulting in no wave dispersion. For this case, $c_i(k)$ presents a minimum of approximately 0.23 m/s as gravity and surface tension balance at $\lambda \approx 1.7$ cm (Lamb, 2005). Waves propagating with a celerity lower than the minimum phase velocity cannot exist as the stabilising forces of gravity and surface tension prevent them from appearing. Longer waves are only governed by gravity and their maximum celerity is $(gD)^{1/2}$.

Even when the forcing mechanisms are weak, infinitesimal perturbations can grow to waves of finite amplitude thanks to resonance phenomena (Brocchini & Peregrine, 2001). The resonance usually takes place when the speed of a disturbance matches the celerity of free waves. A disturbance within the flow at height z propagating parallel to the flow at the time-averaged local speed $U(z)$, where $0 < U(z) < U_S$, meets the resonance conditions when:

$$U(z) = U_S + c_i(k)/\cos(\theta) \tag{2.7}$$

where θ is the angle of propagation of the wave with respect to the flow direction.

Only waves moving against the flow ($\theta < 0$) can resonate as long as $U_S > 0.23$ m/s. For a given wavenumber k, Equation 2.7 defines a height z, called critical layer depth, where the resonance can occur. Depending on the nature of the disturbance and the characteristics of the velocity profile at the critical layer, the surface can become unstable, leading to wave growth.

This mechanism, known as "shear instability" or "critical layer instability", received numerous theoretical and numerical studies (Yih, 1972; Caponi et al., 1991; Morland et al., 1991; Young & Wolfe, 2014), but has never been experimentally validated for a sheared fluid below the free surface.

Another form of resonant wave growth was numerically analysed by Teixeira and Belcher (2006). In their model the disturbance, initially consisting in a homogeneous turbulent pressure field, interacted with the interface of an infinitely deep constantly sheared flow according to a rapid distortion formulation. At the first stages of its evolution, turbulence promoted the resonant growth of free waves with the same celerity and wavelength of the pressure fluctuations, while it redistributed its energy across directions and scales as it approached the surface. The stabilisation of the wave amplitude was interpreted as evidence of waves not satisfying the resonance condition due to on their dispersion relation and forced to follow the speed of the pressure disturbance, $c(k) \approx U(z)$.

Following Equation 2.7 and the existence of a minimum of $c_i(k)$, the critical layer can occur only between the bed position and a maximum height z, where $U_S - U(z)$ results greater than 0.23 m/s. For typical subcritical open-channel flows, the surface-relative velocity $U_S - U(z)$ is small in the upper half of the flow, therefore, the critical layer can only be relatively far from the surface and in proximity of the bed. As resonant pressure and free-surface fluctuations must be distant from each other, the strength of their interaction is small. Considering a similar value for U_S, a shallower depth produces a shorter distance of the critical layer from the surface. In the same manner, when the surface velocity increases the critical layer moves towards the surface, allowing a broader spectrum of waves to satisfy resonance conditions.

Savelsberg et al. (2006) investigated the relation between the free surface and the underlying hydrodynamics. In their study the free surface was defined via the space-time surface gradient field obtained through a laser scanning technique. The free-surface gradient was preferred over the elevation as the spectral energy of the former decays much slower than the latter for increasing wavenumber. This allowed greater accuracy in the measurement of the smaller features. Spatial auto-correlations at time-lag 0 of the surface gradient rapidly decreased for larger spatial lags, in particular along the transverse direction. The auto-correlation also oscillated between positive and negative values as seen in Horoshenkov et al. (2013). The Taylor's frozen turbulence hypothesis was tested using time series of the surface gradient in the spanwise direction. From the analysis it resulted that the hypothesis was not valid for the free surface above a turbulent flow but held for the underlying velocity field. The cause was ascribed to the presence of gravity-capillary waves that Savelsberg et al. (2006) linked with the turbulent velocity field beneath the surface as the wavelength of the waves was similar to the integral scale of the turbulent velocity.

The strength of the correlation between the surface and the underlying turbulence was later evaluated in Savelsberg and Van De Water (2008). In their experiments the free surface was characterised by small deformations (mainly shallow and rounded wrinkles) despite an active grid generating relatively strong turbulence. The free surface gradient was correlated with the normalised convective acceleration, $(\boldsymbol{u}\cdot\nabla)\boldsymbol{u}$, where $\boldsymbol{u}$ is the turbulence velocity vector. For a fully developed turbulent condition the correlation function resulted rather small (0.04). The absence of a strong correlation between the gradient of the free surface and the underlying turbulent velocity field implied the independence of free-surface dynamics. The convective acceleration was later decomposed into two terms representative of strain and rotation which were both correlated with the surface gradient field. Strain correlation was seen to be twice than the rotation correlation, suggesting a predominance of upwellings and downwellings than vertical vortices. The energy spectrum of the surface gradient showed features with relatively small wavenumbers advecting at the mean flow velocity. These waves were outweighed by other patterns which approximately followed the dispersion relation for gravity-capillary waves. The wavelength of the gravity-capillary waves was similar to the longitudinal integral length scale of the sub-surface turbulence field. This suggested that the free surface was mostly excited by the largest sub-surface turbulence scales. Spatial correlation of the streamwise and spanwise surface gradient at different locations had an isotropic behaviour when the turbulence was isotropic and were anisotropic when turbulence was the same. In conclusion, Savelsberg and Van De Water (2008) found that gravity-capillary waves dominated the surface. The free surface also inherited the integral length scale and anisotropy from the sub-surface turbulence for lower wavenumbers, while the surface displayed an independent behaviour for higher wavenumbers.

This research was further extended in Savelsberg and Van De Water (2009). Here, the amplitude of surface gradient fluctuations was seen to correlate with the turbulent Reynolds Number. The wavenumber spectrum for the free-surface gradient presented a steep decrease proportional to k^{-6}. They also observed a small dependence on Reynolds Number for the phase velocity along the spanwise direction for the active grid case. Finally, the length scales of the surface gradient and the integral scales of the sub-surface turbulence resulted non-proportional for both the cases of active and passive grids, probably caused by the different manner of mechanical agitation.

Image-based methods rely on the assumption that the free-surface patterns are advected with the surface velocity. As waves can also be dispersive significant errors are likely to occur in the surface velocity estimations. Tani and Fujita (2018) analysed Space-Time Images (STI) (Fujita & Tsubaki, 2002; Fujita et al., 2007) of orthorectified flow videos of the surface of rivers. The Fourier transform in space and time of this data was used to derive the frequency-wavenumber spectra of the surface elevation. It was discovered that the most of the spectral energy laid along the dispersion relations of both turbulence and gravity-capillary waves. This represented a clear evidence of the presence of gravity-capillary waves on the surface, undermining the initial hypothesis of the propagating wave texture. Gravity-capillary waves were then removed by applying a filter and obtaining a noticeably improvement in the accuracy of the flow velocity estimates via the STI method.

Topography-induced Stationary Waves

The appearance of waves at the surface of a flow over topography has been studied extensively, also beyond linear theory, but mostly limited to the steady case, with localised topography, and for an irrotational flow. An extensive review of such studies is Aksel and Schörner (2018).

A small bed roughness element can be interpreted as a perturbation of a flat bed. Similar in concept to a pressure perturbation, waves with a range of wavelengths and directions of propagation can be excited by the bed, including forced evanescent waves and free resonant waves (Harband, 1976). As the disturbance occurs where $U(z) = 0$, the resonant waves must be fixed in time and have frequency $f = 0$. This can only happen when waves propagate against the flow at the same speed at which they are advected. Following Equation 2.7 it must be that:

$$c_i(k) = -U_S \cos(\theta). \tag{2.8}$$

These waves are called stationary waves but are also known as standing waves (Rayleigh, 1883). As 0.23 m/s represents the minimum phase velocity of a gravity-capillary waves it is obvious that a solution for Equation 2.8 is only possible when $U_S > 0.23$ m/s. Slower surface velocities result in waves propagating also upstream, even when moving against the flow. Equation 2.8 also defines a specific relation between wavenumber and angle of propagation. When the bed disturbance is localised in space, all waves satisfying this relation concur in causing a peculiar wake-pattern in the far-field, like the one produced by a moving ship. However, when the bed roughness is homogeneous, stationary waves can combine incoherently without producing a recognisable waveform.

Stationary waves were generally associated with spatial variations of the bed shear stress and formation of three-dimensional bed forms over mobile beds (Chanson, 2000). A few useful relations to estimate the wavelength and amplitude of stationary waves have been reviewed by Chanson (2000). For a given surface velocity, the stationary wave with the largest wavelength is the gravity wave with the crest perpendicular to the flow ($\theta = 180°$). This wave can form only if the flow is subcritical, i.e. 0.23 m/s $< U_S < (gD)^{1/2}$. Dolcetti and García Nava (2019a) derived the wavelength of this flow-perpendicular stationary wave, λ_0, for a power-function velocity profile ($U(z) \propto z^n$, where n is the exponent of the power-function) as:

$$\lambda_0/D = 2\pi Fr_0^2\{[I_{-(0.5+n)s}(2\pi D/\lambda_0)]/[I_{(0.5-n)s}(2\pi D/\lambda_0)]\} \tag{2.9}$$

where $Fr_0 = U_S/(gD)^{1/2}$ is the Froude Number based on the free-surface velocity, I_φ is a modified Bessel function of the first kind of degree φ and $s = \mathrm{sgn}(0.5 - n)$ is the result of the sign function.

Equation 2.9 can be simplified assuming short (relative to the depth) waves and a velocity profile with constant shear, i.e. $U(z) \propto nz$, as (Teixeira, 2019):

$$\lambda_0/D = 2\pi Fr_0^2/(1 + nFr_0^2). \tag{2.10}$$

A Fourier analysis similar to the one used by Savelsberg and Van De Water (2009) was applied by Dolcetti et al. (2016) to two orthogonal arrays of wave gauges in a laboratory flume with a bed formed by 25.4 mm wide regular spheres. The frequency-wavenumber spectra of the surface elevation were interpreted based on a linear wave model for a power-function velocity profile (Fenton, 1973; Burns, 1953). The behaviour of longer waves could be evaluated more clearly here than in Savelsberg and Van De Water (2009) due to a larger measurement area.

Whenever the free-surface velocity was greater than 0.23 m/s) stationary waves were clearly identified by a peak of the frequency-wavenumber spectrum at $f = 0$. According to Equation 2.8 stationary waves can have different combinations of wavenumber and directions, however, only stationary waves with their front perpendicular to the direction of the flow were observed. Also, the wavelengths of these waves were predicted well by Equation 2.10. These stationary waves resulted in dominant features on the free surface despite the absence of localised obstacles at the bed. As observed by Horoshenkov et al. (2013), the spatial correlation of the surface elevation fluctuated in space, but here with the wavelength λ_0 instead of L_0.

The frequency-wavenumber spectra measured by Dolcetti et al. (2016) can be observed in Figure 2.6. The energy resulted concentrated along specific lines (an almost straight line in the streamwise spectrum and an ellipse in the lateral spectrum). These lines correspond approximately to the projections of the ellipse in red in Figure 2.7, which represents the dispersion relation of waves with constant wavelength λ_0 and with θ that varies in all directions. Posing $k_0 = 2\pi/\lambda_0$ as the wavenumber of the stationary wave with wavelength λ_0, the frequency of these waves is found from Equations 2.6 and 2.8 as:

$$f(k_0) = k_0 U_S[1 + \cos(\theta)] = (k_0 + k_x)U_S \tag{2.11}$$

where k_x is the streamwise component of vector $\boldsymbol{k_0}$.
For $\theta = \pi$, $f(k_0) = 0$, resulting in a stationary wave. When $\theta \neq \pi$, the gravity-capillary waves are freely propagating and $f(k_0) > 0$. Similar patterns in the spectra could not be observed when $U_S < 0.23$ m/s. In this case, the spectra identified forced waves advecting at the mean flow velocity together with freely propagating gravity-capillary waves.
Dolcetti et al. (2017) suggested that forced waves can still occur (at least in the capillary range) together with stationary waves and that their amplitude grows faster with the increasing Froude Number than the amplitude of free waves (hypothesis later confuted by Yoshimura and Fujita (2020)). Dolcetti et al. (2016) discovered that the Froude Number decreased the steepness of the surface frequency spectra, suggesting higher contribution of shorter scales and so rougher surface textures at higher Froude Numbers.

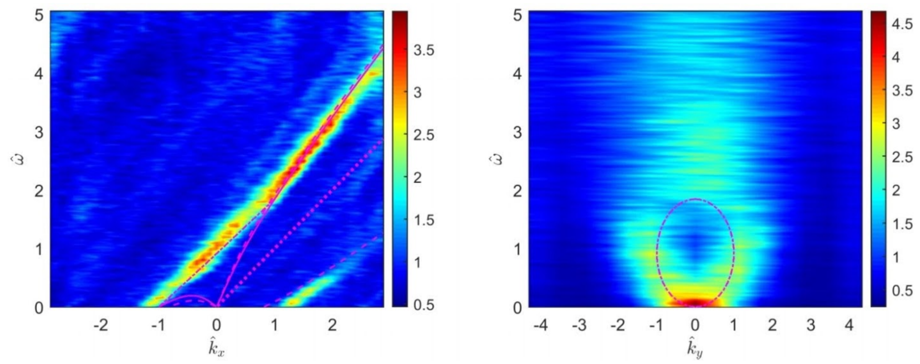

Figure 2.6: Streamwise (left) and spanwise (right) non-dimensional frequency–wavenumber spectra for the case $U_S > c_{min}$. Frequency and wavenumber were non-dimensionalised using the wavenumber of the stationary wave, k_0. The contours were non-dimensionalised to compensate for the decay with frequency. Reproduced with authorisation from Dolcetti et al. (2016).

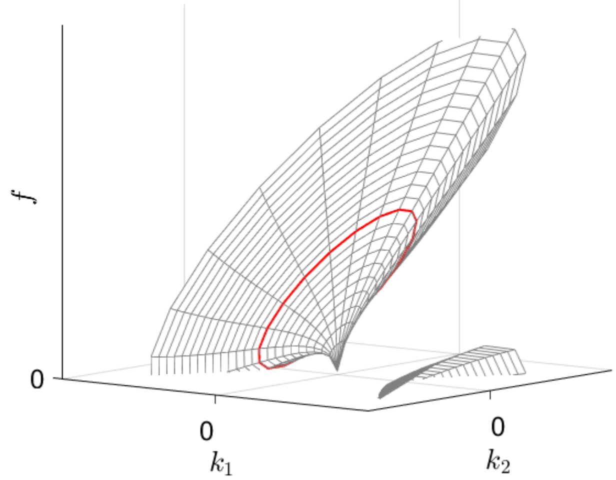

Figure 2.7: Representation of the three-dimensional dispersion relation shell (Eq. 2.6). k_x and k_y are the components of the wavenumber vector in the streamwise and lateral directions, respectively. The two surfaces represent the two solutions for upstream and downstream propagating waves. The red line indicates the frequency of the waves with wavelength λ_0 for different directions of propagation. Reproduced from Muraro et al. (2021).

Like Savelsberg and Van De Water (2009), Dolcetti et al. (2016) explained the presence of forced waves via the mechanism described by Teixeira and Belcher (2006). However, when the appropriate conditions are met, stationary waves are seen to dominate the free surface. The scaling of the correlation function and of the dynamic surface fluctuations with the wavelength λ_0 also indicated the importance of stationary waves. These findings highlighted a role of the bed topography much stronger than previously thought.

The same data set of Dolcetti et al. (2016) was evaluated with a wavelet-based analysis by Dolcetti and García Nava (2019b). The wavelet-based analysis provided a better three-dimensional representation of the frequency-wavenumber spectra, allowing a more detailed characterisation of the surface patterns. It was also possible to define the angular spectrum of the waves with wavenumber k_0. Applying the framework suggested by Legleiter et al. (2017), Dolcetti and García Nava (2019b) proposed a simplified surface model based on an inverse Fourier transform of a surface spectrum, $S_S(k, \theta)$, described by:

$$S_S(k, \theta) \propto \exp\{b[\cos(\theta - \pi) - 1]\}\delta(k - k_0) \tag{2.12}$$

where b is an angular distribution parameter which was found varying between 1 and 2, and δ is a delta-function that excludes all waves with wavelength different from λ_0 from the model. According to this model the free surface could be described as a linear combination of freely propagating waves with the same wavelength λ_0 but different direction of propagation. The model also allowed Dolcetti and García Nava (2019b) to explain the oscillating behaviour of the space-time correlation function observed by Horoshenkov et al. (2013). The model was further improved by Dolcetti et al. (2020), producing a series representation of the full spatial-temporal correlation:

$$\begin{aligned} W(\rho, \tau) = {} & a_0 J_0(k_0|\boldsymbol{\rho} - \boldsymbol{U_S}\tau|)\cos(k_0 U_S \tau) + \\ & + \sum_{\varphi=1}^{\infty} a_\varphi (-1)^{\varphi/2} \Big[J_\varphi(k_0|\boldsymbol{\rho} - \boldsymbol{U_S}\tau|)\exp(-ik_0 U_S \tau) + \\ & + J_\varphi(-k_0|\boldsymbol{\rho} - \boldsymbol{U_S}\tau|)\exp(ik_0 U_S \tau) \Big] \end{aligned} \tag{2.13}$$

where a_φ are the series coefficients that depend on the angular spectrum and J_{varphi} is the Bessel function of the first kind of order φ.

Dolcetti et al. (2020) made use of this equation to interpret the autocorrelation of images of the interface of a shallow river. Similarly to laboratory measurements, the river surface slope spectra (Lubard et al., 1980) reported waves with wavelength λ_0. The measured correlations oscillated in space and time and were matched by the behaviour of the trigonometric and Bessel functions in Equation 2.13.

According to the model of Dolcetti and García Nava (2019b) an observer moving along the flow at the mean surface flow velocity U_S should observe a periodic inversion of the surface shape, η:

$$\eta(x = U_S t, t) = A\cos[k_0 U_S(t - t_0)] \tag{2.14}$$

with A being the wave amplitude and t_0 the initial time step.

This behaviour resembled to the one proposed by Nichols et al. (2016), where the fluctuations occur with frequency $f_{shm} = U_S/L_0$. The model also derived a frequency of $K_0U_S/(2\pi) = U_S/\lambda_0$ for flow conditions examined by Noss et al. (2020), explaining the quasi-periodic fluctuations observed by the drifter.

A comparison of the characteristic surface frequencies observed by Nichols et al. (2016), Dolcetti and García Nava (2019b) and Noss et al. (2020) with the ones proposed by the model of Dolcetti and García Nava (2019b) are reported in Figure 2.8 (Muraro et al., 2021). In the picture the non-dimensionalised stationary wave wavelength λ_0/D (derived from both Equations 2.9 and 2.10 for two velocity profile having exponents, $n = 0$ and $n = 0.5$) was plotted with the corresponding equivalent wavelengths observed by Nichols et al. (2016) and Noss et al. (2020), derived as:

$$\lambda_0/D = U_S/(f_{shm}D) = L_0/D. \tag{2.15}$$

The three data sets were well fitted by the model, although different exponents for the power-function velocity profile were needed for matching the data. In fact, using two different velocity profiles allowed to define a region in which the predictions were in a agreement with observations. It was hypothesised that stationary waves may control the scales of the surface deformation over

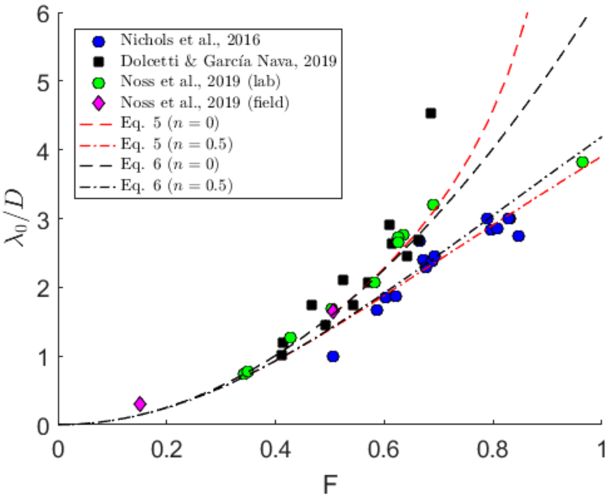

Figure 2.8: Non-dimensionalised dominant surface scale measured by Nichols et al. (2016), Dolcetti and García Nava (2019b) and Noss et al. (2020) compared to the wavelength of stationary waves predicted by Equation 2.9 (power-function velocity profile) and Equation 2.10 (constant-shear profile and short waves) with power-function exponent $n = 0$ and $n = 0.5$. The frequency values measured by Noss et al. (2020) have been converted to an equivalent spatial scale as $\lambda_0 = U_S/f_{shm}$. Fr is the bulk Froude Number. After Muraro et al. (2021).

a broad range of hydraulic regimes. The bed roughness forcing was then suggested to be the governing mechanism for the generation of the free-surface wave pattern rather than turbulence as previously suggested (Fujita et al., 2011; Horoshenkov et al., 2013; Nichols et al., 2016). Nonetheless, it was not possible to determine the cause for the selective growth of waves with wavelength λ_0 not oriented against the flow (i.e. not stationary waves). Dolcetti and García Nava (2019b) invoked the triad resonance mechanism proposed by Zakharov and Shrira (1990). This mechanism allows the transfer of energy between a stationary wave, a freely propagating wave with the same wavelength, and a forced wave or a (turbulent) sub-surface flow perturbation. To produce a resonant interactions among multiple waves a deviation from linear theory is required. This seems possible as Dolcetti (2016) reported a weakly non-Gaussian probability distribution of the surface elevation. However, the measurements of the surface spectrum broadening are contradicting (Dolcetti & García Nava, 2019b) and the triad resonance theory is based on a hypothesis that does not rigorously apply to shallow flows.

2.3 Flows over Permeable Beds

Flows over permeable beds are ubiquitous as almost all of the geophysical natural flows but also a wide number of industrial processes occur above boundaries formed by porous and permeable materials. In industry, porous media are known to promote heat, chemical and mass transfers due to their larger specific surface area. For these reasons, they are often employed in nuclear plants (El Hassan et al., 2015), fuel cells (Wang et al., 2001), catalytic reactors and heat exchangers. On the environmental side, permeable beds play a significant role in sediment transport (Garcia, 2008; Hester et al., 2013), turbulence generation (Best, 2005), morphodynamics (Harrison & Clayton, 1970), water quality aspects (Nagaoka & Ohgaki, 1990; Svensson & Rahm, 1991; Nakamura & Stefan, 1994), scalar transfers (Boano et al., 2014), spawning habitats (Gayraud & Philippe, 2003; Arntzen et al., 2006), coastal defence, chemical exchanges between vegetation and atmosphere (Finnigan, 2000) and meteorological as, to some extent, even urban areas can be considered as permeable walls.

Despite the great importance and interest towards this kind of flows, the physics of flows overlying permeable surfaces is not as well understood as over an impermeable boundaries. In particular, the interaction between the free-surface region and the porous media has not sufficiently been investigated. For open-channel flows, most of the numerical studies involved laminar flows (Beavers & Joseph, 1967; Rudraiah, 1985; Choi & Waller, 1997), while a limited number of simulations explored turbulent conditions, probably due to the high computational cost and difficulties in properly define the conditions at the interface (Mendoza & Zhou, 1992). Similarly, experiments suffered and still suffer due to technical difficulties in the observation of the flow quantities in the near-bed region and within the porous bed. Over the last 20 years, advances in technology and development of new techniques allowed to improve the quality of both experimental observations and simulations. Nonetheless, it was not possible to obtain an exhaustive understanding of dynamics over permeable beds. Different viewpoints have emerged, some of them completely contrasting each other, therefore, only speculations can be advanced. The reason is due to the complex behaviour of the flow in near-bed and subsurface regions, which is highly affected by wall characteristics. For this reason, a comprehensive investigation of the turbulent flow behaviour above pervious beds would require a broad range of bed surface geometries, roughness types, grain size distributions, bed thickness, porosity, permeability, slopes and submergences to be tested, which is unfeasible for the time and costs involved.

It is common practice to treat a permeable bed like an impermeable boundary having the same surface texture and infer the velocity, stress and pressure distributions, and friction and diffusion coefficients regardless of the effects of bed porosity (Stoesser et al., 2006). This assumption is extremely simplifying as the flow that moves through the porous media and the one in the overlying region interact in a complex manner, giving rise to weaker or stronger accordingly to the wall permeability. Examples of such a influence are the slip velocity (i.e. the non-zero velocity that occurs over rough beds in correspondence of the top of the bed elements) and turbulent exchanges of mass and momentum, which are responsible for additional shear stresses in the near-bed region (Nezu, 1977).

Another spread custom consists in evaluating the two regions as separate, assuming turbulent flow above the bed and an underlying Darcian flow (Cardenas & Wilson, 2007; Jin et al., 2010; Janssen et al., 2012). The coupling is then attempted by imposing mass, velocity and pressure vertical continuity. This approach is inaccurate as a small change in the boundary conditions would severely compromise the quality of the coupling as small variations in one field can have important consequences for the other (Gupta & Paudyal, 1985; Pokrajac & Manes, 2009).

The most relevant experimental, numerical and analytical studies of the characteristics of a turbulent flow over a permeable bed are presented over the next pages. Subsection 2.3.1 presents the approach introduced by Nikora et al. (2001) for correctly evaluating open-channel flows over permeable rough boundaries, while Subsection 2.3.2 treats the flow behaviour in the free flow region above the bed.

2.3.1 Spatially-averaged Equations

Open-channel flows over rough beds (either impermeable or permeable) cannot be fully described by the traditional Reynolds equations (time-averaged Navier-Stokes equations) (Nikora et al., 2001). This occurs as near the bed the heterogeneity of the interface and the three-dimensional behaviour of the flow lead to a violation of some preliminary assumption for the Reynolds equations (2D approximations and similarity) and so a rigorous assessment of this region. Reynolds equations can still be used to describe most of the depth for large depth-roughness height ratios flows over rough beds. However, the near-bed region of these flows and low submergence flows must be described using a different set of equations.

Spatial averaging was first introduced for multiphase systems in porous media flows by Whitaker (1967) and Gray (1975). Later, Smith and McLean (1977) and Wilson and Shaw (1977) suggested applying a further spatial averaging procedure (either areal or volumetric) to the Navier-Stokes equations. However, only recently double-averaging was extended to open-channels flows (Nikora et al., 2001). The main advantage of this approach is that flow quantities are spatially averaged and can be related to roughness parameters from the averaging of the same spatial domain. The bed heterogeneity is therefore on average incorporated in these equations.

To obtain the spatially-averaged equations, the first step consists in the definition of the spatial-averaging procedure. Following Smith and McLean (1977), Raupach and Shaw (1982) and Giménez-Curto and Lera (1996), the areal averaging at a generic height z is given by:

$$\langle V \rangle(x, y, z, t) = \frac{1}{A_f} \int_{A_f}\!\!\int V(x', y', z, t)\, dx'\, dy' \tag{2.16}$$

where V represents a flow quantity defined in locations not occupied by the bed roughness, angle brackets explicit the spatial averaging procedure, A_f is the area occupied by the fluid on the plane z considered with the total area A_0. For the reference system, x is orientated along the main flow direction, y defines the spanwise direction, while z points normally the bed; from these direction the corresponding velocities are u, v and w. Finally, t defines time. In the integrand it was chosen to replace (x, y) with (x', y') to emphasise that the dependence of $\langle V \rangle$ in (x, y) is only due to domain variations within (x, y).

Given the generic Reynolds equation expressed in tensor notation:

$$\frac{\partial \bar{u}_i}{\partial t} + \bar{u}_i \frac{\partial \bar{u}_j}{\partial x_i} = g_i - \frac{1}{\rho} \frac{\partial \bar{p}}{\partial x_i} - \frac{\partial \overline{u_i' u_j'}}{\partial x_j} + \nu \frac{\partial^2 \bar{u}_i}{\partial x_j^2}, \tag{2.17}$$

where overbar denotes time-averaging and the prime is used for the turbulent component (i.e. difference between instantaneous and time-averaged components), g is gravitational acceleration, p indicates pressure and ν kinematic viscosity, and applying Equation 2.16 to Equation 2.17, it is possible to obtain two different spatially-averaged equations according the z plane that is considered with regards to the elevation of the highest roughness crest, z_c. For the region above the bed, $z > z_c$:

$$\frac{\partial \langle \bar{u}_i \rangle}{\partial t} + \langle \bar{u}_i \rangle \frac{\partial \langle \bar{u}_j \rangle}{\partial x_i} = g_i - \frac{1}{\rho} \frac{\partial \langle \bar{p} \rangle}{\partial x_i} - \frac{\partial \langle \overline{u_i' u_j'} \rangle}{\partial x_j} - \frac{\partial \langle \tilde{u}_i \tilde{u}_j \rangle}{\partial x_j} + \nu \frac{\partial^2 \langle \bar{u}_i \rangle}{\partial x_j^2}. \tag{2.18}$$

Wavy overbar (tilde) indicates a disturbance in the variable given by the difference between the time-average and the double-averaged component.

For the region beneath the roughness crest, $z < z_c$:

$$\frac{\partial \langle \bar{u}_i \rangle}{\partial t} + \langle \bar{u}_i \rangle \frac{\partial \langle \bar{u}_j \rangle}{\partial x_i} = g_i - \frac{1}{\rho} \frac{\partial \langle \bar{p} \rangle}{\partial x_i} - \frac{1}{A} \frac{\partial A \langle \overline{u_i' u_j'} \rangle}{\partial x_j} - \frac{1}{A} \frac{\partial A \langle \tilde{u}_i \tilde{u}_j \rangle}{\partial x_j} + \nu \frac{\partial^2 \langle \bar{u}_i \rangle}{\partial x_j^2} + \nu \left\langle \frac{\partial^2 \tilde{u}_i}{\partial x_j^2} \right\rangle - \frac{1}{\rho} \left\langle \frac{\partial \tilde{p}}{\partial x_i} \right\rangle. \tag{2.19}$$

Here, A represents the ratio of area occupied by fluid to the total area A_0.

Similarly, the same procedure can be applied to the continuity equation. From the form used in the Reynolds equation:

$$\frac{\partial \bar{u}_i}{\partial x_i} = 0, \tag{2.20}$$

it derives:

$$\frac{\partial \langle \bar{u}_i \rangle}{\partial x_i} = 0 \quad \text{for} \quad z \geq z_c \tag{2.21}$$

$$\frac{\partial A \langle \bar{u}_i \rangle}{\partial x_i} = 0 \quad \text{for} \quad z < z_c \tag{2.22}$$

Differently from Equation 2.17, Equations 2.18 and 2.19 contain additional terms:

- $\langle \tilde{u}_i \tilde{u}_j \rangle$ is result of spatial averaging and it is due to spatial disturbances in the time-averaged flow. This term is known as "dispersive stress" (Wilson & Shaw, 1977) or "form-induced stress" (Giménez-Curto & Lera, 1996).
- $(1/\rho)\langle \partial \tilde{p} / \partial x_i \rangle$ represents the form drag, while $\nu \langle \partial^2 \tilde{u}_i / \partial x_j^2 \rangle$ is the viscous drag; both only appear in the equation valid beneath the roughness crest.

Note that the averaging-order (either time+space or space+time) is influential as it yields to identical formulations (Pedras & De Lemos, 2001).

The vertical section of a flow overlying a pervious bed can be subdivided in multiple regions according to the framework proposed by Nikora et al. (2001). Depending on the appearance and importance of terms not observable for flows over smooth and impermeable surfaces, five regions can be identified as depicted in Figure 2.9:

1. outer layer: the most superficial region where viscous and form-induced terms are negligible, so that spatially-averaged and time-averaged equations are equal. Following Nezu et al. (1993) approach, this region corresponds to the near-surface and intermediate regions and behaves similarly to the outer region for open-channel flows over smooth surfaces as velocity distributions can be derived from the velocity defect law as suggested by Hinze (1987).
2. logarithmic layer: viscous and form-induced terms are still negligible and spatially-averaged and time-averaged quantities are similar. The layer resembles the logarithmic layer for flows over smooth surface. Velocity distributions follow the logarithmic behaviour as long as time-averaged velocities are considered (Raupach et al., 1991). Differently for the above layer, the logarithmic layer might not be observed as for its existence the deepest observable depth, H, (distance between the free surface and the troughs of the roughness) must be much greater than the height of the roughness elements, Δ. If this occurs, then the logarithmic layer is present between $(2-5)\Delta < (z - z_t) < 0.2H$.
3. form-induced layer: this region is affected by viscous and form-induced effects due to the flow separation from the roughness elements (Giménez-Curto & Lera, 1996). For this reason, it can be considered analogue to the buffer sublayer in smooth beds. This layer is bounded between the bed roughness crests and whichever above layer (either outer or logarithmic layer) and represents the portion $0 < (z - z_c) < (1-4)\Delta$. Typically, the upper boundary of this layer can be identified using either the dispersive shear stress $-\langle \tilde{u}\tilde{w} \rangle$ or the variance of time-averaged streamwise velocity $-\langle \tilde{u}\tilde{u} \rangle$.
4. interfacial layer: region affected by viscosity, bed heterogeneity and form drag. It is similar to the viscous sublayer over smooth beds. This layer occupies the region between the top and the bottom of the roughness elements. More precisely, the region when porosity is observed changing from the unity value in the free-flow region to a constant value within the pervious boundary.
5. subsurface layer: the most profound region where the flow is driven by gravity and mo-

mentum fluxes from above. The flow is governed by the Darcy, Forchheimer and Brinkman equations.

In literature, outer and logarithmic layers are often together represented as surface flow region; similarly, form-induced and interfacial layers are mostly not individually considered but grouped to form the roughness layer (also know as roughness sublayer (Raupach et al., 1991)).

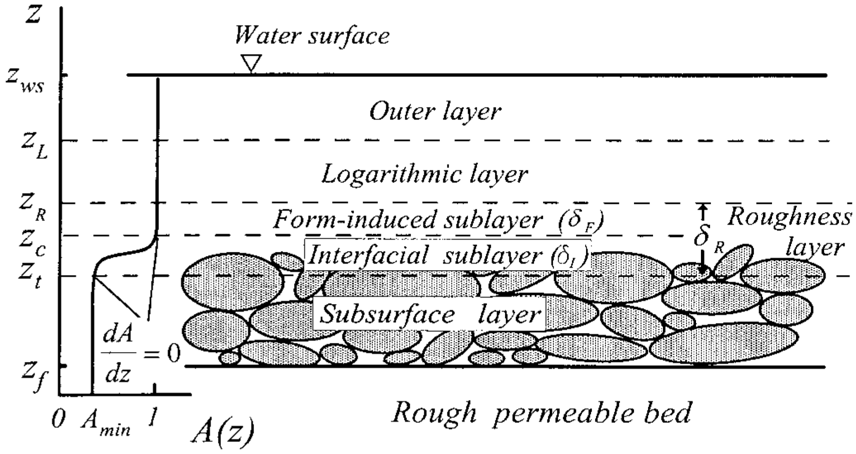

Figure 2.9: Layer subdivision for flows over a permeable rough beds. Notice, z_{ws} represents the height of the water surface, z_c is the height of the roughness crest, A is a function that for rough permeable beds is equal to porosity. After Nikora et al. (2001).

In consideration of the relative smoothness, H/Δ, different layers can coexist:

- flow with high relative submergence, $H > \Delta$: all the layers exist.
- flow with small relative submergence, $(2-5)H\Delta > H > \Delta$: the most superficial layers cannot exist and the form-induced layer represents the upper flow region.
- flow over partially inundated rough bed, $H < \Delta$: interfacial layer is the upmost layer.

Double-averaging approach is a powerful expedient to investigate the flow dynamics in the near-bed region where the high heterogeneity of the interface and the complexity of the flow field cause the Reynolds equations to no longer hold. In fact, local flow properties can often change in space, the use of double averaging, however, establishes global uniformity as it is imposed the flow properties do not vary along the streamwise direction (Nikora et al., 2004).

For this reason Nikora et al. (2001) suggested its use should become a standard in the evaluation of open-channel flows over rough (either pervious or impermeable) beds.

2.3.2 Surface Flow

The flow over a permeable bed presents a series of particularities compared to the same hydraulic condition over a bed having the exact same roughness texture but impermeable. One of the most peculiar features is probably the streamwise velocity profile (Fig. 2.10), characterised by larger deviations from the shape typically encountered over an impermeable surface as the solid interface is approached. Not only, a permeable bed allows a subsurface flow, therefore a non-zero velocity within the bed, to exist. As velocity continuity must be ensured throughout the section, the velocity profile varies from the velocity values defined by the logarithmic law (and relative corrections) in the free-flow region to values described by Darcy's law for flows into porous boundary. This permits the appearance of non-zero velocity values at the interface.

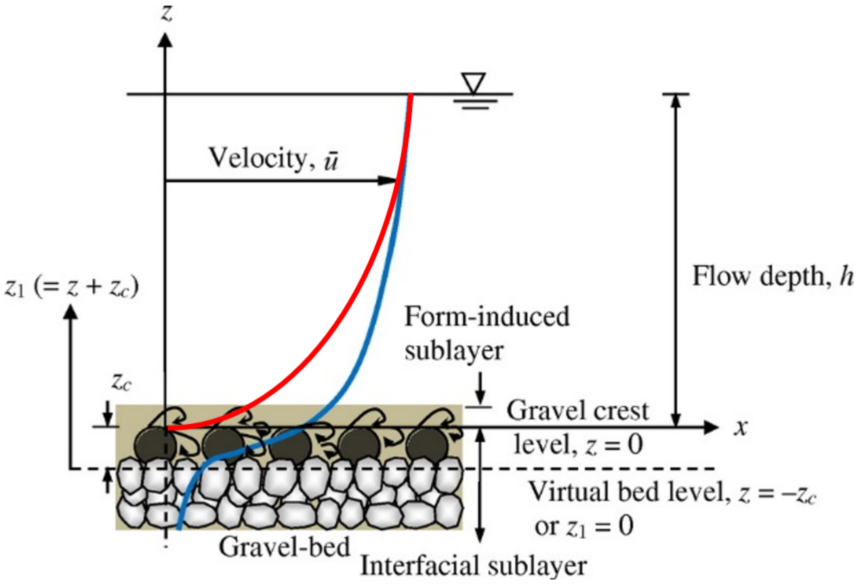

Figure 2.10: Velocity profiles over a permeable (blue) and impermeable beds (red). Typically, velocity profiles over permeable bed are considered analogue to the ones over impermeable surfaces. Modified from Dey and Das (2012).

Munoz Goma and Gelhar (1968), Ruff and Gelhar (1970) and Chu and Gelhar (1972) are considered pioneering studies on interaction of a turbulent flow with a permeable boundary. Despite the technical limitations of the time, they observed the friction factor to maintain a dependency with the Reynolds Number, that additional Reynolds stress arose due to the porous interface and that the velocity profile was well fitted by the logarithmic law as long as the von Kármán constant, κ, ranged between 0.26 and 0.29.

Other earlier investigations by Lovera and Kennedy (1969), Zagni and Smith (1976) on open-channel flows revealed larger values for the friction coefficient over permeable rough beds compared to impermeable ones with the same texture. Lovera and Kennedy (1969) and Zagni and Smith (1976) further observed the friction factor, after having reached a plateau, started increasing again with Reynolds Number at $Re = 10^5$. This increment was suggested being a consequence of additional energy dissipation due to momentum exchanges across the bed surface.

Later Zippe and Graf (1983) presented a study on turbulent boundary layers in which impermeable and permeable surfaces were compared. During the experiments, performed in large wind tunnel facility and evaluated by means of Prandtl tubes and anemometers, not only the influence of permeability was tested, but also the effect of the bed thickness for the permeable bed. It was found that the streamwise velocity profiles for all the type of boundaries were well fitted by the Coles' wake law as long as the shear stress was obtained from the momentum balance. The friction coefficient, f, was higher over permeable surfaces compared to impermeable ones having the same texture. For the former, f was observed increasing with the Reynolds Number and the bed thickness. Over impermeable surfaces, the friction factor was independent from Re. Increasing Reynolds Numbers and bed thicknesses also deepened the position where the no-slip condition occurs (plane where the time-averaged streamwise velocity is 0).

Gupta and Paudyal (1985) performed a series of laboratory tests aimed at comparing friction factor and velocity distributions for a turbulent flow over a gravel bed and its corresponding impermeable counterpart. Velocity profiles, measured using a hotwire anemometer, for both types of bed followed the Prandtl-von Kármán universal velocity distribution law (i.e. a logarithmic distribution). However, the logarithmic law had to be vertically adjusted for the permeable bed case in order to take into account the slip velocity at the interface. The von Kármán was observed to be much smaller (0.28) for the rough permeable bed and slightly smaller (0.38) for the rough impermeable boundary, suggesting larger energy dissipation rate in the mean flow. Friction factor was greater over the permeable bed and increased with the Reynolds number.

The effect of a porous interface was analytically evaluated by Mendoza and Zhou (1992) as a perturbation of an equivalent turbulent flow over an impervious bed on the same bed texture. It was suggested that the momentum exchange at the boundary, causes the disappearance of the viscous sublayer and an extension of the turbulent region within the bed. As a consequence, a downwards shift for the origin of the mean velocity logarithmic profile occurs, giving rise to non-zero velocity at the interface. The existence of a porous bed was assumed to also generate larger Reynolds stresses due to the momentum transfer. Mendoza and Zhou (1992) also suggested that additional stresses along the vertical direction give rise to additional mean pressure which enhances the sediment entrainment. The friction factor was found to depend on the water depth, the channel slope and the Reynolds Number. Comparing the Reynolds-averaged Navier-Stokes equations for the permeable and impermeable cases, Mendoza and Zhou (1992) confirmed the findings present in Nezu (1977), that the von Kármán constant for pervious beds is smaller than the value proposed in literature for impermeable beds, i.e. 0.41. This suggested that an active momentum and energy transfer occurs at the porous interface.

An experimental study was proposed in Prinos et al. (2003) where the permeable surface was simulated as a group of transverse cylindrical rods for a range of diameters, arrangements and densities. It was found that the rods arrangement (i.e. the porous layer structure) has limited influence of the flow characteristics in the near-bed region. Mean velocities were observed to be lower throughout the depth when compared with ones over an identical impermeable bed. This trend was accentuated for increasing values of the Darcy Number, Da $= K/H^2$ (K is bed permeability). This was imputed to turbulence penetration within the porous media and associated momentum transfer. The mean velocity were assumed to deviate from the logarithmic law due to κ and the constant of integration. For this reason, it was suggested the flow over a permeable interference cannot be identified as a boundary layer but as mixing layer. The turbulent shear stress increased towards the bed and peaked in correspondence of the interface.

Stoesser et al. (2006) presented a numerical study of a turbulent flow over two layers of cubically-packed spheres. Statistics were evaluated at two different spanwise location: the first section (Top) was directed along the crests of the spheres where the maximum porosity value occurred, while the second section (Valley) ran over the interface between spheres, therefore indicating the minimum porosity plane. Normalised time-averaged streamwise velocity profiles for the two sections released small difference only near the roughness where recirculation due to fluid separation took place in the Top section and a slip velocity was present along the Valley section. As the difference between the sections was minimal, it was assumed a small extension of the roughness layer. All the turbulent velocity intensities peaked in correspondence of the interface due to momentum and mass exchanges across the bed. Quadrant analysis (Raupach, 1981) revealed the dominance of sweep and ejection events. The frequency and magnitude of these events (1/3 of the events were 19 times stronger than the average Reynolds stress) led to the conclusions that sweeps and ejections were the responsible for mass and momentum transfers.

This investigation was later continued in Stoesser et al. (2007) where a bed composed of three layers of cubically arrange spheres was numerically examined. Mean and turbulent velocity components resulted similar to the ones presented in Stoesser et al. (2006). On this occasion, spatially-averaged pressure measurements were evaluated and showed maximum values on the windward side of the spheres along the Top section, with magnitudes up to 4 times the average bed Reynolds stress. No differences in pressure values were seen on the Valley plane from the free-flow region. Pressure maxima along the Top section were attributed to streamwise velocity fluctuations as resembling power spectra were observed.

In Pokrajac and Manes (2009) the comparison between impermeable and permeable beds for open-channel turbulent flow was performed using cubically-packed spheres arranged to form a 1-layer and a 5-layer sphere thick beds. The basic geometry was preferred as it allowed to better characterise the nature of the interaction between surface and underlying flows. Measurements were carried out by means of a Particle Image Velocimetry (PIV) system and, due to the periodicity of the wall geometry, focused, as usual for cubically-packed spheres bed, on two vertical sections at different spanwise positions (Top and Valley). These were chosen to observe the flow heterogeneity along the transverse direction. Small difference in double-averaged velocity between the impermeable and permeable cases were noticed, with higher values over impermeable beds. This suggested higher values for f over pervious surfaces. A deepening of the zero velocity plane was also observed along the Valley section due to a higher momentum penetration, however, the distinction between the velocity profiles disappeared while moving towards the free surface. Vertical velocities were barely perturbed by the bed permeability but strongly affected by spatial heterogeneity. Along the Top section a stationary recirculation vortex was noticed over the spheres' tops. These were caused by the flow separation near the crest and successive reattachment at the downstream sphere. The small differences noticed between the permeable and impermeable cases were mostly observed along the Valley region, where downward motions took place in the gap between consecutive spheres. This was imputed to flow separation position: as the flow for the impermeable case was faster and more energetic, separation occurred further downstream, where the fluid had already acquired significant downward motion; on contrary, the slower fluid for the permeable case caused the separation to occur near the crest where the vertical component was still weak. Streamwise and bed-normal turbulent intensities were found similar for the permeable and impermeable cases. Changes due to spatial heterogeneity were observed only in the near-bed region, with higher turbulent velocities along the Top section. Intense turbulent generation was here observed as a result of the shearing between high momentum fluid in the free region and low momentum fluid below.

The same bed geometries used by Pokrajac and Manes (2009) were also used in Manes et al.

(2009). Similarly, the flow was evaluated along a Top and Valley sections. Normalised double averaged velocities were found to be lower above permeable beds, suggesting higher values for f. The friction factor was also seen to increase for higher Reynolds Numbers. Normalised spatially-averaged turbulent intensities and Reynolds stress were similar for the permeable and impermeable cases. Turbulent intensities peaking in proximity of the bed roughness and decayed exponentially moving towards the free surface. The Reynolds stress followed a linear increment at deeper positions and started to rapidly decrease approaching the bed due to the arise of form-induced and viscous stresses. Dispersive stresses were found larger over the impermeable surface. No effects due to the bed permeability were noticed on the normalised TKE generation term. This suggested the increment in the friction factor was due to additional stress produced within the bed induced by shear penetration.

An explanation for the Reynolds Number dependence of the friction factor for flows over permeable beds was attempted in Manes et al. (2011). To do so, a series of experiments over smooth, rough impermeable and permeable beds were performed. The increment in the Reynolds Number was achieved by changing the flume slope. This allowed to keep the submergence constant and to isolate the effects of the Reynolds Number alone. Also here the friction factor was observed increasing with the Reynolds Number without reaching a plateau, indicative of hydraulically rough regime. Manes et al. (2011) suggested to possible motivations for this behaviour:

- progressively deeper momentum penetration within the porous bed: for turbulent flows over porous media the effective hydrodynamic roughness has to be referred to the thickness of the transitional layer and not to the grain size. As this thickness increases, an increment on the effective roughness height occurs. This corresponds to smaller relative submergences for the same water depth, hence, greater friction factors.

- higher pressure drag: at low Reynolds Number values, not all the grains might produce pressure drag due to sheltering effects. However, for higher Re, more particles might experience flow separation and so generate drag. This leads to an increment in f even if the thickness of the transitional layer remains constant.

Manes et al. (2011) concluded suggesting that both the mechanisms might be responsible for the observed behaviour of the friction factor. It was also speculated that the independence of f from the Reynolds Number (i.e. hydraulically rough regime) might be restored for sufficiently high Re values when the entire bed thickness is object of momentum penetration. Such regime, however, might occur at values so high for Re to not to find practical applications.

An attempt to give a phenomenological description of the rising regime can be found in Manes et al. (2012) where a numerical model based on the work of Gioia and Chakraborty (2006) was used. According to the model, the bed interface is populated by eddies which govern the momentum transfer. As the Reynolds Number increases, also larger eddies having enough energy to penetrate the wall are developed. The total shear stress is therefore formed by two components: one associated with the momentum exchange due to eddies at the interface and one that takes into account the effects of permeability and large-scale motions. From the

Figure 2.11: Friction factor as a function of Reynolds Number. Dashed lines are derived from the model by Gioia and Chakraborty (2006) which considers only the small interfacial vortices. Solid lines take also into account the effect of permeability and large-scale motions. Peculiarity of the plot are the belly observed for higher relative submergences and the asymptotic behaviour of f at high Reynolds Numbers. After Manes et al. (2012).

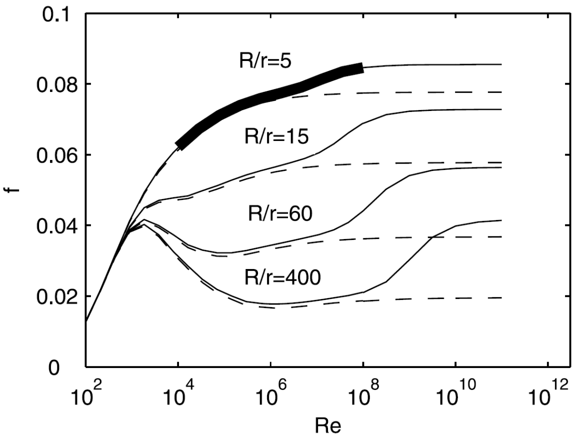

analysis of these components it was that the “s-shape” for the friction factor is result of the simultaneous effects of low relative submergences and permeabilities. For low submergences f increases with Reynolds Number until the plateau is reached. Further increments in Re cause the wall to become effectively permeable to the large scale motions, causing the growth of the friction factor. At higher values of relative submergence, the curve starts to lose the s-shape and displays a belly (Fig. 2.11). This was explained as, for the same Re value, higher relative submergences see slower interstitial velocities, leading to higher momentum contrast and friction factor. Finally, for Reynolds Number tending to infinity, the curve returns to be Re-independent as the entire bed thickness is affected by fluid shear.

Cooper et al. (2018) presented a series of tests where the turbulent flow over different permeable beds and their impermeable facsimile was evaluated using a PIV system. To produce a surface having the identical texture of the pervious counterpart, Cooper et al. (2018) employed the casting techniques presented in Buffin-Bélanger et al. (2003). In contrast with the previous findings, Cooper et al. (2018) found that normalised double-averaged streamwise velocity was higher over permeable beds within the interfacial sublayer with values 5-20% higher at the roughness crest level. Velocity was higher also in the upper part of the flow for two permeable beds. Turbulent velocity intensities were lower over the permeable surfaces, however, 12-34% larger Reynolds stresses were measured as a result of higher coherency in time. Nonetheless, TKE was 30% lower over the permeable beds. Streamwise and vertical spatially-averaged velocity intensities were lower for pervious interfaces. Similar behaviour was observed for the form induced stress (65-87% less) due to a weak correlation of its components, suggesting a limited role of this component in the momentum transfer. More energetic sweeps and ejections were confirmed over permeable beds, in agreement with the high turbulence correlation coefficient to induce high and low pressure zones that caused blowing and suction of water at the interface. It was suggested that these downward and upward motions are responsible for the development of high and low pressure regions that promote the mass and turbulent momentum transfer. The importance of these motions was assessed via Proper Orthogonal Decomposition (POD) analysis. It was observed that more energy containing within permeable beds’ modes. The first three eigenvalues, indicators of the importance of coherent structures in the production of TKE, concurred up to 27% of the total energy for permeable beds flows. These finding suggested a more efficiency in momentum transfer by turbulence over permeable surfaces. This efficiency and the lower TKE were indicated as cause for the higher spatially-averaged velocities. As a consequence, smaller friction factors for permeable beds were expected, in contraction with previous findings.

Experiments involving a cubically-packed spheres beds similar to those run by Pokrajac and Manes (2009) and Manes et al. (2009) were also performed by Kim et al. (2018). Three beds were here tested: rough impermeable (composed by hemispheres), rough permeable (1.5 spheres thick) and thick rough impermeable (4.5 spheres thick). Akin Pokrajac and Manes (2009) and Manes et al. (2009), two sections at different spanwise locations (Top and Valley) were examined using a PIV. Inner scaling the streamwise velocity for both impermeable and permeable beds revealed comparable trends to the smooth-wall case except for a downward shift that increased with bed thickness. The shift was attributed to the increased friction that occurred over pervious surfaces. Downward shifts for the impermeable and thin permeable bed were similar and two profiles diverted only in the near-bed region. Therefore, it was assumed that a thin permeable bed, with the exception of the interface area, could be mainly dominated by topological effects rather than permeability. Overall the profiles displayed a good collapse with the smooth bed case, Townsend's wall similarity hypothesis (Townsend, 1999), which claims that conditions at the wall set the bulk characteristics of the flow while turbulence adjusts itself to be similar to the smooth-wall flow when scaled with these characteristics, was then considered valid. The zero-plane displacement (i.e. the location where the time-averaged streamwise velocity is null or reaches a constant value) was found similar for the impermeable and thin permeable cases, highlighting the similarity between the two beds. For the thick permeable bed, the plane was further below, suggesting a deeper momentum penetration, hence higher friction. No changes at Double-averaged streamwise velocity profiles were attributed at the effect of permeability. On contrary, bed thickness was observed having a high influence. Reynolds shear stresses resulted higher in the Valley region for permeable beds due to momentum exchange. For the Top section, however, a decrease of the Reynolds shear stress was observed for the thickest permeable bed while thin permeable and impermeable surfaces showed an opposite behaviour, remarking the similarity between the two cases. As a consequence, the thick permeable bed presented limited spanwise variability, suggesting that bed thickness affects the near-wall turbulence structure. Profiles of flow first- and second order statistics for all cases collapsed well. This finding strengthen the idea of the existence of an outer-layer similarity, regardless of the bed thickness and permeability influence on the interface region. The extent of similarity region, however, was affected by these two quantities.

Navaratnam et al. (2018) conducted a set of experiments aiming at quantifying the effect of porosity and grain orientation on flow resistance. To this purpose a waterworked gravel bed and its impermeable cast counterpart were examined. Different textures of an armour layer were evaluated by rotating the impermeable tiles of 180°. The highest value for the friction factor was seen for the rotated cast and lower relative submergence values, suggesting that grain orientation has a significant influence on flow resistance. The difference from f values for both gravel and impermeable gradually faded for increasing relative submergence. Comparison between gravel bed and impermeable cast showed higher values for the friction factor for the impermeable bed at lower submergences. The trend was opposite for higher submergences. Navaratnam et al. (2018) suggested this behaviour may be due to an overestimation of the bulk velocity caused by the impossibility to measure the subsurface flow. Estimating the hyphoreic flow and deducting it from the observed discharge permitted a better representation of the low submergence cases. Indeed, the derived friction factors resulted higher over the permeable bed. The higher friction factor for the cast bed at low submergences was also explained by greater standard deviation of the surface elevation resulting from the casting procedure.

2.4 Flow Field and Water Surface Measurement Techniques

The aim of this thesis is to identify the linkage between the bulk flow properties and the free-surface behaviour. To achieve this, it is necessary to consider both the hydrodynamics and the surface wave patterns, possibly at the same time. Many technologies can be employed to measure the 3D flow field and the dynamic behaviour of the water surface. The description, however, might be diverse from technique to technique due to different working principles and characteristics of the method (e.g invasiveness of the instrument). For these reasons, only the most promising technologies for flow and free surface description are presented over the next pages: Subsection 2.4.1 introduces the characteristics of PTV and compares it against PIV, after it focuses on the Shake-The-Box (STB) technique that was used in this research; Subsection 2.4.2 analyses methods to retrieve the instantaneous 3D shape of a dynamic liquid surface, focusing later on DIC; Subsection 2.4.3 is a short presentation of how wave probes arrays operate.

2.4.1 Particle Tracking Velocimetry

Flow characterisation represents the ability to adequately describe and understand the physical processes behind the observed behaviour of a fluid phase. Hot Wire Anemometry (HWA) is considered one of the first techniques used to investigate the motion in turbulent fluids. Despite important advantages, like high temporal resolution, the method has been abandoned due to its intrusiveness, the complexity of the probes to measure orthogonal components and that it generally measures at single, or a very small number of points. On contrary, the use of optic based techniques has grown. Among the multitude of optical methods, PTV and PIV represent the most popular to measure 2D and 3D velocities non-intrusively. Both rely on the discrete observation from two or more different points of view of essentially buoyant particles (tracers) that have been previously dispersed in a fluid. For these methods, stereoscopic visualisation of the tracers is critical as the triangulation of an object can be determined from images obtained from two cameras as long as the positioning of these cameras is known and the collinearity condition is assumed (target, camera projective centre and image point lie on a straight line) (Akutina, 2015). The flow field behaviour is then inferred from the movement of such tracers, meaning that these tracers are the information carriers (Hadad & Gurka, 2013).
The characteristics of these two methods can be summarised as follows:

- PTV is a Lagrangian particle tracking method; at each time-step particles are firstly triangulated to determine their coordinates in space and later trajectories are obtained from such positions (Maas et al., 1993). Velocity field is finally derived from the derivative of trajectories.

- PIV is an Eulerial method; images are subdivided in interrogation windows and via spatial correlation methods the velocity vectors are calculated for each region. The vectors represent the average velocity of the tracers in a window (Dabiri & Pecora, 2020). It follows that PIV does not focus on the single tracer but it evaluates group of particles or particular "patterns" in successive time-steps (Fujita et al., 1998).

Conceptually, the difference between PTV and PIV is represented in Figure 2.12.

PTV is considered one of the oldest techniques for flow characterisation (Chiu & Rib, 1956; Jacobi, 1980; Sheu et al., 1982). At the early stages, the particle tracking was performed manually, while automatic routines were only developed in second half of the 1980s (Chang et al., 1985; Adamczyk & Rimai, 1988; Kobayashi et al., 1989; Papantoniou & Dracos, 1989; Nishino & Kasagi, 1990). Despite the automation of the tracking procedures, only a limited number of tracers could be employed to prevent the arising of ambiguities in the identification of tracers and then biasing the results. Because of this, PTV methods suffered from limited spatial resolution (Maas et al., 1993).
In the same period, Adrian (1988) defined the fundamentals of 2D PIV technique. Here the flow field was derived from the auto-correlation function of double-exposed continuous images. This allowed higher levels of seeding particles to be dispersed in the flow, leading to an increase of the spatial resolution of the measurements. This resulted in a better characterisation of the velocity field compared against contemporary PTV. Since then, PIV has been continuously improved: Willert and Gharib (1991) introduced digital cameras, Westerweel (1993) defined the criteria for the sub-pixel accuracy, Elsinga et al. (2006) developed tomographic PIV which allowed the spatially high resolved 3D characterisation of a flow up to 0.05 particles-per-pixel (ppp), Wieneke (2008) for volume self-calibration and Atkinson and Soria (2009) for the reconstruction of particles as intensity peaks in a voxel space. These improvements delivered calibration errors down below 0.1 pixels (Schanz et al., 2015). Nonetheless, PIV has an important downside caused by its very cardinal principle: the spatial resolution of the velocity measurements is limited by the dimension of the interrogation window, which acts as a low-pass filter. Because of this, PIV cannot be used when strong velocity gradients are expected or when fine flow structures are studied (Schanz et al., 2016). For this reason, Kähler et al. (2012) recommends the use of particle tracking methods when it comes to investigate near-wall or near-surface regions or in

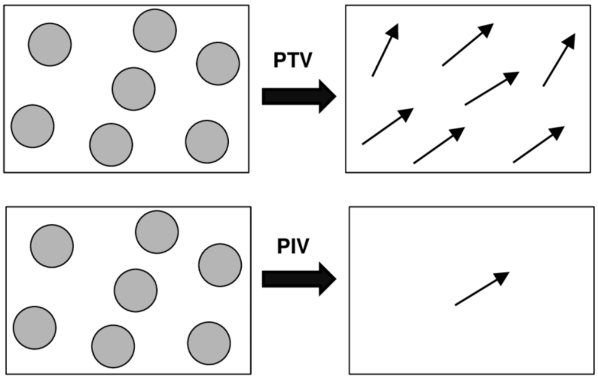

Figure 2.12: Conceptual difference between PTV and PIV methods: PTV derives velocity information from the motion of individual tracers, whereas PIV from the movement of groups of particles. As a consequence, PTV can lack of spatial resolution to prevent ambiguities while defining the tracks, while PIV imposes a filter on the data providing locally-averaged velocities. Reproduced with authorisation from Zoheidi (2018).

presence of highly-sheared flows. Furthermore, PIV methods have high memory requirements, they are extremely time consuming and are affected by ghost particles (Schanz et al., 2015). The development in hardware and software technologies allowed PTV to return competitive again: Willneff (2003) defined an algorithm that made use of the resolved velocity and acceleration fields at previous time-steps to find the particles in the successive time frame, significantly reducing the computational time for the analysis and the number of ambiguities (Lüthi et al., 2005); the introduction of an iterative particle placement routine instead of more traditional triangulation methods by Wieneke (2013) permitted seeding concentration comparable to tomographic PIV. Further considerations on PTV methods can be found in the recently published review by Pecora (2018).

A major breakthrough in PTV technology was presented by Schanz et al. (2013b) with the introduction of the STB system and its improvement in Schanz et al. (2015). STB makes use of the advances in 3D PTV (Willneff, 2003; Wieneke, 2013) and in tomographic PIV (Elsinga et al., 2006; Wieneke, 2008; Scarano, 2013; Schanz et al., 2013a) and the time-resolved information that can be derived from previously processed time-steps (Schanz et al., 2015). Known trajectories are then used to predict the particle coordinates at the successive time-step. The predicted particle configuration is used to initialise an iterative procedure aimed at refining and correcting the particles placement. Once accuracy tolerance is reached the algorithm focuses on the identification of new particles. As an improvements in on reconstruction property (e.g. position accuracy, ghost particle ratio, percentage of found tracks) leads to advances in other properties, the process is considered self-stabilising (Schanz et al., 2015). This highly reduces the probability of obtaining ghost particles and speeds up processing time.

The basic concept of the STB method relies on two assumptions: particles within the measurement volume do not disappear; knowledge of a particle trajectory allows to fairly accuratly estimate its positioning in the next time-step.

Initially, no information about the particles positioning is available, the algorithm has then to converge on a stable solution before being able to use time-resolved data to predict the behaviour of the particles for the next time-step. For this reason, it is possible to identify three different phases for the algorithm: initialisation, convergence and converged state.

In the initialisation phase, valid for the first instants, particles identification is performed using iterative triangulation procedures. These particles are considered "particle candidates" as only particles for which a track can be identified can be considered real. Trajectories are then derived from the distribution of particle candidates by applying a search radius around either the particle position or a predicted location. Particles satisfying such criterion are then considered "real particles".

Once the convergence phase is reached, the time-resolved system is used to determine the solution for the next time-step. Assuming that the trajectories are known for a certain number of time-steps t_n, the STB scheme for the single time-step t_{n+1} is:

1. perform a fit to the last k positions of tracked particles using an optimal Wiener filter (Wiener, 1949) based on the estimations of the signal and noise spectra of the particle location signals.

2. predict the position of the particles in the next time-step by evaluating the Wiener coefficients.

3. ‘shake’ the particles to a more correct position using residual image (Wieneke, 2013) and adjust the intensity to eliminate the predicted error.

4. identify new particles entering the measurement domain using iterative positioning routines and assign them the ”particle candidates” status.

5. ‘shake’ all particles again to correct for residual errors.

6. remove the particles that leave the volume or that have intensity falling below a certain threshold.

7. iterate steps 4, 5 and 6.

8. add new tracks for all the newly identified particles within four consecutive time-steps.

After such a process, the entirety of these tracks can be predicted for successive time-step t_{n+2}. In the converged phase the process is the same as in the convergence phase and is represented in Figure 2.13. At this stage, however, the number of tracks remains nearly constant as tracers entering the measurement volume equal the ones leaving.

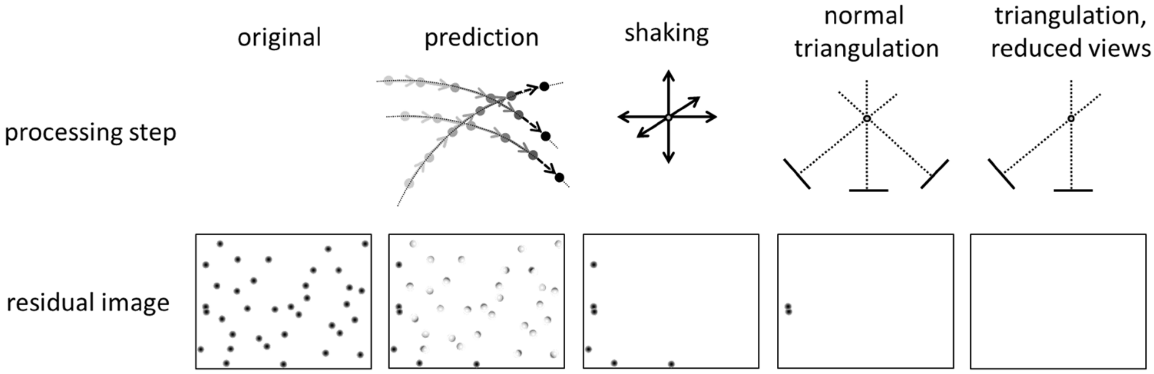

Figure 2.13: PTV STB procedure in converged phase displaying the evolution of the image residuals (bottom) at different steps (top). Reproduced with authorisation from Schanz et al. (2016).

Discrete tracks can be interpolated onto an Eulerian grid to allow the evaluation of flow properties and the identification of the flow structures. Each component of the flow field is modelled as a weighted sum of three dimensional and evenly spaced quadratic B-splines in which the weights are determined according to known flow velocities (Gesemann, 2015). This produces a series of linear equations for each known flow velocity at some particular position. The solution of this system is a flow field sampled on a regular grid. To maintain the accuracy at the particle positioning, the system of B-splines oversamples the flow field (roughly 5-20 splines per particle). Furthermore, splines interpolating empty cells have only to respect smoothness and divergence criteria, whereas the ones in non-empty cells have also to describe the velocity data of the particles.

2.4.2 Digital Image Correlation

The three-dimensional reconstruction of the shape of an object is a matter of interest in many fields, e.g. medicine (Vandenberghe et al., 2001), civil engineering (Kwak et al., 2013; Liu et al., 2016), archaeology (Brunetaud et al., 2012; Guidi et al., 2014) and geography (Lizarazo et al., 2017). Typically, the digital reconstruction are represented as point clouds, mesh and geometric models (Fig. 2.14) (Ma & Liu, 2018).

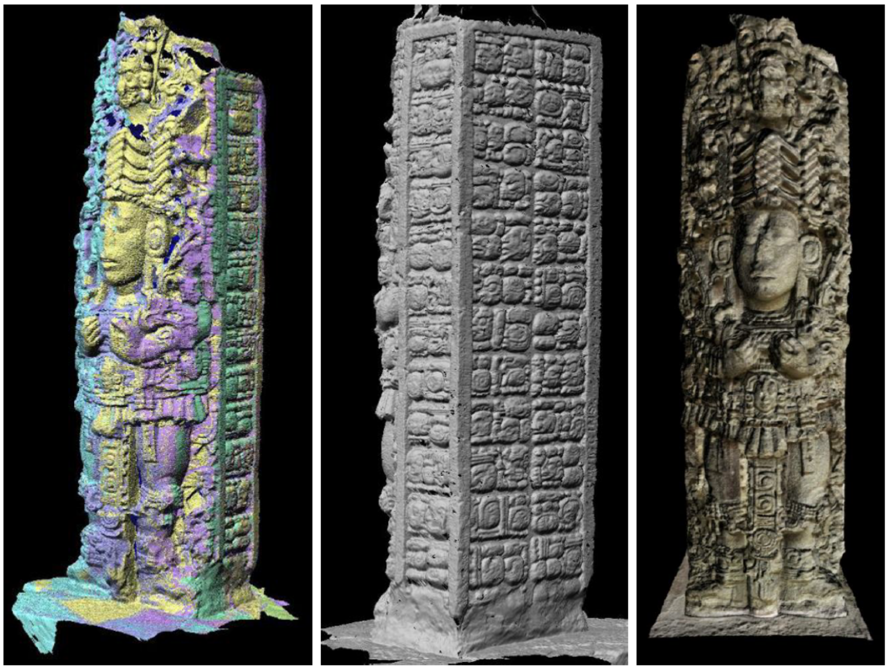

Figure 2.14: 3D reconstruction of a statuette. Left image shows the point clouds obtained from a laser scanner. Central image represents the point clouds converted into a polygonal mesh. Right image depicts the application of a texture for photo-realistic visualisation. Derived from Remondino (2011).

Reconstruction techniques can be subdivided between contact or non-contact methods or by the type of instrumentation used (optical, acoustic and electromagnetic waves). Non-contact techniques have the advantage not to perturb or damage the object which shape needs to be acquired. This characteristic is extremely important when it is time to investigate delicate or constantly deforming objects like a water free surface can be. For this, invasive methods can cause the creation of undesired waves and perturb the original wave pattern.

Acoustic methods have already been used to locally reconstruct a dynamic air-water interface or to derive areal surface waves properties like mean roughness height, frequency-wavenumber spectra and surface velocity (Cooper et al., 2006; Fukami et al., 2008; Nichols et al., 2013; Johnson & Cowen, 2017; Dolcetti, 2016). Similarly, Barrick (1972), Walsh et al. (1985), Wang et al. (1991), Plant et al. (2005) and Welber et al. (2016) used radio waves, while Zhang and Cox (1994), Weigand (1996), Devriendt et al. (1998), Dabiri and Gharib (2001) and Fujita et al. (2007) and made use of optical techniques for the same purposes. The main advantage of acoustic and radio methods is that the free surface represents a highly reflective interference due to the higher impedance of water than air (Nichols et al., 2013). On contrary, this is not often valid for optical techniques. For this latter case, the evaluation of the free-surface characteristics may be affected by the bed surface distortion caused by the interface. On the other hand, both acoustic and radio solutions require a highly delicate calibration when there is the need to 3D reconstruct a surface area.

The evaluation of the free-surface shape and of its characteristics by means of optical techniques is well established. The first investigations can be dated back to early 20th century (Laas, 1905; Kohlschutter, 1906). Since then, advances and understanding in optics have greatly improved and many different techniques were established. Even a brief description of all these techniques would be quite lengthy and is beyond the purposes of this manuscript. For these reasons, the reviews produced by Jähne et al. (1994) and Pan (2018) are recommended.

Following the framework proposed by Jähne et al. (1994), all the optical reconstruction techniques can classified into two distinct categories: shape-from-shading and shape-from-stereo.
Shape-from-shading methods (Horn, 1977) derive the local slope of the free surface from the irradiance at the image plane. The light intensity depends on the angle of incidence of the light and on the viewing angle. The major flaw of these methods is that the surface gradient (a 2D quantity) is referred to the image irradiance, which is a scalar quantity. The coupling between surface gradient and image intensity is therefore underdetermined for all the slopes except where local extrema occur. For all the other locations different solutions are possible so that constrains need to be introduced in order to identify a unique solution (typically smoothness). Shape-from-shading methods can be further subdivided into two categories: shape-from-reflection and shape-from-refraction. Shape-from-reflection method (Cox & Munk, 1954) can only be used only for a limited range of slopes. Furthermore, illumination introduces a series of difficulties. In order to tackle the low water reflectivity bright light sources are required, however, as most of the light can penetrate into water, a large backscatter is present. The major obstacle consists in cutting off the reflections to prevent bias. Employing natural illumination is possible as long as the lighting conditions either remain constant throughout the duration of the measurement or vary in one direction (e.g. it gets brighter and brighter), which is quite unlikely. The method is also limited by the linear assumption between light intensity and surface slope, which does not hold. Shape-from-refraction technique (Hughes et al., 1977; Lange et al., 1982; Bock & Hara, 1995) is more suitable when a clear medium like water is examined. Compared to the shape-from-reflection method, shape-from-refraction allows a wider range of slopes to be detected and is less sensitive to the non-linearity of the gradient-irradiance relation. However, it requires the light source to be place under water or the bottom to be transparent which significantly limits the applicability of the method outside laboratories. It follows that only limited water depths can be investigated with this technique. Therefore, shape-from-shading methods present numerous disadvantages that make them inapplicable to evaluate the free-surface behaviour of agitated flows over opaque beds (Douxchamps et al., 2005).
In shape-from-stereo techniques (Banner et al., 1989; Shemdin, 1990) the reconstruction of the free surface is derived from the parallax between corresponding points from two different points of view. For this reason, reconstruction is not possible when a region cannot be observed from both the views (e.g. in case of high breaking waves). Also, the same point on the free surface can be represented by different light intensities in the cameras. Where this mismatch occurs,

parallax cannot be calculated and the surface cannot be recreated. This technique is highly sensitive to the cameras resolution, in particular for short waves: it might happen that short waves can be horizontally resolved, but their height cannot. Furthermore, when natural illumination is used, the technique is not too much dissimilar from a shape-from-reflection method, with all the related complications. These problems can be overcome if an artificial source of illumination is used (Jähne et al., 1994) as shown in Jähne and Waas (1989) and in Waas and Jähne (1992).

Among the various optical methods, DIC is probably the most popular as it can accurately measure and reconstruct a surface, providing simplicity in its use, robustness and flexibility according to its target (Pan et al., 2009; Pan, 2018). DIC was initially developed by Peters and Ranson (1982) and over the years it has been continuously improved (Peters et al., 1983; Sutton et al., 1983; Sutton et al., 1986; Vendroux & Knauss, 1998; Lu & Cary, 2000; Schreier, 2000; Tong, 2005; Yoneyama et al., 2006) to enhance the accuracy, reduce the computational and time costs and expanding the application range (Pan et al., 2009). Several variations of DIC are currently available, however, most of them can be classified into 2D or 3D methods (Pan, 2018). 2D DIC is used to evaluate in-plane deformations of planar objects. To this purpose, out-of-plane deformations must not affect the in-plane components or they have to be small enough to be negligible (Chu et al., 1985). When curved objects are examined or when out-of-plane components cannot be ignored, 3D DIC needs to be employed. The complete theory behind image correlation is quite lengthy as it focuses on the evaluation of the deformation of the target, the correlation algorithms and the interpolation rules needed to produce a digital surface reconstruction. For this reason, Chu et al. (1985) is recommended to fully grasp the theory of DIC. The basic assumption of image correlation is that an object reflects light differently according to its deformation state. Assuming that the intensity patterns specific for the original and deformed configurations are unique and in an univocally correspondence to the respective surfaces, it is possible to derive the deformation information by comparing the different irradiance values (Chu et al., 1985). Displacements and deformations are obtained from comparisons with images of the target at its original state by maximising a similarity function (e.g. least-squares) for the intensity values (Lecompte et al., 2006). As the brightness value of a single pixel is not enough to produce a unique signature, groups of neighbour pixels need to be considered. This collection of pixels is usually called a “subset” or “facet”. In a similar manner to PIV (Hild & Roux, 2012), the information here derived represents the average of all the values observed inside an interrogation window. The images, once subdivided in smaller regions, are then cross-correlated to identify matches and to obtain the instantaneous surface profile and its evolution over time. However, for cross-correlation to work, the surface under investigation requires a pattern on it or more exactly, random gray level intensity variation (Pan, 2011). It is the speckle pattern that carries the information regarding the specimen deformation as it is assumed the pattern deforms together with the target (Pan, 2011). When it comes to evaluate the interface of a liquid, this requirement can be satisfied either by dispersing buoyant tracers on the surface (Douxchamps et al., 2005; Turney et al., 2009) or by projecting a pattern on a previously tinted liquid (Takeda et al., 1982; Tsubaki & Fujita, 2005; Cobelli et al., 2009; Wu et al., 2022). Typically, titanium dioxide is used for this purpose, however, Nichols et al. (2020) suggests this additive can modify the water characteristics even in limited concentrations.

On the other hand, the use floating seeding particles can be challenging as several difficulties can arise: identification of the right type of tracers, their availability, distribution, illumination, creation of the speckle pattern and coating problems induced by the flow (Turney et al., 2009). The latter problems result quite obvious once consulted Lecompte et al. (2006) and Yaofeng and Pang (2007) which provide a comprehensive investigation on the characteristics and quality requirements for the speckle pattern.

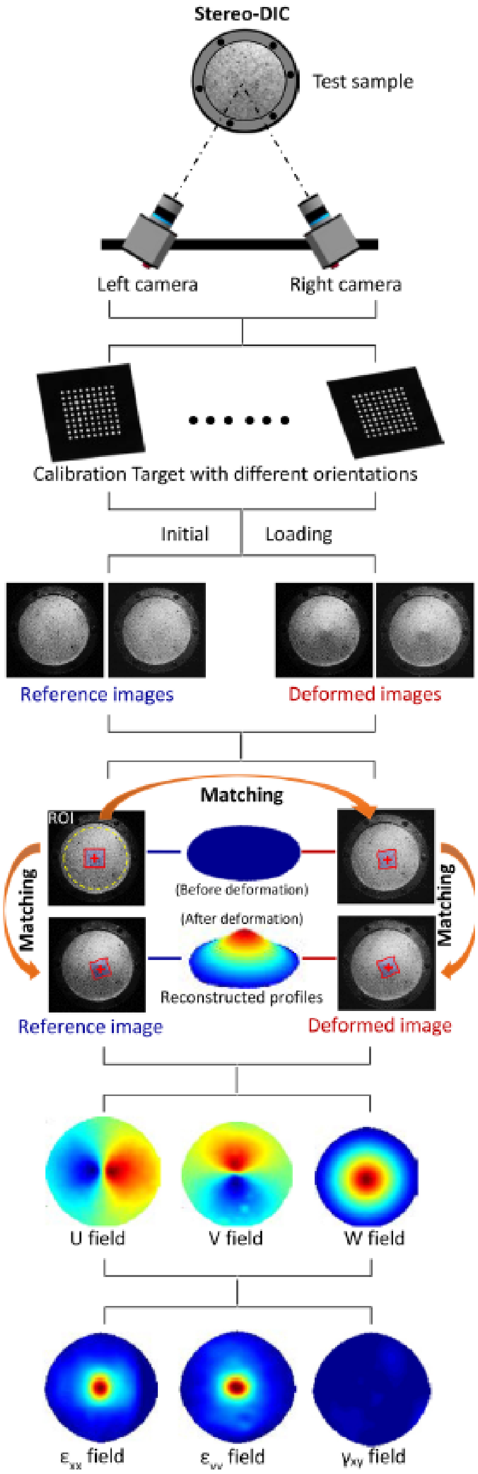

Figure 2.15: Experimental procedure of 3D DIC technique. Reproduced with authorisation from Pan (2018).

3D DIC (Luo et al., 1993), also known as stereo-DIC, is probably the most reliable and performing technique among shape-from-stereo methods. This method (Fig. 2.15) makes use of two synchronised cameras to reconstruct the 3D shape and deformation of an object using stereography, i.e. the observation of an object from two different points of view (Pan, 2018). Differently from 2D DIC, 3D DIC cannot retrieve the spatial collocation of the target without stereovision calibration. This is needed to identify the intrinsic (i.e. camera-dependent parameters that are needed to link the pixel coordinates with the camera's internal reference system, e.g. focal length and type of lens) and extrinsic (i.e. attributes that define positioning and orientation of the camera's reference system respect with the world reference system, e.g. cameras' respective positioning) parameters of the two cameras (Pan, 2018). Different forms of calibration are possible, however, using a planar calibration target with a precise geometry as proposed by Zhang (2000) has become the standard method due to its ease and accuracy. Influence of calibration parameters (e.g. number of images, size and pattern of the calibration target and image quality) on the system reliability was evaluated by Reu (2013). In a 3D DIC system, correlation between images can be achieved only if both stereo and temporal matchings are resolved (Orteu, 2009). Stereo matching is the identification of the same portion of target by the two different cameras, while temporal matching is the tracking of a facet in time. Temporal tracking in 3D DIC picks up the methods already well established from 2D DIC. Stereo matching is more challenging. Typically, a shifting window for the image of one camera is correlated to a fixed window on the image produced by other camera. The shifting window is then moved on the first image to produce a curve of correlation scores. The displacement producing the highest value of correlation defines the stereo matching (Orteu, 2009). It follows that 3D DIC operates image correlation both in space and in time to reconstruct the shape of an object and its evolution over time. Due to the high non-linearity of perspective projection, stereo matching requires second-order functions to guarantee robustness of the method. These functions, however, are computationally expensive, causing stereo matching to be much more time consuming that temporal matching. For this reason, the strategy that is usually adopted is to first perform the stereo matching between the two cameras at the initial time-step and then the temporal matching for the single cameras (Pan, 2018) as shown in Figure 2.16.

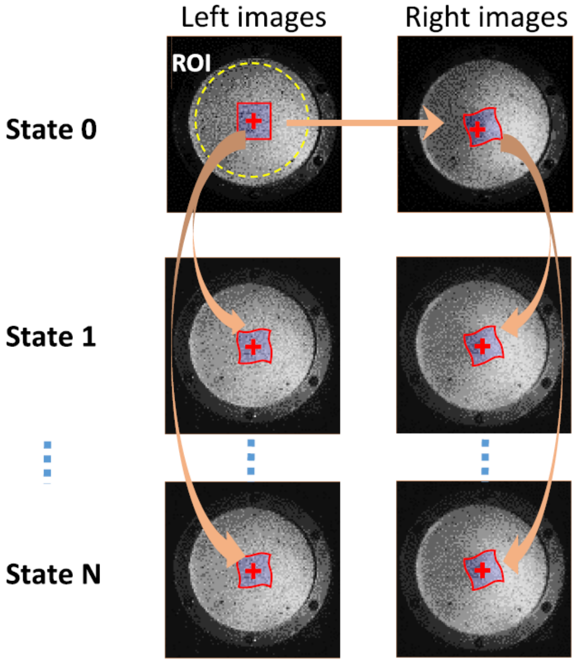

Figure 2.16: Typical strategy for 3D DIC matching: stereo matching between left and right cameras is first achieved before the temporal matching for each subsequent series of images. Reproduced with authorisation from Pan (2018).

DIC techniques (both 2D and 3D) have proved to be powerful and reliable methods to digitally reconstruct the shape of an object, its evolution in time and the displacement and deformation fields that result. These are the motivations for which it finds broad use in industrial, engineering, academic and research environments. Considering its adaptability, it is highly likely it will find further fields of application in the future as it represents the most practical and powerful instrument to reconstruct the shape of an object (Pan, 2018).

2.4.3 Wave Probes

Wave probes, often also known as wave gauges, are devices used to determine the instantaneous local elevation of a liquid over time. They are typically composed by two parallel rigid or tensioned wires (Fig. 2.17) and positioned to vertically pierce through the liquid interface. Wave gauges can be distinguished between resistive and capacitive devices according to the device that monitors them. An electric current constantly energises the probes, the response, however, varies over time according the instantaneous local liquid level. In fact, as the water level fluctuates more or less wire is submerged, producing a change in system resistance or capacitance.

Wave gauges are employed in both laboratory and field campaigns as well as in industrial and civilian applications. Many applications are related to ocean and sea characterisation (Mitsuyasu, 1977; Donelan et al., 1985). The greater interest towards the sea-surface behaviour than rivers led to limited employment of wave gauges in the latter field (Chang et al., 1979). Only recently have wave gauges started to being employed for evaluating the instantaneous free-surface elevation in open-channel flows (Nichols, 2013; Horoshenkov et al., 2013; Dolcetti et al., 2016).

Wave probes are popular as they are cheap, reliable and easy-to-use (Liu et al., 1982). Nonetheless, probes present many downsides: the limits in the quality and quantity of the data that can be extracted (Young, 1994), the possibility of providing local measurements only and their intrusiveness. For these reasons, wave probes are being supplanted by remote sensing techniques. Nonetheless, they are still being utilised, mostly as reference systems to validate measurements or to test new technologies due to their high accuracy.

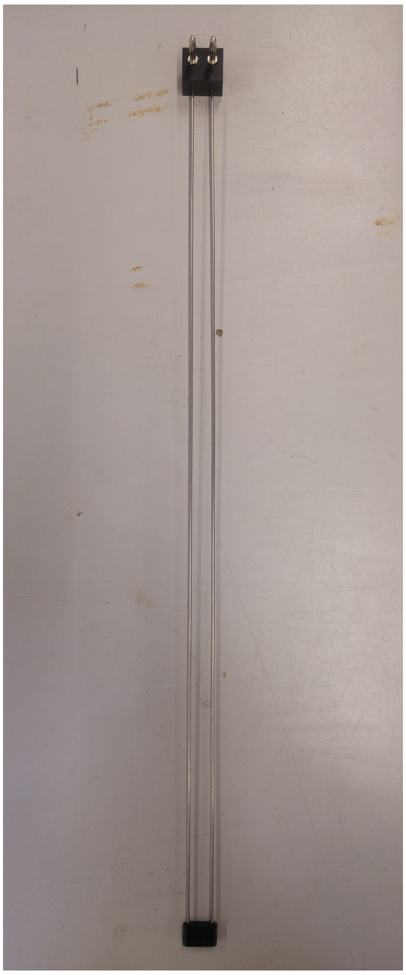

Figure 2.17: An example of rigid wire wave gauge.

2.5 Literature Gaps and Conclusions

This review of the currently available literature for both the dynamics of a free surface and the hydrodynamics over a permeable bed produced an overview of work in different areas and allowed some more general views to be identified. It was found that consensus did not exist in a number of areas. This disagreement might be caused by the experimental capabilities that existed at the time of various studies, or that observations of different phenomena took place

and the academic community was not able to reconcile the observations with a general theory linking free-surface behaviour and the underlying hydrodynamics.
Deductions from this lack of a general consensus are then proposed over the next pages: Subsection 2.5.1 focuses on the open question regarding the governing mechanism of the free-surface behaviour of a shallow turbulent flow; Subsection 2.5.2 critically examines the effect of a permeable bed on the surface flow dynamics; as last, Subsection 2.5.3 summaries the gaps in the literature that have been identified.

2.5.1 Ambiguities on the Governing Mechanisms of the Free-surface Behaviour

The most interesting observation from the studies here reviewed is about the typology of wave patterns that dominate the free surface. Fujita et al. (2011), Horoshenkov et al. (2013) and Nichols et al. (2016) propose that these waves are turbulence-induced fluctuations. That gravity-capillary waves are the most relevant patterns is supported by Savelsberg et al. (2006), Savelsberg and Van De Water (2008), Savelsberg and Van De Water (2009), Dolcetti et al. (2016) and Dolcetti and García Nava (2019b). In particular, Dolcetti et al. (2016) and Dolcetti and García Nava (2019b) further specify that these waves are stationary waves.

The theory of the turbulence-induced waves is supported by direct visualisation (Gharib & Weigand, 1996; Fujita et al., 2011) of vortex interacting with free surface and locally rising the depth. By means of space-time images, Fujita et al. (2011) observed newly created features advecting at approximately the free-surface velocity. This mechanism for the free-surface pattern appears sensible as eddies increase their streamwise advection velocity while moving upwards until they reach the free-surface velocity. Waves travelling at the flow surface velocity were also observed by Horoshenkov et al. (2013) using an array of wave probes, by Nichols et al. (2016) with space-time images and by Tani and Fujita (2018) via of space-time images and frequency-wavenumber spectrum. From these observations it is speculated that, after the impact of an eddy, the free surface begins to oscillate according to the simple harmonic motion model described by Nichols et al. (2016). The complexity of the surface pattern can be explained as a superposition of different single responses occurring in many points in space and out of phase. These features continue to oscillate while moving downstream until viscosity dissipates them or new surface features superseded them. According to Nichols et al. (2016), these features can generate gravity-capillary waves that propagate in all the directions.
Patterns moving with the surface velocity and generated by the flow turbulence were confirmed also by Savelsberg et al. (2006), Savelsberg and Van De Water (2008) and Savelsberg and Van De Water (2009). However, these features were deemed of secondary importance compared with dispersive gravity-capillary waves. Capillary-waves may be generated through a form of resonance different from the one suggested by Teixeira and Belcher (2006). This was hypothesised as the wavelength of the dominant gravity-capillary waves was found close to the sub-surface turbulence integral scale but the turbulent velocity was an order of magnitude smaller than the minimum phase velocity. In the experiments carried out by Savelsberg et al. (2006), Savelsberg and Van De Water (2008) and Savelsberg and Van De Water (2009) turbulence was produced using active and passive grids which is different from the turbulence met in rivers where it is

mostly generated by the instabilities in the boundary layer near the rough bed. It follows the length scales are differently scaled from those expected in gravity-driven open-channel flows.

The observations by Dolcetti et al. (2016) and Dolcetti and García Nava (2019b) suggest it is the flow condition that defines the free-surface pattern generation mechanisms. When the free-surface velocity is slower than the minimum phase velocity for gravity-capillary waves in still water ($c_{min} = 0.23$ m/s) the dominant pattern is composed by turbulent-induced waves through the forcing non-resonant growth proposed by Teixeira and Belcher (2006). When $c_{min} > 0.23$ m/s the free surface is dominated by stationary waves and by freely propagating gravity-capillary waves travelling in all the directions with the same wavenumber k_0. The spatial period L_0 measured by Horoshenkov et al. (2013) and predicted by Nichols et al. (2016) can in fact be predicted well in terms of the wavelength of stationary waves with the analytically derived wavenumber k_0. Dolcetti and García Nava (2019b) proposed that the free-surface fluctuations observed by Horoshenkov et al. (2013) and Nichols et al. (2016) were not localised manifestations of turbulence, but gravity-capillary waves that were probably created by an interaction between the rough bed and the sheared current. For this reason, Dolcetti and García Nava (2019b) proposed that stationary waves mediate the transfer of energy between propagating waves and turbulence modes, causing a selective growth of waves whose scale and velocity match the wavenumber k_0. Together with waves with wavenumber k_0, gravity-capillary waves with different wavenumbers and turbulence-induced wave patterns may also occur.

Dolcetti et al. (2016) and Dolcetti and García Nava (2019b) based their analysis on time-space Fourier and wavelet transforms. One can argue that these are more robust techniques than space and time cross-correlation used in earlier studies by Horoshenkov et al. (2013) and Nichols et al. (2016), however, other studies making use of Fourier analysis did not observe stationary waves. A possible motivation could be the limited spatial window of the measurements. In Savelsberg et al. (2006), Savelsberg and Van De Water (2008) and Savelsberg and Van De Water (2009) the spatial extent for investigating the surface was only 50 mm. In Fujita et al. (2011) the length of the field of view was 135 mm. For similar flow conditions Dolcetti et al. (2016) reported the presence of strong stationary waves with wavelength varying between 85 to 100 mm, therefore the spatial window may have been too small. Also, even larger stationary patterns with wavelength between 70 and 180 mm were observed for experiments with characteristics close to the ones tested in Nichols et al. (2016) where the area of interest was 220 mm long. Horoshenkov et al. (2013), Nichols et al. (2016) and Dolcetti et al. (2016) tested similar flow regimes but different bed textures. It might be that the wave dominating mechanism differs according to the flow and bed morphological conditions. In Dolcetti et al. (2016) regular spheres with the diameter of 25.4 mm were employed, while in the other two studies a gravel bed with mean grain size of 4.4 mm was used, implying that, for the same flow condition, different submergences were tested. For this reason, the influence of the bed on the free-surface behaviour may be limited to only lower submergences, while turbulence-induced features dominate when the submergence is high. The role of submergence is currently unclear as results by different authors, collected at a wide range of submergence, are contradicting. For example, in the experiments by Fujita et al. (2011) and Nichols (2013) the submergence fell in the range of conditions tested by Dolcetti et al. (2016) but a different free-surface behaviour was observed. This suggests that the type of response of the free surface is not only defined by the submergence but also by the bed morphology itself. According to Noss et al. (2020) instead, the dynamics of the interface is sensitive to the submergence, being affected by turbulence for high values of submergence and showing stationary waves for small values of it. Therefore, no single dominating mechanism appears to govern the free-surface behaviour.

Despite different points of view, most of studies support the existence of a spatial organisation for the free surface. Savelsberg et al. (2006) observed oscillating correlation functions for the instantaneous surface gradient and different behaviours between the streamwise and spanwise directions. Savelsberg and Van De Water (2008) suggested that the spatial correlation behaviour depended on the turbulence field, behaving isotropically if the turbulence is isotropic or anisotropically when turbulence is anisotropic. Horoshenkov et al. (2013) proposed an analytical expression of the average spatial correlation function for the free-surface elevation (Eq. 2.2). This equation has its parameters that are related to the turbulence in the bulk flow, has an oscillating behaviour and decreases in amplitude with the distance. Dolcetti et al. (2016) observed for the case of mean surface velocity below 0.23 m/s a smooth decay for the correlation of the elevation with horizontal scales approximately equal to the water depth. For mean surface velocity higher than 0.23 m/s the correlations fluctuate with period defined by k_0.
The Taylor's frozen turbulence hypothesis was tested in Savelsberg et al. (2006) and it was found not valid at the free surface due to gravity-capillary waves, but holding for the sub-surface velocity field. The inapplicability of the Taylor's hypothesis is hinted by the oscillon model of Nichols et al. (2016), which claims that surface features oscillate vertically over space and time while the sub-surface structures persist as they are advected by the flow.
The early free-surface roughness observations in Cooper et al. (2006) suggest that rougher interfaces occur over hydraulically rougher beds. Also, tests with low water depth and high bed resistance produce many small laterally elongated boils, while high water depth and lower hydraulic resistance are characterised by fewer and bigger features. Horoshenkov et al. (2013) reported linear relationships between the surface roughness height and the water depth, and the average velocity. In Nichols et al. (2016) rougher surfaces were observed for higher Froude Numbers, but here the water roughness height was also a function of the bed slope. In Dolcetti et al. (2016) higher Froude Numbers were linked to slower decays of the spectra at higher frequencies, i.e. more energy was contained in these frequencies. As a consequence, rougher water surfaces should be seen for higher Froude Numbers. However, no clear relation between the standard deviation of the surface depth and the Froude Number was identified. Noss et al. (2020) reported that the surface roughness was more affected by the near-surface velocity, the Reynolds Number and the shear velocity rather than the mean flow velocity. The shear velocity relation showed a high coefficient of determination for both flume experiments and streams.

What controls the behaviour of the free surface is yet to be conclusively understood. At the moment, three different hypotheses, all supported by evidence, have been proposed. They are: (i) turbulence-induced features, (ii) travelling gravity-capillary waves, (iii) stationary waves.
A majority of studies suggest that an open-channel flow is likely to be characterised by a specific free-surface wave pattern of waves which is unique to the hydraulic condition and morphology of the channel. However, there is no agreement regarding the linkage between the observed

wave patterns and bulk flow parameters. It is likely that several factors contribute to the generation of these waves. Therefore, it is of importance to determine the extent of their relative influence. To do so, the best strategy consists in evaluating the free surface by means of frequency-wavenumber spectra and spatial correlation functions. Comparing these results with the spectra and correlations for the velocity components at different heights in the flow field might allow to determine whether this linkage exists or not.

2.5.2 Flow Characteristics of Permeable Beds

Most of the investigations over permeable beds were aimed at identifying the friction factor, f. This parameter determines the head loss due to friction for a given length to the average velocity of a fluid flow. This parameter is function of the Reynolds Number and the relative roughness. As a consequence, four regimes are possible:

- laminar flow: dominated by viscous forces and occurring for Reynolds Numbers up to 2000. The velocity is described by Poiseuille's law and the friction factor depends linearly on the inverse of the Reynolds Number.
- transitional flow: this region, spacing Re = 2000-4000, is dependent on Reynolds Number only. A rapid increase of the friction coefficient can be seen as consequence of the formation of the viscous sublayer. However, precise value for f due cannot be estimated due to important instabilities present in the flow.
- turbulent in hydraulically smooth regime: this condition appears for Re $>$ 4000. The regime is still dependant on the Reynolds Number, but also on the relative submergence.
- turbulent in hydraulically rough regime: this condition appears for Re $>$ 4000. Contrary to the hydraulically smooth regime, the friction factor is function of the relative roughness only, hence, completely independent from the Reynolds Number and so viscosity.

Belonging to one or the other turbulent regimes depends on the boundary surface roughness and the thickness of the viscous sublayer. It means that a pipe with a given roughness can be either hydraulically smooth or hydraulically rough according to the conveyed discharge. This implies that the passage from the smooth to the rough regime is not immediate but gradual as the pipe roughness are more and more exposed to the flow due to viscous sublayer thinning. This transitional phase is characterised by an intermediate behaviour between smooth and rough regime, meaning that it depends on both Re and the relative roughness.

Parameterisation of the friction factor behaviour was possible to Colebrook (1939) who presented the semi-empirical relation (Eq. 2.23):

$$f^{-1/2} = -2\log[e_s/3.71D + 2.52/(Ref^{-1/2})] \tag{2.23}$$

where e_s is the equivalent roughness, defined as the dimension of the sand grain used by Nikuradse in his experiments that gives the same resistance value in the hydraulically rough regime, and d is the pipe diameter. The graphic representation of Equation 2.23 was produced by Moody (1944) (Fig. 2.18).

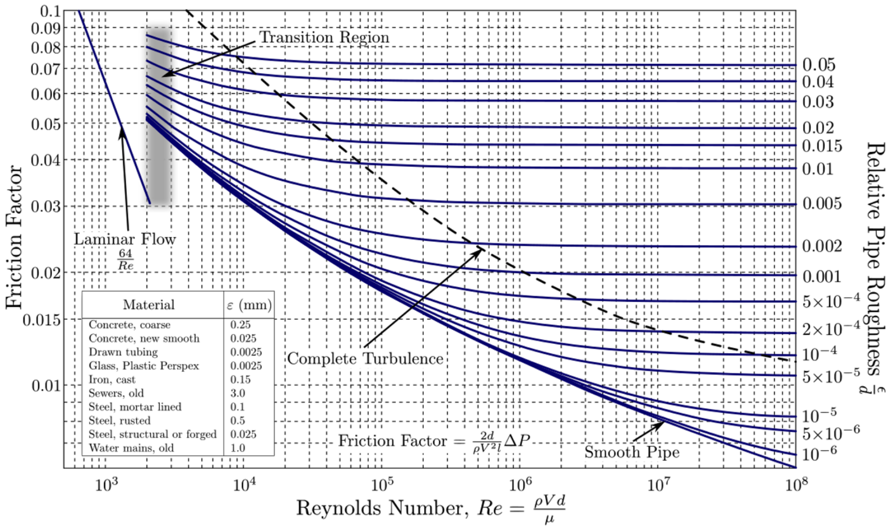

Material	ε (mm)
Concrete, coarse	0.25
Concrete, new smooth	0.025
Drawn tubing	0.0025
Glass, Plastic Perspex	0.0025
Iron, cast	0.15
Sewers, old	3.0
Steel, mortar lined	0.1
Steel, rusted	0.5
Steel, structural or forged	0.025
Water mains, old	1.0

Figure 2.18: Moody's Diagram. Derived from Beck and Collins (2017).

These formats were created for pipe flow where an impermeable boundary was assumed. Most of the geophysical flows occur over permeable boundaries, implying that relations derived for pipe might not to be fully applicable. Indeed, several studies (Zagni & Smith, 1976; Mendoza & Zhou, 1992; Breugem et al., 2006; Pokrajac & Manes, 2009; Manes et al., 2009; Kim et al., 2018) suggest that the friction factor is higher for flow over permeable beds compared to flows over the same bed geometry but imperious. Differently, an opposite trend was observed by Cooper et al. (2018). Special consideration is given to Cooper et al. (2018) later.

Surprisingly, f for permeable bed does not show a stable plateau at high Reynolds Numbers (i.e. hydraulically rough regime) as for flow over impervious wall, but still shows a dependency on Re (Lovera & Kennedy, 1969; Ruff & Gelhar, 1970; Chu & Gelhar, 1972; Zippe & Graf, 1983; Gupta & Paudyal, 1985; Mendoza & Zhou, 1992; Manes et al., 2009; Manes et al., 2011). As a consequence, the plot for the friction factor against Reynolds Number shows a characteristic s-shape. Manes et al. (2011) proposed that the cause for this dependency might be due to progressive momentum penetration and/or additional pressure drag due to no longer sheltered grains. Manes et al. (2012) attributed the increment of f to permeability and relative submergence. Higher permeabilities were found promoting deeper penetration of large scale motions, hence, momentum transfer. A hydraulically rough regime is then observed when the entire bed thickness contributes at momentum exchange. Relative submergence at high Reynolds Numbers, however, is responsible for an anomalous behaviour of friction factor. The curve deviates more and more for the s-shape profile due to the appearance of belly. This was explained as slower seepage velocities are observed for increasing relative submergences at a given Reynolds Number. This strengthens the momentum disparity between free-flow and subsurface regions and leads to an increment of the friction factor. The friction factor is also speculated to become independent again from the Reynolds Number at high Reynolds Numbers. Manes et al. (2011) proposed this might happen when the entire thickness of the bed collaborates and/or all the grains experience flow separation. Agreement can be found in Manes et al. (2012).

Friction factor was also seen being affected by bed texture orientation (Navaratnam et al., 2018). This influence, however, is gradually abated by relative submergence. Bed thickness also promotes higher f values (Zippe & Graf, 1983). The influence of wall permeability is more challenged: Prinos et al. (2003) and Manes et al. (2012) suggest higher permeability value should increase the friction factor, while Pokrajac et al. (2007) and Kim et al. (2018) did not observed such influence.

As a consequence of the increased friction factor, slower streamwise velocity profiles are observed over permeable beds (Prinos et al., 2003; Pokrajac & Manes, 2009; Manes et al., 2009; Kim et al., 2018). Except for a downward shift, inner scaled profiles resembled the smooth-wall case (Ruff & Gelhar, 1970; Zippe & Graf, 1983; Gupta & Paudyal, 1985; Mendoza & Zhou, 1992; Kim et al., 2018), suggesting the validity of Townsend's wall similarity hypothesis (Townsend, 1999). Similarity for permeable beds was typically achieved by adjusting the parameters of Prandtl-von Kármán universal velocity distribution law. While a deepening of the zero-plane position (Zippe & Graf, 1983; Gupta & Paudyal, 1985; Mendoza & Zhou, 1992; Pokrajac & Manes, 2009; Kim et al., 2018) is acknowledged due to the relaxation of the no-slip condition at the solid interface, changes at the values of the von Kármán constant, κ, are less accepted. To abide at the logarithmic law, lower values for κ must be assumed (0.26-0.29 for Munoz Goma and Gelhar (1968), Ruff and Gelhar (1970), Chu and Gelhar (1972), Gupta and Paudyal (1985) and Nezu et al. (1993)), suggesting larger energy dissipation rate in the mean flow an active momentum and energy transfer occurs at the porous interface. On the other hand, Zippe and Graf (1983) observed Townsend's wall similarity without need to change κ. These facts open at the need of deeper considerations on the scaling quantities (Pokrajac et al., 2006). Prinos et al. (2003), on contrary, suggested that the need for a change in the von Kármán constant is evidence that a flow over a permeable bed cannot be considered as boundary layer type but a mixing layer type.

Turbulent intensities were found similar for the permeable and impermeable cases (Pokrajac & Manes, 2009; Manes et al., 2009), with greater values in correspondence of the interface (Stoesser et al., 2006; Manes et al., 2009). In fact, frequent and highly energetic large scale motions, and in particular sweeps and ejections, were reported by Stoesser et al. (2006) and Cooper et al. (2018).

Munoz Goma and Gelhar (1968), Ruff and Gelhar (1970), Chu and Gelhar (1972), Mendoza and Zhou (1992) and Prinos et al. (2003) reported higher Reynolds stresses over porous surface and peaking at the interface. Manes et al. (2009), however, reported no changes from the impermeable case and suggested the Reynolds stress rapidly decay towards the bed and is favour dispersive and viscous components. This difference has to be attributed at the double-averaging procedure implemented in Manes et al. (2009).

In contrast to most of the previous findings is Cooper et al. (2018). In this study higher normalised double-averaged streamwise velocity, lower turbulent velocity intensities, larger Reynolds stresses and low form-induced stresses were noticed over permeable beds. A possible explanation might be imputed at the characteristics of the beds considered impermeable. Cooper et al. (2018) used the casting technique to replace Cooper et al. (2018) a 400x400 mm portion of the gravel bed, corresponding to 5% and 80% of the flume length and width. The short extent of the impermeable tile might have been not sufficient to allow the development of the flow characteristics over a permeable bed. Furthermore, the introduction of an impermeable boundary adjacent to a permeable wall could have caused transitory effects that might explain the particular observed behaviour.

2.5.3 Literature Gaps Summary

The gaps in the literature found in Subsections 2.5.1 and 2.5.2 can be summarised as follows:

- despite the acknowledgement that the free surface is not populated by a single type of surface motion (turbulence-induced features, gravity-capillary waves and stationary waves) but by a variety of them, a consensus on the dominant mechanism has not been found. It results that different hydraulic and morphological conditions were tested and various measurement techniques were employed. This suggests that the absence of agreement might be ascribed to this inconstancy. Indeed, many researchers speculated that boundary conditions such as hydraulic and bed parameters might promote the development of a specific free-surface pattern rather than the others.

- impermeable boundaries are infrequent in nature, still most of the research is done over impermeable surfaces. This hints that a mismatch between what is experimentally tested and what is observed in nature might exist. Furthermore, the little literature available on this topic has divergent conclusions on several topics (e.g. friction factor, momentum transfer and von Kármán constant).

2.6 Key Notes for Experimental Practice

Following the review of past studies, it is possible to derive some recommendations to improve the quality of future (numerical, experimental and analytical) investigations:

- use of permeable walls: typically, impermeable surfaces are preferred over the pervious analogue for practical reasons and similarity between the two cases is tacitly assumed. As it was shown, the flow behaviour over a permeable bed is extremely different from over impermeable surfaces. It follows that the validity of the literature findings that were obtained in studies over impermeable beds can be questioned as different from what is observed in nature.

- simultaneous flow-surface measurements: to completely characterise the relation between free-surface and bulk flow dynamics the two flow fields should be evaluated at the same. The feasibility, however, is limited by technical reasons for laboratory experiments and further hindered for field tests. Analytical and numerical studies do not suffer for these limitations but the difficulty arises in correctly defining the boundary conditions, especially in correspondence of the air and bed interfaces.

- volumetric flow measurements: planar measurements (unless parallel to the bed) do not take into account the lateral variability as related phenomena (e.g secondary currents, streaks and up/downwellings) cannot be observed and spatially-averaged quantities and form-induced components cannot be properly characterised. These processes have a strong influence on the overall dynamics of the flow field, therefore, a correct description can only be achieved when 3D velocity measurements are performed.

- large Field of View (FOV): according to Roy et al. (2004), coherent structures typically have to advect for a length equal to 3-5 time the water depth before crossing the entire water depth. This length must be completely measurable to observe the evolution of a coherent structure.
- high space and time resolutions: in order to pick up the smaller structure and high-frequency phenomena.
- free-surface mechanism: it is hinted the free surface might be dominated by three different types of waves (turbulent-induced, gravity-capillary waves and stationary waves). As the dominance might differ according to the boundary conditions, different flow conditions aimed at exploring the surface velocity range around 0.23 m/s should be tested.

Chapter 3

Experiments

3.1 Introduction

The statements of the literature review described in Subsection 2.2.2 and supported by the outcomes from the studies by Savelsberg and Van De Water (2008), Dolcetti et al. (2016) and Dolcetti and García Nava (2019b) clearly demonstrate that the free surface of a turbulent open-channel flow possesses different dynamics according to the hydraulic regime. It seems that the free-surface behaviour is dominated by features advecting at the free-surface velocity when the free-surface velocity is below the minimum phase velocity for gravity-capillary waves (0.23 m/s), while gravity-capillary waves govern for free-surface velocities above such a threshold.
Subsection 2.2.2 also evidences that some forms of resonance relating the wave growth to the speed of a disturbance in the flow exist. This implies that not only the surface velocity but also the depth-averaged velocity needs to be considered for assessing of the extent and importance of these phenomena. Hence, three different classes of flow conditions must be investigated to better understand the dynamics of the free surface. These classes of conditions are:

- Class I: both free-surface and bulk flow velocities below the minimum phase velocity of gravity-capillary waves ($\bar{U}_B, \bar{U}_S < 0.23$ m/s). This regime should be governed by free-surface velocity advecting features, suggesting they might be related to, possibly even generated by, coherent structures interacting with the air-water interface.

- Class II: bulk velocity below 0.23 m/s but surface velocity above this threshold ($\bar{U}_B < 0.23$ m/s and $\bar{U}_S > 0.23$ m/s). The surface velocity exceeds the minimum phase velocity, suggesting the dominance of the free-surface behaviour by gravity-capillary waves. The depth-average velocity for such a condition would be relatively low, limiting but not impeding the resonance phenomena and so generating observable gravity-capillary waves. Coherent structures might still be affecting the free-surface behaviour. This regime may be characterised by a transitioning dominance of the free surface from turbulence-induced features to gravity-capillary waves.

- Class III: both free-surface and bulk flow velocities above the minimum phase velocity ($\bar{U}_B, \bar{U}_S > 0.23$ m/s). This regime should be mostly characterised by gravity-capillary waves produced through resonance.

This Chapter focuses on the experimental phase of this research, from the description of the technical apparatus to the final data processing. The Chapter is organised as follows: Section 3.2 gives a general overview of the flume used; Section 3.3 focuses on the description of the instrumentation used to characterise the flow and the free surface; Section 3.4 describes and discusses the preliminary tasks, ranging from the creation of the permeable bed to the identification of the hydraulic conditions; Section 3.5 reports on the details of the tested flow regimes; and lastly, Section 3.6 contains information on all the aspects of the data processing.

3.2 Flume Overview

The experiments were carried out in the the Hydrodynamics Laboratory at the University of Sheffield. The recirculating flume, pictured in Figure 3.1, has a total length of 20 m and a working length of 15 m, a width of 0.503 m and a wall height of 0.5 m. Walls and bottom consist of glass elements to permit the observation of the body of flow from the sides and below.
The seven 2.5 m long panels that compose the flume are supported by adjustable U-shaped elements to allow independent repositioning. These sections are placed on two parallel 20 m IPE600 profiles that confer high rigidity and high inertial mass to the flume.
A manual hydraulic jack connected to the beams permits the flume slope to be changed from 0 to 1/50. Once the flume slope is changed it can be mechanically clamped in position.


(a) (b)

Figure 3.1: a) Side view of part of the flume used in this investigation. b) View from the upstream section.

The flume is supplied by a submersible pump which draws water from a 4.5x3.5x1.2 m (Length x Width x Height (L-W-H)) tank placed downstream of the flume outlet. To prevent the propagation of vibrations to the flume, the pump is placed on a mattress of porous material and always covered with water in the downstream tank.
As the impeller speed cannot be adjusted, the flow rate is regulated by an actuator controlled butterfly valve positioned at approximately halfway along the flume inlet delivery pipe. The actuator is powered using compressed air and controlled via LabVIEW. The discharge is evaluated by a digital flowmeter with an accuracy of 0.1 l/s (Fig. 3.2a). This device is connected to a National Instruments (NI) Data Acquisition (DAQ) system and sampled every 5 seconds.

The water is first transported to a 0.6x0.6x1.0 m (L-W-H) inlet tank located at the upstream end of the flume to regularise the inflow. The inlet tank is filled with 85 mm wide porous elements that restrict the size of any large flow feature and so reduce any form of inlet effect (Fig. 3.2b).

(a) (b)

Figure 3.2: a) The in-line placed flowmeter. b) Porous elements used to break down inflow effects.

Once the system has reached an equilibrium, the water flows through the 15 m long flume before reaching the outlet section where an adjustable gate is present (Fig. 3.3a). By positioning the gate to have a positive slope it is possible to adjust the normally gradually accelerating flow profile and obtain uniform flow conditions within the working length of the flume.
Downstream of the gate the water falls for 2 m before being returned into the downstream tank that contains the submerged pump.
This flume configuration was chosen to physically disconnect the flow in the flume from the water tank containing the pump so as to limit any possibility of pump vibrations influencing conditions within the flume.

The flume is also equipped with a system of aluminium rails running along the entire length on both sides of the flume (Fig. 3.3b). These rails are set to be parallel to the flume bottom and are used to create a reference system for measuring bed and water surface heights and positioning and referencing the measurement systems. The aluminium rails are mounted on adjustable screw elements to allow their vertical repositioning and so compensate any potential misalignment caused by the flume structure.

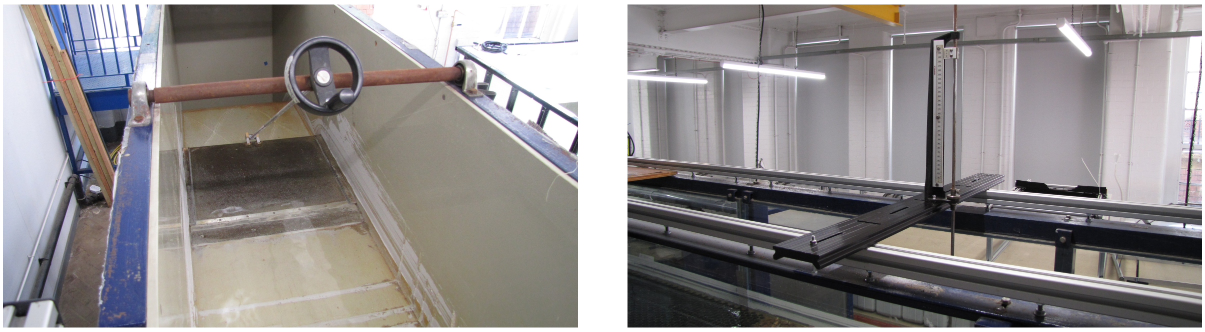

(a) (b)

Figure 3.3: a) The outlet tail gate can be adjusted by means of a knob to create a local positive slope and allow uniform flow conditions to be established upstream in the experimental section. b) The system of parallel rails is used to define a reference system.

3.3 Experimental Setup

To address the different objectives of this investigation a number of different systems were used. Hereafter, the typology and characteristics of the systems, as well as the reasons that led to their choice, are reported. Subsection 3.3.1 focuses on the evaluation of the hydrodynamics; Subsection 3.3.2 describes the systems used to investigate the free-surface behaviour.

3.3.1 Measurement of the Flow Field

Based on the review of methods to evaluate a flow field in Subsection 2.4.1, a PTV STB system was chosen to study the hydrodynamics. This system was preferred for multiple reasons:

- volumetric measurements
- high sampling frequency
- tracers density similar to tomographic PIV, resulting in high spatially resolved data sets
- possibility to evaluate highly sheared flows
- low computational requirements
- short computational times
- low numbers of ghost particles
- possibility of post-processing to convert the sparse tracks into a regular orthogonal grid

Figure 3.4: Imager MX 4M camera with a blue light bandpass filter used for PTV.

The PTV system was composed by four monochromatic Imager MX 4M cameras provided by LaVision. Characteristics of the cameras are a resolution of 2048x2048 pixels and a pixel size of 5.5x5.5 μm^2. These cameras mounted 35 mm F/1.6 Ricoh lenses and were equipped with 410-490 μm bandpass filters (blue light passing) (Fig. 3.4). Filters were used to minimise the influence of external light sources and prevent the appearance of fake particles.

Cameras were installed on a stiff structure placed on the laboratory floor on one side of the flume at 9.3 m from the inlet. The frame was positioned so that the average distance between the cameras and the centreline of the flume was 960 mm (Fig. 3.5a).

A linear configuration for the cameras had to be necessarily opted for instead of a cross configuration because of the laboratory layout. Cross configuration is mostly preferred as it provides more viewing directions into the measurement volume, maximising the accuracy in the triangulation of the particles and so the performance of the PTV system. A linear configuration, instead, only provides viewing directions from a common plane, resulting in a larger widthwise particle positioning error. However, when carefully set up, both configurations can yield excellent results and the difference in the performance is negligible.

A first couple of cameras was set to an angle of 15° respect with the normal to the flow direction, while the second couple of cameras was tilted with an angle of 30° respect with the streamwise direction. The resulting geometry of the PTV setup was as proposed in Figure 3.5b.

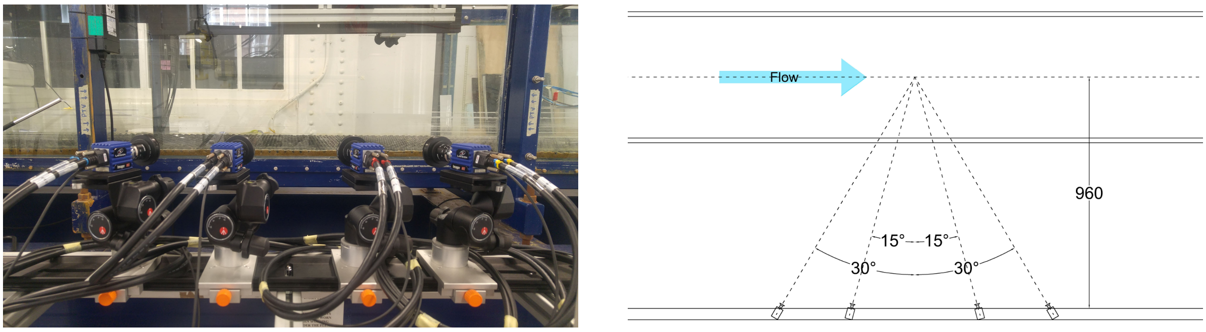

(a) (b)

Figure 3.5: a) Side-viewing PTV cameras in a linear configuration. b) Geometry sketch of the PTV system.

The cameras of the PTV system were positioned to have a FOV of 300x300 mm^2 along the streamwise and vertical directions, respectively. These dimensions were chosen to visualise the flow field for a length that was several times the water depth as Roy et al. (2004) reported that the turbulent structures can have a length up to 6 times the water depth.

In order to image the same volume from different angles, the cameras could not be positioned at the same distance from the flume. For this reason, the cameras were not characterised by the same Ground Sample Distance (GSD) value (i.e. the camera spatial resolution). The average GSD value, given by Equation 3.1, resulted of 0.15 mm/pixel.

$$GSD = \frac{S_{CF} * S_L}{C_{FL} * I_{px}} \tag{3.1}$$

where S_{CF} is distance between the camera's sensor and the flume centreline, S_L is the dimension of the sensor given by the product of the pixel size and number of pixels, C_{FL} is the focal length of the lens and I_{px} is the dimension in pixels of the image.

The cameras were focused on the flume centreline and the aperture was set at 8 (out of 16) as a compromise between large depth of field and lighting. To allow the images to be directly saved on the hard drive, the size of the images had to be contained. This was achieved by setting the cameras to a bit depth of 10, resulting in images with 1024 shades of light intensity.

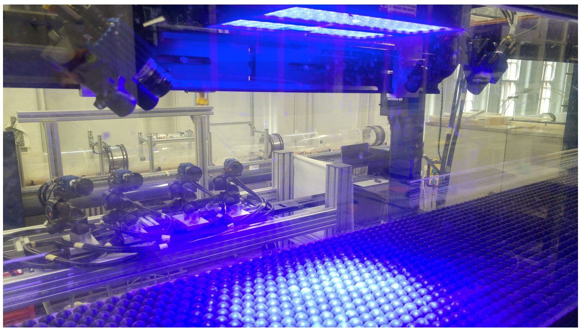

Figure 3.6: LED array.

Two blue Light Emitting Diode (LED) Flashlight 300 provided by LaVision were used to illuminate the fluid volume. The LEDs, having a length of 337 mm and width of 117 mm, were positioned side by side along the length so that the total illuminating area was 337x234 mm^2 (streamwise and lateral, respectively). Considering the presence of a rough bed and in order not to interfere with the cameras, the lighting array was placed 0.60 m above the bed pointing downwards (Fig. 3.6). It follows that the LEDs shined through the water free surface. As the light beams presented a divergence angle of 8°, a 505×402 mm^2 area resulted illuminated in correspondence of the bed level. The illuminated area was therefore larger than the FOV of the PTV cameras.

To visualise the flow field, the flow was seeded with polyamide particles provided by LaVision. The particles were characterised by a narrow distribution with an average diameter of 100 μm. The particle density was 1.01 g/cm^3, slightly denser than water. Nonetheless, the tracers, due to their size and negligible difference of density, behaved as essentially neutrally buoyant elements.

3.3.2 Characterisation of the Free Surface

The free surface was studied using two instruments: an optical DIC system and an array of conductive wave probes. The choice of using different techniques was made as Subsection 2.4.2 highlighted the difficulties in monitoring a liquid interface by means of optical methods.

The DIC system was composed by two Imager MX 4M cameras (same as the ones used for the PTV system) mounting 16 mm F/2.0 M112FM16 Tamron lenses but no filters (Fig. 3.7a).

The cameras were secured onto a stiff bar hanging from the ceiling and isolated from the flume to prevent any vibrations within the flume from affecting the DIC measurements. This mounting bar was placed 9.3 m from the flume inlet and was set to be as parallel as possible to the flume bed at a height of 395 mm from the top of the spheres.

The DIC cameras were placed at a distance 0.70 m from each other, one upstream and one downstream of the LEDs, at an angle of 41.5° with respect to the bed normal. The resulting geometry of the DIC setup was as shown in Figure 3.7b.

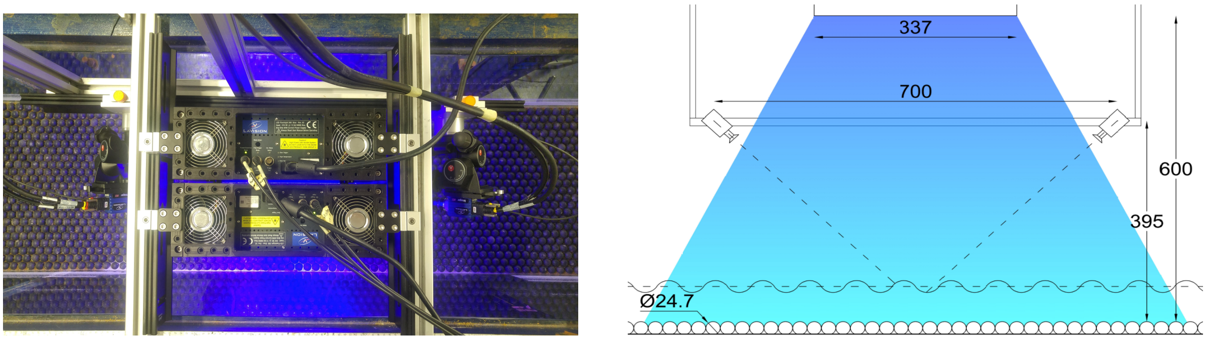

(a) (b)

Figure 3.7: a) Top view of the DIC cameras and LED array. The LED array can be seen between the two cameras. b) Geometry sketch of the DIC system.

In relation to the bed level, the GSD of the DIC cameras, resulted of 0.17 mm/pixel, while the FOV was 363x363 mm^2. During the experiments the distance between cameras and flow free surface varied from case to case according to the water depth of each test. Because of this, the camera spatial resolution was higher than the value reported above.

Due to the cameras' inclination with respect to the bed normal direction, the sections of the photo that imaged the furthermost parts of the free surface could not be used. This happened as the cameras' angle was too deep, causing these parts of the images to be too much different for the correlation routine of the DIC analysis to work. As a consequence, the part of the FOV that could effectively be reconstructed was approximately 10% smaller than the reported value. Also, the varying cameras-surface distance caused a further reduction. In the end, the effective FOV of the DIC system resulted smaller than the illuminated area.

The cameras were centred on the flume centreline with a lens aperture was of 16 in order to have a depth of field as wide as possible and so having as much of the FOV as possible in reasonable focus. Once again, to limit the size of the images, the cameras bit depth was set to 10, corresponding to 1024 shades of light intensity.

To permit the reconstruction of the free surface, POS-IBW 300 cenospheres produced by Possehl Erzkontor GmbH & Co. KG were employed. Cenospheres are ceramic hollow spheres characterised by a density lower than water (0.7 g/cm^3). This specific material was chosen as it presents an off-white colour that permitted the formation of a speckle pattern sufficiently unique for the DIC to work. Compared to other buoyant surface tracer candidates, like hollow glass spheres or silver-coated hollow glass spheres, cenospheres do not produce any electrostatic interactions, meaning that surfactants are not required to prevent coalescing and lumping. Cenospheres are also hydrophilic and do not stick to the water-air interface. Tracers failing to do so would impact on the surface tension (Turney et al., 2009).

The material was characterised by an initial range of diameters between 90-315 μm. The cenospheres had to be sieved to isolate the fraction having diameters ranging between 90 and 280 μm. This upper threshold value was chosen as for larger diameters the Stokes number, St, defined as the ratio between the particle and fluid characteristic time scales, becomes greater than 0.1. The Stokes number is used to verify the capability of a particle to follow the flow without disturbing it (Akutina, 2015). Tropea et al. (2007) suggested tracers having $St < 0.1$ are able to correctly describe the flow with an accuracy error below 1%. The sieved material resulted in Stokes numbers between 0.08 and 0.1.

To verify the accuracy and the reliability of the DIC, an array of wave probes was also installed at the 10 m location from the inlet (Fig. 3.8a). The array, which geometry is shown in Figure 3.8b, was mounted on a Vernier scale to allow its precise vertical repositioning in relation to the different flow depths.

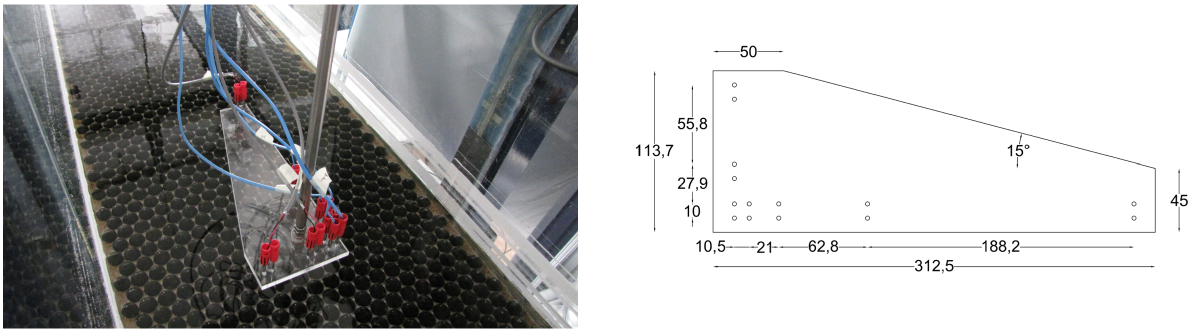

(a) (b)

Figure 3.8: a) Wave probe array. b) Geometry of the wave probe array.

The array was formed by seven wave probes, positioned so that 5 were aligned along the centreline and the other 2 were perpendicular to this direction on the side of the most upstream one. This arrangement allowed to have 5 wave probes describing the free-surface behaviour along the streamwise direction and 3 probes along the spanwise direction.
The streamwise length of the array was 282.5 mm, while along the spanwise direction it was 83.7 mm long. Given this, the array was characterised by a streamwise Nyquist spectral wavenumber (i.e. maximum observable wavenumber), $k_{Nyq,x}$, of 200.2 rad/m, while along the spanwise axis the Nyquist spectral wavenumber, $k_{Nyq,y}$, was 150.1 rad/m. The spectral wavenumber resolution was 10.5 rad/m and 30.0 rad/m along the streamwise and spanwise directions, respectively. The lower spectral wavenumber resolution along the spanwise direction was caused by the smaller number of probes along this direction.

The probes were connected to a Churchill Controls wave monitor and energised at different frequencies to prevent any mutual interference. Wires were compensated to allow the establishment of a linear relationship between voltage and surface elevation. To allow the sampling of the wave probe data, the wave monitor was connected to a National Instrument 8 channels acquisition card and recorded on a National Instrument PXIe-8108 embedded control system with LabVIEW.

3.4 Preliminary Experimental Phase

This Section is used to describe all the preliminary tasks that were needed prior to running the flow conditions later examined in the main experimental phase. This stage of the process was needed to correctly identify the hydraulic regimes that would be needed to verify the hypotheses first introduced in Section 1.3. This phase was also needed to evaluate the performances of the PTV and DIC systems and adjust their settings to maximise their performance and the quality of the later experiments. Subsection 3.4.1 describes all the preliminary actions needed before the creation of the bed, Subsection 3.4.2 reports the process of formation of the permeable composite bed and Subsection 3.4.3 presents the procedure for the identification of the final experimental flow conditions.

3.4.1 Initial Tasks

A number of preliminary tasks were required before beginning with the creation of the bed. These actions mainly concerned the definition of a single reference system that could be used for all the instruments and the development of a strategy to correctly align all the devices to such a reference system.

The first task was the recalibration of the longitudinal aluminium profiles described in Section 3.2. To correctly perform the alignment, a still water level was used as a reference for the horizontal plane: the flume was first set to what it was thought to be the horizontal position, inlet and outlet were then impermeably sealed and later the flume was partially filled with water. After the filling, the flume was left to rest for at least two hours to allow any long period features produced by the filling procedure to dissipate. Eventually, a flat still water level was obtained.

A point gauge with a Vernier scale and having a precision of 0.1 mm was mounted on rigid bar positioned across the flume on the longitudinal parallel bars (Fig. 3.9). The gauge was used to measure the height of the water surface at different sections along the flume. Alignment with the horizontal plane would have been reached only when all the measurements reported the same value. To prevent any form of false positive as a result of a fortunate combination of misalignment of the two parallel rails, the pointer was aligned not with the centreline of the flume but positioned at a quarter of the flume width from the flume wall. In this way, each of the deviations of the two sides were weighted according to their distance from the point gauge. The pointer was then moved along the flume and the positioning of one rail was adjusted to have the same height throughout the length. The same procedure was then performed on the other rail before moving once again to the first side. The alignment continued until the same free-surface height (within an error of 0.1 mm) was iteratively reached on both the side of the flume. The rails in such a configuration were reckoned aligned along the horizontal plane. The alignment was periodically verified to prevent any form of bias caused by rails deformation (e.g. because of an environmental temperature change), but no deviations from the set positioning were found.

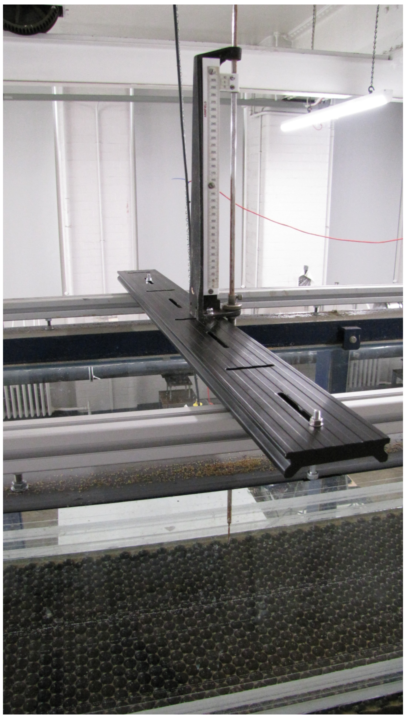

Figure 3.9: Point gauge equipped with a Vernier scale.

The next step consisted in the identification of the position of the centreline of the flume. A ruler was used to do so before drawing the centreline on the glass (Fig. 3.10a). For aligning the systems on this locus two pairs of small laser pointers were mounted on stiff transverse bars that were placed on the recently aligned parallel measurement rails (Fig. 3.10b).

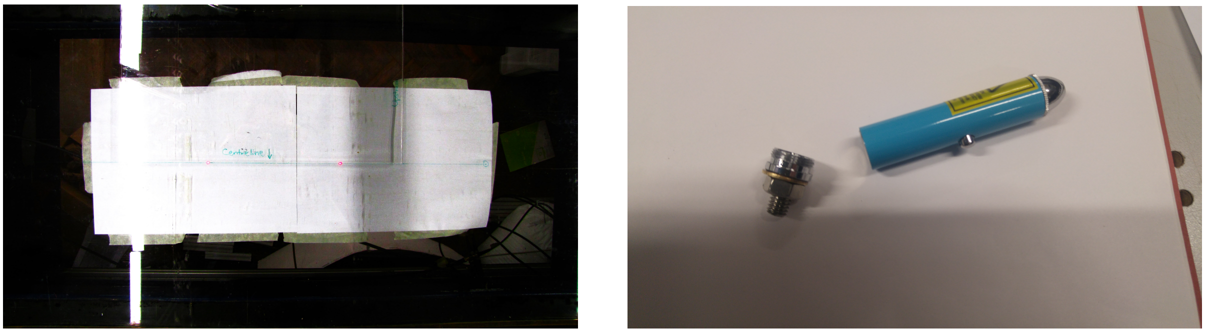

(a)

(b)

Figure 3.10: a) Flume centreline (displayed in green). Lasers used for the alignment are also visible. b) Laser pointers used for the alignment of the calibration plates.

To determine the linkage between the free surface and the underlying hydrodynamics it was necessary to match the local reference systems of the PTV and DIC systems to this global one. As the origin of the PTV calibration plate lies on the frontal side, this face was positioned along the centreline. To save the position of the flume axis and allow the correct positioning of the plate once the bed was formed a couple of lasers were used. Aligning these lasers with the front face was difficult, so it was preferred to align them on a line drawn on the plate that represented half of the plate thickness (Fig. 3.11a). The plate was then installed on a traverse line to verify the goodness of the alignment produced by the lasers in operative conditions (Fig. 3.11b).

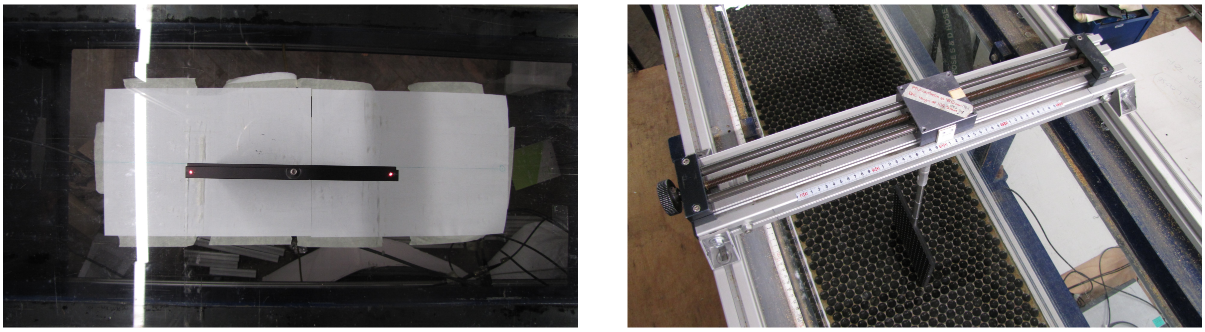
(a) (b)

Figure 3.11: a) Alignment of the lasers for the PTV calibration plate. b) Traverse line mounting the PTV calibration plate.

A ruler was used to determine the projection of the origin of the PTV calibration plate on the flume bottom. The PTV plate was later removed from the traverse line and replaced by a laser. By rotating the screw on the traverse line, the position of the laser was adjusted to match the PTV origin projection. This step was crucial as it permitted the alignment along the streamwise direction of the PTV and DIC reference systems.
A second couple of lasers was used for the alignment the DIC calibration plate. The lasers were positioned so that their ray collimated with the centreline.

This set of actions allowed both the plates to have their x-direction oriented along the centreline and to have the local reference systems aligned on the horizontal plane (plane defined by the measurement rails). The vertical alignment, needed to complete the matching of the two systems, was later performed by measuring the height of the origin of two plates with the point gauge. As the quality of the DIC calibration improves according to the vicinity of the plate to the surface that needs to be reconstructed, the vertical positioning of the DIC plate changed from experiment to experiment. For this reason, the measurement of the origins had to be performed in every test.
In terms of accuracy, this method permitted to align the PTV and DIC plates along the centreline with an error up to 1°, while the matching of the two systems was possible with an error of less than 0.2 mm along the three directions.

3.4.2 Bed Formation

Once these alignments were complete it was possible to proceed with the bed creation. During this experimental campaign it was decided to use a novel composite bed made of both large plastic spheres and coarse sand.

Spheres have been employed in a number of studies (Zagni & Smith, 1976; Zippe & Graf, 1983; Manes et al., 2006; Pokrajac et al., 2007; Manes et al., 2008; Manes et al., 2009; Pokrajac & Manes, 2009; Nichols, 2013; Dolcetti et al., 2016; Kim et al., 2018) for different size, texture orientations, working fluid and of course flow regimes and slopes. Sphere constructed beds present highly idealised geometry, much different from the more "random" bed arrangements found in nature. Spheres were often preferred as they are easily deployable, facilitate the measurement of the subsurface flow, periodicity and promote turbulence penetration. Spheres only, however, cannot correctly describe the hydrodynamics over a pervious bed. In fact, while moving from the top to the bottom of such a bed, porosity initially decreases and a minimum is observed halfway down the sphere. Further downwards porosity increases until it reaches unity at the base of the flume. This pattern of porosity represents something not encounterable in nature.

For these reasons, it was decided to create a composite spheres-sand bed: the upper layer made of spheres was chosen to allow the comparison of the results of this investigation with previous studies, while the coarse sand was used as a foundation and to fill the gaps in order to confer realism in terms of vertical porosity distribution to the bed. As a consequence, the bed simulated armouring-like conditions (i.e. when the surface bed material has a critical shear stress significantly higher than the applied shear stress, therefore preventing any form of scouring and local sediment transport) and with a nearly constant porosity profile below the mid-level of a sphere (so creating a more natural vertical porosity profile). This expedient allowed to obtain a bed similar to the ones observed in the middle-upper stage of a river.

Figure 3.12: 24.72 mm wide plastic spheres.

A total of 339 spheres were used to determine the geometrical characteristics of these elements (Fig. 3.12). Using a digital Vernier caliper with an accuracy of 0.01 mm, an average diameter, ϕ, equal to 24.72 mm and a standard deviation of σ_ϕ of 0.20 mm were determined. This deviation was a consequence of their manufacturing process. Nonetheless, the deviation from a perfect spherical shape was very small.

Granulometric properties of the sand were derived using sieves from a sample of 0.871 kg (Fig. 3.13). The coarse sand presented a very narrow grain size distribution as nearly 99% of the total mass was retained by the 600 and 850 μm apertures. For this narrow grain size distribution a uniform permeability value was expected, with little spatial variability.

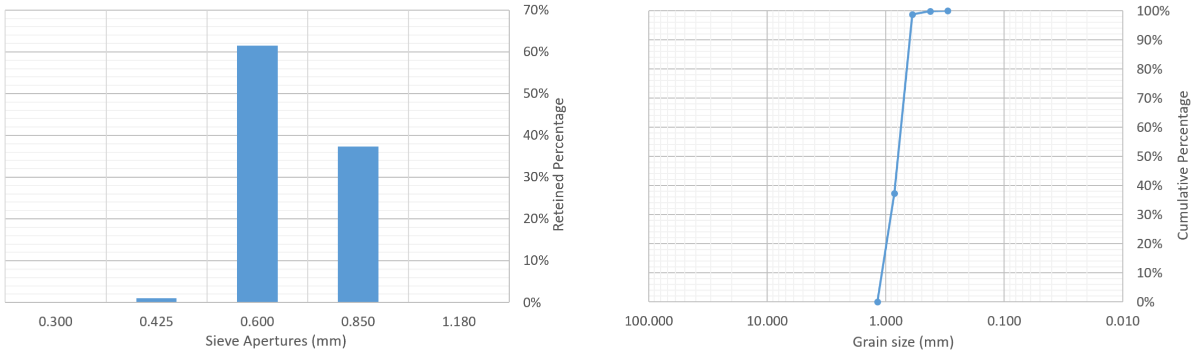

(a) (b)

Figure 3.13: a) Sand particle size distribution. b) Cumulative grain size distribution.

The formation of the bed started with laying gravel of a nominal particle size of 25 mm in the initial 4.8 m of the flume to form a region of uniform thickness equal to 25 mm. This choice was made as not enough spheres were available to cover the entire flume. Covering the initial section with gravel not only allowed to have continuity on the bed surface height with the composite bed that would be formed later, but also enhanced the development of the turbulent boundary layer. As the gravel size was comparable with to the spheres' diameter, the turbulence here produced was reckoned to have characteristics similar to the ones expected over the composite bed.
Two transverse bars were used to keep the gravel in place. Later, the flume was tilted at a slope of 1/250 and the gravel bed was waterworked for 2 days up to a flow rate of 34 l/s. This operation allowed the randomly distributed gravel to re-orient accordingly to the flow and obtain a more natural appearance (Fig. 3.14). The flume was finally set flat again and the elevation of the gravel was checked to verify the absence of lateral gradients. No lateral gradients were observed.


Figure 3.14: Initial section covered in gravel.

This bed was essentially static after being waterworked and so was used for all subsequent experiments.


Figure 3.15: Sand foundation laid between section 4.8 m and the end.

As mentioned before, the boundaries of the flume are made of glass. Glass is a supercooled liquid, therefore, it deforms with time. This results quite evident when a force is applied, however, even glass own weight is sufficient to trigger the warping process. In fact, bulges were found at the centre of the glass panels composing the bottom of the flume as they are supported only along the edges. This inconvenience was resolved by laying a thin layer of sand from section 4.8 m to the end of the flume (Fig. 3.15). The sand was later consolidated to obtain an even and uniform foundation for the spheres.

Over the sand layer, spheres were one by one positioned to avoid disruption of the foundation. Differently, the first 30 cm after the gravel part and the final 30 cm near the outlet were covered not by individual spheres but by packs of five elements glued together (Fig. 3.16a). This choice was made to increase the stability of the arrangement of spheres in correspondence of transitions (gravel and spheres, upstream; and end of the flume and outlet, downstream) due to the larger critical shear stress requirements for the entrainment. Caution was taken to place the spheres in order to avoid "undulations" of the surface geometry and so the establishment of anomalies in the flow field. Also, spheres were positioned so that the top of the spheres along the central line coincided with the flume centreline.

The gravel at the inlet and the composite bed at the outlet were secured using 25x25x500 mm transverse drilled bars (Fig. 3.16b). These bars presented a number of 1 mm wide holes for not obstructing the flow.

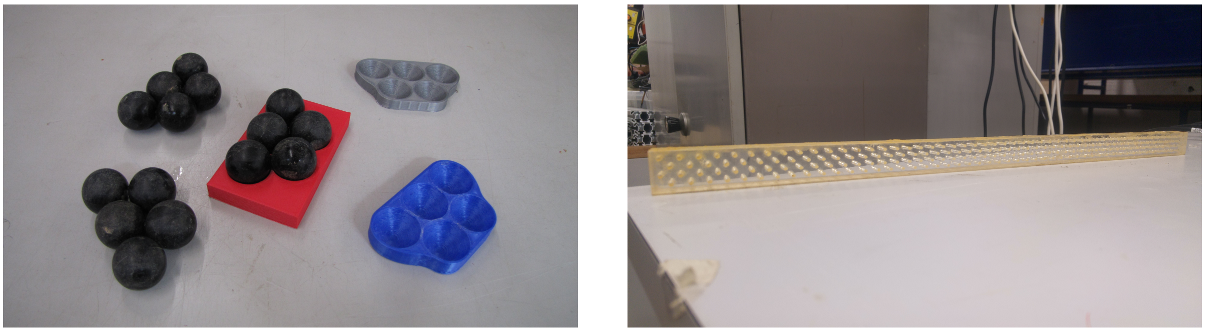

(a) (b)

Figure 3.16: a) Packs composed of five spheres. b) Drilled bar used at the inlet and outlet.

Once verified the elevation of the spheres and excluded the possibility of lateral gradient, the spheres were stabilised in their place by gently sprinkling coarse sand from above until nearly complete submerged (Fig. 3.17a).
The flume was tilted to a slope of 1/500 and the discharge was gradually increased (steps of 4 l/s every 15 minutes) up to 25 l/s. At this flow rate the bed was waterworked for 15 hours. As the shear stress was sufficiently high to pass the threshold of incipient motion conditions for the coarse sand, the procedure permitted the removal of the excess of sand from the previous step (Fig. 3.17b).

(a) (b)

Figure 3.17: a) Sand sprinkled over the spheres for stabilisation. b) Waterworking of the composite bed in progress. Gradual removal of the excess of sand was observed.

As the excess of sand was removed, the discharge was slowly decreased (steps of 4 l/s every 15 minutes) to prevent any damage that potential under-pressures within the bed might have caused to the bed. The flume was then set flat and the height of the spheres was measured using the point gauge. The check permitted the possibility to demonstrate that no lateral or longitudinal gradients had formed while the waterworking was taking place.

At the end of the procedure, the resulting bed was composed of spheres embedded in consolidated sand, with only the top half of the hemispheres exposed to the action of water (Fig. 3.18).

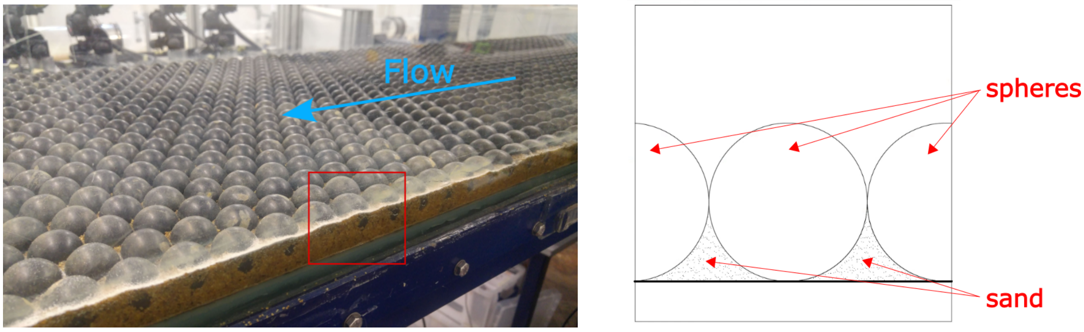

(a) (b)

Figure 3.18: a) View of the composite bed. Hemispheres emerging out of the sand can be observed. b) Side view sketch of the composite bed.

Figure 3.19: Example of bed failure.

The main advantage of this type of bed is that it resembles a river natural gravel bed but presents a regular geometry. In a laboratory environment, this bed is a compromise between the complexity but reality that a gravel bed can give, and the practicality resulting from using standard geometries. Nonetheless, it also presents some technical downsides. From the static point of view, the presence of sand leads to a hyperstatic configuration (i.e. the constrains are more than the degrees of freedom). Hyperstatic systems are highly affected by thermal variations which produce additional internal stress. Indeed, the first cause of failure for this bed was the spheres' thermal expansion induced by the progressively warming of water, resulting in portions of the bed bulging above the general bed level (Fig. 3.19). Another failure reason was the continuous cycle of spheres expansion and shrinkage caused by water absorption and drying.

Due to the fragility and short life expectancy of this bed, more extensive measurements of the bed properties and characteristics (e.g. porosity, permeability and structure function) could not be performed and had to be estimated. Furthermore, to carry out all the necessary preliminary tasks, the bed had to be recreated several times. Caution was taken to minimise the differences between the various beds.

3.4.3 Identification of the Flow Conditions

The next step after the creation of the composite bed consisted in the identification of an appropriate set of experiments aimed at exploring a range of free-surface velocities and, possibly, different free-surface deformation mechanisms.

A first consideration concerned the flume slope. The relatively large size of the spheres (ϕ = 24.72 mm) and the armouring-like condition was analogous to the beds typically observed

in the middle-high sections of streams, where the bed slope ranges between 1/1000 and 1/250. Therefore, a representative slope of 1/500 was chosen for conducting this preliminary exploration of the flow conditions.
The flume was tilted at this slope, inlet and outlet of the flume were once again sealed and the flume filled with water. The chosen slope was verified measuring the height of the still water surface using the point gauge. Inlet and outlet were finally unblocked.

No prior relationships between the free-surface velocity, the discharge and the outlet gate position were known for this type of bed. For this reason, a first linkage between the discharge and the outlet gate had to be found. This was needed for identifying the gate positions that allowed the establishment of a reach of uniform water depths that were as long as possible and especially along the sections that contained the PTV and DIC measurement systems.
As the PTV and DIC systems were to be centred at section 9.33 m, care was taken to set at least the part of the flume between sections 7.33 m and 11.33 m (i.e. 2 m upstream and downstream the centre of the region of interest) in uniform flow conditions.
For a given flow rate, the water depth between sections 7.23 m and 11.43 m was measured with a spacing of 0.30 m for a range of gate positions. This operation was performed by means of a point gauge that was zeroed in correspondence of the top of the spheres. A linear fit was then performed once these measurements had been made to determine the slope of this trend (Fig. 3.20). The correct gate position was identified as the one producing a trend with angular coefficient equal to zero. This followed as the flume rails supporting the point gauge were aligned with the composite bed, so that the angular coefficient of the trend represented the difference between the water surface slope and the bed slope.

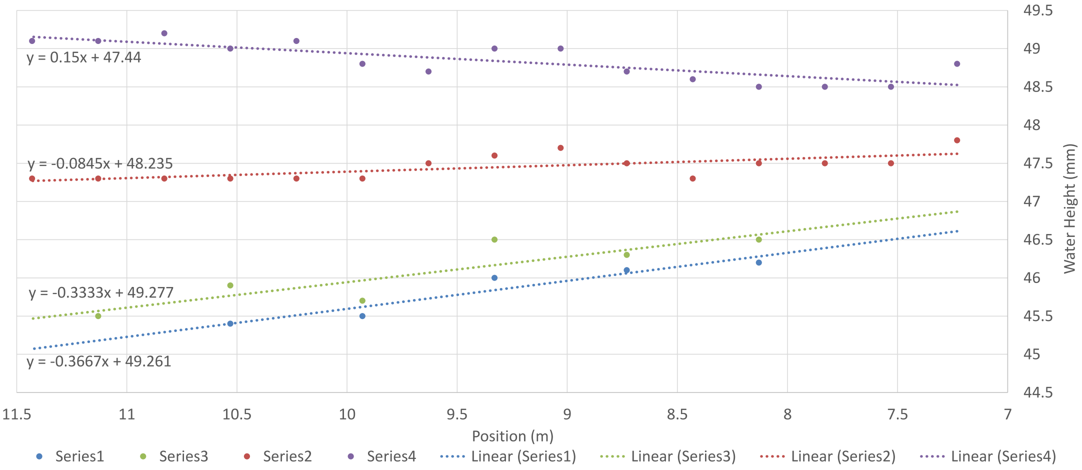

Figure 3.20: Water surface profiles for different outlet gate positions for flow rate Q = 6.31 l/s. Markers indicate the observed water height, while the colour-corresponding dotted lines represent the linear trendline. The equations of the fitting lines, expressed in mm/m, represented the slope of the measured free-surface profiles and were used to identify the uniform flow conditions.

The procedure was repeated for several other flow rates, allowing a relationship between discharge and tail gate position that delivered uniform flow conditions to be determined. This was later fitted with a cubic function (Fig. 3.21).

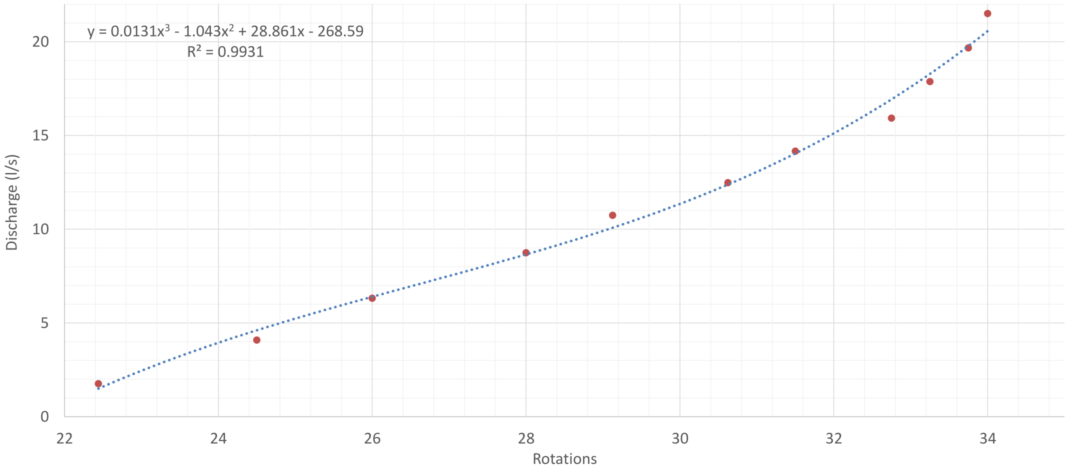

Figure 3.21: Discharge-gate relation to obtain uniform flow conditions in the region of interest (red markers) and cubic fitting (blue dotted line) for a composite bed over a slope of 1/500. Fitting equation is displayed on the top left corner. "Rotations" reported in the horizontal axis indicates the required number of rotations of the knob controlling the tail gate to move the gate to the position that allowed the free-surface profile and bed slopes to be the same.

The discharge-uniform water depth relationship was also derived and fitted with a square function (Fig. 3.22).

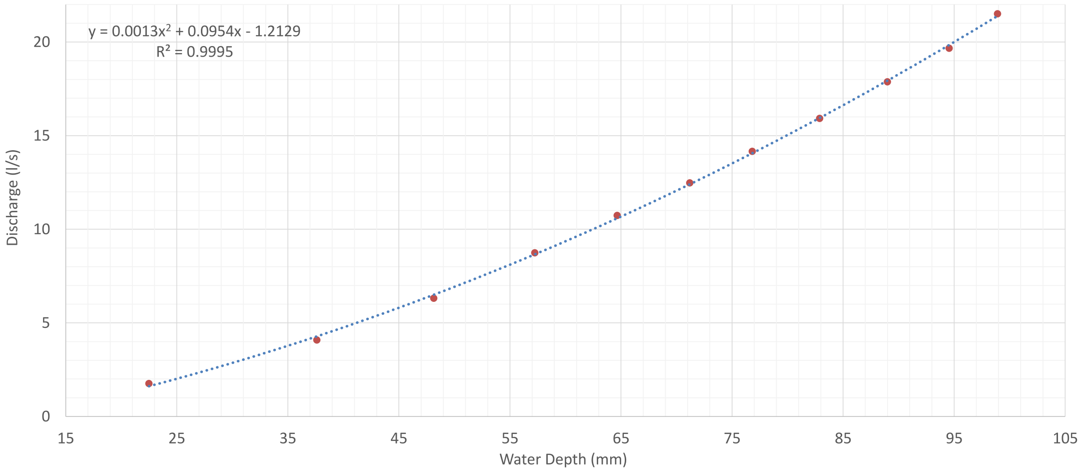

Figure 3.22: Discharge-uniform water depth relation (red markers) and square fitting (blue dotted line) for a composite bed over a slope of 1/500. Fitting equation is displayed on the top left corner.

The final step of the preliminary stage was determining the free-surface velocity for the same set of conditions as before. The free-surface velocity was estimated from the average time required by a buoyant object to travel between sections 8.705 and 9.955 m (i.e. 0.625 m upstream and downstream the area of interest). The floater was released in correspondence of the transition between gravel and composite bed (section 4.8 m) to have enough space (3.9 m) for accelerating and achieve a stable velocity. Ten time measurements were taken under uniform flow depth conditions using a stopwatch before averaging the measurements to obtain the free-surface velocity. The free-surface velocity error was related to uncertainties in correctly measuring the travelling time of the buoyant object between the two sections. As this uncertainty was not directly quantifiable, it was estimated from the human reaction time to visual stimuli in simple reaction time tests, equal to 0.190 s (Wilkinson & Allison, 1989). The time uncertainty was set to be twice this reaction time value as the error could have occurred at both the beginning and the end of measuring procedure. Considering the distance between the two measuring sections, the experimental error affecting the free-surface velocity varied between 6.0% for the slowest flow conditions and 21.0% for the higher flow rates.

Depth-averaged velocity was instead calculated dividing the time-averaged flow rate obtain from the flowmeter by the flow cross-sectional area defined by the uniform flow depth.

The relation between free-surface and depth-averaged velocities and its linear fitting are represented in Figure 3.23.

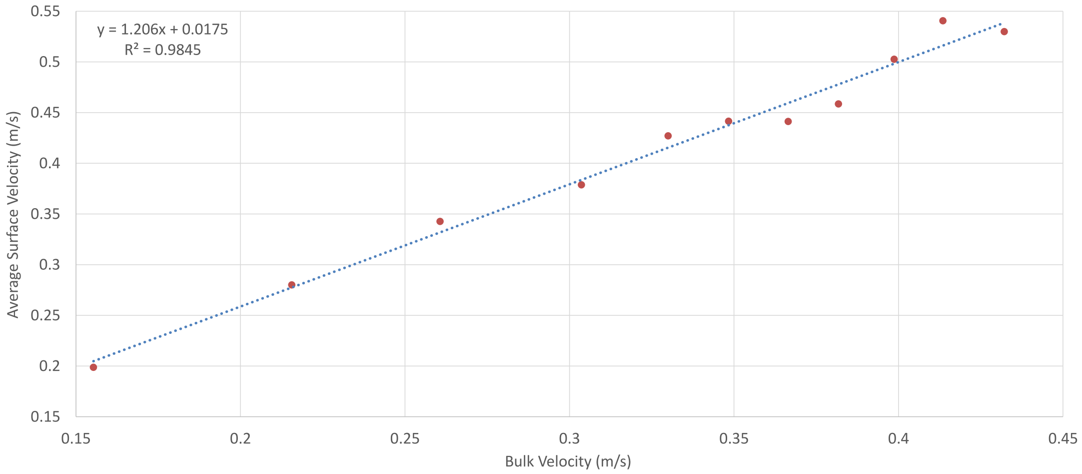

Figure 3.23: Free-surface and depth-averaged velocities relation (red markers) and linear fitting (blue dotted line) at uniform flow conditions for a composite bed over a slope of 1/500. Fitting equation is displayed on the top left corner.

The ratio between depth-averaged and free-surface velocities was found having a more variable behaviour, varying with the water depth between values of 0.76 and 0.81 (Fig. 3.24).

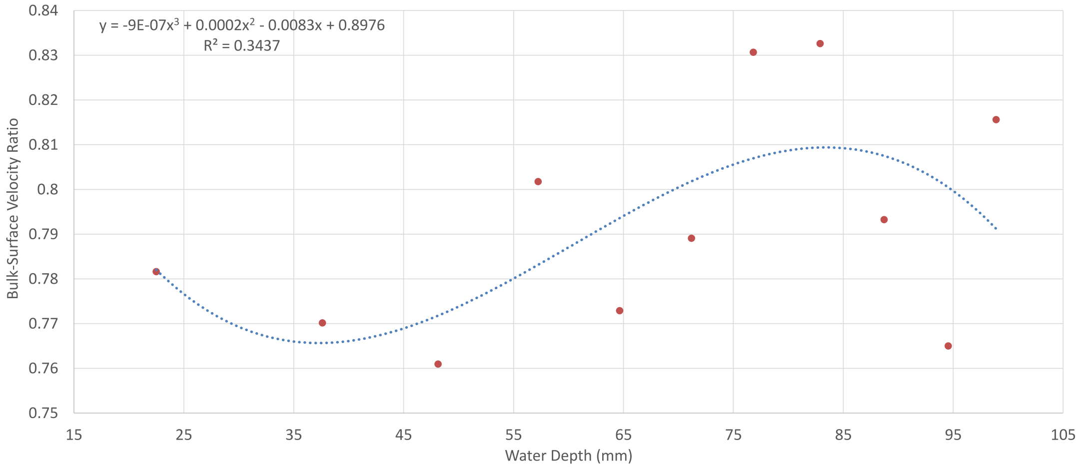

Figure 3.24: Bulk-surface velocity ratio at different uniform water depth (red markers) and cubic fitting (blue dotted line) for a composite bed over a slope of 1/500. Fitting equation is displayed on the top left corner.

As specified in Section 3.1, three different classes of experiments were needed to fully characterise the free-surface behaviour. Because the free-surface velocity is the discriminant of the type of test, the desired time-averaged free-surface velocity was first chosen and later, considering the previously found relations, the conditions reported in Table 3.1 were identified for the representative slope of 1/500.

Test	$\bar{U}_S$ (m/s)	$\bar{U}_B$ (m/s)	U_{rat}	D (mm)	Q (l/s)	Re	Fr	D/ϕ	u^* (m/s)	AR
FC1	0.22	0.17	0.77	21.5	1.9	3600	0.37	0.87	0.020	23.4
FC2	0.30	0.24	0.80	30.8	3.6	7300	0.44	1.25	0.023	16.3
FC3	0.36	0.28	0.78	49.9	6.8	13800	0.40	2.02	0.029	10.1
FC4	0.42	0.33	0.79	64.4	10.6	21000	0.42	2.61	0.032	7.8
FC5	0.49	0.39	0.80	81.3	15.6	31400	0.44	3.29	0.035	6.2
FC6	0.55	0.44	0.80	96.2	21.1	41900	0.45	3.89	0.037	5.2

Table 3.1: Characteristics of the flow conditions tested for slope 1/500. $\bar{U}_S$ is time-averaged surface velocity; $\bar{U}_B$ is time- and depth-averaged surface velocity; U_{rat} is the depth-averaged and time-averaged surface velocity ratio; D is uniform water depth, derived using the Gauckler-Strickler formula; Q is discharge; Re is Reynolds Number; Fr is Froude Number; D/ϕ is relative submergence; u^* is shear velocity; AR is aspect ratio.

The same sequence of operations aimed at identifying the flow conditions was repeated over a slope of 1/1000. For this case, the conditions are reported in Table 3.2.

Test	$\bar{U}_S$ (m/s)	$\bar{U}_B$ (m/s)	U_{rat}	D (mm)	Q (l/s)	Re	Fr	D/ϕ	u^* (m/s)	AR
FC1	0.22	0.17	0.77	27.3	2.3	4600	0.33	1.10	0.016	18.4
FC2	0.30	0.24	0.80	50.7	6.6	12000	0.34	2.05	0.020	9.9
FC3	0.36	0.28	0.78	61.2	8.1	17000	0.36	2.48	0.022	8.2
FC4	0.42	0.33	0.79	99.8	16.8	32600	0.33	4.04	0.026	5.0
FC5	0.49	0.39	0.80	125.0	23.4	48200	0.35	5.08	0.029	4.0
FC6	0.55	0.44	0.80	175.2	38.7	76500	0.34	7.10	0.032	2.9

Table 3.2: Characteristics of the flow conditions tested for slope 1/1000. $\bar{U}_S$ is time-averaged surface velocity; $\bar{U}_B$ is time- and depth-averaged surface velocity; U_{rat} is the depth-averaged and time-averaged surface velocity ratio; D is uniform water depth, derived using the Gauckler-Strickler formula; Q is discharge; Re is Reynolds Number; Fr is Froude Number; D/ϕ is relative submergence; u^* is shear velocity; AR is aspect ratio.

Depth values proposed in Tables 3.1 and 3.2 were estimated from the depth-averaged velocity using the Gauckler-Strickler formula while assuming a constant value of 50 $m^{1/3}/s$ for the Strickler coefficient (Strickler, 1924) (i.e. 0.02 $s/m^{1/3}$ for the Manning coefficient). This value was considered representative of the range of Strickler coefficients observed for a series of conditions with discharge varying between 1.76 and 21.5 l/s.

As mentioned before, this type of composite bed is extremely fragile, reason for which it had to be rebuilded many times. It follows that the different beds were similar but not identical. Due to the short life span, bed properties could not be collected, preventing a statistically comparison between the various formations. Because of this, the relations here found were considered valid only in first approximation and had to be validated and in case corrected each time a new bed was used. Nonetheless, these relationships allowed to identify the hydraulic regimes that would be tested, reducing the working time of the final beds used in this investigation.

3.5 Experiments

3.5.1 Overview

Defining a linkage between the flow dynamics and the free-surface behaviour is the primary purpose of this investigation. However, this task is extremely challenging, mainly due to technical limitations of the experimental setup and the proximity to the air-water interface.

According to Schanz et al. (2015) the PTV system is able to correctly describe the flow field up to tracers densities of 0.125 ppp, corresponding to 1 particle over an area of 8 pixels or 1 particle in a square 2.82 pixels wide (note that this concentration does not represent the physical concentration of tracers in the flow field, but it rather describes how much of the camera sensor can be occupied by the tracers). This concentration results incompatible with the DIC requirements of surface entirely (or even partially) coated. As simultaneously running the PTV and DIC systems to obtain the best performance for each method was impossible, it was chosen to evaluate the flow field and the free surface at two different times, according to the following scheme:

- phase 1: the flow was evaluated by means of PTV only; this was needed to maximise the level of detail in the flow behaviour description.
- phase 2: this step focused on maximising the free-surface reconstruction via DIC; to do so, high concentrations of surface tracers were used, allowing to have a continuous coated surface over a relatively large area.

Due to this plan of action, it was not possible to evaluate completely identical conditions for the two systems. Nonetheless, the repetitions of the different hydraulic regimes had a high grade of similarity. Hence, the details of each flow conditions will be presented twice: one specific for the PTV run and one for the DIC run.

A second goal of this study is evaluating how bed texture orientation influences both flow field and free-surface dynamics. This objective was achieved by testing the same hydraulic conditions over two different spheres surface arrangements: quincunx (Fig. 3.25a) and alternate (Fig. 3.25b). For a quincunx arrangement the flow travelled above sequence of spheres crests and troughs, while for an alternate packing the flow travelled above either the culmination of the spheres (crests) or at the plane of the sand (troughs). For this reason, this arrangement resembled longitudinally extended bars. It follows that the two arrangements are identical but rotated by 90° in relation to the main direction of the flow.

The third goal was to investigate the role of submergence and to achieve this, two different slopes were tested over the quincunx arrangement: 1/500 and 1/1000. Once again, the discriminating factor was the free-surface velocity, therefore, the flow conditions over the two slopes were compared for matching free-surface velocity.

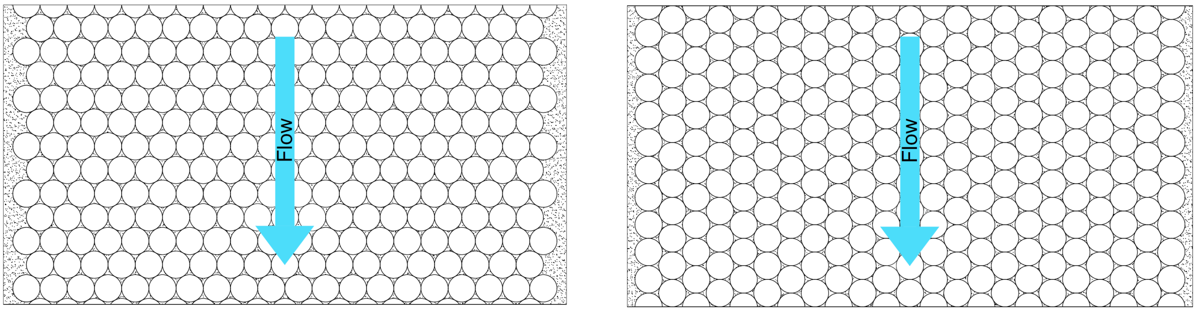

(a) (b)

Figure 3.25: a) Top view sketch for the quincunx arrangement. While moving from upstream to downstream the flow encounters tops and crests alternatively. b) Top view sketch for the alternate arrangement. While moving from upstream to downstream the flow travels above either series of spheres' top or troughs. This bed texture resembles longitudinally bars.

3.5.2 Experimental Procedure

Once the final bed for each of the arrangements was formed, the first step was the validation of the discharge-depth and discharge-gate relations found in Subsection 3.4.3 as the final test beds were not the same as the one used when the relationships were derived. Good agreement was generally found and only small adjustments had to be applied from case to case.

The experimental procedure was different from phase 1 to phase 2 as the different setup forced a change in the order of actions to prevent any interference with the measurement systems. For the phase 1 experiments (PTV), the task pipeline was:

1. datum definition: using the point gauge, the datum was defined on the top of the sphere along the centreline and at the centre of the region of interest.
2. verification of the uniform flow conditions: water surface elevation was measured between sections 7.23 m and 11.43 m every 0.30 m with the point gauge.
3. PTV cameras alignment with the free surface: as the near-surface region was considered of great importance, aligning the cameras to the free surface level allowed the characterisation of this region. If this had not been done and instead the cameras had been placed at half of the depth, the interface would have been observed from below and through it, possibly biasing the results of the near-surface hydrodynamics. Once completed this operation, flow was stopped to carry out all the preliminary procedures.
4. calibration plate alignment: the calibration plate was mounted on the traverse line, inserted in the flume and aligned along the centreline using the lasers.
5. PTV plate referencing: the height of the origin of the calibration plate was measured to determine the vertical shift that was needed to be applied to the PTV calibration to have the origin of its reference system coinciding with the top of the sphere located at the centre of the region of interest.
6. pre-calibration tasks: the flume was filled to submerge the calibration plate; cameras were also centred at the origin of the plate.

7. PTV calibration: the centreline was identified as datum along the spanwise direction; the calibration plate was imaged at 13 different positions between -120 and +120 mm with a spacing of 20 mm; this allowed to obtain a high level of accuracy for the PTV calibration along the transverse direction; from this moment great attention was paid to not touch the cameras' frame.
8. post-calibration task: the calibration plate was removed and the flume was gradually drained.
9. setting the condition: discharge and tail gate position identified at step 1 were set once again and the flume was left running for 60 minutes; following preliminary tests this time was observed to be long enough to allow the establishment of uniform flow conditions.
10. wave probes calibration: the wave probe array was inserted into the flume and probes were partially immersed; 5 minutes long acquisitions were taken at three different vertical positions; water temperature was also taken.
11. data acquisition: using a sampling rate of 100 Hz, 3000 images were first collected for performing the self-calibration procedure and later two 5 minutes long (30000 images) acquisitions were taken; simultaneous wave probes data was collected with a sampling frequency of 500 Hz; water temperature measurements were taken again.
12. final verification of the uniform flow conditions: the height of the free-surface profile was one last time taken between sections 7.23 m and 11.43 m every 0.30 m with the point gauge to determine the water depth and derive the slope of the water surface profile.
13. free-surface velocity measurement: free-surface velocity was measured 20 times using the same method presented in Subsection 3.4.3; the floater was placed at different spanwise locations to permit the measurement of the 2D spatially-averaged surface velocity.

For the phase 2 experiments (DIC), the procedure was:

1. datum definition: using the point gauge, the datum was defined on the top of the sphere along the centreline and at the centre of the region of interest.
2. verification of the uniform flow conditions: the water surface elevation was measured between sections 7.23 m and 11.43 m every 0.30 m with the point gauge. Once uniform conditions for the combination of flow rate and tail gate position were verified, the flow was stopped to carry out all the preliminary procedures.
3. preliminary tasks: installation of wave probe frame, lasers for the DIC plate alignment and traverse line with the laser used for matching the origins of the reference systems.
4. pre-calibration tasks: plate was placed inside the flume; as the reconstruction quality depended on the proximity of the plate to the free surface, shims were used to rise the plate as close to the expected free-surface position as possible; the height of the calibration plate was measured to determine the distance between this plane and the free surface.
5. calibration plate alignment: the plate was aligned using the three positioning lasers; once

completed, lasers and traverse line were removed.

6. DIC cameras alignment: cameras were aimed at the origin of the plate to maximise the field of view; LEDs were also placed above the region of interest.
7. DIC calibration: between 40 and 50 images were collected with different plate positioning and tilting; different positions allowed to fully calibrate the FOV, while various plate tilting permitted a better reconstruction of the free-surface features; from this moment great attention was paid to not touch the DIC cameras.
8. post-calibration task: removal of the calibration plate.
9. setting the flow condition: discharge and gate position identified at step 1 were set again and the flume was left running for 60 minutes; following preliminary tests this time was seen to be long enough to allow the establishment of uniform flow conditions.
10. pre-acquisition tasks: skimmers positioned in the large downstream tank were used to recirculate the buoyant particles; the nozzles injecting the water-tracers mixture via peristaltic pumps were positioned at the flume inlet and aligned with the water surface.
11. data acquisition: while sprinkling the buoyant tracers in correspondence of section 4.8 m, two 5 minutes long 100 Hz acquisitions (30000 images) were taken; simultaneous wave probes data was collected with a sampling frequency of 500 Hz; a final set of wave probes data was later taken to verify the free-surface statistics in absence of buoyant tracers; water temperature was also measured.
12. wave probes calibration: probes were partially immersed and 5 minutes long acquisitions were taken at three different vertical positions; water temperature was taken again.
13. final verification of the uniform flow conditions: the height of the free-surface profile was one last time taken between sections 7.23 m and 11.43 m every 0.30 m with the point gauge to determine the water depth and derive the slope of the water surface profile.
14. free-surface velocity measurement: the free-surface velocity was measured 20 times using the same method presented in Subsection 3.4.3; the floater was placed at different spanwise locations to permit the measurement of the 2D spatially-averaged surface velocity.

3.5.3 Measured Test Conditions

Table 3.3 reports the details of the experiments over the quincunx arrangement of spheres for slope 1/500. Each experiment is named using a specific scheme of three alphanumeric symbols. The first character for this set of tests is "Q" as the experiments belong to the "Quincunx" series. The second character is a number that indicates which of the flow conditions presented in Table 3.1 the test resembles to. The third and last character is either "H" or "S". The "H" series (after "Hydrodynamics") refers to the phase 1 group of tests when the PTV only was used. The "S" series (after "Surface") indicates the phase 2 experiments with the DIC.

Test	Q (l/s)	D (mm)	$\bar{U}_B$ (m/s)	$\bar{U}_S$ (m/s)	U_{rat}	Re	Fr	D/ϕ	AR	i_{diff} (10^{-5})
Q1_H	2.05	21.6	0.19	0.23	0.80	4200	0.41	0.87	23.3	0.8
Q1_S	1.93	20.6	0.19	0.23	0.80	4000	0.41	0.83	24.4	0.1
Q2_H	3.63	31.0	0.23	0.31	0.76	7900	0.42	1.25	16.2	0.4
Q2_S	3.53	30.6	0.23	0.31	0.74	7700	0.42	1.24	16.4	-0.9
Q3_H	6.99	46.5	0.30	0.38	0.78	15300	0.44	1.88	10.8	6.2
Q3_S	7.12	46.8	0.30	0.39	0.78	15700	0.45	1.89	10.7	7.5
Q4_H	10.80	61.5	0.35	0.44	0.80	23800	0.45	2.49	8.2	4.5
Q4_S	10.84	61.4	0.35	0.44	0.80	24200	0.45	2.48	8.2	-4.5
Q5_H	15.82	76.4	0.41	0.51	0.82	35200	0.48	3.09	6.6	-3.5
Q5_S	15.85	76.5	0.41	0.51	0.81	34700	0.48	3.09	6.6	3.0
Q6_H	21.33	91.0	0.47	0.56	0.83	47500	0.49	3.68	5.5	-7.2
Q6_S	21.56	91.9	0.47	0.58	0.81	47400	0.49	3.72	5.5	-8.6

Table 3.3: Tests belonging to the "Q" series (Quincunx, 1/500). Q is discharge; D is uniform water depth; $\bar{U}_B$ is depth-averaged velocity; $\bar{U}_S$ is surface velocity; U_{rat} is the depth-averaged and surface velocities ratio; Re is Reynolds Number; Fr is Froude Number; D/ϕ is relative submergence; AR is aspect ratio; i_{diff} is the difference between the surface profile slope and the bed slope.

Table 3.4 reports the characteristics of the flow conditions tested once again over the quincunx spheres texture but over the 1/1000 slope. Similarly to the name convention used for the other set of conditions, the experiments over this slope have a "M" as the first of the identifying characters as the 1/1000 slope was "Mild" compared to the 1/500 one tested before.

Test	Q (l/s)	D (mm)	$\bar{U}_B$ (m/s)	$\bar{U}_S$ (m/s)	U_{rat}	Re	Fr	D/ϕ	AR	i_{diff} (10^{-5})
M1_H	1.99	26.5	0.15	0.20	0.76	4200	0.29	1.07	19.0	-2.4
M1_S	2.03	26.0	0.15	0.20	0.78	4500	0.31	1.05	19.3	-4.1
M2_H	4.27	41.5	0.20	0.26	0.78	9300	0.32	1.68	12.1	-7.8
M2_S	4.56	42.7	0.21	0.28	0.77	10100	0.33	1.73	11.8	-5.5
M3_H	7.62	58.9	0.26	0.33	0.79	16600	0.34	2.38	8.5	-3.3
M3_S	4.92	48.0	0.20	0.25	0.81	10700	0.30	1.94	10.5	23.7
M4_H	17.35	100.4	0.34	0.43	0.80	37400	0.35	4.06	5.0	-4.2
M4_S	16.17	97.4	0.33	0.41	0.80	35800	0.34	3.94	5.2	1.4
M5_H	21.37	114.1	0.37	0.43	0.87	46200	0.35	4.62	4.4	-1.7
M5_S	20.23	112.2	0.36	0.44	0.81	43600	0.34	4.54	4.5	8.3
M6_H	24.15	125.7	0.38	0.43	0.88	51600	0.34	5.09	4.0	5.3
M6_S	23.56	125.3	0.37	0.46	0.82	51400	0.34	5.07	4.0	3.7

Table 3.4: Tests belonging to the "M" series (Quincunx, 1/1000). Q is discharge; D is uniform water depth; $\bar{U}_B$ is depth-averaged velocity; $\bar{U}_S$ is surface velocity; U_{rat} is the depth-averaged and surface velocities ratio; Re is Reynolds Number; Fr is Froude Number; D/ϕ is relative submergence; AR is aspect ratio; i_{diff} is the difference between surface profile and bed slopes. M3_S (displayed in red) was discarded as it did not satisfy uniformity conditions.

A failure of the valve that regulates the flow rate occurred while measuring flow condition M3_S, causing the discharge to be lower than the target value. As a consequence, the DIC measurements were performed over a progressively decelerated flow field. As uniform flow conditions were not satisfied, M3_S was discarded and will not be presented in the rest of the thesis.

Table 3.5 reports the characteristics of the flow conditions tested over the alternate spheres texture for a slope of 1/500. Using the standard name convention, the experiments over this type of bed have a "A" as the first of the identifying characters as the spheres arrangement was "Alternate".

Test	Q (l/s)	D (mm)	$\bar{U}_B$ (m/s)	$\bar{U}_S$ (m/s)	U_{rat}	Re	Fr	D/ϕ	AR	i_{diff} (10^{-5})
A1_H	1.78	21.9	0.16	0.20	0.80	3600	0.35	0.89	23.0	2.6
A1_S	1.79	22.0	0.16	0.20	0.81	3600	0.35	0.89	22.9	-
A2_H	3.44	33.5	0.20	0.26	0.77	6900	0.36	1.36	15.0	3.2
A2_S	3.46	33.8	0.20	0.26	0.78	7000	0.35	1.37	14.9	-
A3_H	6.94	49.7	0.28	0.35	0.80	14600	0.40	2.01	10.1	-0.6
A3_S	6.77	50.0	0.27	0.34	0.79	13800	0.38	2.02	10.1	-
A4_H	10.65	64.0	0.33	0.41	0.80	22300	0.42	2.59	7.9	-1.4
A4_S	10.53	64.8	0.32	0.41	0.79	21600	0.41	2.62	7.8	-
A5_H	15.58	81.1	0.38	0.47	0.81	32200	0.43	3.28	6.2	0.6
A5_S	15.51	81.6	0.38	0.48	0.79	31600	0.42	3.30	6.2	-
A6_H	21.08	95.3	0.44	0.55	0.81	42500	0.45	3.86	5.3	2.0
A6_S	21.14	97.0	0.43	0.55	0.79	43100	0.44	3.92	5.2	-

Table 3.5: Tests belonging to the "A" series (Alternate, 1/500). Q is discharge; D is uniform water depth; $\bar{U}_B$ is depth-averaged velocity; $\bar{U}_S$ is surface velocity; U_{rat} is the depth-averaged and surface velocities ratio; Re is Reynolds Number; Fr is Froude Number; D/ϕ is relative submergence; AR is aspect ratio; i_{diff} is the difference between the surface profile slope and the bed slope.

No measurements of the surface profile slope are available for DIC tests belonging to the "A" series as data was lost. However, the similarity in flow rates and depths between PTV and DIC tests for corresponding flow conditions suggests that the DIC tests were highly likely to have surface profiles parallel to the bed.

3.6 Data Processing

Due to the different nature and sources of the various data sets (images for PTV and DIC, and text files for wave probes and discharge), raw data had to undergo distinct forms and steps of processing. All the processing can be framed into two different types:

- internal processing: this step, exclusive to PTV and DIC images, was performed in LaVision's DaVis environment; it includes all the sequence of operations required to convert raw images to either a vector flow field or to a scalar surface height field onto a regular orthogonal grid having the same reference system and datum (i.e. the top of the sphere along the centreline in the middle of the FOV).

- external processing: all the data sets needed to be processed via MATLAB; this procedure allowed to manipulate and elaborate the raw or pre-processed data, and to derive the final results presented in Chapter 4.

3.6.1 Internal Processing

The first step for both the PTV and DIC analyses consisted in the system calibration. The images of the calibration plate collected before the tests were aggregated in a single data set and used to derive the cameras' intrinsic and extrinsic parameters, allowing to link the pixel coordinates to a specific position in the real world. Several media were encountered between the cameras composing the PTV system and the flow field (air, glass and water). Furthermore, local micro variations might have been present in these media (especially in the glass composing the flume). As all these variations could have had an impact on the quality of the calibration, a polynomial fit was used to derive the calibration of PTV system. On contrary, as there was only air between the cameras of the DIC system and the free surface, a single pinhole model could be used. Figure 3.26a presents the PTV calibration, while figure 3.26b shows the DIC calibration.

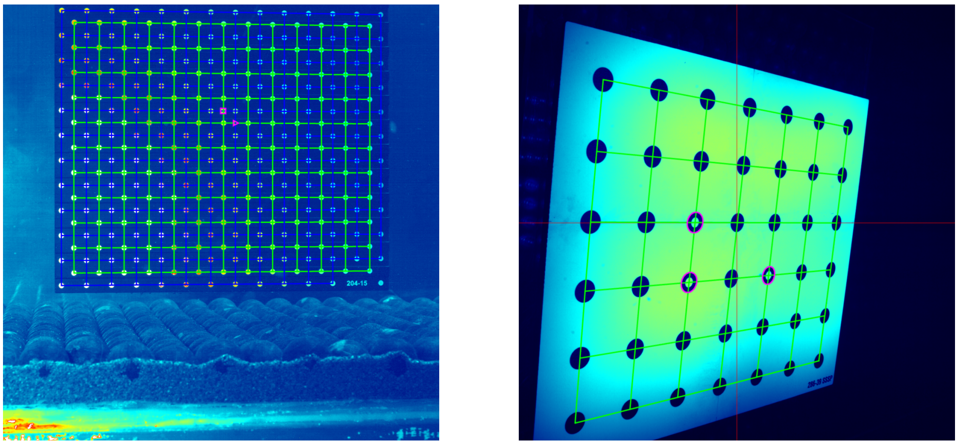
(a) (b)

Figure 3.26: a) Camera view of the PTV calibration plate. b) Camera view of the DIC calibration plate.

Due to the large number of images collected for this procedure (13 for the PTV and 40-50 for the DIC), low fit errors were produced. In fact, the system returned fit errors ranging between 0.1697 and 0.1840 pixels for the PTV data sets, whilst fit errors between 0.040 and 0.065 pixels were reported for the DIC measurements.

Once the PTV and DIC calibration procedure was completed the PTV and DIC data set were processed differently.

Particle Tracking Velocimetry

The processing of the PTV images was the most complex due to the number of cameras (the system could not run on a single computer) and the sequence of steps required to obtain the flow field.

The first step was to merge the two groups of raw images from the two computers into a single data set. Even at this stage tracers could be recognised (Fig. 3.27), though they were barely distinguishable. For this reason the images had to be pre-processed to improve the visibility of the particles before the evaluation with the tracking algorithm.

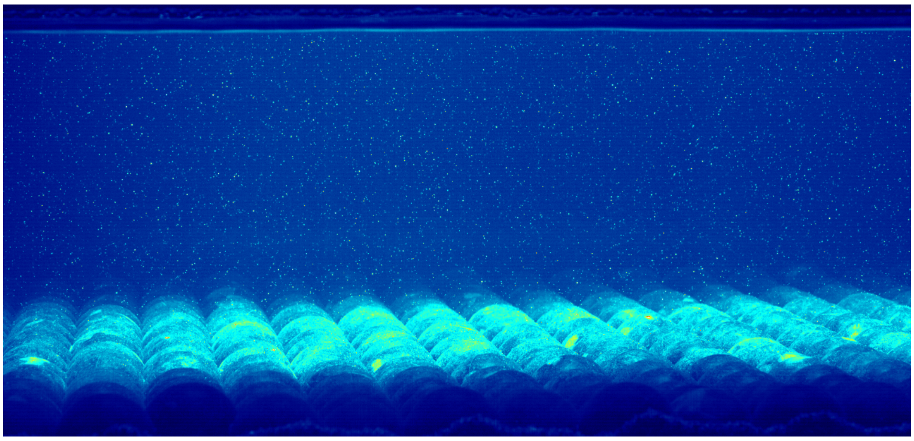

Figure 3.27: Raw PTV image in false colours from camera 2 for flow condition Q6_H.

The pre-processing firstly consisted in calculating the time-average intensity values for each pixel and later subtracting this component from every photo to obtain images with fluctuating light intensity values (Fig. 3.28). The procedure is similar to the Reynolds decomposition in time-averaged and turbulent components. Subtracting the time-averaged values was preferred than subtracting the minimum observed values at each pixel to limit background noise.

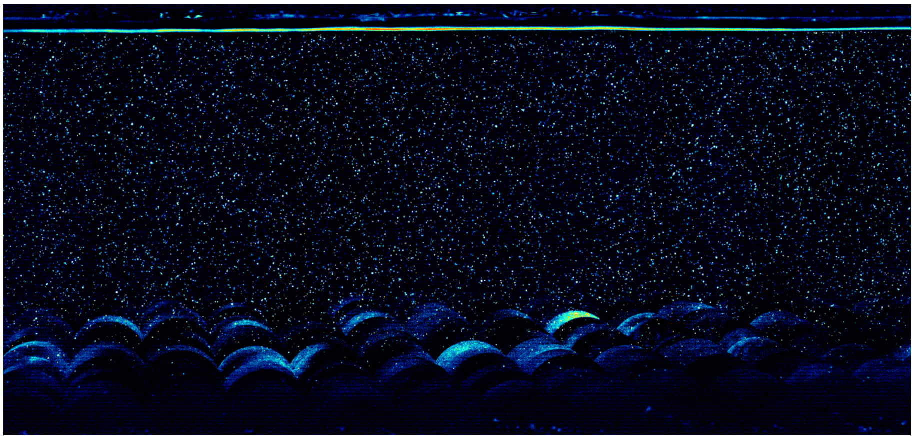

Figure 3.28: Fluctuating light intensity component for camera 2 for flow condition Q6_H. The image refers to the same frame plotted in Figure 3.27.

Particles were still difficult to identify. The images were adjusted to suppress background noise, normalise variable light intensity due to the oscillating free surface, smooth particles form, sharpen the contrast and enhance particle intensities. An example of the output of such a procedure is shown in Figure 3.29.

After this series of pre-processing operations, tracers could be easily identified and distinguished. The images were reckoned ready to be used in the self-calibration procedure (Wieneke, 2008; Schanz et al., 2016). Self-calibration is a procedure that makes use of the dispersed particles in the fluid to iteratively refine their position and derive adjustment coefficients for the PTV calibration to increase the overall accuracy. To further enhance the correction, the total volume can be divided in sub-volumes and obtain specific corrective coefficients for each sub-volume. For the present investigation, an independent 3000 frame long image data set was acquired for this purpose. It was chosen to subdivide the volume in 25 parts (5x1x5, along the streamwise,

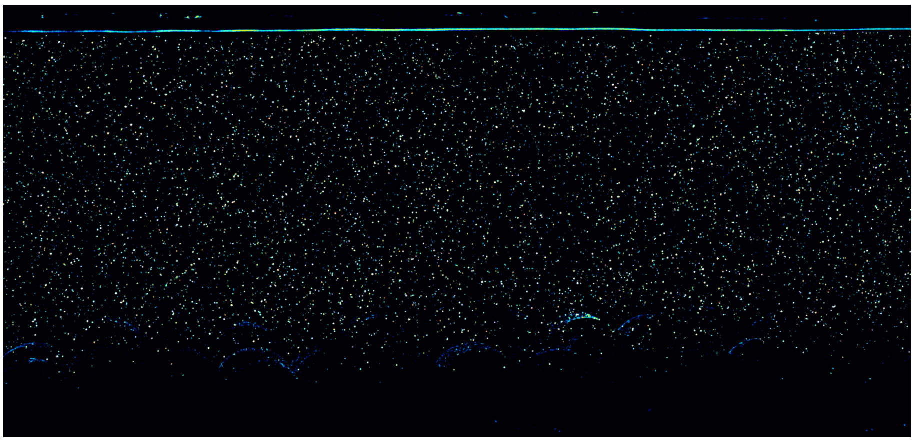

Figure 3.29: Enhanced light intensities for camera 2 for flow condition Q6_H. The image refers to the same frame plotted in Figure 3.27.

the vertical and the spanwise directions, respectively). This permitted to greatly improve the calibration, reducing the fit error estimated by the system to 0.0033-0.0085 pixels. The experimental error of the velocity measurements is a combination between the spatial error arising from the uncertainties related to the positioning of the tracers and the temporal error in the sampling. The PTV system returned a precision in time equal to 10^{-5} s, suggesting that the temporal error could be considered negligible. The spatial-related error was evaluated from the fit error and acquisition frequency (Raffel et al., 2018). Considering the GSD of the PTV system and the frame rate of 100 Hz, the error in the velocity measurements was estimated between 0.00005 and 0.00013 m/s.

Pre-processed images were evaluated by the STB tracking algorithm following the procedure described in Schanz et al. (2016). The output of this procedure can be seen in Figure 3.30.

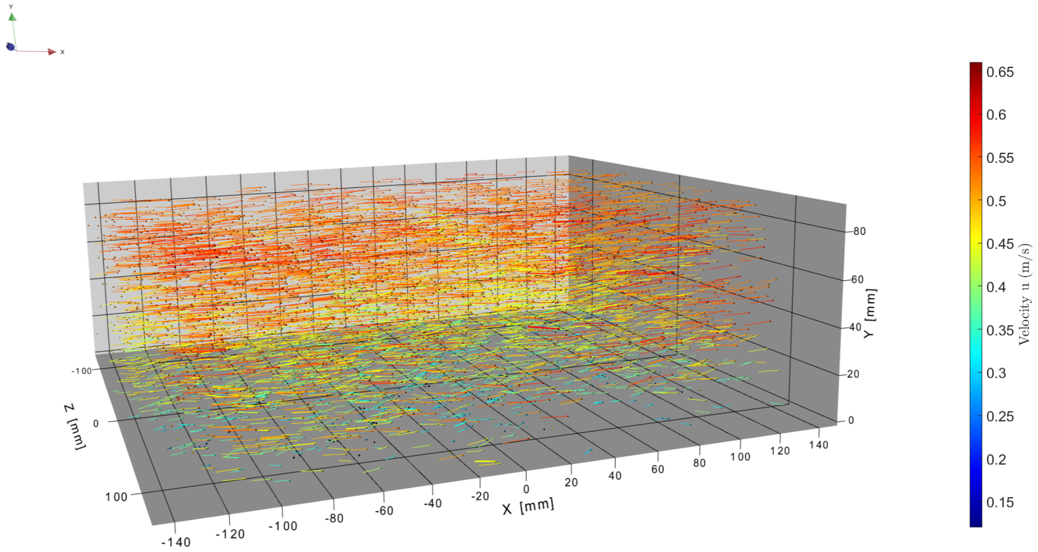

Figure 3.30: Tracks for flow condition Q6_H. Colourbar on the right side indicates instantaneous streamwise velocity.

As a last step, a binning procedure was applied to the tracks file to aggregate the trajectories. An interrogation window of 80 pixel with an overlap of 75% allowed a PTV spatial measurement resolution of 20 pixel, corresponding to 3.02 mm (Fig. 3.31).

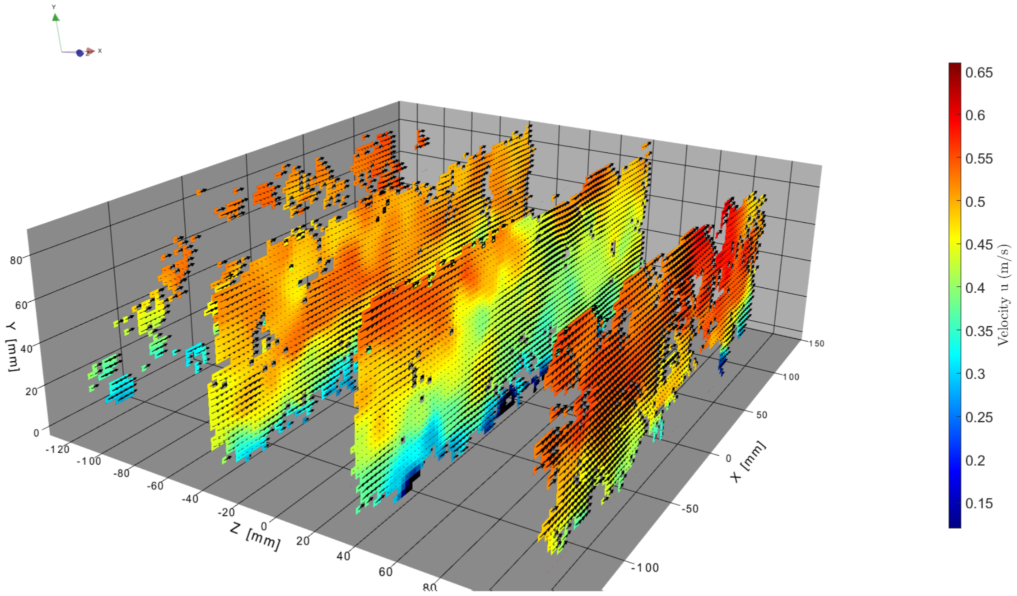

Figure 3.31: Binning output for flow condition Q6_H. To facilitate visualisation only 1 slice every 25 mm is presented in this image. Colourbar on the right side indicates instantaneous streamwise velocity.

These binning outputs could then be processed in MATLAB.

Digital Image Correlation

Due to the inconstancy of methods used to introduce the buoyant tracers and the turbulent behaviour of the flow (in particular upwellings and secondary currents), a uniform coating of the free surface could not be attained for the higher flow rate experiments. Figure 3.32 presents a raw image from the test Q6_S, patches can be observed where tracers were not present.

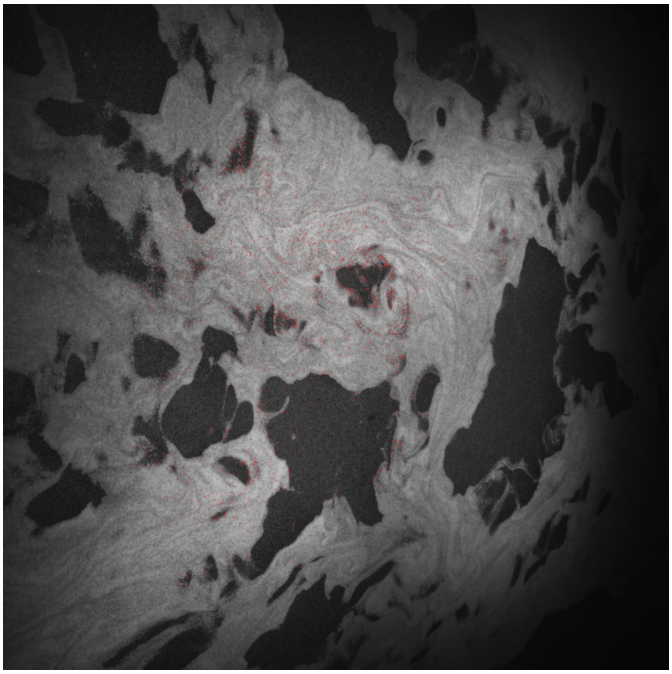

Figure 3.32: Raw DIC image from flow condition Q6_S.

Nonetheless, sufficiently large portions of the interface were always coated by tracers. Also, recognisable unique patterns could be seen on the coated part of the surface. These qualitative considerations suggested it was suitable to directly proceed with the surface 3D reconstruction without pre-processing. The assumption was later tested in the analysis of DIC data.

Differential DIC correlation analysis was performed imposing a facet size of 21 pixels and a step size (i.e. displacement of the interrogation window) of 13 pixels. Facet and step sizes were chosen as optimal compromise between spatial accuracy and uniqueness of the speckle pattern. As the surface-cameras distance changed from test to test, the spatial resolution of the measurements varied between 1.50 mm and 2.21 mm in both streamwise and lateral directions. Figure 3.33 shows the reconstructed area for Figure 3.32, while Figure 3.34 displays the free-surface height field for the same Figure. Obviously, reconstruction was limited only to regions coated with tracers. Therefore, it was assumed no corruption of the free-surface height data occurred because of the missing coating.

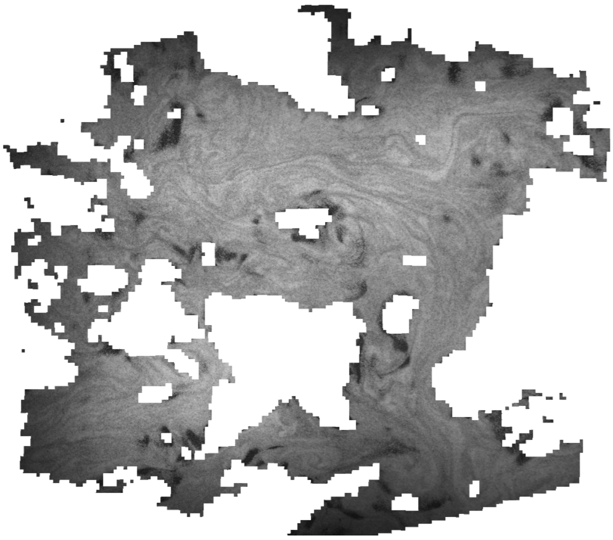

Figure 3.33: Reconstructed surface for Figure 3.32 for flow condition Q6_S.

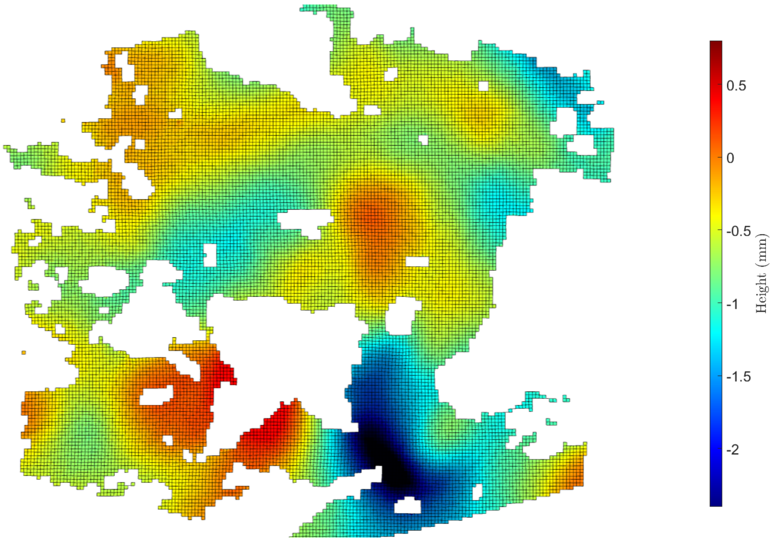

Figure 3.34: Free-surface height field for Figure 3.32 for flow condition Q6_S. Colourbar on the right side indicates surface height (mm).

3.6.2 External Processing

Particle Tracking Velocimetry

PTV measurements could have been affected by a slight misalignment of the calibration plate, resulting in a violation of the continuity equation. The angular corrections needed to be applied at the reference system were determined from a symmetrical portion of the flow field through a minimisation procedure with the following iterative scheme:

1. calculate the time-average velocities at each measurement location for the flow field.
2. apply a rotation to the original flow field, F_{init}, to derive the rotated flow field, F_{rot}, according to:

   $$F_{rot}(x, y, z, t) = R_{3D}(\alpha, \beta, \gamma) F_{init}(x, y, z, t) \tag{3.2}$$

   where R_{3D} is the rotation matrix, (α, β, γ) are the rotations around the vertical (yaw), transverse (pitch) and longitudinal (roll) axes, respectively, for the PTV. The 3D rotational matrix is defined as:

   $$R_{3D}(\alpha, \beta, \gamma) = \begin{bmatrix} \cos\alpha\cos\beta & \cos\alpha\sin\beta\sin\gamma - \sin\alpha\cos\gamma & \cos\alpha\sin\beta\cos\gamma + \sin\alpha\sin\gamma \\ \sin\alpha\cos\beta & \sin\alpha\sin\beta\sin\gamma + \cos\alpha\cos\gamma & \sin\alpha\sin\beta\cos\gamma - \cos\alpha\sin\gamma \\ -\sin\beta & \cos\beta\sin\gamma & \cos\beta\cos\gamma \end{bmatrix}$$

   For the first iteration $(\alpha, \beta, \gamma) = (0°,\ 0°,\ 0°)$. Angles were allowed to space between ±5° with a step of 0.1°.
3. trim the sides of the volume to get rid of edge effects (e.g weak illumination).
4. spatially average (along the streamwise and vertical directions) the lateral velocity at different spanwise locations and spatially average (along the streamwise and spanwise directions) the vertical velocity at different vertical locations.
5. calculate the lateral and vertical volumetric fluxes for each spanwise and vertical location.
6. sum the singular fluxes to determine the net lateral volumetric flux and the net vertical volumetric flux over the entire considered volume.
7. if the net lateral flux, the net vertical flux and their sum were below the tolerance value, save the triplet of angles that produced such a result, otherwise return to step 2 with a new triplet of angles.

The triplet of angles that verified the vertical and lateral continuity was valid only in first approximation and it was used to impose a rotation on the PTV tracks file. A new binning procedure was then performed, which allowed to correctly bin the trajectories on the correct interrogation volume. The minimisation procedure was repeated again to obtain a triplet of angles of second attempt. The entire procedure was repeated until the correction angles were smaller than 0.01°.

The flow field data was finally considered correct and ready for analysis.

Digital Image Correlation

Errors committed during the calibration (e.g misalignment of the plate, non-uniformities in the plate support) could have affected the quality of the reconstruction. In fact, the reconstructed instantaneous surface height field presented deviations from the expected water level.
To compensate this anomaly, the reconstructed area was time-averaged to determine the time-averaged surface height of each pixel. This field represented the spatial trend inherited from the plate misalignment during the calibration procedure. A linear 3D regression was then performed on the time-averaged field to determine the best fitting plane. The intercept of this plane, being the vertical shift of the instantaneous surface height field from the mean water level, was subtracted from the instantaneous surface height field data. Angular misalignments were corrected by first determining the tilting angles of the best fitting plane and later imposing a rigid 3D rotation with these angles to the shifted instantaneous height field:

$$S_{el,corr}(x,z,t) = R_{3D}(\aleph,\beth,\daleth)S_{el}(x,z,t) \tag{3.3}$$

where $S_{el,corr}$ is the correct surface elevation field, $(\aleph,\beth,\daleth)$ are the rotations around the vertical, transverse and longitudinal axes for DIC, respectively, and S_{el} is the surface elevation field after the subtraction of the vertical shift component from the surface height field.

This procedure allowed to obtain a correct instantaneous surface fluctuation field around a mean water level set to a value of 0 mm.

Wave Probes

Wave probes data were immediately processable in MATLAB after their acquisition.
The first step consisted in determining the converting voltage-elevation factors. For this purpose, the voltage time series collected for different vertical positioning of the wave probe array were averaged over time. As the wires had been compensated earlier for the lead and linearity between the time-averaged voltage values and array vertical positioning could be invoked, the converting coefficients were derived for each wave probe using a linear regression.
The converting coefficients were so applied to the voltage time series, obtaining the instantaneous surface elevation in millimetres. The converted series were later downsampled to 100 Hz (frequency decimating factor of 5) and then filtered using a second order band-pass Butterworth filter with cutoff frequencies of 0.1 Hz and 50 Hz. The ceiling frequency of 50 Hz was chosen to remove electrical noise that might have affected the measurements.

Chapter 4

Results and Discussion

4.1 Introduction

Analysis and discussion of the experiments reported in Subsection 3.5.3 are here presented. As stated in Section 3.1, three different classes of hydraulic conditions can be identified:

- Class I: flow regimes with $\bar{U}_B < 0.23$ m/s and $U_S < 0.23$ m/s
- Class II: conditions with $\bar{U}_B < 0.23$ m/s and $U_S > 0.23$ m/s
- Class III: flow conditions with $\bar{U}_B > 0.23$ m/s and $U_S > 0.23$ m/s

Categorisation with this framework of the flow conditions reported Subsection 3.5.3 is proposed in Table 4.1:

Classification of the Flow Conditions			
Class	Series		
	Q	M	A
1	Q1_H, Q1_S	M1_H, M1_S	A1_H, A1_S
2	Q2_H, Q2_S	M2_H, M2_S	A2_H, A2_S
3	Q3_H, Q3_S, Q4_H, Q4_S, Q5_H, Q5_S, Q6_H, Q6_S	M3_H, M3_S, M4_H, M4_S, M5_H, M5_S, M6_H, M6_S	A3_H, A3_S, A4_H, A4_S, A5_H, A5_S, A6_H, A6_S

Table 4.1: Class categorisation of the measured flow conditions according to the scheme based on depth-averaged and free-surface velocities.

Due to the large number of data sets, the results of just one flow condition per Class for each series are here fully reported. On this purpose, it was chosen to use the flow condition ”1” as representative of Class I, flow condition ”2” to describe Class II and flow condition ”4” to represent Class III. The characteristics of the other conditions are presented in aggregated plots to better evaluate how the flow dynamics evolves for progressively higher flow rates. The entirety of the results can be found in the Appendix.

Results presented in this Chapter are also discussed with reference to previous studies. As the scope of this study is to verify whether a linkage between the free surface and the underlying hydrodynamics exists or not, particular emphasis is dedicated to this matter. Consequently, deeper forms of analysis are explored aimed at presenting a clearer evidence of this relationship.

First, Section 4.2 focuses on the validation of the velocity and surface elevation data sets. Section 4.3 shows the results obtained from the analysis of the PTV data. Section 4.4 presents the findings about the free-surface behaviour. Finally, Section 4.5 compares the free-surface and bulk flow dynamics to determine the origin of the surface wave patterns.

4.2 Data Validation

This Section focuses on the validation of the collected data set. An experimental validation is first needed to verify the uniform flow conditions and the adherence of the hydraulic conditions to the theory.

Due to the nature of the collected data sets, validation was performed in different ways according to the target of the devices used during the experimental campaign (i.e. PTV, DIC and wave probes). For this reason, this Section is split in two parts: Subsection 4.2.1 focuses on the velocity data obtained from the PTV, while Subsection 4.2.2 is about the free-surface elevation fields derived from DIC and wave probes.

4.2.1 Validation of the Velocity Field

The procedure for the validation of the velocity data was composed of two phases: the first part was aimed at verifying uniform flow conditions, while the second step focused on checking whether the experiments adhered to the theoretical behaviour (so that they could be compared to the other tests proposed in the literature) or not.

Uniform Flow Conditions

A preliminary indication whether an experiment was performed in uniform flow conditions was given by the parameter i_{diff}, difference between the measured free-surface gradient between sections 7.23 m and 11.43 m and the bed slope. As reported in Tables 3.3, 3.4 and 3.5, i_{diff} was found to be withing the range $\pm 10^{-4}$ m/m for all flow conditions except one that was discarded (i.e. M3_S). This suggested that the flow was not progressively accelerating or decelerating in the measurement area. This check, however, was not sufficient to guarantee that uniform flow conditions were indeed met. For this reason, the actual PTV measurements were used to conduct such a verification.

The criterion that defines the establishment of uniform flow conditions is that the flow field does not vary in space. Two-dimensional flows, however, are characterised by limited variability, both along space and time. This behaviour not only manifests through the randomness and intermittency of turbulence, but also in the form of pulsations of the flow (low-frequency motions containing fine turbulence) unrelated to turbulence (Nezu & Nakagawa, 1993). An example of such a low-frequency phenomena is the meandering of secondary currents observed in Onitsuka and Nezu (2001), Tamburrino and Gulliver (2007) and Cameron et al. (2017).

The stationarity of the flow field was ascertained by subdividing the 300 seconds long PTV data set into 5 60-second-long periods and calculating the time averaged components for each of them. Later, the average value among the five periods was calculated. The five-period average was subtracted from each of the time-averaged periods and then the difference was divided by the five-period average to obtain the percentage variation of each period respect with the five-period average. Finally, the mean value among the periods of this percentage variation was calculated. In this sense, stationarity was assumed when the five-period average percentage variation was found below 1%. The averaged percentage variation was always below the threshold value, suggesting the stationarity of the velocity field for all the flow conditions.

Spatial uniformity along the streamwise direction was later investigated. As stationarity was already proved, the time averages of the velocity components at each location were considered. These matrices were averaged along the spanwise direction to obtain a series of velocity profiles representative of the different streamwise sections. The double-averaged (time-, streamwise- and spanwise-) velocity profile was subtracted from the laterally-averaged velocity profiles and later used to divide this difference. This represented the percentage deviation from the double-averaged value. Finally, the 2D matrices were averaged along the vertical direction to derive the average percentage variation for each streamwise-spanwise section. Again, spatial uniformity was assumed when the section percentage variation was found below 1%. The section percentage variation was always found below the threshold value, suggesting the spatially uniformity of the velocity field for all the flow conditions.

All flow conditions verified both temporal and spatial constancy, suggesting that uniform flow conditions could be invoked.

Alignment with the Theory

Validation of the velocity measurements is typically conducted by checking the global momentum balance of the flow (Pokrajac et al., 2006; Manes et al., 2009; Suga et al., 2010). Specifically, the shear velocity derived from the observed total fluid stress (i.e. sum of the turbulent and dispersive stress components), u^*_τ, is compared with the shear velocity obtained from the global momentum balance, u^*_b.

Two distinct formulations for the shear velocity from the global momentum balance are often considered:

- $u^*_{b,RH} = (gR_HS)^{1/2}$: this represents the minimum value the shear velocity can have. It assumes that the sidewalls and the bed impose the same resistance per unit of area on the flow.
- $u^*_{b,D} = (gDS)^{1/2}$: this formulation implies that the sidewalls exert a negligible resistance per unit of area on the flow. It follows that this is the maximum value that the shear velocity can assume.

Validation is typically achieved when u^*_τ has a value between $u^*_{b,RH}$ and $u^*_{b,D}$.

More troublesome is finding the correct location where to evaluate u^*_τ due to the presence

of a rough permeable bed. In fact, any locations between the spheres' top and bottom can be considered plausible.
On this matter, Pokrajac et al. (2006) examined different definitions for the shear velocity in order to identify the most suited universal scaling velocity.

- $u^*_{\tau,0}$: this shear velocity is evaluated from the total fluid shear stress at the level of the roughness crest.
- $u^*_{\tau,d}$: this definition is derived from the extrapolated total fluid shear stress in correspondence of the zero-plane displacement (i.e. the location where the time-averaged streamwise velocity is null or reaches a constant value).
- $u^*_{\tau,log}$: obtained by fitting the experimental data to the logarithmic law of the wall.
- $u^*_{\tau,bed}$: shear velocity derived from the total fluid shear stress at the level of the roughness bottom.

Pokrajac et al. (2006) suggested that $u^*_{\tau,0}$ could be the best formulation for the shear velocity as it is less prone to uncertainty.

To evaluate the goodness of $u^*_{\tau,0}$ as scaling velocity, the observed double-averaged streamwise velocity profiles were normalised using the respective $u^*_{\tau,0}$ and put in a logarithmic plot against wall units (Fig. 4.1).

This definition of shear velocity produced a poor collapse of the velocity profiles for some cases, suggesting that $u^*_{\tau,0}$ was not the appropriate choice as scaling velocity for this set of experimental data.

A new definition for the shear velocity had to be sought in $u^*_{\tau,d}$. This definition, however, requires knowing the position of the zero-plane displacement, d_0, which is unknown a priori. Koll (2006) proposes an objective graphical way to derive d_0 using the part of the streamwise velocity profile that lies in the logarithmic layer. Nikora et al. (2001) suggests that the logarithmic layer occurs in the lowest 20% of the depth part of the flow. However, plotting the double-averaged streamwise velocity profiles in linear and logarithmic scales revealed that both the roughness and logarithmic layers extended much above the theoretical boundaries given in Nikora et al. (2001). The observed part following a logarithmic behaviour was therefore used instead of the part within the boundaries suggested by the literature. The method, however, was not consisted as unreliable values for d_0 were reported in some of the tests.
Kim et al. (2020) performed tests over a bed similar to the one here examined. Reviewing other studies employing beds made of spheres, they observed that d_0 can vary between (0.1-0.15)ϕ according to the different arrangements. Using the modified Clauser chart method (Perry & Li, 1990), Kim et al. (2020) confirmed the observations about the zero-plane displacement. Furthermore, Kim et al. (2020) observed that d_0 did not changed with the Reynolds Number, supporting the idea that the zero-plane displacement is a characteristic depending on the bed topography only when the flow is in fully-rough conditions (Stull, 2003). Following the findings of Kim et al. (2020), it was chosen to use a constant d_0 for all conditions. Its value was identified from the average between the values observed by other studies (Defina, 1996; Singh et al., 2007;

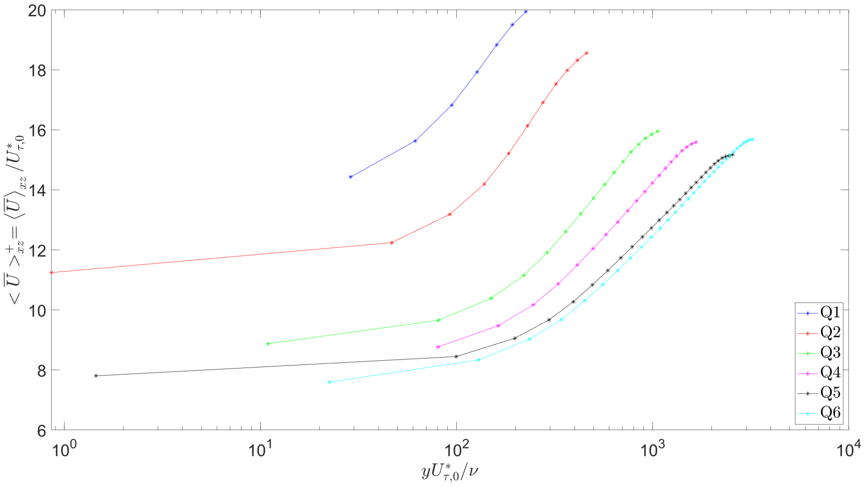

(a) "Q" series.

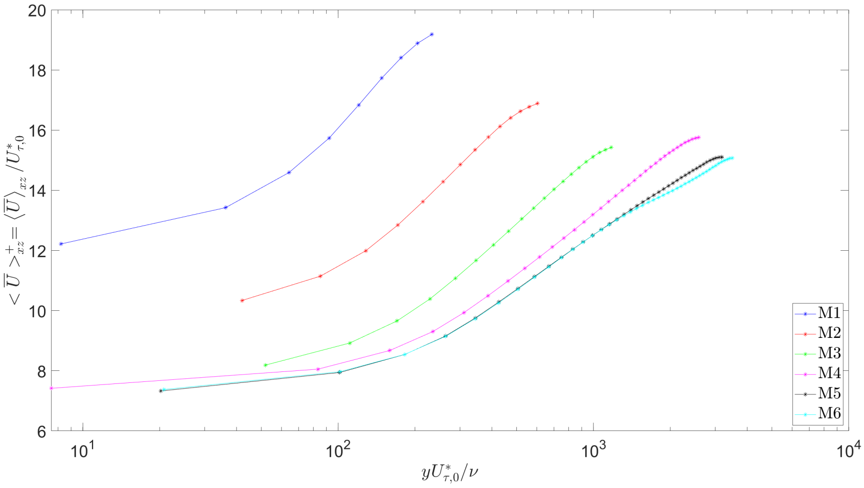

(b) "M" series.

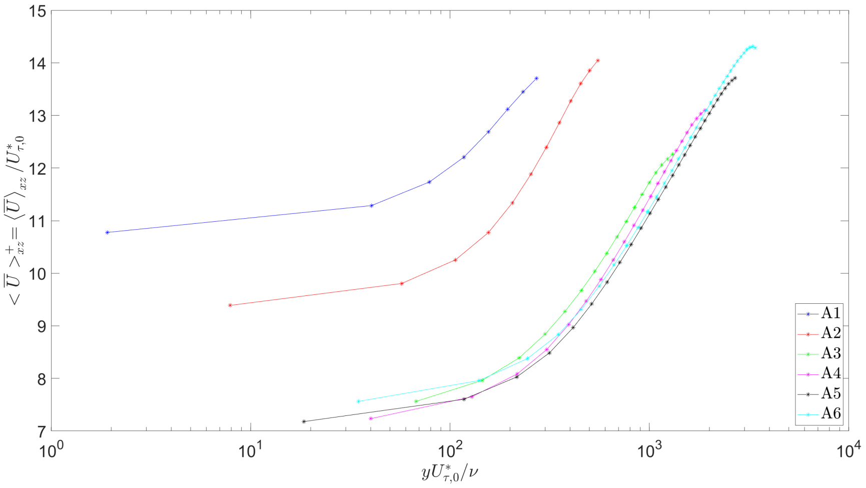

(c) "A" series.

Figure 4.1: Logarithmic law of wall plots. In this case $u^*_{\tau,0}$ was used as scaling velocity.

Kim et al., 2020) over similar bed arrangements and submergences. The zero-plane displacement was set as $d_0 = 0.11\phi = 2.72$ mm below the top of the roughness.

The double-averaged streamwise velocity profiles normalised by $u^*_{\tau,d}$ in a logarithmic plot against wall units are proposed in Figure 4.2.

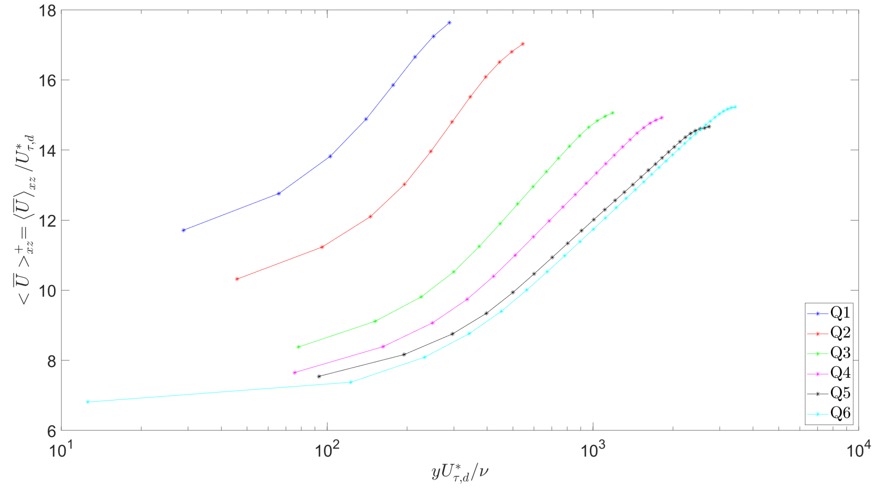

(a) "Q" series.

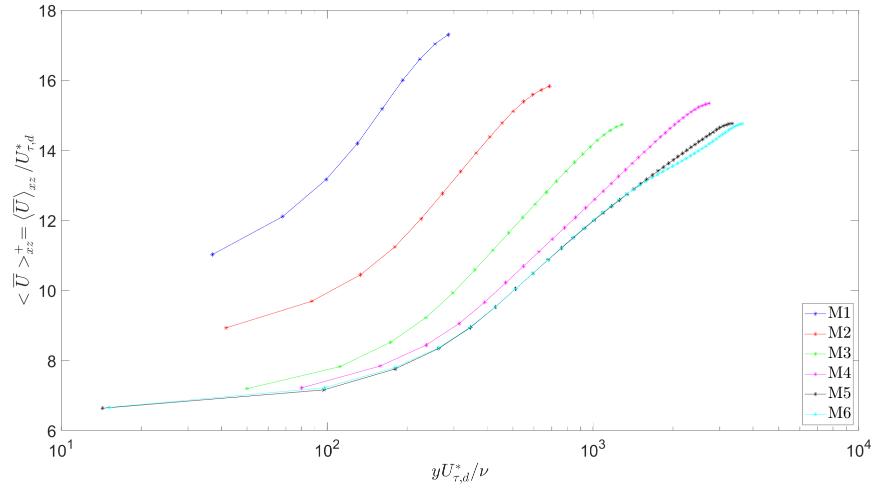

(b) "M" series.

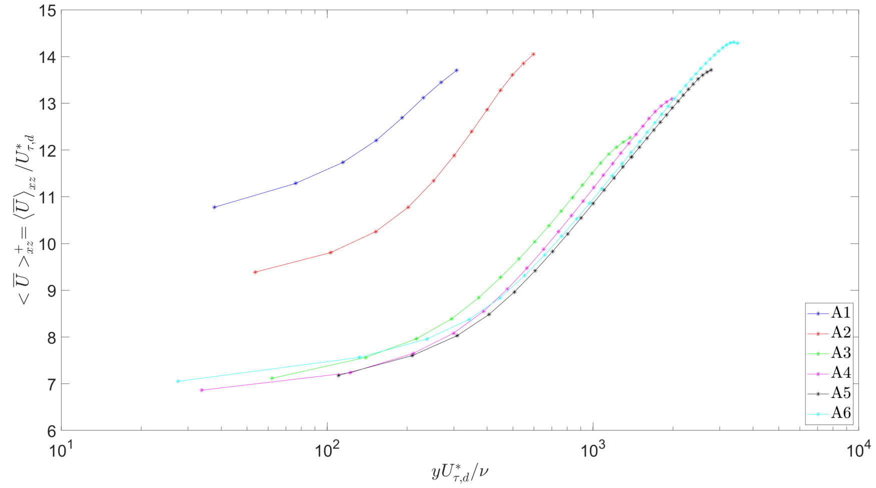

(c) "A" series.

Figure 4.2: Logarithmic law of wall plots. In this case $u^*_{\tau,d}$ was used as scaling velocity.

This scaling velocity provided a better collapse of the velocity profiles than $u^*_{\tau,0}$. The normalised profiles of the shallowest conditions, however, were seen once again not to collapse with the other normalised profiles. The shear velocity $u^*_{\tau,d}$ was therefore compared against $u^*_{b,RH}$ and $u^*_{b,D}$ to validate the goodness of the experiments. As while defining $u^*_{\tau,d}$ the vertical location of the zero-plane displacement was considered, $u^*_{b,RH}$ and $u^*_{b,D}$ were adjusted to take d_0 into account in their calculation. Table 4.2 reports the values of $u^*_{\tau,d}$, $u^*_{b,RH}$ and $u^*_{b,D}$ for the tested flow conditions.

Shear Velocities (m/s)							
Series	Shear Velocity	Tests					
		1_H	2_H	3_H	4_H	5_H	6_H
Q	$u^*_{\tau,d}$	0.012	0.019	0.025	0.029	0.034	0.037
	$u^*_{b,RH}$	0.021	0.024	0.028	0.032	0.034	0.037
	$u^*_{b,D}$	0.022	0.026	0.031	0.035	0.039	0.043
M	$u^*_{\tau,d}$	0.010	0.016	0.021	0.027	0.029	0.029
	$u^*_{b,RH}$	0.016	0.019	0.022	0.027	0.028	0.029
	$u^*_{b,D}$	0.017	0.021	0.025	0.031	0.034	0.035
A	$u^*_{\tau,d}$	0.013	0.017	0.027	0.031	0.034	0.037
	$u^*_{b,RH}$	0.021	0.025	0.029	0.032	0.035	0.037
	$u^*_{b,D}$	0.022	0.027	0.032	0.036	0.041	0.044

Table 4.2: Shear velocities $u^*_{\tau,d}$, $u^*_{b,RH}$ and $u^*_{b,D}$ for different flow conditions.

$u^*_{\tau,d}$ results smaller than the theoretical minimum value $u^*_{b,RH}$ for the shallowest flow conditions. The cause of this deviation from the theoretical thresholds is speculated to be due to the limited submergences of the shallowest tests.

Considering that $u^*_{\tau,d}$ was in line with $u^*_{b,RH}$ for the higher flow regimes, it was chosen to replace $u^*_{\tau,d}$ with the latter definition of shear velocity. This change did not affect the higher flow rates but only the lower ones. Figure 4.3 reports the double-averaged streamwise velocity profiles normalised by $u^*_{b,RH}$ in a logarithmic plot against wall units.

A good collapse was observed for all the conditions, although the ”A” series tests provided a better fit that the tests over the ”Q” and ”M” series. This suggested the goodness of $u^*_{b,RH}$ as a scaling factor for velocity.

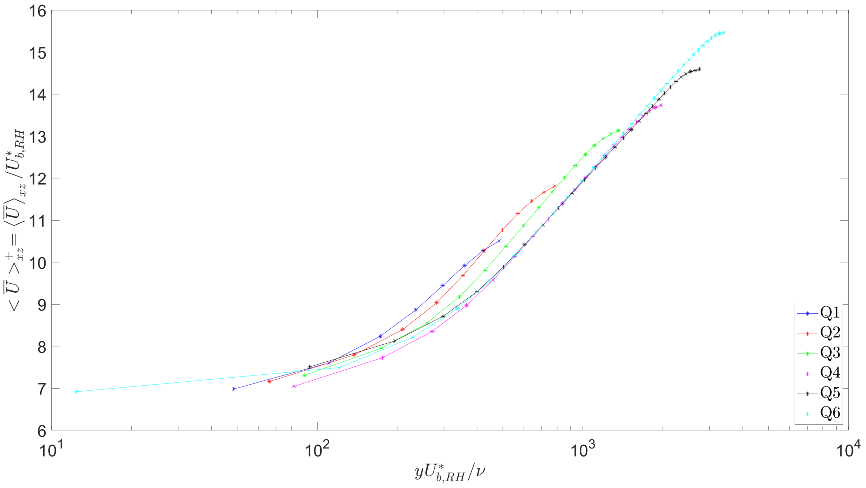

(a) "Q" series.

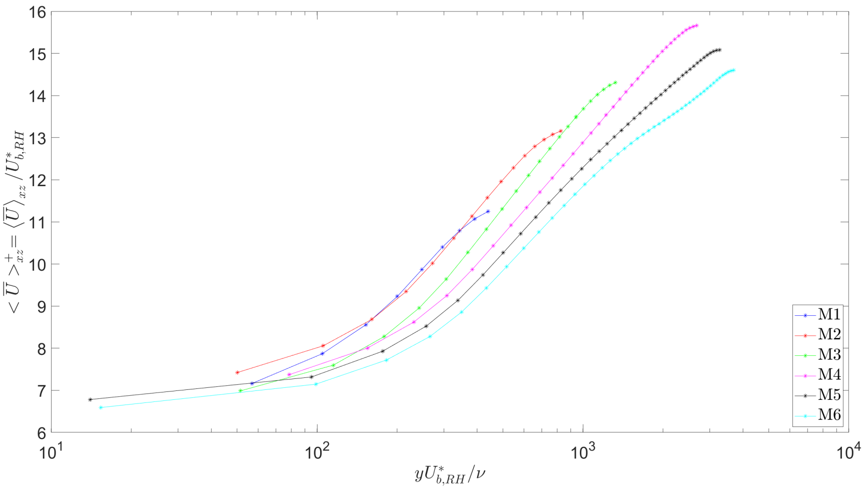

(b) "M" series.

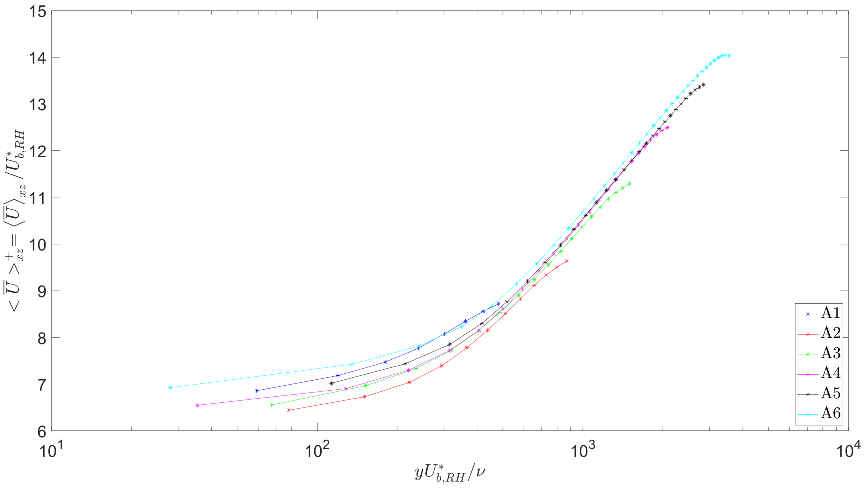

(c) "A" series.

Figure 4.3: Logarithmic law of wall plots. In this case $u^*_{b,RH}$ was used as scaling velocity.

4.2.2 Validation of the Surface Data

Similarly to the velocity data, validation of the surface elevation data obtained from the DIC and probes was performed in two steps. The first step consisted in the verification that the signals were spatially uniform and stationary over a long time period in order to verify that no long term lateral water slope was present and that the long term streamwise water slope was steady and had a uniform value. The second part was the actual validation of the free-surface measurements where distributions of the DIC and wave probes were compared.

Signal Verification

DIC measurements were not continuous but were affected by gaps in both space and time due to a non-uniform tracer coating as Figure 3.32 suggests. For this reason, verifying the stationarity and spatial uniformity of the reconstructed surface elevation field was not trivial.

A first attempt to verify the stationarity was conducted by subdividing the data sets into five 60 seconds long periods and calculating the overall (space and time) average and standard deviation for each segment. As the free surface fluctuated around the mean surface level, the averages were close to 0.000 mm. Different mean values were reported among the periods. The variation was within 5% of the overall average values. The reason for this behaviour was attributed to the unsteadiness and non-uniformity of the coating (and so of the reconstruction). In fact, an area interested by downwellings might have been better represented in one period, while an area affected by upwellings might have been better described in another period. Standard deviations looked stable in time (Tab. 4.3).

Standard Deviation of Surface Elevation Time Series for DIC (mm)							
Series	Test	Periods (s)					Total
		1÷60	60÷120	120÷180	180÷240	240÷300	
Q	1_S	0.076	0.077	0.076	0.075	0.074	0.081
	2_S	0.136	0.128	0.124	0.118	-	0.125
	3_S	0.326	0.325	0.327	0.323	0.299	0.323
	4_S	0.592	0.588	0.578	0.576	0.565	0.582
	5_S	0.691	0.696	0.737	0.717	0.714	0.712
	6_S	0.606	0.579	0.594	0.599	0.573	0.591
M	1_S	0.049	0.048	0.050	0.049	0.049	0.051
	2_S	0.066	0.067	0.061	0.061	0.061	0.067
	3_S	-	-	-	-	-	-
	4_S	0.105	0.105	0.106	0.107	0.095	0.123
	5_S	0.133	0.120	0.110	0.112	0.107	0.117
	6_S	0.123	0.159	0.124	0.131	0.125	0.142
A	1_S	0.072	0.069	0.065	0.062	0.066	0.074
	2_S	0.118	0.109	0.105	0.094	0.089	0.108
	3_S	0.268	0.264	0.251	0.256	0.246	0.258
	4_S	0.321	0.320	0.315	0.295	0.300	0.313
	5_S	0.400	0.402	0.395	0.403	0.387	0.399
	6_S	0.615	0.689	0.606	0.638	0.659	0.643

Table 4.3: Standard deviation of the surface elevation time series for DIC for different flow conditions.

A constant standard deviation, however, is not enough to guarantee the stationarity of processes, not even in a weak-sense. For this reason, stationarity had to be verified using an augmented Dickey-Fuller test (Dickey & Fuller, 1979). Due to the large size of the time series, it was not possible to perform the test over the entire duration. Data sets were then split into two 150 second long segments before conducting the test on each part. The test rejected the null hypothesis of a unit root against the autoregressive alternative (significance level $\alpha_s = 0.05$) for all the cases, implying the stationarity of the surface elevation field in all reported tests.

Spatial uniformity was checked by comparing the distributions of the surface elevation at different streamwise locations. Data sets were then divided into 6 spatial sections approximately 50 mm long. A preliminary Kolmogorov-Smirnov test (significance level $\alpha_s = 0.05$) was performed to verify whether the sector data samples could be described by a Gaussian distribution, always rejecting the null hypothesis. Standard deviations are reported in Table 4.4. Both means and standard deviations were found to change from section to section within 5% the overall average values. This difference was once again assumed to be caused by the gaps in the measurements. However, as the differences were small, the surface processes were considered spatially uniform.

Spatial Standard Deviation of Surface Elevation for DIC (mm)								
Series	Test	Sections (mm)						Total
		-150÷-100	-100÷-50	-50÷0	0÷50	50÷100	100÷150	
Q	1_S	0.085	0.078	0.078	0.079	0.079	0.089	0.081
	2_S	0.128	0.126	0.125	0.123	0.122	0.122	0.125
	3_S	0.337	0.331	0.325	0.319	0.316	0.313	0.323
	4_S	0.601	0.592	0.580	0.576	0.570	0.570	0.582
	5_S	0.723	0.718	0.717	0.709	0.703	0.701	0.712
	6_S	0.604	0.594	0.595	0.584	0.580	0.588	0.591
M	1_S	0.051	0.049	0.050	0.049	0.049	0.058	0.051
	2_S	0.065	0.067	0.068	0.067	0.067	0.066	0.067
	3_S	-	-	-	-	-	-	-
	4_S	0.123	0.123	0.122	0.122	0.122	0.121	0.123
	5_S	0.119	0.117	0.116	0.118	0.117	0.117	0.117
	6_S	0.144	0.144	0.141	0.141	0.141	0.140	0.142
A	1_S	0.076	0.073	0.072	0.072	0.072	0.079	0.074
	2_S	0.109	0.107	0.107	0.106	0.106	0.111	0.108
	3_S	0.264	0.261	0.258	0.255	0.254	0.253	0.258
	4_S	0.319	0.316	0.314	0.312	0.308	0.308	0.313
	5_S	0.403	0.405	0.398	0.395	0.399	0.392	0.399
	6_S	0.652	0.661	0.639	0.634	0.632	0.646	0.643

Table 4.4: Spatial standard deviation of surface elevation for DIC for different flow conditions.

Both spatial uniformity and stationarity were verified, suggesting that the surface elevation field satisfied uniformity conditions.

The water level data collected from the 7 wave probes located just downstream of the DIC system were also used. An augmented Dickey-Fuller test was again chosen to verify the stationarity of the probes measurements. The data sets had to be divided in two 150 second long periods before performing the test. The test always rejected the null hypothesis of a unit root against the autoregressive alternative (significance level $\alpha_s = 0.05$), implying the temporal stationarity.

Spatial uniformity was evaluated by considering the distributions for each probe. A preliminary Kolmogorov-Smirnov test (significance level $\alpha_s = 0.05$) was performed to verify whether the data samples could be described by a Gaussian distribution, always rejecting the null hypothesis. The standard deviation for each probe was finally calculated and are reported in Table 4.5. With the exclusion of a few values that are unrealistic and therefore are associated to a malfunction of the wave monitor, the statistics were not found to change substantially between different wave probes, verifying once again the spatially uniformity of the water surface when flow conditions were steady and uniform.

Standard Deviation of Surface Elevation for Wave Probes (mm)								
Series	Test	Probe						
		1	2	3	4	5	6	7
Q	1_S	0.142	0.121	0.118	0.145	0.096	0.245	0.133
	2_S	0.146	0.175	0.165	0.163	0.129	0.192	0.137
	3_S	0.295	0.300	0.298	0.298	0.254	0.313	0.296
	4_S	0.518	0.500	0.505	0.458	0.427	0.538	0.484
	5_S	0.619	0.607	0.622	0.586	0.549	0.652	0.627
	6_S	0.546	0.523	0.497	0.536	0.441	0.544	0.509
M	1_S	0.122	0.141	0.135	0.875	0.103	0.178	0.112
	2_S	0.136	0.107	0.155	0.151	0.110	0.235	0.121
	3_S	-	-	-	-	-	-	-
	4_S	0.128	0.121	0.138	0.182	0.158	0.140	0.125
	5_S	0.160	0.135	0.177	0.208	0.219	0.188	0.154
	6_S	0.171	0.162	0.204	0.212	0.295	0.166	0.168
A	1_S	0.149	0.118	0.128	0.777	0.104	0.164	0.116
	2_S	0.154	0.133	0.127	0.690	0.114	0.200	0.131
	3_S	0.216	0.210	0.303	2.266	0.192	0.274	0.212
	4_S	0.277	0.256	0.281	0.383	0.218	0.306	0.263
	5_S	0.359	0.320	0.354	0.714	0.339	0.385	0.345
	6_S	0.593	0.562	0.558	0.586	0.509	0.589	0.549

Table 4.5: Standard deviation of the distributions of surface elevation for wave probes for different flow conditions.

As spatial uniformity and stationarity were verified, the surface elevation field satisfied again uniformity conditions.

Comparison of Measurements

To verify the goodness of the DIC system at reconstructing the shape of a dynamic surface like the air-water interface, the DIC and wave probes measurements were compared against each other. Histograms of the DIC measurements and PDFs of wave probe 1 are plotted for different flow conditions and bed arrangements in Figure 4.4.

Figure 4.4 shows that the distributions of the DIC and probes measurements do not always match. This is particularly evident for the shallower flow conditions where the DIC returns distributions much narrower than the probe. This discrepancy, however, decreases with the flow rate and is negligible for the higher regimes.

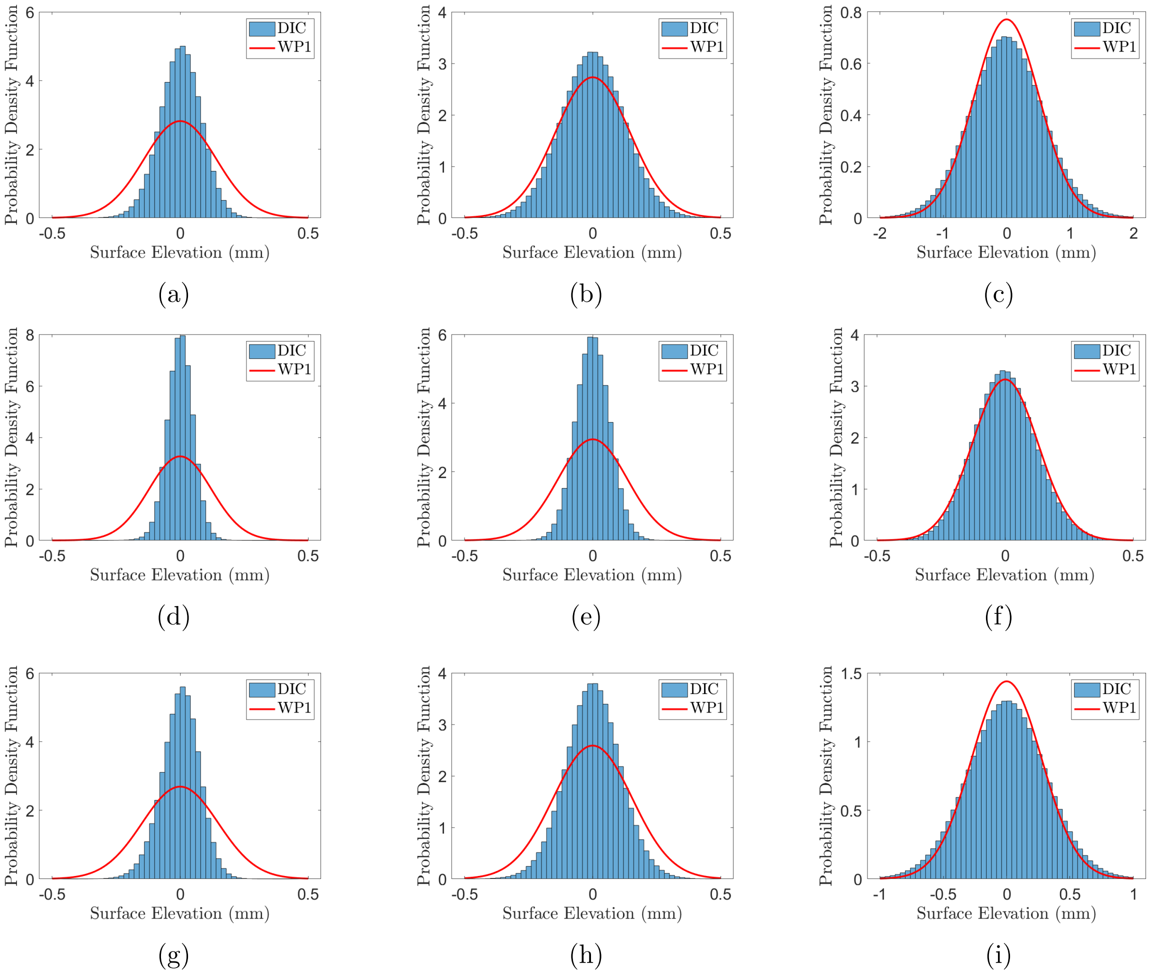

(a) (b) (c)

(d) (e) (f)

(g) (h) (i)

Figure 4.4: Histogram of DIC measurements compared with the PDF of wave probe 1 for different flow conditions. a) Q1_S. b) Q2_S. c) Q4_S. d) M1_S. e) M2_S. f) M4_S. g) A1_S. h) A2_S. i) A4_S.

Wave probes are considered to be a highly accurate instrument for monitoring the fluctuations of the free surface, while DIC is a technology that is mostly suited for the evaluation of the deformation of solid surfaces (e.g. plates and rebars). For this reason, the distributions of the probe data are considered more reliable than the DIC ones.
The DIC appears to struggle at determining the larger surface fluctuations at the lower regimes. It is suggested that the thin layer of buoyant tracers might have attenuated the vertical extent of the free-surface fluctuations at the lower regimes. This behaviour was instead not observed at higher flow rates as the turbulent structures and secondary currents effects managed to disrupt the layer of tracers, preventing them from affecting the free surface.

Statistical analysis of DIC data is of limited importance as it can be biased by the effects of the tracer coating. More important is the spectral analysis as it can be used to determine the dynamic behaviour of the free surface. For this reason, a comparison between the spectra derived from DIC and wave probes data sets was performed (Fig. 4.5).

Comparisons between the surface elevation spectra collected using DIC and wave probes reveal that there are no difference for frequencies below 10 Hz, while the spectra diverge at higher

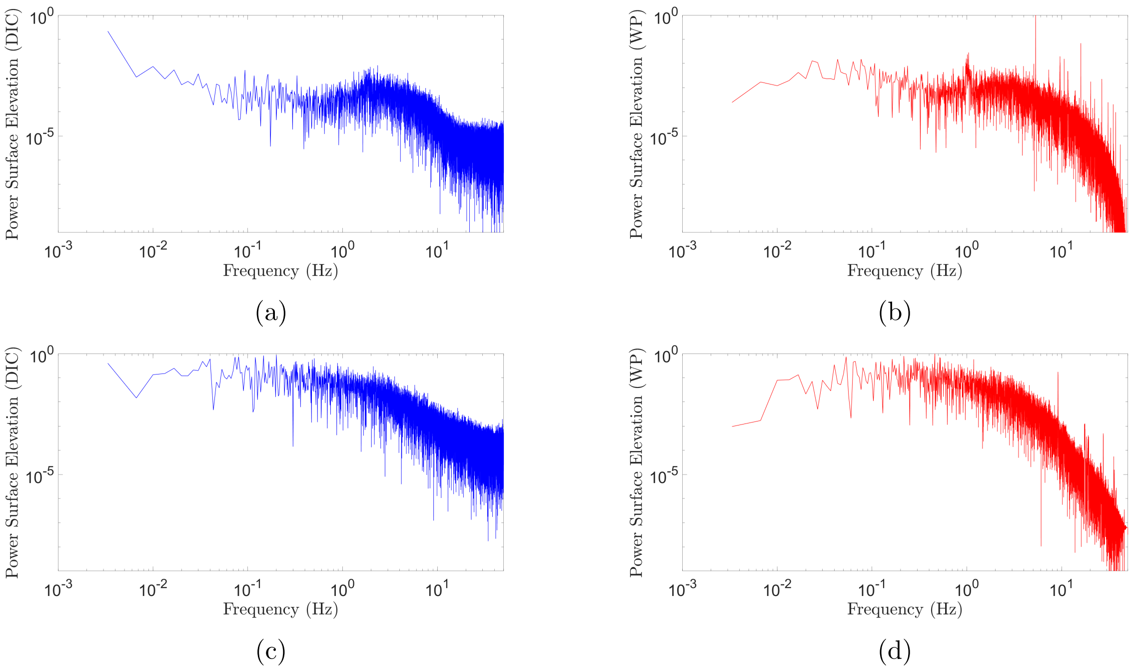

Figure 4.5: Comparisons between power spectra of surface elevation. a) Q1_S with DIC. b) Q1_S with wave probe. c) Q4_S with DIC. d) Q4_S with wave probe.

frequencies. The roll off visible in the probe data is a consequence of the internal low-pass filter of the wave monitor.

It can therefore be said that the DIC is capable of replacing the wave probes in the monitoring of the dynamic free surface at the scope of studying its behaviour. DIC, however, is characterised by a higher spectral resolution compared to the wave probe array. Also, the data is not affected by the presence of filters. For these reasons, only the results derived from the use of the DIC system will be presented over the next pages.

4.3 Flow Field

Six flow conditions were tested over two statistically identical beds having different texture orientations and two slopes, for a total of 18 tests. Over the next pages, velocity profiles, turbulent intensities, form-induced (alias dispersive) intensities and stress components from PTV measurements are examined.

The spatial datum for all measurements is set in correspondence of the zero-plane displacement defined in Subsection 4.2.1 at half the length of the investigated domain and the along the centreline. The convention used sees the x-axis oriented along the streamwise direction, the y-axis along the vertical direction and the z-axis along the transverse direction to complete the right-hand reference system. Corresponding velocities are indicated with U, V and W, respectively. Over-bar denotes time averaging, while angle brackets mean spatial averaging with angle bracket subscript indicating the direction the spatial averaging was performed along.

Considerations on the velocity profiles are proposed in Subsection 4.3.1, turbulent intensities are discussed in Subsection 4.3.2, dispersive intensities are presented in Subsection 4.3.3 and stresses are shown in Subsection 4.3.4.

4.3.1 Velocity Profiles

Normalised double-averaged streamwise velocity profiles plotted against relative depth for the different series and conditions are presented in Figure 4.6.

As expected for flows over permeable beds, the normalised double-averaged streamwise velocity for all the cases is non-zero in correspondence of the top of the spheres. Here, normalised streamwise velocity varies between 6.5 and 7.5, corresponding to a dimensional streamwise velocity between 0.13-0.26 m/s over the experimental range. Data demonstrates a slight increase in the slip velocity (i.e. the non-zero velocity that occurs over rough beds in correspondence of the top of the bed elements) with the flow rate. This would suggest either a progressive deepening of the zero-plane displacement d_0 or an increment of the seepage velocity with the flow rate. Typically, direct observations of the zero-plane displacement are not available. Also, for the tests reported here, the low quantity of tracers present in the interfacial layer, the chosen angle for the cameras and the obstruction to the view exerted by the spheres made it not possible to accurately evaluate the double-averaged flow field below the elevation of the spheres' tops and so determine where d_0 could lie. In these conditions, the zero-plane displacement is typically derived from routines aimed at maximising the fitting with the logarithmic law (Ruff & Gelhar, 1970; Chu & Gelhar, 1972; Gupta & Paudyal, 1985). The validity of this operation, however, is contested. Stull (2003) and later Kim et al. (2020) proposed that the position of the zero-plane does not vary with the Reynolds Number. If this view is accepted then the higher slip velocity appears to be caused by an increment of the seepage velocity.

Normalised double-averaged streamwise velocity profiles for flow conditions belonging to Class I show a linear trend along most of the depth and start bending only towards the free surface. This suggest that the roughness layer is not limited to the near-bed region but can extend up to 50-70% of the depth depending of the flume slope (50% for tests over 1/1000, 70% over 1/500). Above the profiles bend and assume the typical shape observed in the outer layer given by the logarithmic law with the appropriate corrections observed in the most superficial layer. As suggested by Nikora et al. (2001) the logarithmic layer can be suppressed in flow conditions that have limited relative submergence. For these cases, the roughness layer is directly followed by the outer layer.

Similar considerations can be advanced for regimes belonging to Class II and Class III. Here, the upper limit of the roughness layer progressively is pushed more and more towards the bed as the water depth increases. However, even for flows in Class III, the roughness layer can exist up to 15-20% of the depth. In parallel, as depth increases, a logarithmic layer appears and grows in size, occupying the portion of the depth that was interested by the roughness layer at lower flow rates. The logarithmic layer is seen to extend up to 50-60% of the depth, with lower values for the gentler slope. Above the profile can be described by the log law with the outer layer corrections.

Bed arrangement does not appear to play a major role of defining the shape of the velocity profiles. On contrary, flume slope has an influence as it lowers the higher boundaries of the

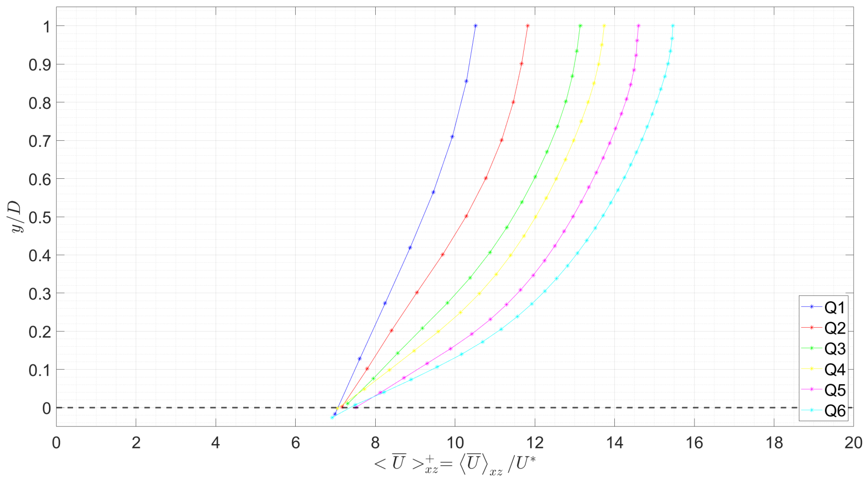

(a) "Q" series.

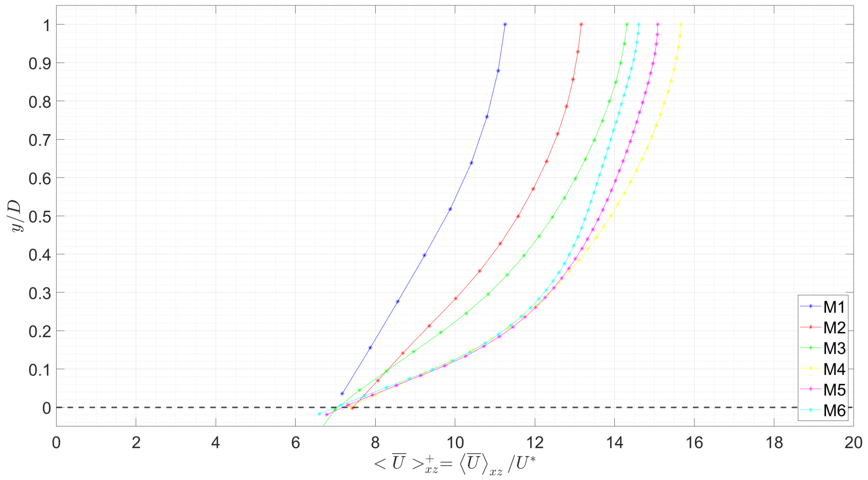

(b) "M" series.

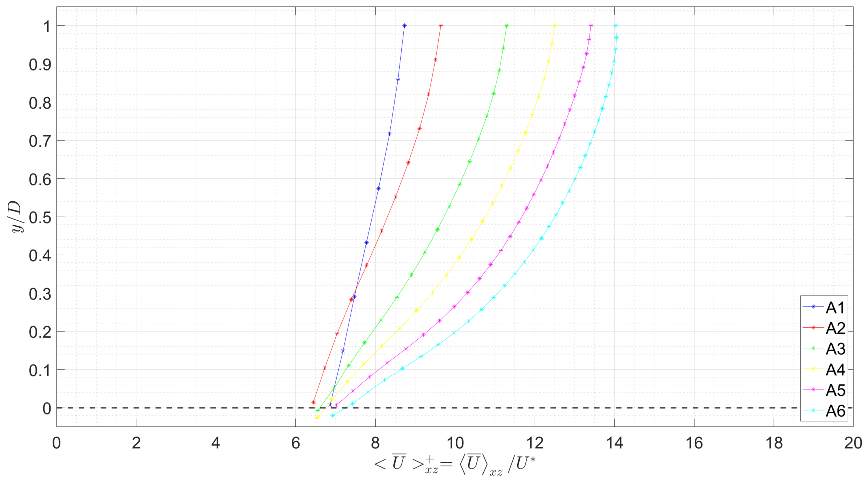

(c) "A" series.

Figure 4.6: Normalised double-averaged streamwise velocity profiles for different flow regimes.

layers. This is due to an increased relative submergence respect with conditions over 1/500 for the same free-surface velocity. However, an exception can be seen for M5_H and M6_H. Normalised double-averaged streamwise velocity profiles for these hydraulic regimes initially follow the same trend of the profile for M4_H. However, the profiles diverge at 20% of the depth in correspondence of the transition from the roughness to the logarithmic layer. Above the profiles appear rearward respect M4_H. This anomalous behaviour might be explained by the small aspect ratio of two flow conditions.

Larger non-dimensional values of normalised double-averaged streamwise velocity were observed along the entire water column over the quincunx arrangement, independently of the flow class. This behaviour indicates that higher friction coefficients take place over the alternate bed. As mentioned earlier, the quincunx arrangement sees a sequence of tops and troughs along the same spanwise position, while the alternate arrangement presents either just tops or just troughs (Fig. 3.25). The latter bed case promotes higher momentum penetration within the bed as trough sections are preferential ways of infiltration due to the absence of impermeable obstacles (Pokrajac & Manes, 2009). Furthermore double-averaged statistics are here being observed, spatial-averaging is known to smooth the effects of spatial heterogeneity that characterises non-regular beds. This means that even lower velocities are expected over the top sections, whilst higher ones occur over the trough sections of the alternate bed. The velocity difference between the two spanwise section can favour the arise of additional stresses. The more efficient momentum extraction from the flow core and the presence of additional stresses implicate that higher friction factors occur over the alternate bed arrangements. Hence, for the same flow rate and depth, lower streamwise velocities are observed.

4.3.2 Turbulent Intensity Profiles

This Subsection focuses on the normalised double-averaged turbulent velocity profiles. Streamwise intensities are plotted in Figure 4.7, vertical intensities in Figure 4.8 and spanwise intensities in Figure 4.9.

Normalised streamwise turbulent velocity intensity (Fig. 4.7) is seen to increase quasi-linearly while moving away from the free surface for the shallowest flow conditions belonging to Class I and II. The profile appears to be nearly constant or slightly increasing with linear trend in the near-surface region. Below, the profile shows a significant increase starting from the 75-80% of the depth while maintaining a linear behaviour. A different trend can instead be observed for condition A1_H as an initial decrement is followed by a constant value and later by a growth. As the flow rate rises and flow conditions in Class III are tested, the shape of normalised streamwise turbulent velocity intensity changes and two inflection points develop, one near the free surface and one near the bed. Above the near-surface point, the profile remains nearly constant for the intermediate flow conditions or shows a small decrement for the higher regimes. Between the two points the profiles increase with a linear trend. Further below, the profile keeps increasing but with a lower pace than above. The position of the upper inflection point is approximately at 75-85% of the depth and it seems moving upwards for increasing flow rates. On contrary, the lower inflection point occurs at (0.2-0.4)D and it moves towards the bed for

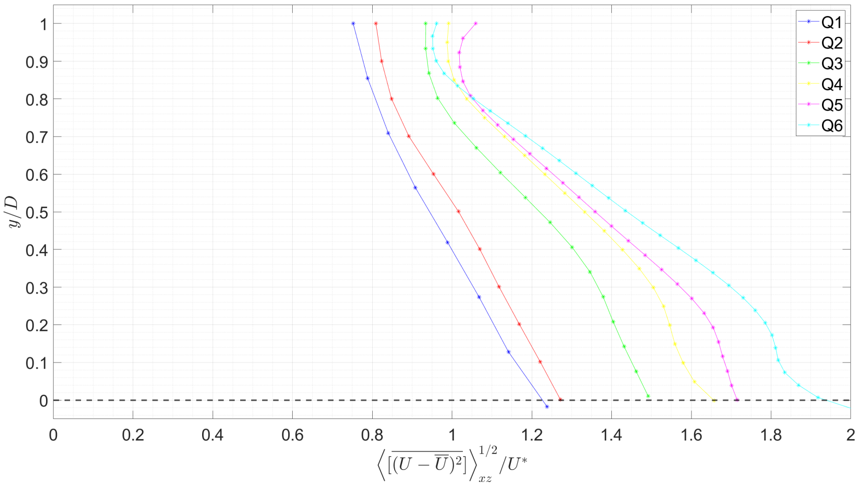

(a) "Q" series.

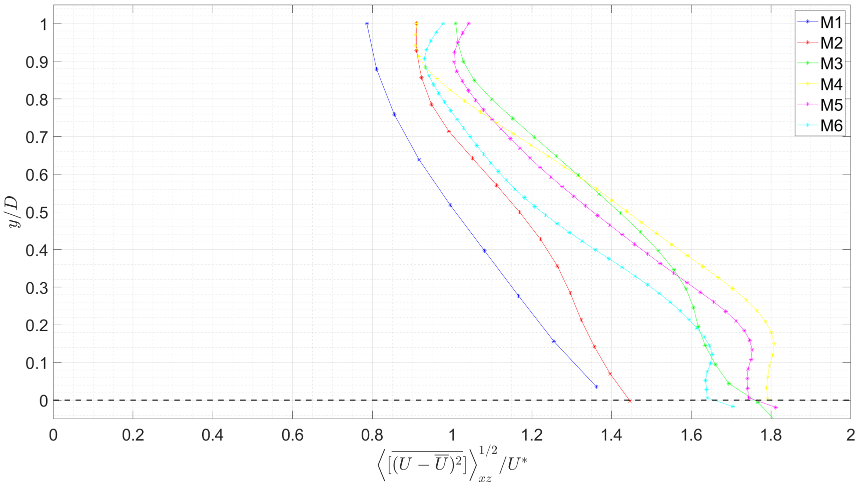

(b) "M" series.

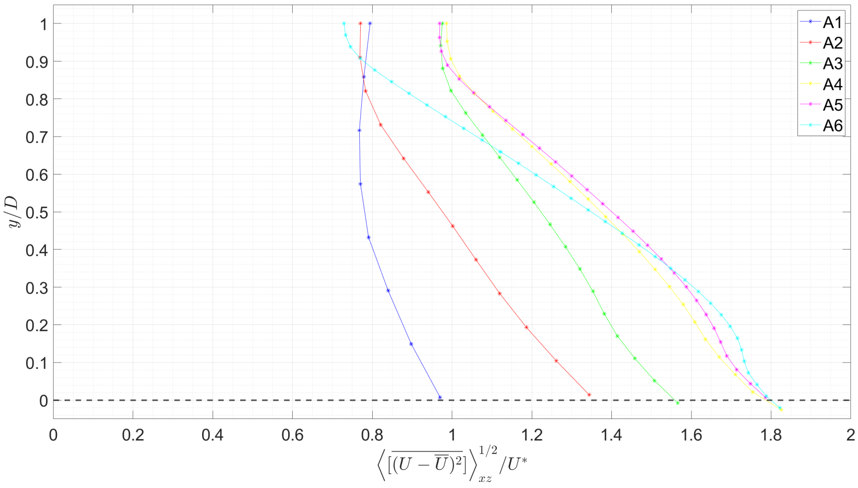

(c) "A" series.

Figure 4.7: Normalised double-averaged streamwise turbulent velocity intensity profiles for different flow conditions.

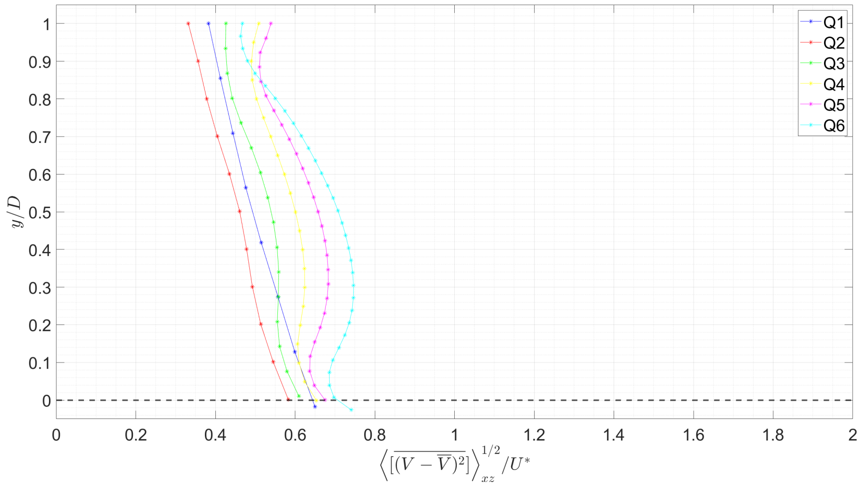

(a) "Q" series.

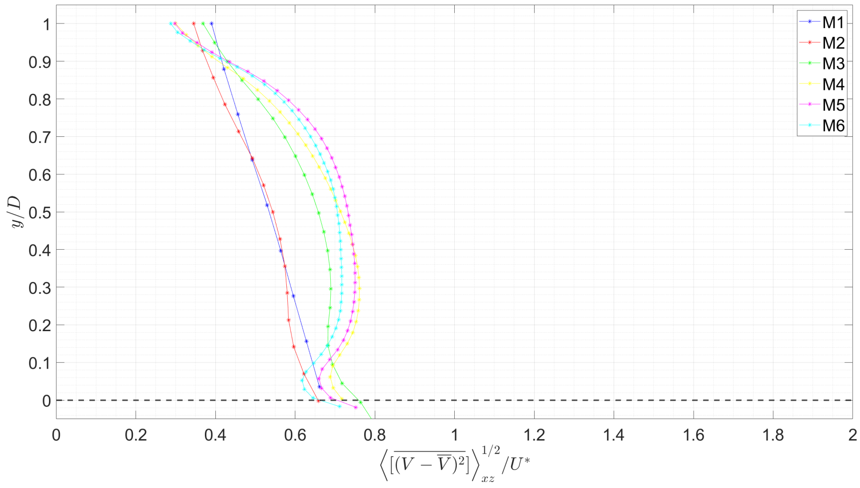

(b) "M" series.

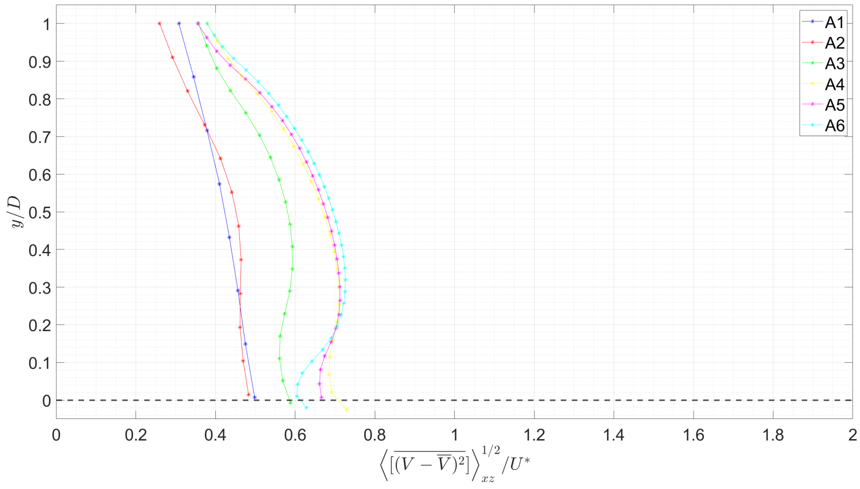

(c) "A" series.

Figure 4.8: Normalised double-averaged vertical turbulent velocity intensity profiles for different flow conditions.

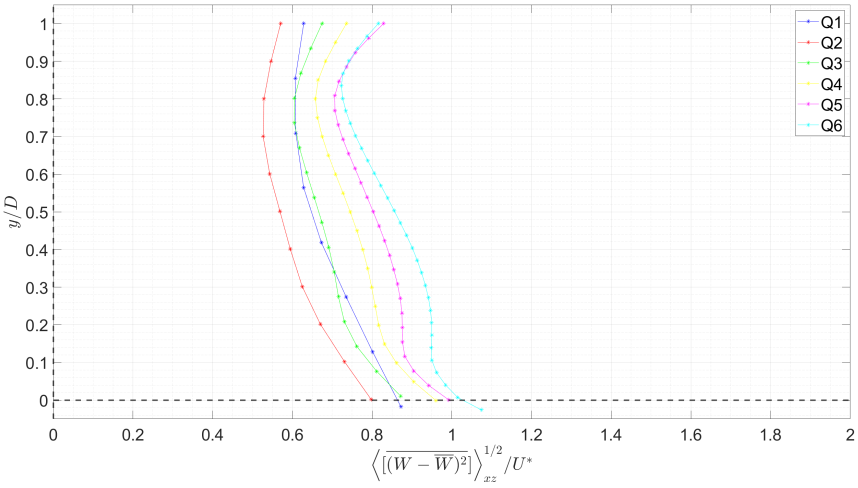

(a) "Q" series.

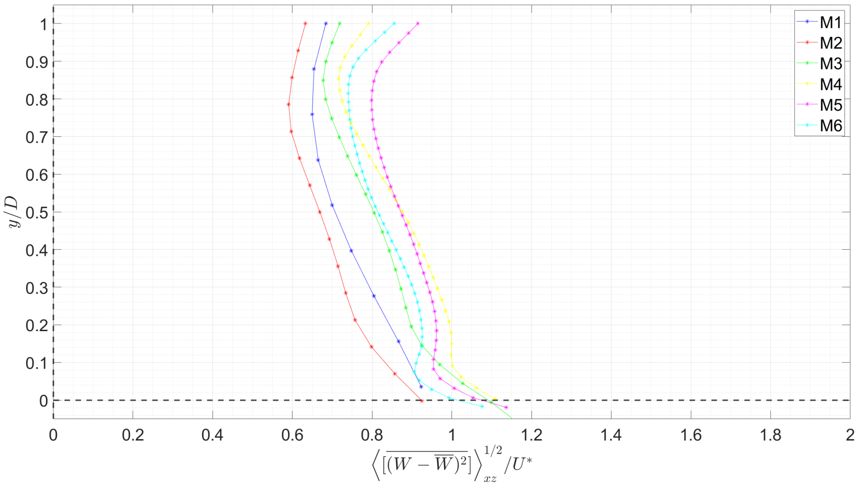

(b) "M" series.

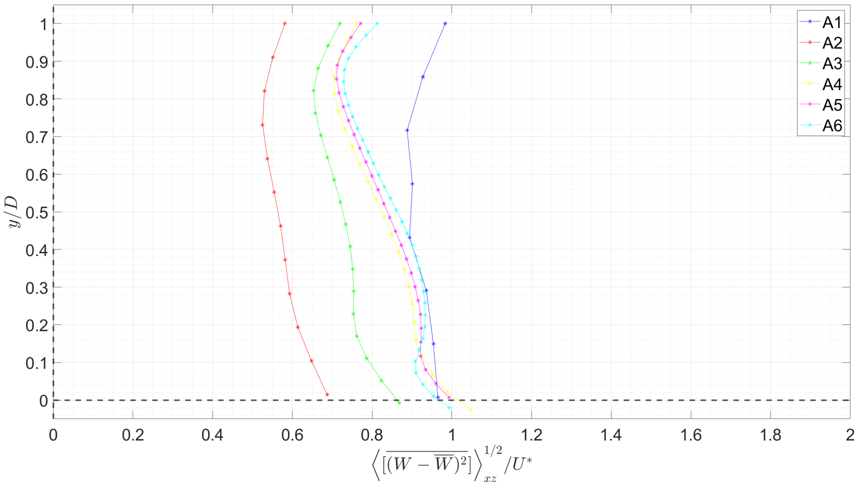

(c) "A" series.

Figure 4.9: Normalised double-averaged spanwise turbulent velocity intensity profiles for different flow conditions.

increasing discharges.
Magnitudes throughout the depth rise for higher flow rates. This behaviour can be observed over different bed arrangements and slopes suggesting that the streamwise turbulent velocity intensity is not significantly influenced by these two factors.

Non-dimensional vertical turbulent velocity intensity profiles (Fig. 4.8) show a linear monotonic increment while moving towards the bottom for flows in Class I.
As the discharge increases, a linearly increasing behaviour can still be observed for the profiles of flows in Class II. However, small deviation from linearity can be noticed, typically between 45-55% of the depth. Nonetheless, maxima still occur in correspondence of the bed level.
Profiles for Class III completely diverge from the linear behaviour. Non-dimensional vertical turbulent velocity intensity increases moving away from the free surface and peak at 30-40% of the depth. The growth is particularly accentuated in the region below (0.85-0.95)D. After the maxima, the profiles decrease and reach local minima around 5-10% of the depth where the profile inflects. Further below an increment is noticed and the intensity reaches values comparable with the maximum observed above. Comparison between the profiles of flows in Class III revealed that the position of the point near the free surface where a change in the increment of the grown rate of the non-dimensional vertical turbulent velocity intensity moves towards the free surface as the depth goes up. On contrary, the location of the maximum and of the inflection point move deeper with the depth.
Particularly different is the magnitude observed near the surface region between Classes I and II, and Class III. In correspondence of the bed, normalised values between 0.50 and 0.75 can be seen.

Non-dimensional spanwise turbulent velocity intensity profiles (Fig. 4.9) show a trend that is shared between flow conditions regardless of the Class. Intensities, initially large in correspondence of the free surface, decrease to a global minimum just the below the surface at 75-90% of the bed. From here, the profile keeps increasing with a trend that is linear for flows in Class I and becomes slightly non-linear as the discharge goes up. Profiles for flows in Class III see an inflection near the bed at 5-10% of the depth where a small decrement followed by an increment occur. For all the regimes a maximum value for the non-dimensional spanwise turbulent velocity intensity can be observed at the bed level.
Spanwise intensity magnitudes do not vary much throughout the depth and show normalised values between 0.7 and 1.1 in correspondence of the bed.

Generally speaking, bed arrangement appears to have limited influence on the turbulent intensity profiles. The hydraulic regime results to be the main cause for the different shape of the streamwise and vertical intensity profiles, moving from linear trends (Classes I and II) to more complex curves (Class III) as the flow rate increases.
Streamwise and lateral intensities increase in the correspondence of the free surface, whilst the vertical ones decrease. This suggests that 3D patterns of momentum redistribution are taking place near the surface from the vertical to the other two components. Transfer of momentum also occurs at the bed level as the vertical intensity is being suppressed in favour of the streamwise and spanwise ones.

4.3.3 Dispersive (Form-induced) Intensity Profiles

Normalised double-averaged dispersive velocity profiles are proposed in this Subsection. Streamwise intensities are plotted in Figure 4.10, vertical intensities in Figure 4.11 and spanwise intensities in Figure 4.12.

Normalised double-averaged streamwise form-induced intensity profiles (Fig. 4.10) appear to be different according to bed texture. Over the alternate arrangement, the magnitude of the form-induced fluctuations appears to decrease as the flow conditions pass from Class I to Class III. On contrary, the magnitude seems to increase moving from Class I to Class III over the quincunx bed texture. Exceptions can be seen for both arrangements and this is due by the presence of secondary currents within the observed domain.
The trend for the profiles, however, is the same independently of the bed configuration. A monotonic increment towards the bed where a peak here occurs for conditions in Classes I and II, while for Class III the profiles increase towards the bed, reach a maximum in correspondence of (0.25-0.4)D where they inflect and later decrease near the bed.
Magnitudes generally appear to be higher over the alternate arrangement as a consequence of the higher bed heterogeneity.

Normalised double-averaged vertical form-induced intensity profiles (Fig. 4.11) show for flows in Classes I and II an exponential increase over the quincunx arrangement while approaching the bed, whilst over the alternate arrangement the trend is linear.
This behaviour changes for Class III as the profiles are more wavy. Over the quincunx arrangement, the profiles initially decrease to a minimum in correspondence of an inflection point at approximately 90% of the depth. The profiles then increase and reach a local maximum at (0.35-0.5)D from the bed. Later, the intensity decreases to a local minimum at 15-25% of the depth where a second inflection is observed. A final increment is then seen until the bed level where the maximum value are reported. Over the alternate arrangement a single inflection occurs near the bed. The trend for these profiles are similar to the ones over the quincunx arrangement except for a monotonic increment between the free surface and the maximum at 35-50% of the depth.
Similarly to normalised double-averaged streamwise form-induced intensity also the vertical intensity observes a decrease in the magnitude while moving from flow condition in Class I to the one in Class II for the alternate arrangement. An opposite behaviour can instead be seen over the quincunx texture with larger values observed for Class III.

Normalised double-averaged spanwise form-induced intensity profiles (Fig. 4.12) show a trend that appears to be unaffected by the Class of the flow and bed arrangement. High values are initially observed at the level of the free surface. Moving away from the free surface the profiles keep decreasing to a minimum value at approximately 35-50% of the depth. Further below the intensity profiles increase and reach the maximum at the bed level.

Observing the general behaviour of the form-induced velocity intensities, it appears clear that the bed arrangement highly influences the shape of the profiles. Flow Class as well affects the profiles as linear trends are typically observed for flows in Classes I and II, while the profiles are

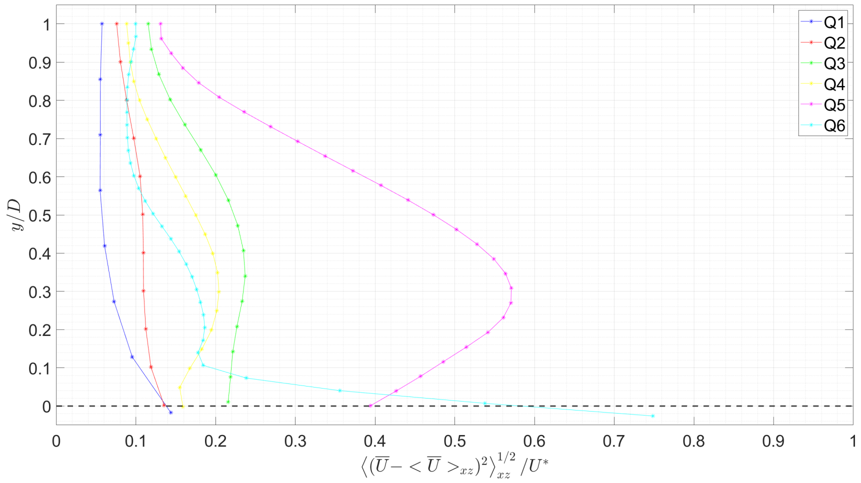

(a) "Q" series.

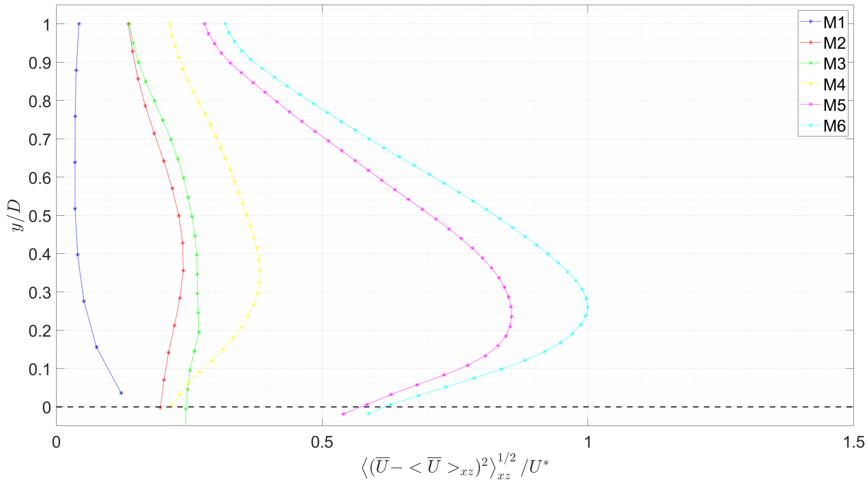

(b) "M" series.

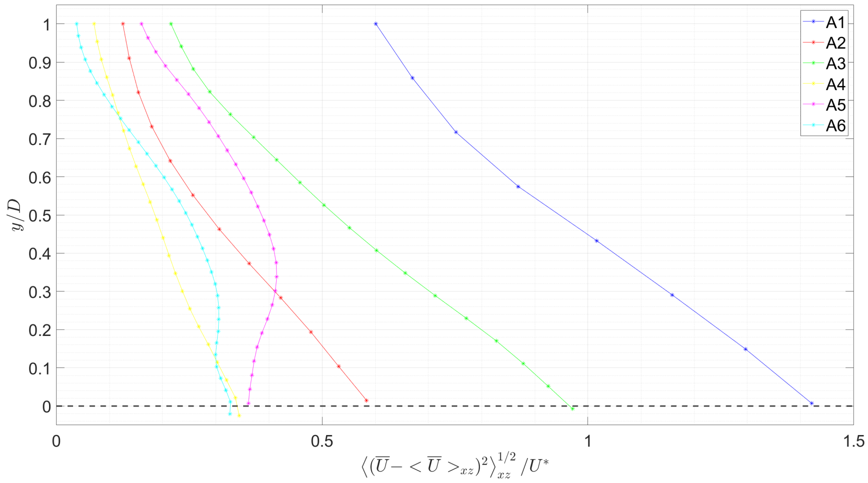

(c) "A" series.

Figure 4.10: Normalised double-averaged streamwise dispersive velocity intensity profiles for different flow conditions.

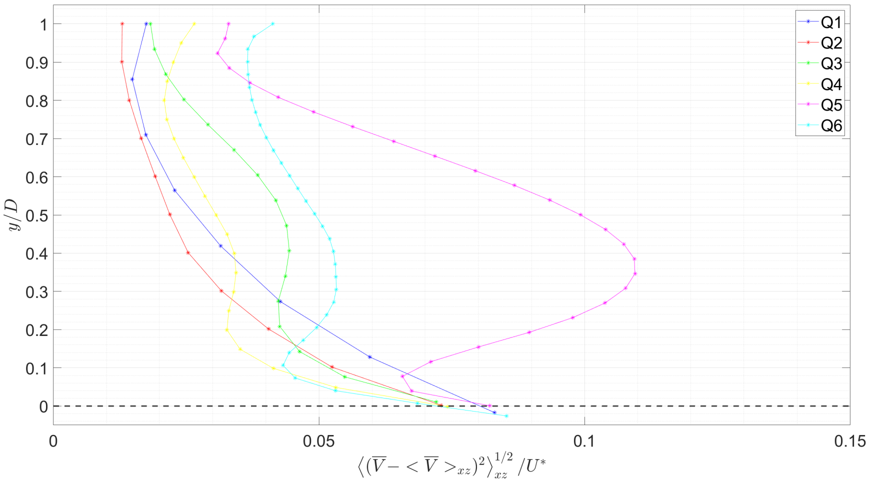

(a) "Q" series.

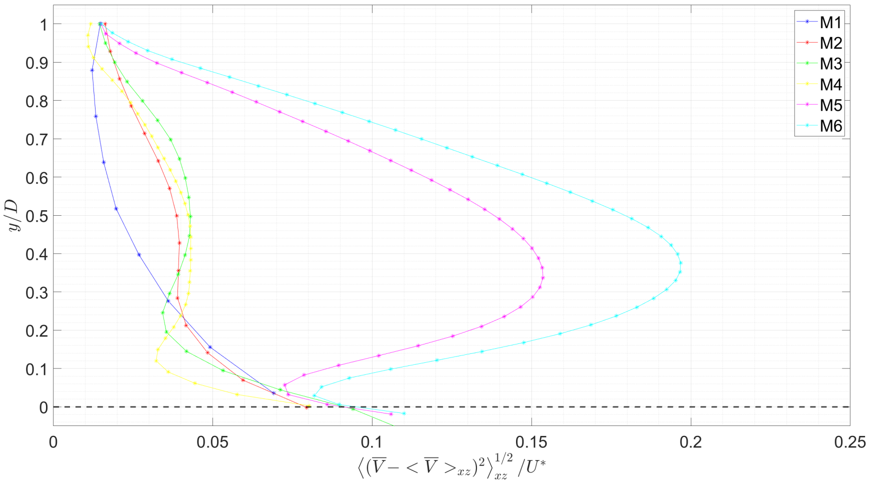

(b) "M" series.

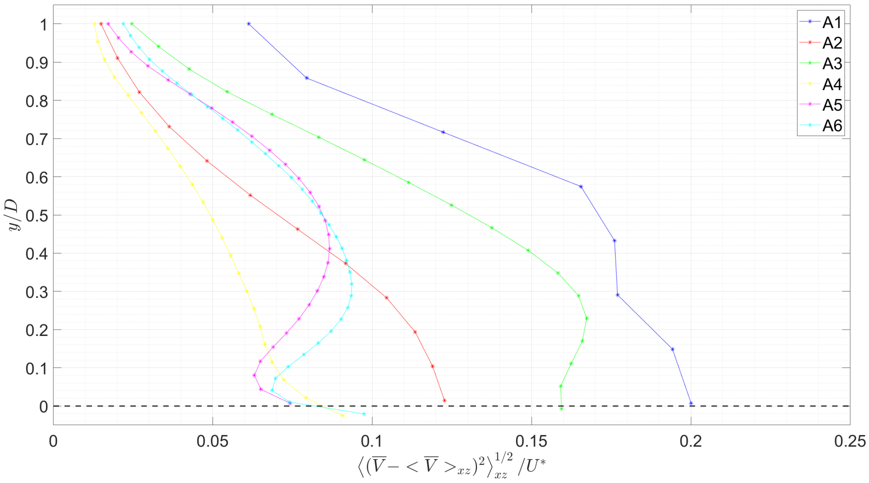

(c) "A" series.

Figure 4.11: Normalised double-averaged vertical dispersive velocity intensity profiles for different flow conditions.

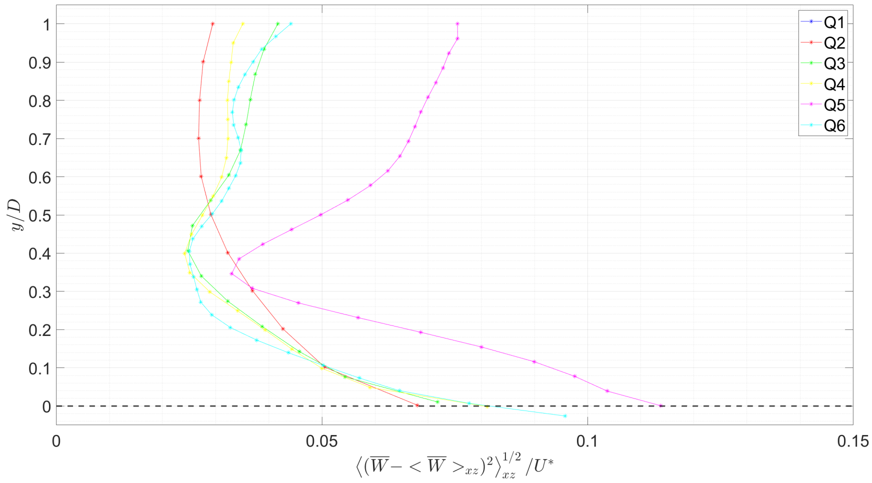

(a) "Q" series.

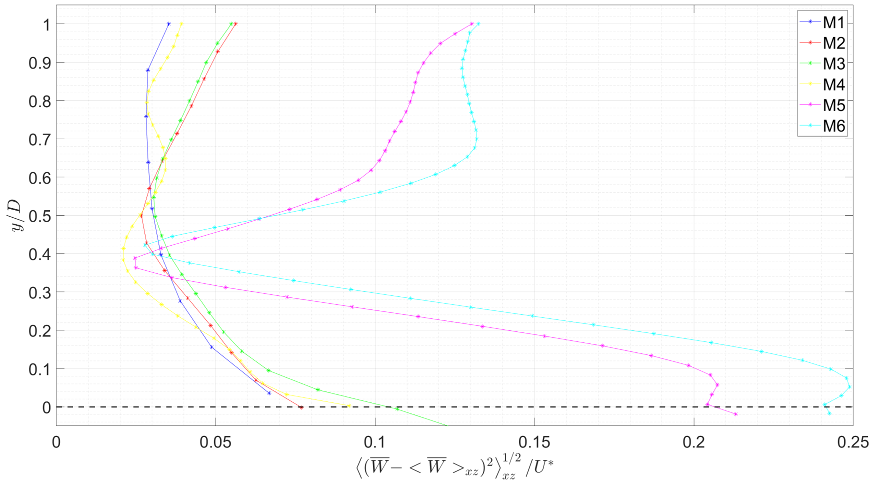

(b) "M" series.

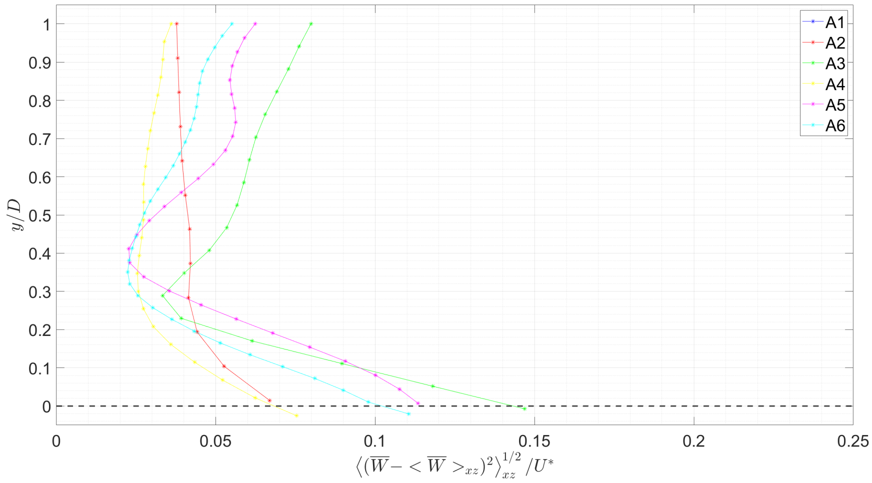

(c) "A" series.

Figure 4.12: Normalised double-averaged spanwise dispersive velocity intensity profiles for different flow conditions.

more complex for Class III.
Streamwise magnitudes result higher than the vertical and spanwise ones. However, they are considerably smaller when compared with the turbulent fluctuations for most of the flow conditions here reported. Exceptions can be observed for conditions in Class I where the streamwise dispersive magnitude is comparable with the turbulent one.

4.3.4 Shear Profiles

Kinematic stresses are presented in this Subsection. Figure 4.13 reports the normalised turbulent stresses, Figure 4.14 shows the normalised dispersive stresses, while Figure 4.15 presents the normalised total stresses.

The normalised double-averaged turbulent cross-product between the streamwise and vertical components (Fig. 4.13) has an identical behaviour over the two beds. It increases linearly moving away from the free surface and peaks at the bed level for conditions in Classes I and II. For Class III regimes, an inflection point arises at (0.2-0.4)D and the cross-product has a maximum here. From here the profile decreases as the bed is approached. Such decrement is more intense as the flow rate increases. Also the position of the inflection point is affected by the flow rate as it moves downwards for higher discharge values.

Normalised double-averaged streamwise-vertical cross-product for the dispersive intensity (Fig. 4.14) appears to be affected by the bed arrangement.
The intensity shows a linear increase over the alternate arrangement for Class I. For Class II an inflection take place at 30-40% of the depth from the bed surface, followed by a nearly constant values down to the bed level. For Class III regimes the profile linearly increases and peaks at an inflection situated at (0.3-0.4)D from the bed. The magnitude then decreases as the bed is approached to half of the peak value at the inflection point.
More uniform is the behaviour of the profile for the quincunx bed as for most of flow conditions the magnitude increases linearly and a peak occurs at 30-40% of the depth above the bed. Below, a decrement is observed, with magnitudes in correspondence of the bed between half and a third of the maximum value.
The trend in the observed magnitudes is opposite between the two bed arrangement, decreasing with the flow rate over the alternate texture and increasing over the quincunx one. This is a consequence of the higher lateral variability of the former bed surface arrangement.

Profiles corresponding to the sum of the form-induced and turbulent momentum fluxes (Fig. 4.15) show similar behaviours over both beds.
The profile is well represented by a linear fit for Class I. However, as the flow rate rises (Classes II and III), an inflection point appears near the bed. While moving from the free surface, the profile value increases and peaks at the inflection point at around (0.3-0.4)D from the bed. Downwards from this inflection point, the profile decreases to a local minimum at the bed. The rate of decay appears to increase for higher flow rates. The inflection point seems to approach the interface as the flow rates increases.
It can be noticed that the dispersive quota over the total kinetic momentum flux is practically non-existent over the quincunx bed arrangement, while over the alternate texture the contribu-

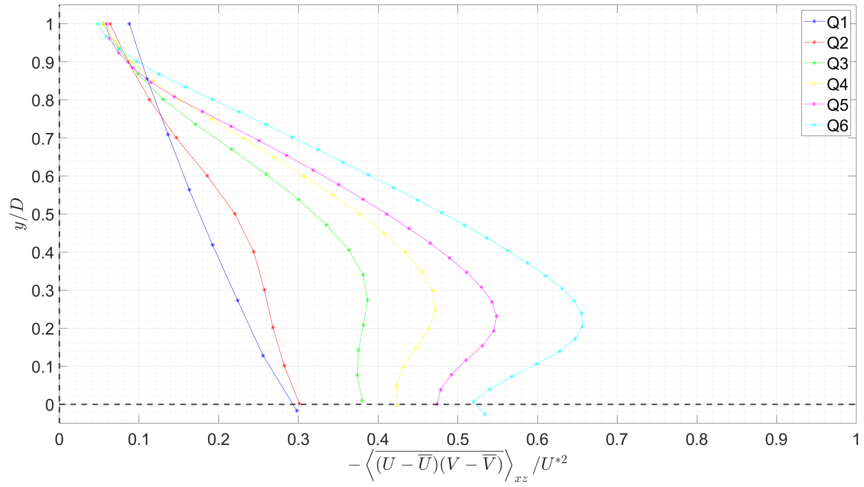

(a) "Q" series.

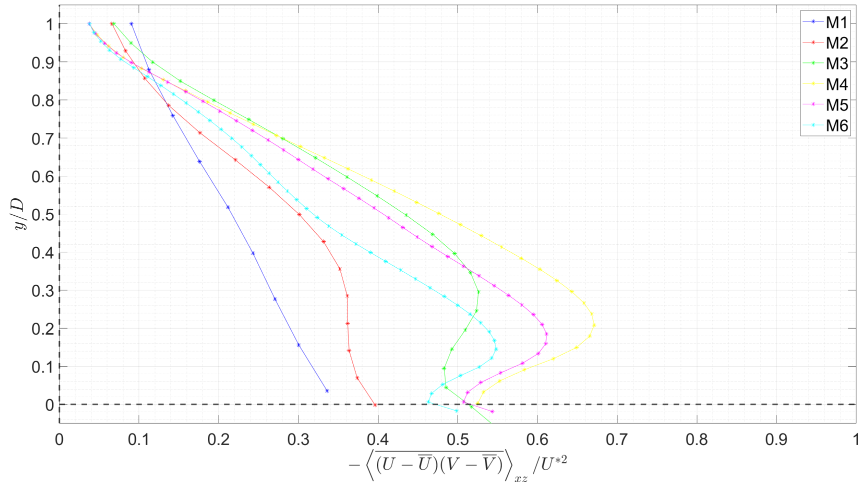

(b) "M" series.

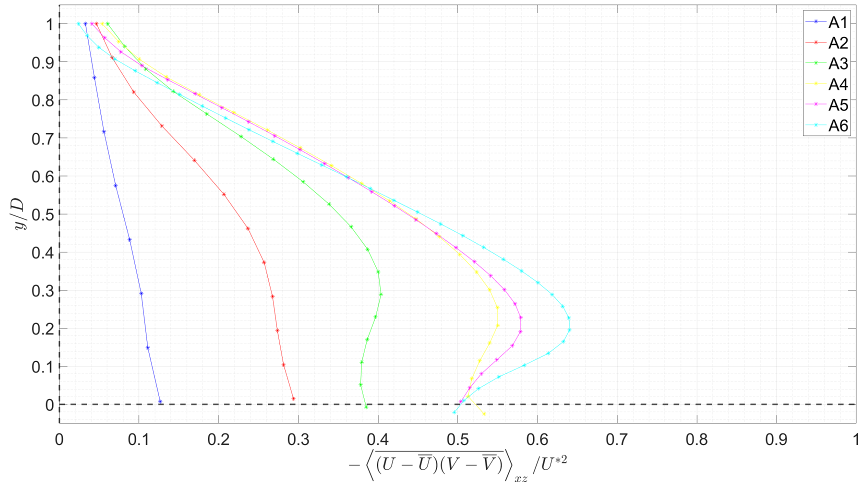

(c) "A" series.

Figure 4.13: Normalised double-averaged kinematic turbulent stress profiles for different flow conditions.

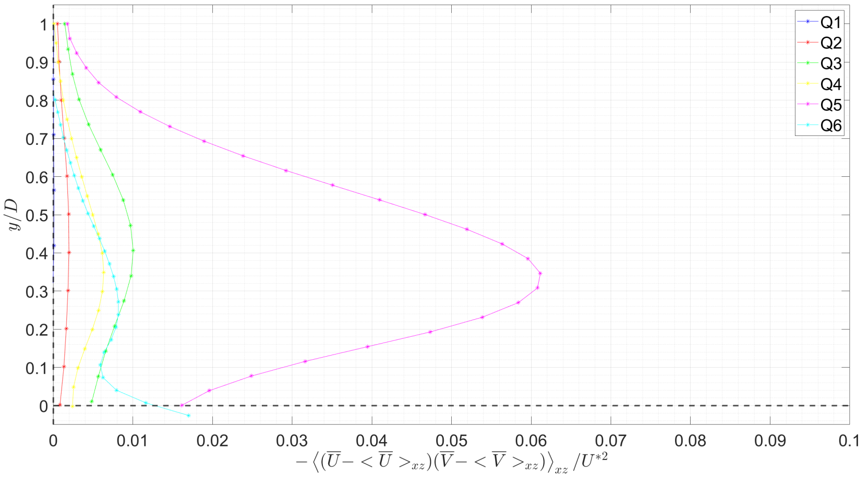

(a) "Q" series.

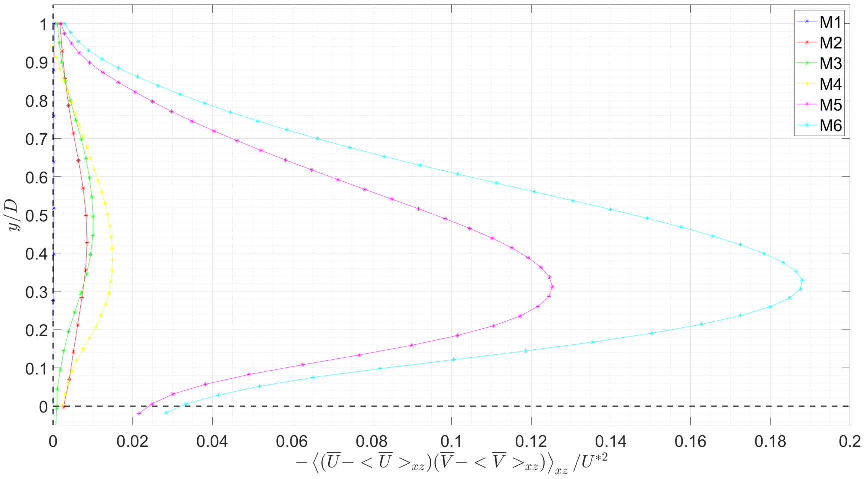

(b) "M" series.

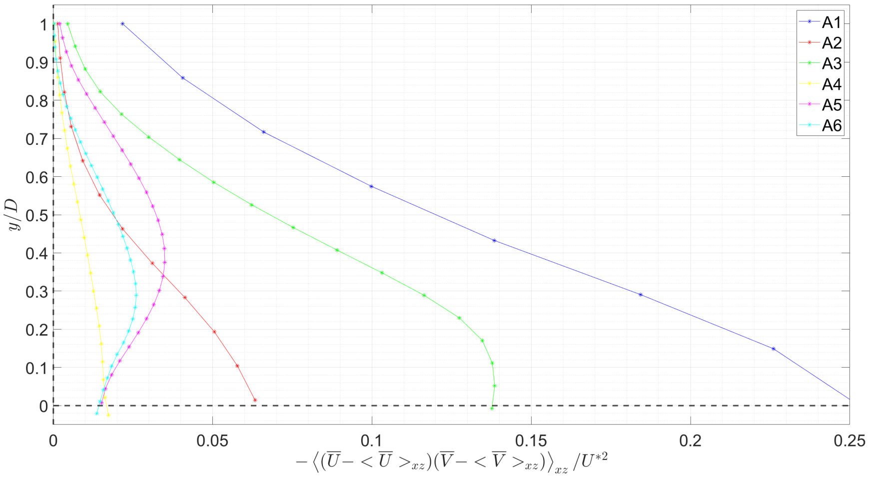

(c) "A" series.

Figure 4.14: Normalised double-averaged kinematic dispersive stress profiles for different flow conditions.

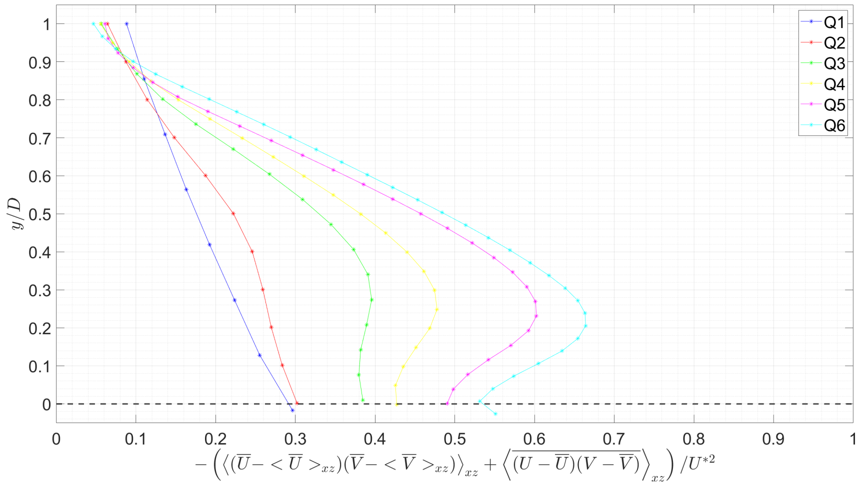

(a) "Q" series.

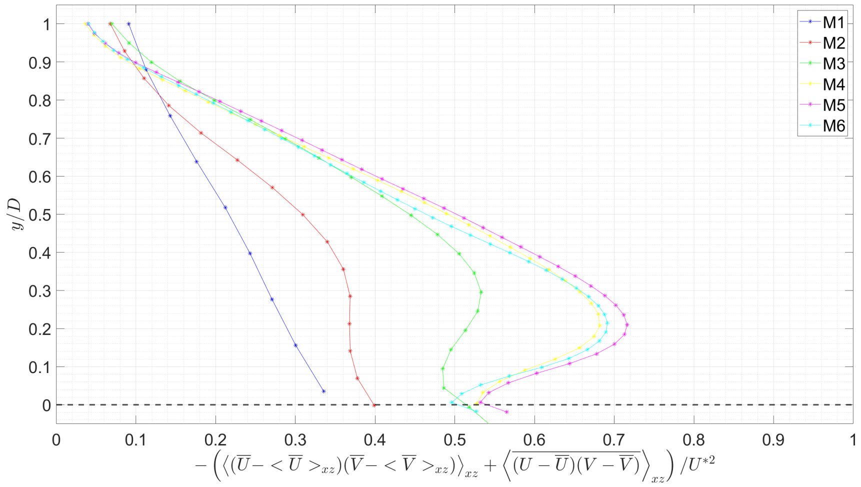

(b) "M" series.

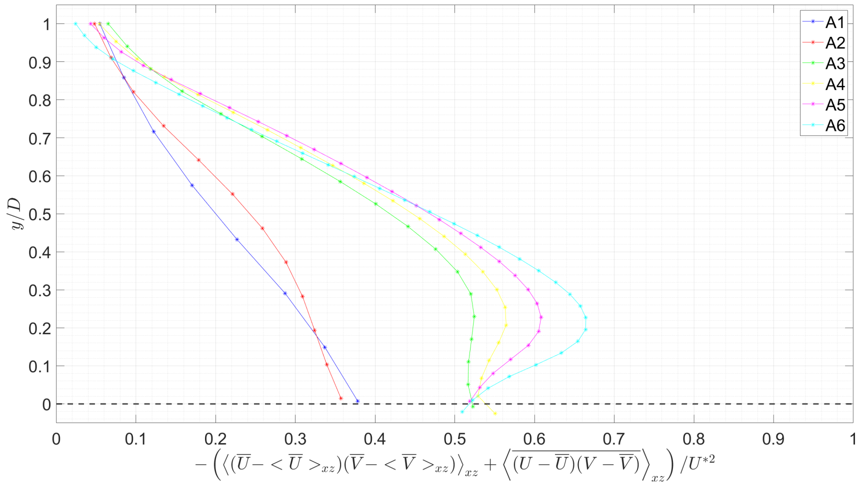

(c) "A" series.

Figure 4.15: Normalised double-averaged kinematic total stress profiles for different flow conditions.

tion of the dispersive stress varies between 60% for Class I to 10% for Class III.
What is surprising is that this dispersive component never completely disappears for higher discharges and can still be observed at the free surface. This further suggests that information on the roughness topography can be observable in the free-surface behaviour.

Comparing the profiles of the different stress components, it appears clear that two different behaviours exist depending on the flow Class.
Class I and II have a typical triangular behaviour throughout the depth and peak at the bed level with observed magnitudes of 0.3-0.4.
Shear stress for flow conditions in Class III initially increases linearly moving away from the free surface. The stress, however, peaks around 20-30% of the depth before decreasing to values of approximately 0.5.
The different shapes of the profiles reveal that different types of momentum transfer mechanisms are active according to the Class of the conditions.
Comparisons between the spatial (dispersive) and temporal (turbulent) shear components show that the turbulent part mostly contributes to the total value of the stress for the majority of the cases. Only exceptions are the conditions in Classes I and II over the alternate bed arrangement where the form-induced part is comparable with the turbulent one as a consequence of the higher bed heterogeneity.

4.4 Free Surface

The aim of this Section is to identify the governing mechanisms of the free-surface behaviour at different flow regimes. To this purpose, DIC measurements were used as characterised by a much higher spatial resolution in both the streamwise and lateral directions compared to wave probes data. The area of measurement of DIC was also many times larger than that covered by the wave probes. This allowed longer wavelengths to be determined at much better frequency resolutions.

This Section is composed by two Subsections: Subsection 4.4.1 presents the results of the DIC data analysis; in Subsection 4.4.2 DIC data is used to present a remote estimation technique of key flow parameters.

4.4.1 Characterisation of the Free-surface Behaviour

According to Dolcetti et al. (2016) and Muraro et al. (2021), three different typologies of free-surface waves can be identified: non-dispersive waves, gravity-capillary waves and gravity-capillary waves having the same wavenumber of stationary waves k_0.

Traditional statistical analysis, using different order moments, was not used for the evaluation of the DIC data. This was done as the intermittent temporal and spatial gaps in the DIC data indicated that this type of traditional analysis approach was not appropriate. Furthermore, simple statistical analysis was not reckoned to be the best tool because it severely limits the understanding of the free-surface dynamics as similar statistical moments might be realised by by different combinations of wavelengths and frequencies.

Spectral analysis was instead chosen for the processing of the free-surface elevation field in order to recognise the different waves patterns that are known to populate the moving water surfaces. The behaviour of the free surface was determined via frequency-wavenumber spectra, $S(k, \omega)$, calculated using the procedure presented in Dolcetti et al. (2022) and proposed in Dolcetti et al. (2023). All spectra were modulated using a common scaling factor to allow a direct comparison between the different flow conditions and also to improve the visualisation, especially at the higher frequencies.

Following Dolcetti et al. (2022), the dispersion relations for the different types of waves were mathematically described as follows:

- non-dispersive patters (Eq. 4.1):

$$2\pi f(k) = \boldsymbol{k} \cdot \boldsymbol{U_S} \tag{4.1}$$

- gravity-capillary waves (Eq. 4.2, after Lamb (2005), Biesel (1950) and Teixeira and Belcher (2006)):

$$\begin{aligned} 2\pi f(\boldsymbol{k}, \boldsymbol{U_S}, D) = {} & [1 - \beta(k, D)]\boldsymbol{k} \cdot \boldsymbol{U_S} \pm \\ & \pm \left\{ \Big[\beta(k, D)\boldsymbol{k} \cdot \boldsymbol{U_S}\Big]^2 + \left[k\left(gD\frac{(1+B)}{B}\frac{\tanh(kD)}{kD}\right)^{1/2}\right]^2 \right\}^{1/2} \end{aligned} \tag{4.2}$$

  where $B = \rho g/(k^2 T)$ is the Bond Number and β is defined as:

$$\beta(k, D) = \frac{(1 - U_{rat})\tanh(kD)}{kD} \tag{4.3}$$

Dolcetti et al. (2022) explained the choice of not using Equation 2.6 and instead opting in favour of Equation 4.2 as the former is applicable when the wave propagation occurs over a flow with constant velocity profiles, while the latter is valid for velocity fields with a linear velocity profile. Dispersion relations derived from more complex but more representative velocity profiles were deemed less suitable for this analysis as they lead to implicit formulations.

Furthermore, as there is not a consensus about the advection velocity of non-dispersive waves (i.e. these waves are suggested to advect with a velocity between the depth-averaged and the free-surface velocities), an ancillary dispersion relation was proposed for this form of patterns. Equation 4.4 is analogous to Equation 4.1, but replaces the free-surface velocity with the depth-averaged velocity:

$$2\pi f(k) = \boldsymbol{k} \cdot \boldsymbol{\bar{U}_B} \tag{4.4}$$

Finally, modified versions of Equations 4.2 and 4.3 are considered, where the general wavenumber value k has been replaced by the wavenumber of stationary waves k_0. k_0 values were derived using the procedure suggested in Dolcetti et al. (2022). Of course, when the free-surface velocity is below the minimum phase velocity for gravity-capillary waves (i.e. 0.23 m/s), stationary waves cannot form, not even if waves propagate against the flow direction. Table 4.6 reports the estimated values for k_0 for all the flow conditions over the two different beds and slopes that could see the presence of standing waves.

Wavenumber of Stationary Waves, k_0 (rad/m)						
Series	Tests					
	1_S	2_S	3_S	4_S	5_S	6_S
Q	-	119.00	73.79	57.76	42.57	33.15
M	-	136.02	-	62.49	54.08	49.25
A	-	158.30	93.30	64.84	47.70	36.71

Table 4.6: Estimates of the wavenumber of stationary waves, k_0, for different flow conditions.

Streamwise and lateral spectra of representative flow conditions for the "Q", "M" and "A" series are depicted in Figures 4.16, 4.17 and 4.18, respectively.

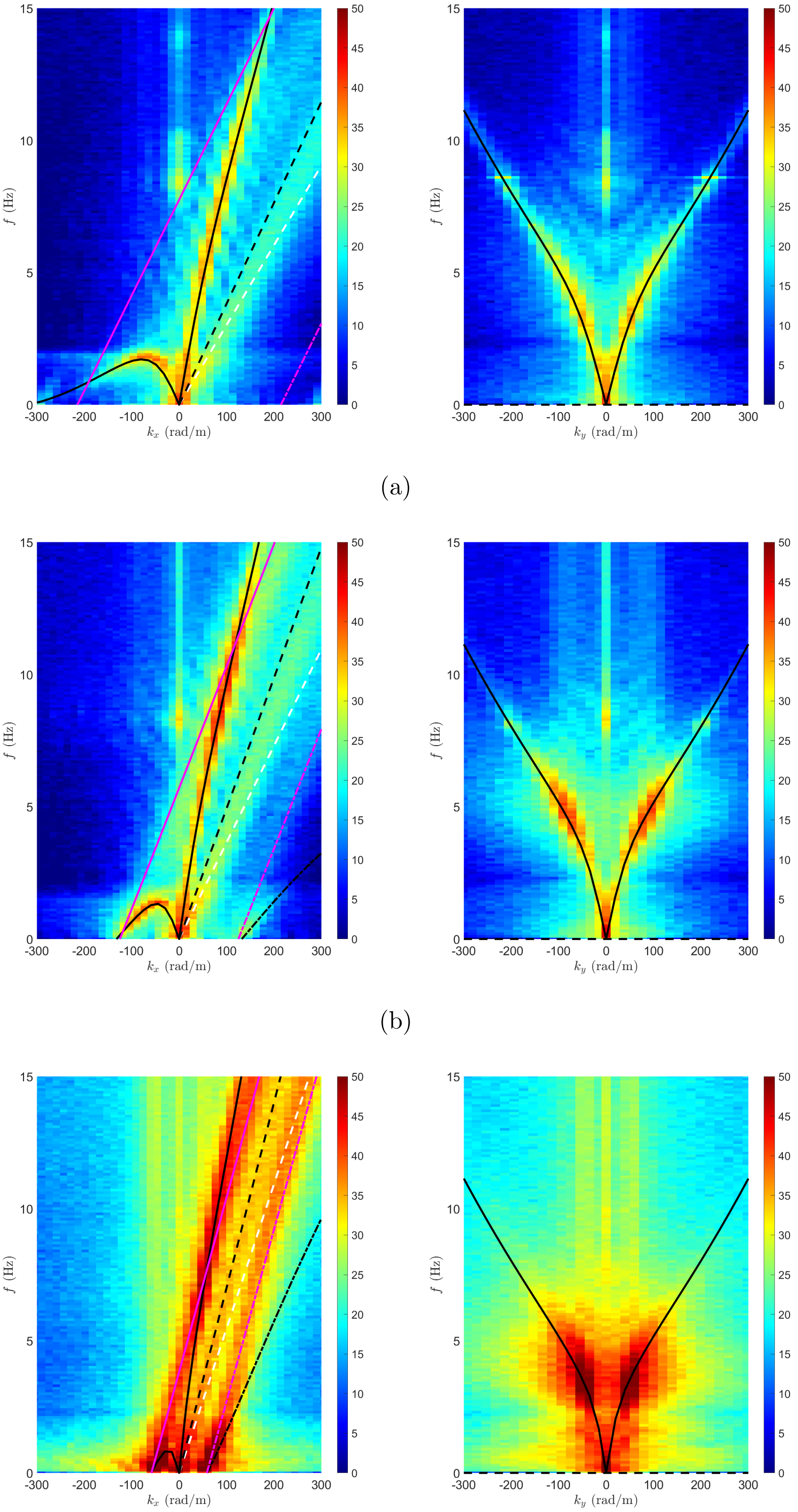

(a)

(b)

(c)

Figure 4.16: Streamwise (left) and lateral (right) frequency-wavenumber spectra for tests of the "Q" series: a) Q1_S, b) Q2_S and c) Q4_S. Black lines: dashed is for non-dispersive patterns with U_S (Eq. 4.1), solid and dashed-dotted indicate the positive and negative solutions for gravity-capillary waves (Eq. 4.2). White-dashed line: non-dispersive patterns with $\bar{U}_B$ (Eq. 4.3). Magenta lines: solid and dashed-dotted are the positive and negative solutions for gravity-capillary waves with k_0 as wavenumber (modified Eq. 4.2).

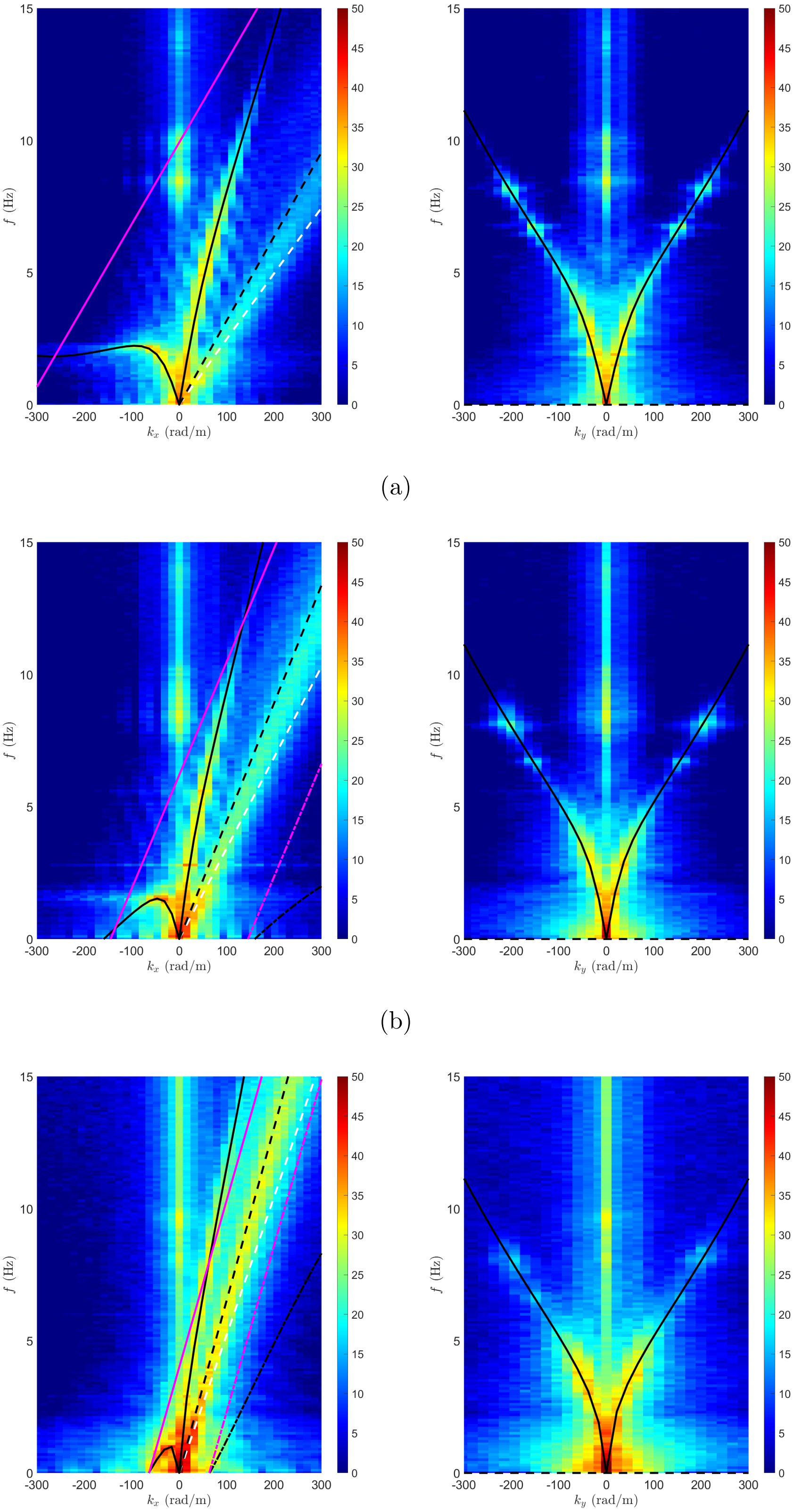

(a)

(b)

(c)

Figure 4.17: Streamwise (left) and lateral (right) frequency-wavenumber spectra for tests of the "M" series: a) M1_S, b) M2_S and c) M4_S. Black lines: dashed is for non-dispersive patterns with U_S (Eq. 4.1), solid and dashed-dotted indicate the positive and negative solutions for gravity-capillary waves (Eq. 4.2). White-dashed line: non-dispersive patterns with $\bar{U}_B$ (Eq. 4.3). Magenta lines: solid and dashed-dotted are the positive and negative solutions for gravity-capillary waves with k_0 as wavenumber (modified Eq. 4.2).

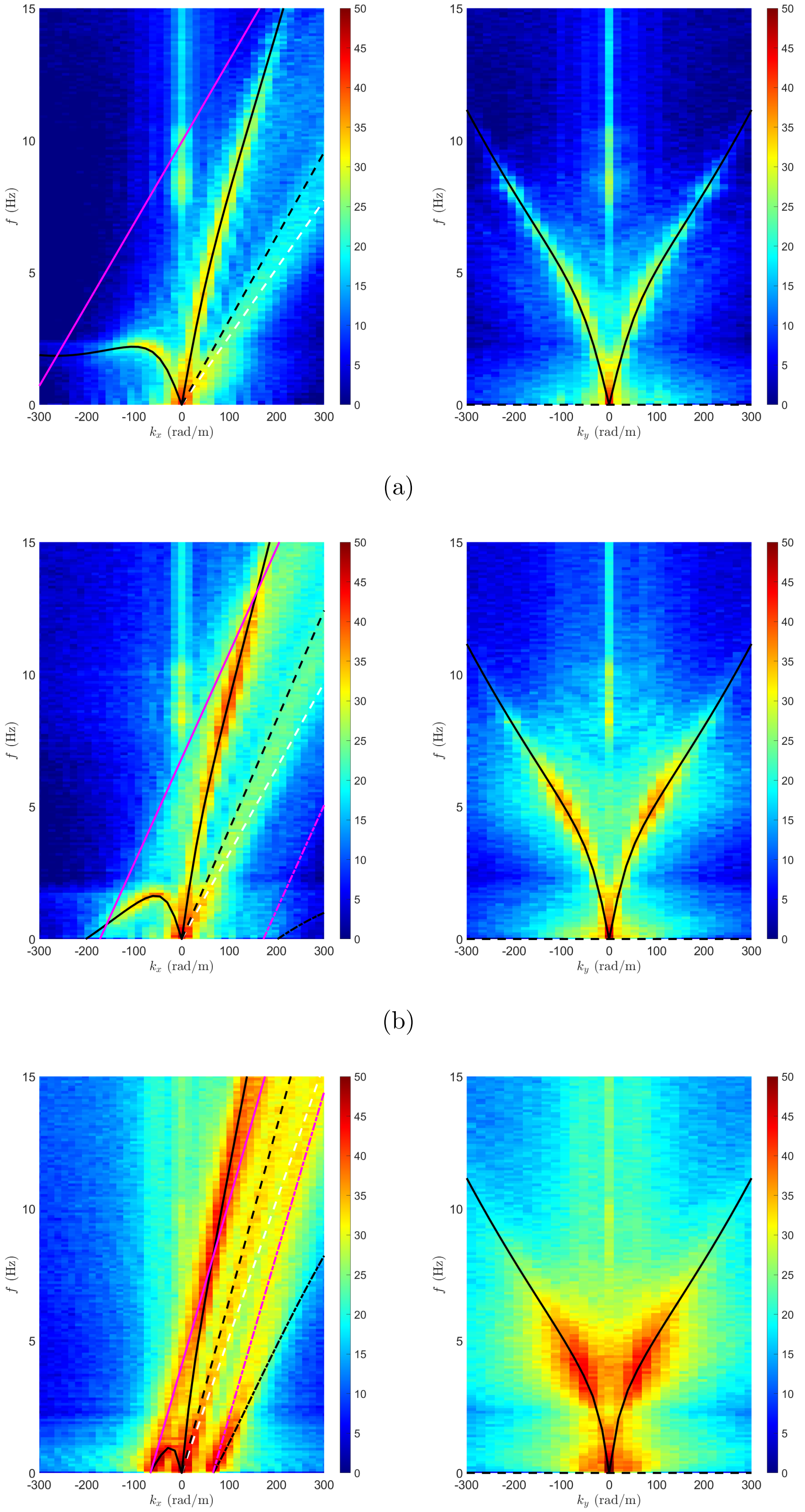

(a)

(b)

(c)

Figure 4.18: Streamwise (left) and lateral (right) frequency-wavenumber spectra for tests of the "A" series: a) A1_S, b) A2_S and c) A4_S. Black lines: dashed is for non-dispersive patterns with U_S (Eq. 4.1), solid and dashed-dotted indicate the positive and negative solutions for gravity-capillary waves (Eq. 4.2). White-dashed line: non-dispersive patterns with $\bar{U}_B$ (Eq. 4.3). Magenta lines: solid and dashed-dotted are the positive and negative solutions for gravity-capillary waves with k_0 as wavenumber (modified Eq. 4.2).

Flow conditions following in Class I ($\bar{U}_B$ & $U_S < 0.23$ m/s)

For flow regimes belonging to Class I (Figs. 4.16a, 4.17a and 4.18a), stationary waves cannot form as the minimum phase velocity for gravity-capillary waves is 0.23 m/s, while here the free-surface velocity is below this threshold value. This means that even the fastest waves propagating against the flow are not fast enough to disperse upstream. Indeed, no evidence of the presence of stationary waves can be seen and only two types of wave patterns exist for this class of flow conditions: gravity-capillary waves and non-dispersive patterns.

Both the upstream and downstream ridges of the dispersive patterns are well fitted by the positive solution of Equation 4.2 that corresponds to classic gravity-capillary waves. The negative solution cannot be observed for this class of flow conditions as it would require an intrinsic wave celerity lower than 0.23 m/s for appearing which is clearly not physically possible.
The non-dispersive ridge results lying between Equations 4.1 and 4.4, but more in favour of the latter dispersion relation. This suggests that for this flow regime the non-dispersive patterns advect downstream with a velocity that is closer to the depth-averaged velocity than the free-surface one.
For Class I conditions standard gravity-capillary waves appear to dominate the free surface as they possess higher levels of spectral energy than non-dispersive patterns. This behaviour is common to all the tests regardless of the series, suggesting that slope and bed texture arrangement do not have an influence on the free-surface dynamics.

As spectra were scaled based on a common factor, a direct comparison between the different series of tests can be advanced. Less spectral energy is contained along the ridges for test M1_S (i.e. slope of 1/1000) than for test A1_S, indicating more limited surface agitation for the former experiment.

The decay of the spectral signatures appears to be different based on the type of wave and seems to be lower for the non-dispersive patterns for gravity-capillary waves. In fact, non-dispersive waves are seen to persist at higher wavenumbers than gravity-capillary waves. For the latter type of waves, the spectral signature decay for wavenumbers above |100| rad/m (i.e. wavelength shorter than 6.3 cm) for M1_S, while this occurs around $k = \pm 150$ rad/m ($\lambda = 4.2$ cm) for A1_S.

The lateral frequency-wavenumber spectra show standard gravity-capillary waves propagating along the lateral direction. As observed in the streamwise frequency-wavenumber spectra, most of the spectral energy is contained withing the smaller wavenumbers. Spectral energy appears to be slightly more concentrated in three locations, one of which is at $k = 0$ rad/m and $f = 0$ rad/s, indicating stationary waves.

Class II flow regimes ($\bar{U}_B < 0.23$ m/s & $U_S > 0.23$ m/s)

Characteristics of flow conditions in Class II (Figs. 4.16b, 4.17b and 4.18b) theoretically allow the presence of stationary waves. However, despite the free-surface velocity being above 0.23 m/s, stationary waves and gravity-capillary waves with k_0 as a wavenumber cannot be observed. As a consequence, these flow regimes show a behaviour resembles to the conditions belonging in

Class I with gravity-capillary waves and non-dispersive patterns populating the free surface.

The dispersive ridges are once again well described by positive solution of Equation 4.2. Furthermore, as conditions for existence are met, the negative solution is observable in the spectra, even weakly.
The non-dispersive ridge lies again between Equations 4.1 and 4.4, but this time is more inclined towards Equation 4.1, suggesting an advection for this type of patterns closer to the free-surface velocity than to the depth-averaged one.

Standard gravity-capillary waves appear to dominate the free surface also for this Class of tests as it is evident from the higher spectral energies contained along these ridges than along non-dispersive patterns.

Tests belonging to the "M" series are again characterised by a lower spectral energy when compared with the other series ("Q" and "A") which were collected over different beds both with a steeper 1/500 slope. This means a smaller surface agitation than for tests of the "Q" and "A" series.
A trend in the decay of the spectral ridges similar to one for Class I is also seen for Class II with the ridge of non-dispersive patterns decaying slower than the ones for gravity-capillary waves.

Similarly to the case in Class I, also here the lateral frequency-wavenumber spectra see the presence of standard gravity-capillary waves. Again, three different spots of particularly high concentration of spectral energy can be noticed, one of which belongs to stationary waves.

Flow conditions in Class III ($\bar{U}_B$ & $U_S > 0.23$ m/s)

Experiments falling in Class III (Figs. 4.16c, 4.17c and 4.18c) are more difficult to describe, mainly because, differently for the other classes, a common trend in the behaviour of the free-surface between the tests belonging to the "Q" and "A" series and the ones of "M" series cannot be observed. In fact, tests of the "Q" and "A" series show the presence of non-dispersive patterns, gravity-capillary waves, stationary waves and gravity-capillary waves with k_0 as a wavenumber, while for tests of the "M" gravity-capillary waves with k_0 as a wavenumber appear to not exist.

The positive solution of the dispersion relation for standard gravity-capillary waves describes well the ridges. At higher wavenumbers, however, the curves diverge more and more from the spectral signatures, this is particularly evident for the negative solution of Equation 4.2.
Gravity-capillary waves with k_0 as a wavenumber are seen to exist in parallel with the standard gravity-capillary waves. These waves also fit particularly well the dispersive ridges at higher wavenumber where Equation 4.2 diverges.
Non-dispersive patterns appear to be progressively more and more well described by Equation 4.1 as the flow rate increases.
For this class of flow conditions gravity-capillary waves and gravity-capillary waves with k_0 as a wavenumber (when the latter exists) appear to dominate over the non-dispersive patterns at all frequencies.

In line with other classes, test of the "M" series are also characterised by a lower spectral energy, suggesting a less dynamic water surface for similar depth-averaged and free-surface velocities than tests over a 1/500 slope.

Gravity-capillary waves and non-dispersive patterns have spectral decays that follow the same trend of the other classes. Gravity-capillary waves with k_0 as a wavenumber instead decay at much slower rate than normal dispersive waves, with a rate that appears to be similar as the non-dispersive patterns' one.

Lateral spectra show the presence of standard gravity-capillary waves. Three points of concentrations of spectral energy can once again be noticed. Their energy content results much higher than the rest of the ridge.

The same free-surface behaviour is observed for all the other flow conditions that can be categorised in this Class and are not shown here.

General Discussion

The present study presents the frequency-wavenumber spectra of the free-surface elevation field for different flow conditions over two different but similar bed arrangements and two slopes.

Similar behaviours can be observed between the spectra of the "Q" and "A" bed arrangements for flow conditions belonging to the same Class, suggesting that the free-surface behaviour is not influenced by the orientation of the bed spheres. This finds agreement with Nikora et al. (2001) which suggests the bed influences the flow hydrodynamics for a limited range above the bed.

Differences, however, can be appreciated in the spectra of Class III conditions when the effect of slope is considered. In fact, gravity-capillary with k_0 as a wavenumber can be observed dominating the air-water interface when the slope is 1/500 ("Q" and "A" series), but not when the slope is 1/1000 ("M" series) where they cannot even be seen. The phenomenon is particularly puzzling and a clear and definitive motivation on this regard cannot be proposed. Nonetheless, a hypothesis can be advanced based on Dolcetti and García Nava (2019b). Dolcetti and García Nava (2019b) invoked the triad resonance mechanism suggested by Zakharov and Shrira (1990) as a possible mechanism responsible behind the nature of gravity-capillary waves with k_0 as a wavenumber. According to this phenomenon, stationary waves are able to mediate the transfer of energy between turbulence modes and dispersive waves, favouring the selective growth of waves not oriented against the flow whose scale and velocity match the wavenumber k_0. Similarly to Dolcetti and García Nava (2019b), some of the conditions required by the theory of Zakharov and Shrira (1990) cannot be rigorously satisfied in this study, nonetheless, it is proposed that the absence of gravity-capillary waves with k_0 as a wavenumber from the Class III flow conditions of the "M" series is due to the energy exchanges provided by the triad resonance mechanism, or better, from the absence of such transfers. In fact, limited contents of energy can be seen in the spectra of the "M" series tests. As the energy levels are low, stationary waves cannot mediate the transfer and lead to the appearance of gravity-capillary waves with $k = k_0$. The absence of gravity-capillary waves with k_0 as a wavenumber is therefore motivated by the limited surface agitation that characterises the entire "M" series.

With consideration to the proposed explanation for the anomalous behaviour of the "M" series, two different free-surface behaviours are proposed and see the dominance of either gravity-capillary waves or gravity-capillary waves with wavenumber $k = k_0$. When the depth-average velocity is below 0.23 m/s, the air-water interface is dominated by gravity-capillary waves, while when $U_B > 0.23$ m/s gravity-capillary waves with k_0 as a wavenumber are the dominating patterns. On this matter, it is important to stress that the dominance of one type of waves does not imply the absence of other forms of waves, but rather the outclassing of one particular type of waves over the others. In fact, non-dispersive patterns or non-dispersive patterns and standard gravity-capillary waves coexist together with the dominating wave types according to the different free-surface behaviour.

The factor that is indicated as responsible for the transition from one behaviour to the other one is the depth-averaged velocity, U_B, triggering the transit when equal to 0.23 m/s. This appears clear when comparing flow regimes belonging to Classes I and II (e.g conditions A1_S and A2_S) which both have a bulk velocity below 0.23 m/s. Different frequency-wavenumber spectra can instead be noticed when looking at flow conditions in Classes II and III, both characterised by a surface velocity above 0.23 m/s. This appears to be quite counterintuitive as the minimum phase velocity for gravity-capillary waves is 0.23 m/s, so such a type of wave should appear stationary as long as it propagates against the flow direction. Therefore, the surface velocity U_S and not U_B should dictate the transition from one behaviour to the other one. A possible explanation for this anomaly relies on the way the stationary waves occur and the lateral non-uniformity of the free-surface velocity. The free surface is known to be populated by high and low speed streaks due to the action of secondary currents (Nakagawa & Nezu, 1981; Nezu et al., 1985). As the tests were characterised by a surface velocity slightly above 0.23 m/s, some surface regions had velocities lower than this threshold. As a consequence, the required condition to allow the development of stationary waves was not met throughout the free surface. This would suggest that stationary waves can form only when the required conditions (i.e $U_S > 0.23$ m/s) are not locally but instead globally met on the free surface. The depth-averaged velocity was therefore seen to be the parameter that determines which mechanism occurs at the free surface simply because when greater than 0.23 m/s it allowed to satisfy the global condition at the free surface and so the appearance of stationary waves.

To the author's knowledge, Dolcetti et al. (2016) is the only study that evaluated the free-surface dynamics of a flow condition belonging to Class I. The study, however, was aimed at identifying the different types of waves that populate the free surface. Flow conditions in Class III were typically tested in Dolcetti et al. (2016) and a single experiment belonging to Class I was performed in order to allow a comparison between tests with surface velocity above and below 0.23 m/s. What they found was that the free surface of the condition in Class I was populated by non-dispersive waves and standard gravity-capillary waves, in agreement with the finding of the present study.

Agreement with Dolcetti et al. (2016) can also be found for flow regimes following in Class III. In fact, dominance of gravity-capillary waves with k_0 as a wavenumber can be seen, while standard gravity-capillary waves and non-dispersive patterns are also present but with a lower spectral energy content. However, Dolcetti et al. (2016) did not observed a different behaviour for flow conditions over the 1/1000 slope as it is for the present study.

Savelsberg and Van De Water (2009) reported the dominance of gravity-capillary and the presence of non-dispersive patterns advecting with a velocity close to the depth-averaged one. However, no sight of stationary waves and gravity-capillary waves with k_0 as a wavenumber was reported, even when conditions that can be framed in Class III were tested. Several conjectures that might justify this behaviour can be proposed. Stationary waves can also be related to bed topography (Harband, 1976; Dolcetti et al., 2016), but Savelsberg and Van De Water (2009) ran their tests over a smooth bed surface. Furthermore, turbulence was generated by means of active grids not by instabilities in the boundary layer near the rough bed as observed in river flows. The absence of a rough bed and the peculiarity of grid-generated turbulence might have prevented triad resonance from occurring. Another possible reason could be the spatially limited range of the technique they used to evaluate the free surface which did not allow to observe standing waves. The experimental rig was also small in dimensions, this could have prevented the longer wavelength waves from forming as there were not sufficiently large turbulent features from which inherit the scale.

The dominance of non-dispersive waves does not also occur. While non-dispersive patterns are clearly seen for all the classes of flow conditions, they are never the most relevant type of waves. Nichols et al. (2016) proposed a model that suggests that this type of patterns has an oscillatory behaviour and follows an underdamped simple harmonic motion. The model also defines a characteristic frequency of oscillation of the surface features, f_{shm}, based on the observed characteristic spatial period of the correlation function of the free surface. If this model was correct, a particularly high concentration of energy would be observed in correspondence of f_{shm}. However, a spike does not occurs in the spectra along the ridge belonging to the non-dispersive patterns in any of the tests.

Lateral spectra clearly show the presence of standard gravity-capillary waves in all the tests, regardless of the Class of flow. Here, three spots of particularly high levels of spectral energy can be observed. One spot occurs at $k = 0$ rad/m and $f = 0$ rad/s, clearly indicating stationary waves. The other two spots occur symmetrically respect with $k = 0$ rad/m and share the same frequency. Wavenumber and frequency at which the concentrations occur with $k \neq 0$ occur change from one flow condition to another. In some cases their frequency is close to the frequency f_{shm} predicted by model by Nichols et al. (2016). The matching, however, is more occasional rather than being consistent for all the conditions, suggesting that the model by Nichols et al. (2016) is not verified for the flow regimes tested here.

4.4.2 Remote Estimation of Flow Parameters

The k-ω algorithm presented in Dolcetti et al. (2023) was designed with the intent of remotely estimating depth and surface velocity of a flow using the images of its free surface. The method initially derives the free-surface elevation field from the light shimmering intensities observed on the surface of a stream and later calculates the frequency-wavenumber spectra. Depth and free-surface velocity are finally derived by maximising the fitting of the dispersion relations of the wave patterns with the observed 3D frequency-wavenumber spectra.

The k-ω algorithm was used with DIC data to test a remote estimation technique of key flow parameters. Measured quantities were not used to constrain the model in order to evaluate the goodness of the recovery routine for a scenario where these parameters are unknown, something that can occur in field observations. Free-surface images were not used as inputs but rather the free-surface elevation field derived using the DIC. The algorithm was initialised using the following parameters:

- depth-averaged/surface velocities ratio: 0.785
- segment duration: 10 s
- search range for the streamwise surface velocity, U_S: 0.1-0.7 m/s
- search range for the spanwise surface velocity, V_S: -0.05-0.05 m/s
- search range for depth: 0.01-0.15 m
- maximum number of iterations: 2

Observed depths and streamwise free-surface velocities, the recovered counterparts, D_{Rec} and $U_{S,Rec}$, respectively, as well as percentage variations between observed and recovered depth, Var_D, and percentage variations between observed and recovered streamwise free-surface velocity, Var_{U_S}, are reported in Table 4.7.

Recovered Flow Characteristics from DIC Surface Data							
Series	Test	D (mm)	U_S (m/s)	D_{Rec} (mm)	$U_{S,Rec}$ (m/s)	Var_D (%)	Var_{U_S} (%)
Q	1_S	20.6	0.24	28.5	0.23	38.3	-3.1
	2_S	30.6	0.31	45.5	0.30	48.7	-4.5
	3_S	46.8	0.39	37.6	0.40	-19.7	2.4
	4_S	61.4	0.44	35.6	0.50	-42.0	13.6
	5_S	76.5	0.51	48.7	0.61	-36.4	19.6
	6_S	91.9	0.58	49.8	0.65	-45.8	12.5
M	1_S	26.0	0.20	34.4	0.19	32.2	-3.0
	2_S	42.7	0.28	150.0	0.26	251.3	-5.7
	3_S	-	-	-	-	-	-
	4_S	97.4	0.41	107.3	0.40	10.2	-2.2
	5_S	112.2	0.44	93.6	0.43	-16.6	-1.6
	6_S	125.3	0.46	75.9	0.44	-39.4	-4.1
A	1_S	22.0	0.20	150.0	0.18	581.8	-10.3
	2_S	33.8	0.26	64.6	0.25	91.3	-4.6
	3_S	50.0	0.34	32.4	0.36	-35.1	5.1
	4_S	64.8	0.41	40.1	0.42	-38.1	3.1
	5_S	81.6	0.48	43.0	0.51	-47.3	6.2
	6_S	97.0	0.55	54.6	0.63	-43.7	15.3

Table 4.7: Depths and free-surface velocities recovered using Dolcetti et al. (2023) for DIC. Rows in yellow indicate tests that required two iterations to retrieve the parameters.

The algorithm returned surface velocity $U_{S,Rec}$ values that have an error of 5% or less for most of the cases. In some occasions, however, the error was bigger, up to 19.6% for flow conditions Q5_S. A different trend was instead seen for the recovered depth D_{Rec} as the returned values were consistently affected by an error ranging between 30% and 50%, while extreme positive and negative deviations from the real values occurred for a limited number of cases.

Dolcetti et al. (2023) algorithm relies on minimising a cost function that evaluates the fitting of different dispersion relations to the full 3D frequency-wavenumber spectrum to derive the estimates for depth and surface velocity. In particular, the cost function evaluates which dispersion relation between the one for non-dispersive patterns (Eq. 4.1) and the positive solution for gravity-capillary waves (Eq. 4.2) produces the best matching.

Free-surface spectra (Figs. 4.16, 4.17 and 4.18) reveal that Equations 4.1 and 4.2 are not always suited to describe the spectral signatures.
On the one hand, non-dispersive patterns are shown to advect with a velocity ranging between the depth-averaged and the free-surface velocities. The propagation of this type of waves results to be better described by Equation 4.4 (i.e. propagation proportional to the depth-averaged velocity, U_B) for shallower flow conditions, while Equation 4.1 (i.e. propagation proportional to the free-surface velocity, U_S) seems to work better for deeper flow regimes. The gradual transition between the two Equations seen in the frequency wavenumber plots hints that the shape of the velocity profile could affect the advection of the non-dispersive patterns. Shear profiles in Subsection 4.3.4 reveal the existence of a region in the proximity of the bed surface characterised by limiting shearing. This region is seen to move further and further from the bed as the water depth increases. Depth-averaged velocity, U_B, is, of course, calculated by considering the full depth of the flow, if a new definition of depth-averaged velocity would be used where only the portion of the depth actively sheared is considered, the resulting velocity would increase with the flow rate. This new velocity could be the right candidate for describing the advection of the non-dispersive waves.
On the other hand, while gravity-capillary waves (Eq. 4.2) are present on the spectra, gravity-capillary waves with k_0 as wavenumber also exist and are a better descriptor of the dispersive spectral ridges. Replacing Equation 4.2 with its modified version with k_0, however, is not trivial as the Equation requires the definition of the wavenumber of stationary waves given by Equation 4.2, which is based on different parameters that are the very same targets of the remote sensing technique. Therefore, the algorithm would be required to iterate the routine until convergence (which is not guarantee due to the complexity of the problem).

A further complication that compromises the positive retrieval of flow parameters appears evident when observing the streamwise spectra (e.g. Fig. 4.16) at higher flow rates. It can be noticed that the ridges representing the streamwise components of the dispersion relations tend to merge into a single one, hindering the likelihood to properly fit the dispersion relations to the appropriate spectral signatures. This is particular evident when the spectral wavenumber resolution is not sufficiently high, which occurs when a short FOV is used.
On the opposite, lateral spectra exhibit clearer signatures belonging to the spanwise component of the positive solution for gravity-capillary waves. This would suggest that this spectrum could be a better candidate for determining the depth. However, Dolcetti et al. (2022) showed that depth has limited influence on the lateral spectrum, or better, depth significantly affects only the portion of the lateral spectrum in the neighbourhood around 0 rad/m. This region

belongs to longer waves ($\lambda > 1$ m). The DIC measurements in the tests were characterised by a limited FOV (i.e. limited spectral wavenumber resolution) that prevented the observation of long wavelengths, impeding the algorithm from accurately estimating depth and free-surface velocity at the same time.

The only ridge that results to be highly sensitive to both depth and free-surface velocity and which signature appears clear is the one that represents the positive solution of gravity-capillary waves propagating upstream (Eq. 4.2) in the streamwise frequency-wavenumber spectra. This curve is monotonically crescent with the wavenumber in still water and when the free-surface velocity is particularly low. For most of the practical cases regarding open-channel flows, however, the free-surface velocity tends to be above 0.20 m/s and the dispersion relation presents a maximum. This maximum occurs in the region where the dispersion relation is still affected by depth. Free-surface velocity governs the concavity of the dispersion relation, while the position of the maximum is influenced by both depth and surface velocity. The two flow parameters can therefore be estimated by considering a constrained system formed by Equation 4.2 and its first derivative. A first constrain would aim at maximising the fitting of Equation 4.2 with the spectral ridge, while a second constrain would be a zero value for the derivative of Equation 4.2 at the wavenumber at which the maximum occurs.

However, depending on the spectral wavenumber resolution, it might be difficult to recognise the maximum if the free-surface velocity is too high. For the spectral resolutions of the DIC measurements of this study, the dispersion relation of gravity-capillary waves propagating upstream is no longer clear when $U_S > 0.45$ m/s.

Following all the above observations, an improvement of the algorithm proposed by Dolcetti et al. (2023) might be achieved by:

- initially determining values for depth and free-surface velocity based on the upstream propagating positive solution of gravity-capillary waves (Eq. 4.2).
- refining the value of depth and surface velocity in order to maximise the fitting of the other spectral signatures.

4.5 On the Generation of the Free-surface Waves

The frequency-wavenumber spectra in Section 4.4 revealed the existence of a spatial and temporal form of organisation on the free surface. The phenomena behind the origin of the different types of waves are, however, complex and difficult to determine. The reason for this uncertainty is due to the difficulty of observing the free surface and the underlying flow field at a sufficiently high spatial and temporal resolutions.

To investigate whether a linkage between the surface waves and the flow field exists or not, the same frequency-wavenumber analysis performed on the surface elevation data was also done on the PTV velocity measurements. This choice was made as frequency-wavenumber analysis permitted to identify a form of organisation on the free surface, so the same type of analysis should allow to observe whether the same form of organisation exists in the flow field or not, therefore supporting or rejecting the hypothesis of a linkage between flow field and free surface.

Subsection 4.5.1 presents the frequency-wavenumber spectra of the PTV measurements, while Subsection 4.5.2 investigates how the analysis of the PTV data can be used to study the origins of the different types of surface waves.

4.5.1 Frequency-wavenumber Spectra of PTV Measurements

Time series of streamwise and vertical instantaneous velocities on 5 uniformly spaced planes parallel to the average level of the free surface were extracted from the PTV measured volume. Care was taken to have at least one plane analysed for each flow layer. These planes were:

- the plane immediately below the surface (plane "A"); this plane was deemed more reliable for this analysis that the plane in correspondence of the surface as the latter could have included both air and water during the collected PTV time series.
- plane at three quarters of the depth (plane "B").
- plane at half the depth (plane "C").
- plane at one quarter of the depth (plane "D").
- the plane immediately above the bed level (plane "E"): the planes below occurred in a region where also spheres were present; for this reason, the planes below the spheres' crest were identified as not suited for the analysis.

Instead of attempting a normalisation unique for each case, the derived spectra were all scaled using a common factor, the maximum observed spectral energy content at each frequency for the least spectrally energetic flow condition. This permitted a direct comparison of the spatial and temporal organisation of the streamwise and vertical velocity fluctuations for different flow conditions.

Subsection 4.4.1 revealed that no dissimilarity exists between flow conditions in Class I and Class II in terms of free-surface behaviour. For this reason, only tests representative of Class I and Class III are proposed. Also, it was chosen to present a selection of the planes defined in the above bullet point. These planes are: "A", "C" and "E". Plane "A" was chosen as it is the plane immediately below the water surfaces, therefore, velocity measurements should be affected by presence of the free-surface wave patterns. Plane "C" is considered to be representative of the logarithmic layer. While Nikora et al. (2001) suggests that the logarithmic layer is situated in the lower 20% of the depth, results showed that for this set of experiments the logarithmic layer extended much above, up to 50% of the depth. Plane "E" represents the roughness layer and it should show different patterns compared to the planes above due to the influence exerted by the bed surface.

Streamwise and lateral spectra of the streamwise turbulent velocity for flow condition A1_H (Class I) in correspondence of planes A, C and E are proposed in Figure 4.19, while the spectra of the vertical turbulent velocity for the same condition and planes are reported in Figure 4.20. Streamwise and lateral spectra for the streamwise and vertical velocity fluctuations for condition A4_H (Class III) at planes A, C and E are instead available in Figures 4.21 and 4.22, respectively.

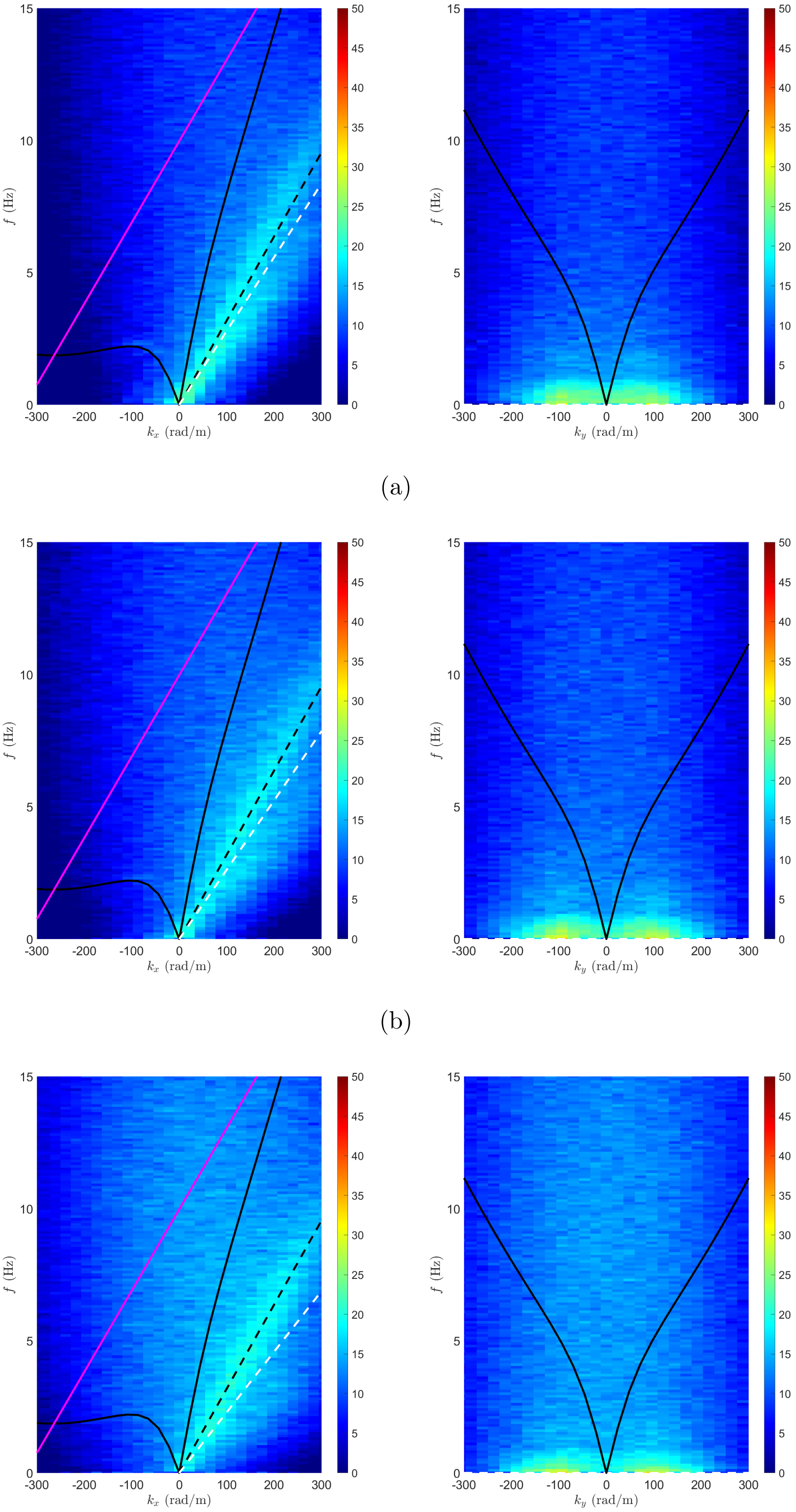

(a)

(b)

(c)

Figure 4.19: Streamwise (left) and lateral (right) frequency-wavenumber spectra of the streamwise turbulent velocity for A1_H at planes a) ”A”, b) ”C” and c) ”E”. Black lines: dashed is for non-dispersive structures advecting at U_S (Eq. 4.1), solid and dashed-dotted are positive and negative solutions for gravity-capillary waves (Eq. 4.2). White-dashed line: structures advecting at $\langle \bar{U} \rangle_{xz,plane_i}$. Magenta lines: solid and dashed-dotted are positive and negative solutions for gravity-capillary waves with $k = k_0$ (modified Eq. 4.2).

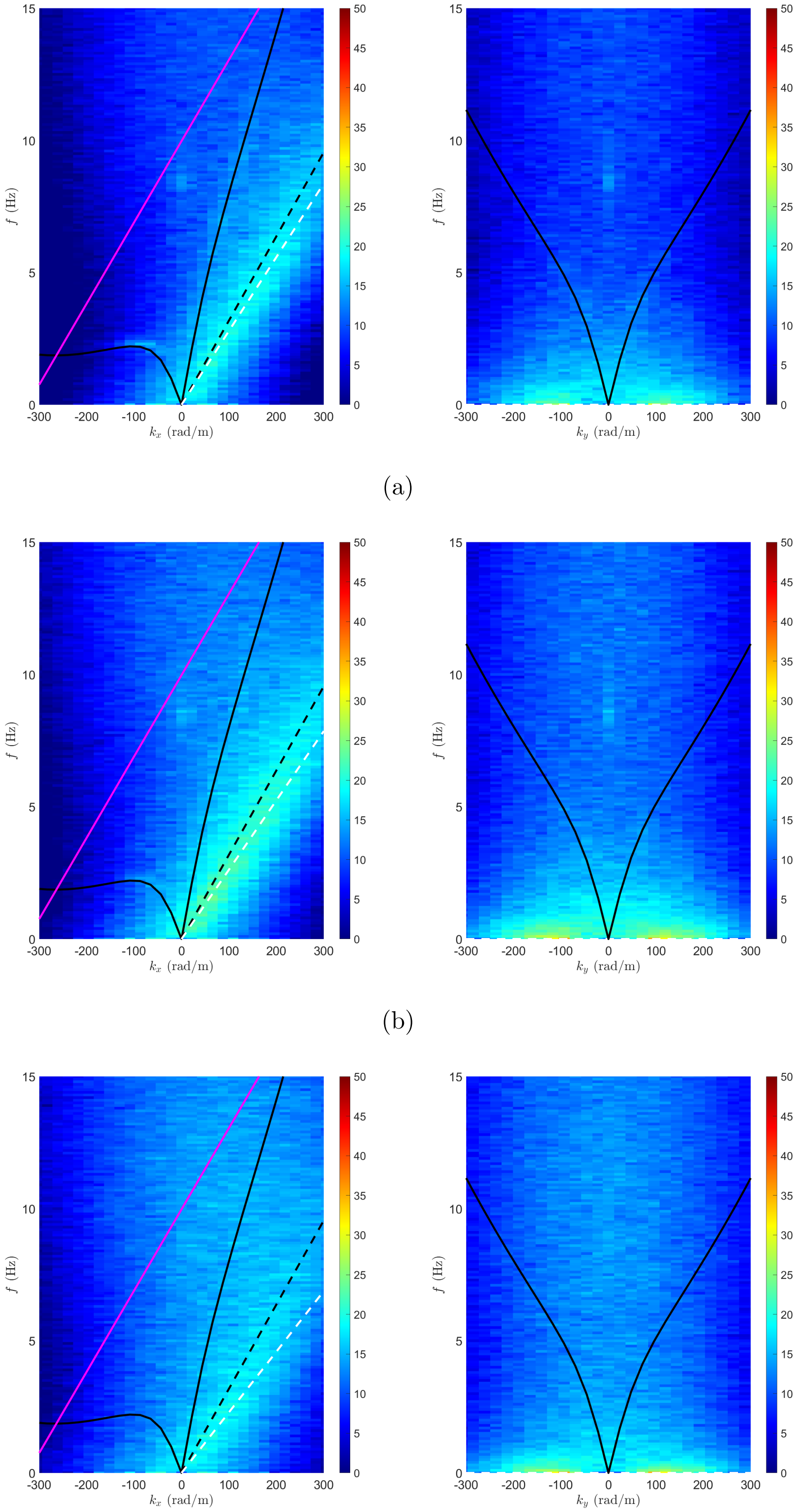

(a)

(b)

(c)

Figure 4.20: Streamwise (left) and lateral (right) frequency-wavenumber spectra of the vertical turbulent velocity for A1_H at planes a) ”A”, b) ”C” and c) ”E”. Black lines: dashed is for non-dispersive structures advecting at U_S (Eq. 4.1), solid and dashed-dotted are positive and negative solutions for gravity-capillary waves (Eq. 4.2). White-dashed line: structures advecting at $\langle \bar{U} \rangle_{xz,plane_i}$. Magenta lines: solid and dashed-dotted are positive and negative solutions for gravity-capillary waves with $k = k_0$ (modified Eq. 4.2).

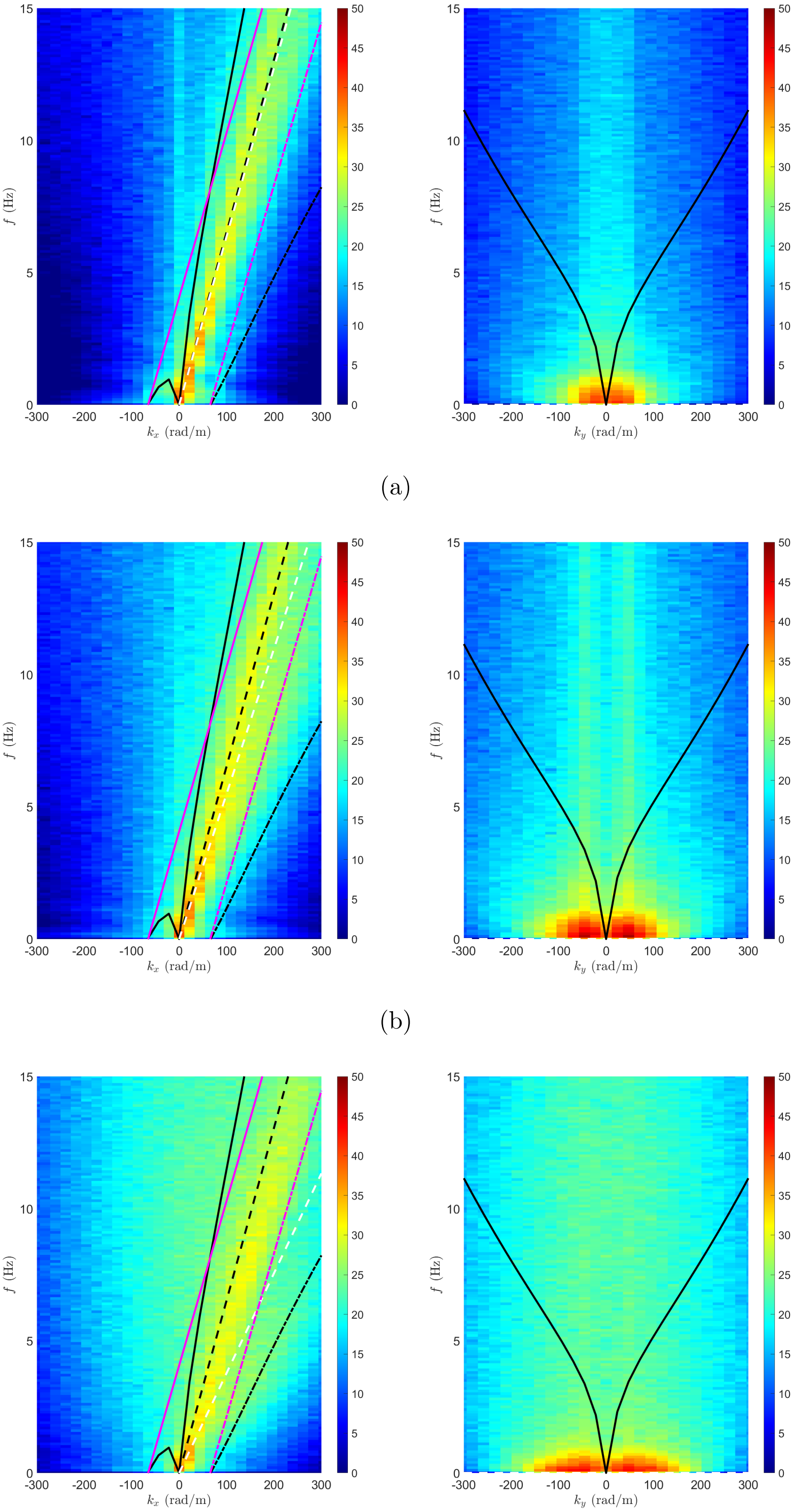

(a)

(b)

(c)

Figure 4.21: Streamwise (left) and lateral (right) frequency-wavenumber spectra of the streamwise turbulent velocity for A4_H at planes a) "A", b) "C" and c) "E". Black lines: dashed is for non-dispersive structures advecting at U_S (Eq. 4.1), solid and dashed-dotted are positive and negative solutions for gravity-capillary waves (Eq. 4.2). White-dashed line: structures advecting at $\langle \bar{U} \rangle_{xz,plane_i}$. Magenta lines: solid and dashed-dotted are positive and negative solutions for gravity-capillary waves with $k = k_0$ (modified Eq. 4.2).

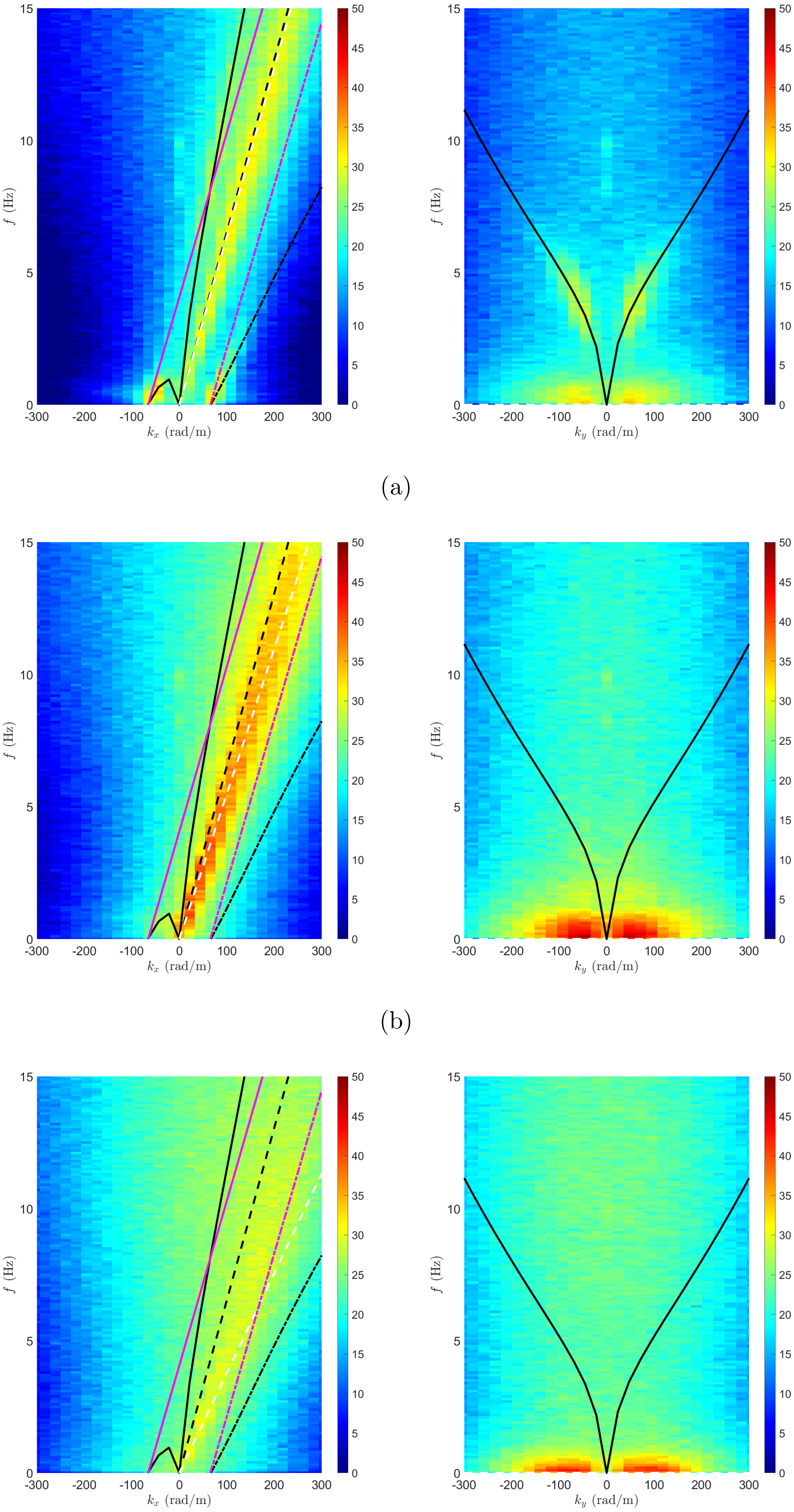

Figure 4.22: Streamwise (left) and lateral (right) frequency-wavenumber spectra of the vertical turbulent velocity for A4_H at planes a) "A", b) "C" and c) "E". Black lines: dashed is for non-dispersive structures advecting at U_S (Eq. 4.1), solid and dashed-dotted are positive and negative solutions for gravity-capillary waves (Eq. 4.2). White-dashed line: structures advecting at $\langle \bar{U} \rangle_{xz,plane_i}$. Magenta lines: solid and dashed-dotted are positive and negative solutions for gravity-capillary waves with $k = k_0$ (modified Eq. 4.2).

Flow conditions following in Class I ($\bar{U}_B$ & $U_S < 0.23$ m/s)

Streamwise frequency-wavenumber spectra of both streamwise and vertical turbulent velocity fluctuations reveal the existence of a single ridge directed in the same direction of the flow. The slope of this ridge, indicating the direction and the velocity at which the turbulent structures are advected, clearly shows that the structures move downstream with a velocity that decreases slightly as the bed is approached. This makes sense as in line with the streamwise velocity profile. However, particular notice has to be paid at the value of velocity observed by the turbulent structures at different depths. In fact, the ridge describing the streamwise turbulent component appears to be better described by the non-dispersive line with U_S (Eq. 4.1) rather than with the local bulk velocity $\langle \bar{U} \rangle_{xz,plane_i}$ (i.e. time, stream- and spanwise-averaged velocity evaluated at the specific plane that is being analysed in the spectra). This would suggest that the streamwise fluctuations advect at a higher speed than the local bulk velocity. On contrary, the vertical turbulent component ridge appears to be well represented by the non-dispersive relation with $\langle \bar{U} \rangle_{xz,plane_i}$, suggesting that the vertical fluctuations are transported downstream at the local bulk velocity.

Energy in the spectra of the streamwise fluctuations decreases with the wavenumber, hence larger structures are promoted. Also the spectral energy diminishes towards the bed. More spectral energy can instead be observed in the spectra of the vertical fluctuations than for the streamwise fluctuations. However, differently the energy initially increases while moving away from the free surface and later decreases in line with the spectra of the streamwise fluctuations. The energy drop in correspondence of the air-water interface can be associated with the presence of the blockage layer that limits the vertical fluctuations and forces the redistribution of energy from the vertical component to the others.

Lateral frequency-wavenumber spectra show high concentrations of energy specularly positioned respect with $k = 0$ rad/m and at $f = 0$ rad/s. These non-propagating elements are suggested to be the manifestation of the secondary currents. The drift that can be observed in the location of the concentration points while moving towards the bed reflects the shape of the secondary cells. These elements do not have the same form throughout the water depth, but appear to shrink as they approach the free surface.

Flow conditions in Class III ($\bar{U}_B$ & $U_S \geq 0.23$ m/s)

Streamwise and lateral frequency-wavenumber spectra of both streamwise and vertical turbulent velocity components reveal the existence of two distinct types of patterns, one that is dispersive and the other one that is non-dispersive.

The dispersive pattern results well described by Equation 4.2 which is the dispersion relation for standard gravity-capillary waves. This pattern is particularly evident in the vertical turbulent component spectra. However, the dispersive signature is weaker compared to the non-dispersive one and only affects the region of the flow field in proximity of the free surface. It is suggested that these dispersive ridges represent the modulation that gravity-capillary waves impose on the underlying hydrodynamics. This is also confirmed by the limited extent of the affected region as the modulation effect exponentially decreases while proceeding deeper. Similar considerations made for the non-dispersive ridge of the flow regimes in Class I can also be advanced for flow conditions in Class III.

Particular concentrations of spectral energy can be observed in correspondence of the wavenumber of stationary waves along the $f = 0$ axis which represents stationary features. Features that can be related to normal gravity-capillary waves are also present but they have weak signatures.

General Commentary

Examination of the frequency-wavenumber spectra of both streamwise and vertical velocity fluctuations revealed the presence of different types of patterns according to the flow condition. Flows belonging to Class I see the presence of a non-dispersive ridge advecting downstream, while flow regimes in Class II (not shown) and Class III present both non-dispersive and dispersive patterns.

Dispersive patterns are only present on the most superficial planes and are weaker and weaker as the distance from the interface increases. These two facts suggest that these ridges depict the modulating effect that the free-surface waves exercise on the underlying flow field. Equation 4.2, describing the dispersion of standard gravity-capillary waves, describes particularly well the dispersive ridges. This is contrary to what is observed in the frequency-wavenumber spectra of the free-surface elevation field where gravity-capillary waves with k_0 as a wavenumber dominate. Dispersive structures with $k = k_0$ can be seen in the spectra of the velocity fluctuations but only at particularly high energetic conditions. However, concentrations of spectral energy can be noticed in correspondence of $k = \pm k_0$ along the $f = 0$ axis only when the depth-averaged velocity U_B is above 0.23 m/s, hence for flow regimes of Class III only.

The non-dispersive ridge appears to behave differently depending on the velocity fluctuation component that is examined. Streamwise fluctuations advect downstream with a velocity that is between the free-surface and local bulk velocities. This trend is consistent throughout the depth and valid for all flow conditions. Vertical fluctuations instead appear to move with a velocity that is close to the local bulk velocity $\langle \bar{U} \rangle_{xz,plane_i}$. This finding suggests that the turbulent velocity components "propagate" at different velocities. At higher wavenumbers, however, the non-dispersive ridge appears to deviate for the linear behaviour and increase their propagation velocity. This behaviour could be induced by the shear that makes the turbulent structures faster and affects the smaller structures in particular.

Spectral energy content decreases with the wavenumber and moving away from the air-water interface. The vertical velocity fluctuation, however, has an initial increment in the spectral energy content below the free surface. This mitigation occurring just below the free surface is caused by a "blockage layer" that limits the vertical fluctuations and promote the other two components.

Lateral spectra show energy concentrations along the frequency axis which are suggested to be the result of secondary currents. As the position of the concentration points are not static while moving towards the bed, it is thought that the shape of the secondary cell is not squared/rectangular, but has a more complex form as they shrink towards the free surface.

4.5.2 Origins of the Surface Wave Patterns

Several hypotheses have been advanced regarding the origin of the free-surface wave patterns, all lacking evidences. This was mainly caused by the difficulty in the observation of the free surface and the underlying flow field at a sufficiently high spatial and temporal resolutions. Frequency-wavenumber spectra of both PTV and DIC measurements have permitted the improvement in the understanding of how the free surface and the flow field interact.

Two motivations regarding the origin of non-dispersive patterns have been proposed:

- coherent structures that are generated in the near-bed region and that rise and impinge on the air-water interface, setting it on motion
- non-resonance phenomena with turbulence

The interaction between coherent structures and free surface has been reported by several experimental studies (Komori et al., 1989; Gharib & Weigand, 1996; Rashidi, 1997; Kumar et al., 1998; Freeze et al., 2003; Smolentsev & Miraghaie, 2005; Fujita et al., 2011; Nichols, 2013). A model that explains the mechanism has also been proposed by Nichols et al. (2016). If the hypothesis was correct, it would be possible to relate scales and generation frequency of coherent structures to the non-dispersive signature in the frequency-wavenumber spectra. Coherent structures are the natural evolution of near-bed bursts that originate from the disintegration of streaks induced by shear. Nezu and Nakagawa (1993) proposed a value for the frequency of generation of near-bed bursts based on the characteristics of flow. This value, however, does not correspond to the frequency of generation of coherent structures as not all the burst manage to evolve into coherent structures. This is confirmed by Grass (1971) who found that only the most energetic elements succeed in crossing the turbulent boundary layer and reaching the free surface. Following Nichols et al. (2016) and Nikora and Goring (2000), it appears that between 30% and 60% of the bursts manage to become coherent structure. However, neither the frequency-wavenumber spectra of the DIC nor the ones of the PTV measurements show particular concentrations of energy at this frequency along the non-dispersive ridge. On contrary, the energy content of the ridges has a monotonic decrease, suggesting that excitation occurs at different scales.

The mechanism of turbulence interaction proposed by Teixeira and Belcher (2006) appears more likely to be the reason behind the generation of the non-dispersive patterns. According to the model, these patterns should advect at the same speed of the features that generated them. Indeed, the non-dispersive ridge of the free-surface spectra was found to match the non-dispersive advecting ridge of the turbulence components in the flow field.

It is therefore suggested that the mechanism suggested by Teixeira and Belcher (2006) is the one mainly responsible for the appearance of the non-dispersive patterns. Together with these waves, non-dispersive patterns originated by the interaction of coherent structures with the free surface might coexist.

Different hypotheses also on the generation of standard gravity-capillary waves have been proposed:

- perturbation by coherent structures
- resonant growth

More puzzling is to find an explanation for the existence of standard gravity-capillary waves. The theories supporting the idea of resonant growth are based on the assumption that the free-surface velocity is equal of above 0.23 m/s. In fact, to allow the birth of a resonating wave having celerity equal to 0.23 m/s, the flow must observe at some point along the water column a velocity value that produces a relative velocity with the free surface equal or above 0.23 m/s. This position is known as critical depth layer. Standard gravity-capillary waves, however, are observed to exist also when U_S is below the minimum phase velocity. This fact obviously contradicts the resonant growth theories.

Any requirement related to the surface velocity can be dropped if gravity-capillary waves are thought to be generated as a consequence of the perturbation of the free surface by means of the non-dispersive patterns (Teixeira & Belcher, 2006; Nichols et al., 2016). This hypothesis, however, cannot explain the energy contents observed along the different ridges in the spectra. If gravity-capillary waves were to be the result of the perturbation caused by turbulent-induced waves, lower or equal levels of spectral energy would be expected along the dispersive ridge than along the non-dispersive one. However, the opposite is observed as standard gravity-capillary waves result more important than the non-dispersive features for all the Class of flow conditions. These waves appear to modulate the underlying hydrodynamics at higher regimes (Class III) as shown by the PTV frequency-wavenumber spectra. This influence, however, is limited to the upper layers.

The existence of stationary waves and freely propagating gravity-capillary waves with k_0 as a wavenumber has been proposed by Dolcetti et al. (2016). This experimental study finds agreement with Dolcetti et al. (2016) as the highest spectral energy concentrations were observed in correspondence of $-k_0$ corresponding to gravity-capillary waves with wavenumber k_0 propagating upstream at the free-surface velocity, hence appearing stationary. Other high concentrations of spectral energy were found along ridges that were fitted well by Equation 4.2 with k_0 as a wavenumber. These waves were generated as a result of the triad resonance mechanism.

Differently from other flow conditions, no gravity-capillary waves with $k = k_0$ were observed for tests belonging to the "M" series. It is supposed that the absence was caused by the limited surface agitation and prevented the triad resonance mechanism from developing gravity-capillary waves with wavenumber $-k_0$.

Chapter 5

Conclusions

5.1 Introduction

Both international and national committees agree that climate change is affecting and will continue to affect the environment and human society in an unprecedented manner. The changes in the water cycle manifest as more intense and frequent downpours which can generate violent flash floods. In order to create effective countermeasures to these erratic phenomena, the characteristics of the fluvial network must be correctly monitored and defined. Surveys, however, are time consuming and not always possible during periods of high flow. For these reasons, research is now focusing on determining the flow and topological characteristics of streams using remote sensing techniques (Cooper et al., 2006; Savelsberg et al., 2006; Fujita et al., 2007; Nichols, 2013; Krynkin et al., 2014; Dolcetti, 2016; Legleiter et al., 2017; Dolcetti et al., 2022). These methods make use of the free-surface wave patterns and empirical relations to infer the desired characteristics.

A clear understanding of the linkage between free-surface behaviour and the underlying hydrodynamics is still missing. The physical processes occurring at the free surface are also debated. It has been suggested that the air-water interface is dominated by non-dispersive turbulence-induced features (Fujita et al., 2011; Horoshenkov et al., 2013; Nichols et al., 2016), by gravity-capillary waves (Savelsberg et al., 2006; Savelsberg & Van De Water, 2008; Tani & Fujita, 2018) and by stationary waves (Dolcetti et al., 2016; Dolcetti & García Nava, 2019b; Dolcetti & García Nava, 2019a).

The behaviour of flows over permeable beds is also discussed. Previous studies focused on the effects of a permeable bed on the overlying hydrodynamics (Zagni & Smith, 1976; Mendoza & Zhou, 1992; Breugem et al., 2006; Pokrajac & Manes, 2009; Manes et al., 2009; Kim et al., 2018; Cooper et al., 2018), the appropriate choice for scaling factors (Pokrajac et al., 2006; Navaratnam et al., 2018) and the effective consistency of constants (Munoz Goma & Gelhar, 1968; Ruff & Gelhar, 1970; Chu & Gelhar, 1972; Zippe & Graf, 1983; Gupta & Paudyal, 1985; Nezu et al., 1993; Prinos et al., 2003). From these broad range of studies, consensus on the mechanisms of momentum transfer between bed and flow was not reached.

To address these uncertainties a series of tests was performed over two statistically identical permeable composite beds having different texture orientations and over two different slopes. In these tests the bulk hydrodynamics and the free surface were observed at staggered times. Characterisation of the hydrodynamics was performed using a state-of-the-art PTV system employing the STB methodology. The free surface was evaluated using a DIC system.

The different findings of the current thesis are summarised in Section 5.2. Section 5.3 aims at giving an answer to the research hypotheses proposed at the beginning of this thesis. Finally, Section 5.4 provides useful recommendations for future works based on the experience gathered during this research and on more recent considerations of previous studies.

5.2 Main Findings

5.2.1 Flow Dynamics of Open-channel Shallow Turbulent Flows

A PTV system was used to study the flow hydrodynamics for a series of tests over a wide range of relative submergences for different bed arrangements and flume slopes.
The system allowed to obtain highly spatially and temporally resolved data which enabled a good characterisation of the near-surface and near-bed regions.
A categorisation of the flow conditions based on three Classes was proposed and permitted to better evaluate the evolution of the flow characteristics.

Test results show that the Class of the flow has direct impacts on the hydrodynamics. A clear distinction can in fact be made between flows in Classes I and II and flows in Class III.
Class I and II conditions are characterised by linearity in the profiles for the different components. This is a consequence of the extension in height of the roughness layer, reaching up to 50% of the depth for tests over 1/1000 and up to 70% of the depth over a 1/500 slope. This large extension results in a suppression of the logarithmic layer. It is thought that this behaviour is mainly caused by the low relative submergence that characterises the hydraulic regimes in Classes I and II.
Class III conditions are instead characterised by complex profiles with deviations from the linear trend occurring in the proximity of the free surface and in the near-bed region. The behaviour near the free surface appears to be due to the redistribution of momentum between the different directions as a consequence of the presence of an interface. Near the bed, statistics are affected by the presence of a rough and permeable bed. Bed roughness is directly involved as it enables the appearance of form-induced components (related to the spatial variability) as a consequence of the bed heterogeneity. Bed permeability instead allows the statistics to be non-zero at the bed level as a result of momentum penetration into the bed.

Bed arrangement also impacts on the flow hydrodynamics. This is particular evident in the region close to the bed. However, the influence of the bed arrangement does not disappear while moving away from the bed, but it is seen to persist up to the near-surface region, even if weakly. The free surface might therefore be affected in ways that can be different from case to case. This would have great importance for remote sensing as it could be possible to infer the bed spatial organisation and flow characteristics from the observed surface wave patterns.

For the tests reported here, different bed arrangements can affect the statistics according to how much momentum they allow to penetrate inside the bed. This influence mostly impacts on the dispersive components, while it appears to have little to none effect on the turbulent (temporal) statistics. However, when comparing the magnitudes of the dispersive and turbulent statistics, it is revealed that spatial variability has limited influence compared to the temporal one for most of the cases. Exceptions can occur when the flow conditions highlight the effects of the bed structure (i.e. conditions with limited relative submergence) where the influence of the form-induced and temporal statistics are comparable.

5.2.2 Free-surface Dynamics in Open-channel Shallow Turbulent Flows

A DIC system was used to investigate the dynamics of the free surface. Contrary to studies such as Tsubaki and Fujita (2005), Cobelli et al. (2009) and Wu et al. (2022) where the water was tainted to provide an opaque medium, here buoyant tracers were used to coat the free surface and allow its reconstruction. Due to the methods used to introduce the particles and the effects of secondary currents and turbulence, it was not possible to provide a constant and uniform tracer coating throughout the free surface imaged by the cameras. As spatially continuous measurements were not achievable, classic statistical tools were not deemed optimal for the processing of the disperse DIC data. Likewise, other indicators such as cross-correlations were highly affected by the presence of gaps in the measurements. Earlier analysis of the PTV data suggested that both spatial and temporal characteristics need to be considered at the same time. For this reason, frequency-wavenumber spectra of the DIC free-surface elevation data sets were computed. Data was seen to be sufficiently resolved in space to derive accurate frequency-wavenumber spectra.

Results show that the free-surface behaviour tends to map following the categorisation of flow conditions based on Classes. In particular, a clear distinction can be made between flows in Classes I and II, and Class III regarding the dominant mechanisms at work on the free surface. This is because flows in Class III see, together with the presence of the same types of waves observable in Classes I and II, the appearance of stationary waves with k_0 as a wavenumber which dominate the free surface.
Ambiguity however exists regarding the presence a particular type of wave that can be generated when stationary waves form that is gravity-capillary waves with $k = k_0$. In fact, these waves do not immediately appear when the transition to Class III occurs for tests over a 1/1000 slope, while they are present since transition takes place over the 1/500 slope. This different behaviour might be explained by the lower energy content for tests performed with the 1/1000 slope.

Comparisons between reconstructed free-surface elevation fields over different flow conditions, slope and bed arrangements allowed to propose the following model for the free-surface behaviour:

- the free surface of flows categorised in Class I are dominated by gravity-capillary waves. Non-dispersive waves, ascribable to non-resonant turbulence interaction proposed by Teixeira and Belcher (2006), also exist but are very limited compared to standard gravity-capillary waves. A motivation for the appearance of gravity-capillary waves cannot be proposed as several questions cannot be answered. In fact, resonant growth cannot occur for flows in Class I, while wave generation following the perturbation of the free surface by coherent structures does not justify the energy content of the two types of waves.

- flows in Class II behave similarly to those of Class I. Theoretically, the characteristics of this flow regime should allow the development of stationary waves as the free-surface velocity is above the minimum phase velocity for gravity-capillary waves. Surprisingly, no sign of stationary waves was reported. It is alleged that, due to secondary currents and the development of low and high speed streaks on the surface, not the entire air-water interface satisfied the conditions of velocity greater than 0.23 m/s. Therefore, free-surface velocity faster than 0.23 m/s should be seen not only as a global but also as a local condition for the establishment of stationary waves.
- flows in Class III are dominated by gravity-capillary waves with wavenumber k_0 and other gravity-capillary waves. Following Dolcetti et al. (2016) and Dolcetti and García Nava (2019b), stationary waves with $k = k_0$ are induced by disturbances on the bed. No clear standing waves can be directly observed as a result of the incoherent combination of disturbances by a homogeneous bed. Gravity-capillary waves with wavenumber k_0 are thought to be originated via the triad resonance mechanism that promotes their specific growth when stationary waves with $k = k_0$ and a sheared flow are also present. Standard gravity-capillary waves and non-dispersive patterns coexist with the other $k = k_0$ waves.

The confirmation of the existence of a form of organisation on the free-surface elevation field of shallow turbulent flow is of great importance. The presence of gravity-capillary waves with wavenumber k_0 is particularly relevant, as the stationary waves that are thought to be their generating mechanism are not only related to the characteristics of the flow field but also to the bed roughness. This has a direct implication when it comes to the monitoring of streams using remote sensing techniques. The observation of the free surface might allow not only to derive key flow parameters like depth and surface velocity but also bed characteristics, which in turn would improve the estimates of the flow rate via a better characterisation of the velocity profile.

5.3 Answering Research Hypotheses

Four research hypotheses were proposed at the beginning of this thesis in Section 1.3 and a series of tests specifically designed to find an answer to such questions were performed. In consideration of the outcomes, the following answers can be advanced:

- Which is (or are) the dominant mechanism(s) that govern(s) the free-surface behaviour?

  Frequency-wavenumber spectra of the free-surface elevation field reveal the existence of two different free-surface behaviours, one occurring when the depth-averaged velocity is below 0.23 m/s and one taking place when the depth-averaged velocity is above 0.23 m/s. For each behaviour a distinct dominant mechanism can be observed.
  When the depth-averaged velocity is below 0.23 m/s, the free surface is dominated by gravity-capillary waves travelling in all directions. Together, non-dispersive patterns also

coexist with limited importance.
When the depth-averaged velocity is above 0.23 m/s, standing waves with wavenumber k_0 and gravity-capillary waves with k_0 as wavenumber dominate the free surface over standard gravity-capillary waves and non-dispersive patterns.

- Is there a sudden transition from one governing mechanism to another one or do they all simultaneously coexist with different intensity?

  The appearance of standing waves with wavenumber k_0 and gravity-capillary waves with k_0 as wavenumber suddenly occurs once the conditions for their existence are satisfied, therefore it can be said that the passage from one type of behaviour to the other one is immediate. While standard gravity-capillary waves can always be considered important components of the surface wave patterns, their relative importance compared to waves with k_0 as wavenumber decreases as more energetic flow conditions are observed.

- Which bulk flow properties can be inferred from the observation of the air-water interface?

  The k-ω algorithm presented in Dolcetti et al. (2023) was tested over a wide range of flow conditions and clearly shows that the free-surface velocity and the water depth can be estimated from the observation of the free surface.
  The presence of waves with k_0 as wavenumber should also enable the possibility to derive the ratio between free-surface and depth-average velocities, and the Froude Number. These two parameters could be used to characterise the shape of the velocity profile, which in turn could lead to the identification of the roughness proprieties of any river bed.

- Can statistically similar beds produce different flow and wave patterns?

  Frequency-wavenumber spectra of the water surface elevation field for tests over the same bed but different slopes were seen to differ in terms of types of waves that populate the free surface for similar flow conditions. The reason for this different behaviour is hard to find but it is suggested that this might be caused by the lower energy levels observed over the milder slope.
  On the contrary, the frequency-wavenumber spectra of water surface waves of tests over different bed arrangements but same slope resulted in similar patterns of surface waves within the 3 flow Classes (I, II and III).
  It can therefore be said the statistically similar beds produce the same wave patterns. What was different between the two bed arrangements was the spectral energy content.
  Different flow patterns can instead be distinguished between the two bed arrangements. The discriminating factors are the dispersive (also know as form-induced) field. As their effects can propagate up to the surface, it might be possible to infer the dispersive field from the strain of the free surface. However, the dispersive field is generally weak and overborne by the turbulent field for most of the cases. Therefore, the influence of the dispersive field might be too small to be identified.

5.4 Recommendations for Future Work

Figure 5.1 reports the key results that focused on the evaluation of the free-surface behaviour in open-channel flows mapped onto a framework that is similar to the one proposed by Brocchini and Peregrine (2001) for the classification of different forms of surface agitation.

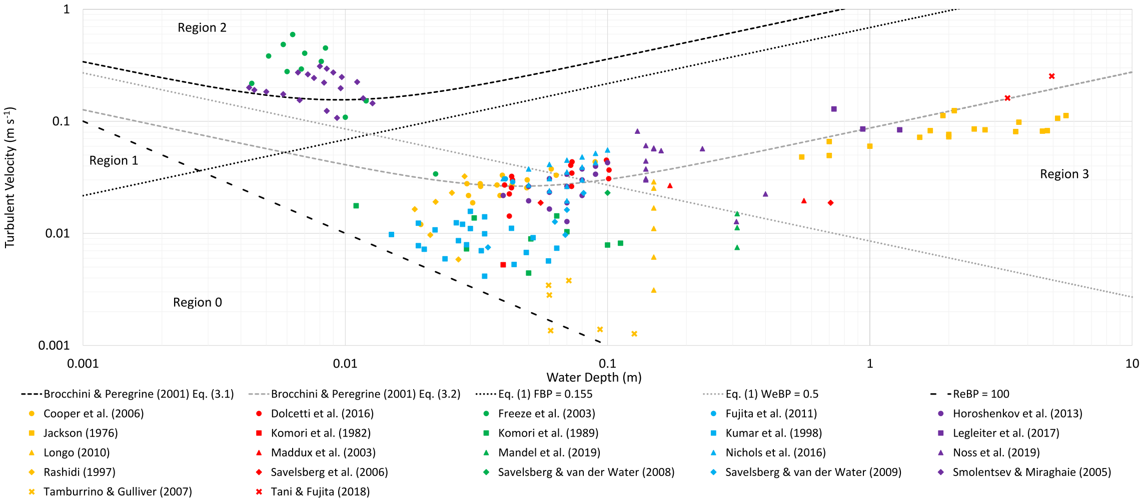

Figure 5.1: Laboratory and field observations organised according to Brocchini and Peregrine (2001) framework. Streamwise turbulent velocity component was defined via bulk velocity using Nezu and Nakagawa (1993). Water depth scales with the size of the largest coherent structures. Black and gray dashed lines are from Equations (3.1) and (3.2) in Brocchini and Peregrine (2001), respectively. Black and gray dotted lines define the separations between the four regions and are obtained from Equation 2.1 using $F_{BP} = 0.155$ and $We_{BP} = 0.5$, respectively. Black dashed-dotted line represents the condition $Re_{BP} = 100$. After Muraro et al. (2021).

The scope of Figure 5.1 is to show the range of past laboratory and field measurements that were aimed at investigating the free-surface behaviour. The measurements are proposed using the existing framework suggested by Brocchini and Peregrine (2001) in order to highlight the regions in which the flow conditions fall and so indicate which regions might be underrepresented. The parameters used for plotting the data are the flow depth and turbulence velocity magnitude. Some assumptions were followed while mapping the plot:

- The streamwise turbulent velocity component, unless clearly reported, was taken as 7.5% of the streamwise depth-averaged velocity, $\bar{U}_B$. This choice was made because in most of the studies the streamwise turbulent velocity and the shear velocity are not reported. The value of 7.5% has been derived from Nezu and Nakagawa (1993) and represents the relative scale between the streamwise turbulent velocity and the depth-averaged velocity over a range of both smooth and rough beds.

- Water depth was used to define the horizontal axis as in most of the cases the length scales of turbulence were not quantified. This choice was made as vertical size of the turbulent macrostructures is limited by and cannot grow larger than the water depth (Shvidchenko & Pender, 2001; Roy et al., 2004).

- The lines subdividing the graph into four sections were obtained from Equations 2.1 and assuming $F_{BP} = 0.15$ and $We_{BP} = 0.5$ (corresponding to 2.92 and 177.78 for the Froude and Weber Numbers, respectively).

The plot reveals that most of the field measurements cluster in region 3. This finds agreement with Brocchini and Peregrine (2001) who identified region 3 as the most appropriate to describe a majority of geophysical surface flows such as rivers and open channels.
Most of the laboratory experiments, however, fall in region 0 or close to the border between region 0 and 3. This suggests that for many laboratory studies the turbulent processes were weaker than the ones observed in open channels and rivers and so they may be non-representative of the large-scale geophysical flows.

Moving towards more representative flow conditions is a challenge for laboratory studies as higher depth-averaged velocities for a given flow depth can only be achieved by reducing the roughness height or by increasing the slope of a laboratory flume. Typically, laboratory flumes are already not very rough, making difficult to implement the first possibility. The most practical solution is to increase the flume slope, however, to maintain the required water depth much larger values of discharge are required. This can be in many cases impractical due to physical limitations on the recirculation systems. This problem also prevents the possibility of testing deeper flow conditions. Another problem can be the reduction in the aspect ratio and so the appearance of steady secondary motions when deeper depths are examined.

It is clear that, due to a series of physical limitations on the facilities, flow conditions located in region 3 are almost unexplored in laboratory studies. While field measurements can observe the flow and surface dynamics at the real scale, the measurement are characterised by much lower spatial and temporal resolutions compared to laboratory investigations. Most of the high-end remote sensing technologies find little to no application in the field due to the fragility and high cost of the instrumentation. As a consequence, field devices are often invasive and so not appropriate when investigating the interaction between surface and hydrodynamics.

It appears clear that region defined by Brocchini and Peregrine (2001) as the most representative of terrestrial flows is almost uncharted. Therefore, future works should be carried out in large-scale facilities or real open channels. Also, on field tests are required to validate the behaviours and relationships observed at the laboratory scale.
While the DIC system can be replaced by more economic and flexible solutions like CCTV cameras, more difficult is to find a valid substitute of the PTV setup. In fact, remote sensing techniques that permit to characterise the flow field are few and have limited performance.

A characterisation of the turbulent phenomena in the flow field also needs to be performed. The identification of coherent structures, their tracking from the near-bed region to the free surface and the observation of their impingement on the interface would allow to better understand the interaction between surface and flow and explain the reason why their effect is less important when compared to gravity-capillary waves. Savelsberg et al. (2006) and Dolcetti et al. (2016) noticed that the influence of coherent structures on the surface dynamics for regimes with surface velocity above 0.23 m/s is limited but still occurring. Smolentsev and Miraghaie (2005) suggests that the deformations induced by these structures can carry information relative to

the flow characteristics. This means that these structures cannot be ignored if the goal is to establish a relationship between flow and free surface.
Examination of the streamwise and vertical components also suggests that vorticity might be correlated with the surface dynamics, especially of the stronger gravity-capillary waves at the higher flow rates.

In the experimental campaign here presented wind effects were ignored due to the complexity of the task. Wind, however, plays an important role in the development of waves at the air-water interface. While fetch is typically limited over rivers and channels, wind speed during storms events can be sufficiently high to induce the formation of wind waves. Because of this, wind effect must be considered and quantified in future works.

Bibliography

Adamczyk, A. A., & Rimai, L. (1988). Reconstruction of a 3-dimensional flow field from orthogonal views of seed track video images. *Experiments in Fluids*, *6*(6), 380–386. https://doi.org/10.1007/BF00196483

Adrian, R. J. (1988). Statistical properties of particle image velocimetry measurements in turbulent flow. *Laser Anemometry in Fluid Mechanics*, *3*, 115–129.

Aksel, N., & Schörner, M. (2018). Films over topography: From creeping flow to linear stability, theory, and experiments, a review. *Acta Mechanica*, *229*(4), 1453–1482. https://doi.org/10.1007/s00707-018-2146-y

Akutina, Y. (2015). *Experimental investigation of flow structures in a shallow embayment using 3D-PTV* [Doctoral dissertation, McGill University].

Arntzen, E. V., Geist, D. R., & Dresel, P. E. (2006). Effects of fluctuating river flow on groundwater/surface water mixing in the hyporheic zone of a regulated, large cobble bed river. *River Research and Applications*, *22*(8), 937–946. https://doi.org/10.1002/rra.947

Atkinson, C., & Soria, J. (2009). An efficient simultaneous reconstruction technique for tomographic particle image velocimetry. *Experiments in Fluids*, *47*(4-5), 553–568. https://doi.org/10.1007/s00348-009-0728-0

Banner, M. L., Jones, I. S. F., & Trinder, J. C. (1989). Wavenumber spectra of short gravity waves. *Journal of Fluid Mechanics*, *198*(-1), 321. https://doi.org/10.1017/S0022112089000157

Barrick, D. (1972). First-order theory and analysis of MF/HF/VHF scatter from the sea. *IEEE Transactions on Antennas and Propagation*, *20*(1), 2–10. https://doi.org/10.1109/TAP.1972.1140123

Beavers, G. S., & Joseph, D. D. (1967). Boundary conditions at a naturally permeable wall. *Journal of Fluid Mechanics*, *30*(1), 197–207. https://doi.org/10.1017/S0022112067001375

Beck, S., & Collins, R. (2017). Moody diagram. https://commons.wikimedia.org/wiki/File:Moody_EN.svg

Best, J. (2005). The fluid dynamics of river dunes: A review and some future research directions. *Journal of Geophysical Research: Earth Surface*, *110*(F4), 2004JF000218. https://doi.org/10.1029/2004JF000218

Betts, R., Haward, A., & Pearson, K. (2021). *The Third UK Climate Change Risk Assessment Technical Report*.

Biesel, F. (1950). Étude Théorique de la Houle en Eau Courante. *La Houille Blanche*, *36*(sup1), 279–285. https://doi.org/10.1051/lhb/1950009

Boano, F., Harvey, J. W., Marion, A., Packman, A. I., Revelli, R., Ridolfi, L., & Wörman, A. (2014). Hyporheic flow and transport processes: Mechanisms, models, and biogeochemical implications. *Reviews of Geophysics*, *52*(4), 603–679. https://doi.org/10.1002/2012RG000417

Bock, E. J., & Hara, T. (1995). Optical Measurements of Capillary-Gravity Wave Spectra Using a Scanning Laser Slope Gauge. *Journal of Atmospheric and Oceanic Technology*, *12*(2), 395–403. https://doi.org/10.1175/1520-0426(1995)012⟨0395:OMOCGW⟩2.0.CO;2

Breugem, W. P., Boersma, B. J., & Uittenbogaard, R. E. (2006). The influence of wall permeability on turbulent channel flow. *Journal of Fluid Mechanics*, *562*, 35. https://doi.org/10.1017/S0022112006000887

Brocchini, M., & Peregrine, D. H. (2001). The dynamics of strong turbulence at free surfaces. Part 1. Description. *Journal of Fluid Mechanics*, *449*, 225–254. https://doi.org/10.1017/S0022112001006012

Brunetaud, X., Luca, L. D., Janvier-Badosa, S., Beck, K., & Al-Mukhtar, M. (2012). Application of digital techniques in monument preservation. *European Journal of Environmental and Civil Engineering*, *16*(5), 543–556. https://doi.org/10.1080/19648189.2012.676365

Buffin-Bélanger, T., Reid, I., Rice, S., Chandler, J. H., & Lancaster, J. (2003). A casting procedure for reproducing coarse-grained sedimentary surfaces. *Earth Surface Processes and Landforms*, *28*(7), 787–796. https://doi.org/10.1002/esp.490

Burns, J. C. (1953). Long waves in running water. *Mathematical Proceedings of the Cambridge Philosophical Society*, *49*(4), 695–706. https://doi.org/10.1017/S0305004100028899

Caballero-Gill, R. P., Herbert, T. D., & Dowsett, H. J. (2019). 100-kyr Paced Climate Change in the Pliocene Warm Period, Southwest Pacific. *Paleoceanography and Paleoclimatology*, *34*(4), 524–545. https://doi.org/10.1029/2018PA003496

Cameron, S. M., Nikora, V. I., & Stewart, M. T. (2017). Very-large-scale motions in rough-bed open-channel flow. *Journal of Fluid Mechanics*, *814*, 416–429. https://doi.org/10.1017/jfm.2017.24

Caponi, E. A., Yuen, H. C., Milinazzo, F. A., & Saffman, P. G. (1991). Water-wave instability induced by a drift layer. *Journal of Fluid Mechanics*, *222*(-1), 207. https://doi.org/10.1017/S0022112091001064

Cardenas, M. B., & Wilson, J. L. (2007). Effects of current–bed form induced fluid flow on the thermal regime of sediments. *Water Resources Research*, *43*(8). https://doi.org/10.1029/2006WR005343

Chang, P., Melville, W. K., & Miles, J. W. (1979). On the evolution of a solitary wave in a gradually varying channel. *Journal of Fluid Mechanics*, *95*(03), 401. https://doi.org/10.1017/S002211207900152X

Chang, T., Watson, A., & Tatterson, G. (1985). Image processing of tracer particle motions as applied to mixing and turbulent flow—I. The technique. *Chemical Engineering Science*, *40*(2), 269–275. https://doi.org/10.1016/0009-2509(85)80066-X

Chanson, H. (2000). Boundary shear stress measurements in undular flows: Application to standing wave bed forms. *Water Resources Research*, *36*(10), 3063–3076. https://doi.org/10.1029/2000WR900154

Chiu, W.-C., & Rib, L. N. (1956). The rate of dissipation of energy and the energy spectrum in a low-speed turbulent jet. *Eos, Transactions American Geophysical Union*, *37*(1), 13–26. https://doi.org/10.1029/TR037i001p00013

Choi, C. Y., & Waller, P. M. (1997). Momentum Transport Mechanism for Water Flow over Porous Media. *Journal of Environmental Engineering*, *123*(8), 792–799. https://doi.org/10.1061/(ASCE)0733-9372(1997)123:8(792)

Chu, T. C., Ranson, W. F., & Sutton, M. A. (1985). Applications of digital-image-correlation techniques to experimental mechanics. *Experimental Mechanics*, *25*(3), 232–244. https://doi.org/10.1007/BF02325092

Chu, Y. H., & Gelhar, L. W. (1972). *Turbulent Pipe Flow with Granular Permeable Boundaries* (tech. rep. No. 148). Dept. of Civil Engrg., M.I.T. Cambridge, Massachusetts.

Cobelli, P. J., Maurel, A., Pagneux, V., & Petitjeans, P. (2009). Global measurement of water waves by Fourier transform profilometry. *Experiments in Fluids*, *46*(6), 1037–1047. https://doi.org/10.1007/s00348-009-0611-z

Colebrook, C. F. (1939). Turbulent flow in pipes, with particular reference to the transition region between the smooth and rough pipe laws. *Journal of the Institution of Civil Engineers*, *11*(4), 133–156. https://doi.org/10.1680/ijoti.1939.13150

Cooper, J. R., Ockleford, A., Rice, S. P., & Powell, D. M. (2018). Does the permeability of gravel river beds affect near-bed hydrodynamics? *Earth Surface Processes and Landforms*, *43*(5), 943–955. https://doi.org/10.1002/esp.4260

Cooper, J. R., Tait, S. J., & Horoshenkov, K. V. (2006). Determining hydraulic resistance in gravel-bed rivers from the dynamics of their water surfaces. *Earth Surface Processes and Landforms*, *31*(14), 1839–1848. https://doi.org/10.1002/esp.1447

Corino, E. R., & Brodkey, R. S. (1969). A visual investigation of the wall region in turbulent flow. *Journal of Fluid Mechanics*, *37*(1), 1–30. https://doi.org/10.1017/S0022112069000395

Cox, C., & Munk, W. (1954). Statistics of the sea surface derived from sun glitter. *Journal of Marine Research*, *13*(2).

Dabiri, D., & Gharib, M. (2001). Simultaneous free-surface deformation and near-surface velocity measurements. *Experiments in Fluids*, *30*(4), 381–390. https://doi.org/10.1007/s003480000212

Dabiri, D., & Pecora, C. (2020). *Particle tracking velocimetry*. IOP Publishing.

Defina, A. (1996). Transverse spacing of low-speed streaks in a channel flow over a rough bed. In *Coherent flow structures in open channels* (pp. 87–99). Wiley; Sons.

Devriendt, D., Douxchamps, D., Capart, H., Craeye, C., Macq, B., & Zech, Y. (1998). Three-dimensional Reconstruction Of A Periodic Free Surface From Digital Imaging Measurements. *Transactions on Engineering Sciences*, *18*.

Dey, S., & Das, R. (2012). Gravel-Bed Hydrodynamics: Double-Averaging Approach. *Journal of Hydraulic Engineering*, *138*(8), 707–725. https://doi.org/10.1061/(ASCE)HY.1943-7900.0000554

Dickey, D. A., & Fuller, W. A. (1979). Distribution of the Estimators for Autoregressive Time Series With a Unit Root. *Journal of the American Statistical Association*, *74*(366), 427. https://doi.org/10.2307/2286348

Dolcetti, G. (2016). *Remote monitoring of shallow turbulent flows based on the doppler spectra of airborne* [Doctoral dissertation, University of Sheffield].

Dolcetti, G., Horoshenkov, K. V., Krynkin, A., & Tait, S. J. (2016). Frequency-wavenumber spectrum of the free surface of shallow turbulent flows over a rough boundary. *Physics of Fluids*, *28*(10), 105105. https://doi.org/10.1063/1.4964926

Dolcetti, G., Hortobágyi, B., Perks, M., Tait, S. J., & Dervilis, N. (2022). Using Noncontact Measurement of Water Surface Dynamics to Estimate River Discharge. *Water Resources Research*, *58*(9), e2022WR032829. https://doi.org/10.1029/2022WR032829

Dolcetti, G., Hortobágyi, B., Perks, M., & Tait, S. (2020). The effect of surface gravity waves on the measurement of river surface velocity. In W. Uijttewaal, M. J. Franca, D. Valero, V. Chavarrias, C. Ylla Arbós, R. Schielen, & A. Crosato (Eds.), *River Flow 2020* (1st Edition, pp. 862–871). CRC Press. https://doi.org/10.1201/b22619-122

Dolcetti, G., & García Nava, H. (2019a). Wavelet spectral analysis of the free surface of turbulent flows. *Journal of Hydraulic Research*, *57*(4), 604–606. https://doi.org/10.1080/00221686.2018.1555561

Dolcetti, G., & García Nava, H. (2019b). Wavelet spectral analysis of the free surface of turbulent flows. *Journal of Hydraulic Research*, *57*(2), 211–226. https://doi.org/10.1080/00221686.2018.1478896

Dolcetti, G., Hortobágyi, B., Perks, M., & Tait, S. (2023). kOmega - a Matlab script to estimate river discharge remotely based on water surface dynamics. https://doi.org/10.5281/ZENODO.7998890

Dolcetti, G., Krynkin, A., Alkmim, M., Cuenca, J., De Ryck, L., Sailor, G., Muraro, F., Tait, S. J., & Horoshenkov, K. V. (2024). Reconstruction of the frequency-wavenumber spectrum of water waves with an airborne acoustic doppler array for noncontact river monitoring. *IEEE Transactions on Geoscience and Remote Sensing*, *62*, 1–14. https://doi.org/10.1109/TGRS.2024.3358672

Dolcetti, G., Krynkin, A., & Horoshenkov, K. V. (2017). Doppler spectra of airborne sound backscattered by the free surface of a shallow turbulent water flow. *The Journal of the Acoustical Society of America*, *142*(6), 3387–3401. https://doi.org/10.1121/1.5015990

Donelan, M. A., Hamilton, J., & Hui, W. H. (1985). Directional spectra of wind-generated ocean waves. *Philosophical Transactions of the Royal Society of London. Series A, Mathematical and Physical Sciences*, *315*(1534), 509–562. https://doi.org/10.1098/rsta.1985.0054

Douxchamps, D., Devriendt, D., Capart, H., Craeye, C., Macq, B., & Zech, Y. (2005). Stereoscopic and velocimetric reconstructions of the free surface topography of antidune flows. *Experiments in Fluids*, *39*(3), 535–553. https://doi.org/10.1007/s00348-005-0983-7

El Hassan, M., Bourgeois, J., & Martinuzzi, R. (2015). Boundary layer effect on the vortex shedding of wall-mounted rectangular cylinder. *Experiments in Fluids*, *56*(2), 33. https://doi.org/10.1007/s00348-014-1882-6

Ellingsen, S. Å., & Li, Y. (2017). Approximate Dispersion Relations for Waves on Arbitrary Shear Flows. *Journal of Geophysical Research: Oceans*, *122*(12), 9889–9905. https://doi.org/10.1002/2017JC012994

Elsinga, G. E., Scarano, F., Wieneke, B., & Van Oudheusden, B. W. (2006). Tomographic particle image velocimetry. *Experiments in Fluids*, *41*(6), 933–947. https://doi.org/10.1007/s00348-006-0212-z

Fenton, J. D. (1973). Some Results for Surface Gravity Waves on Shear Flows. *IMA Journal of Applied Mathematics*, *12*(1), 1–20. https://doi.org/10.1093/imamat/12.1.1

Finnigan, J. (2000). Turbulence in Plant Canopies. *Annual Review of Fluid Mechanics*, *32*(1), 519–571. https://doi.org/10.1146/annurev.fluid.32.1.519

Foster, G. L., Royer, D. L., & Lunt, D. J. (2017). Future climate forcing potentially without precedent in the last 420 million years. *Nature Communications*, *8*(1), 14845. https://doi.org/10.1038/ncomms14845

Freeze, B., Smolentsev, S., Morley, N., & Abdou, M. (2003). Characterization of the effect of Froude number on surface waves and heat transfer in inclined turbulent open channel water flows. *International Journal of Heat and Mass Transfer*, *46*(20), 3765–3775. https://doi.org/10.1016/S0017-9310(03)00197-2

Fujita, I., Furutani, Y., & Okanishi, T. (2011). Advection features of water surface profile in turbulent open-channel flow with hemisphere roughness elements. *Visualization of Mechanical Processes*, *1*(4). https://doi.org/10.1615/VisMechProc.v1.i3.70

Fujita, I., Muste, M., & Kruger, A. (1998). Large-scale particle image velocimetry for flow analysis in hydraulic engineering applications. *Journal of Hydraulic Research*, *36*(3), 397–414. https://doi.org/10.1080/00221689809498626

Fujita, I., & Tsubaki, R. (2002). A Novel Free-Surface Velocity Measurement Method Using Spatio-Temporal Images. *Hydraulic Measurements and Experimental Methods 2002*, 1–7. https://doi.org/10.1061/40655(2002)85

Fujita, I., Watanabe, H., & Tsubaki, R. (2007). Development of a non-intrusive and efficient flow monitoring technique: The space-time image velocimetry (STIV). *International Journal of River Basin Management*, *5*(2), 105–114. https://doi.org/10.1080/15715124.2007.9635310

Fukami, K., Yamaguchi, T., Imamura, H., & Tashiro, Y. (2008). Current Status of River Discharge Observation Using Non-Contact Current Meter for Operational Use in Japan. *World Environmental and Water Resources Congress 2008*, 1–10. https://doi.org/10.1061/40976(316)278

Garcia, M. (Ed.). (2008). *Sedimentation Engineering: Processes, Measurements, Modeling, and Practice* (110th Edition). American Society of Civil Engineers. https://doi.org/10.1061/9780784408148

Gayraud, S., & Philippe, M. (2003). Influence of Bed-Sediment Features on the Interstitial Habitat Available for Macroinvertebrates in 15 French Streams. *International Review of Hydrobiology*, *88*(1), 77–93. https://doi.org/10.1002/iroh.200390007

Gesemann, S. (2015). From Particle Tracks to Velocity and Acceleration Fields Using B-Splines and Penalties. https://doi.org/10.48550/ARXIV.1510.09034

Gharib, M., & Weigand, A. (1996). Experimental studies of vortex disconnection and connection at a free surface. *Journal of Fluid Mechanics*, *321*, 59–86. https://doi.org/10.1017/S0022112096007641

Giménez-Curto, L. A., & Lera, M. A. C. (1996). Oscillating turbulent flow over very rough surfaces. *Journal of Geophysical Research: Oceans*, *101*(C9), 20745–20758. https://doi.org/10.1029/96JC01824

Gioia, G., & Chakraborty, P. (2006). Turbulent Friction in Rough Pipes and the Energy Spectrum of the Phenomenological Theory. *Physical Review Letters*, *96*(4), 044502. https://doi.org/10.1103/PhysRevLett.96.044502

Grass, A. J. (1971). Structural features of turbulent flow over smooth and rough boundaries. *Journal of Fluid Mechanics*, *50*(2), 233–255. https://doi.org/10.1017/S0022112071002556

Gray, W. G. (1975). A derivation of the equations for multi-phase transport. *Chemical Engineering Science*, *30*(2), 229–233. https://doi.org/10.1016/0009-2509(75)80010-8

Guidi, G., Russo, M., & Angheleddu, D. (2014). 3D survey and virtual reconstruction of archeological sites. *Digital Applications in Archaeology and Cultural Heritage*, *1*(2), 55–69. https://doi.org/10.1016/j.daach.2014.01.001

Gupta, A. D., & Paudyal, G. N. (1985). Characteristics of Free Surface Flow Over Gravel Bed. *Journal of Irrigation and Drainage Engineering*, *111*(4), 299–318. https://doi.org/10.1061/(ASCE)0733-9437(1985)111:4(299)

Hadad, T., & Gurka, R. (2013). Effects of particle size, concentration and surface coating on turbulent flow properties obtained using PIV/PTV. *Experimental Thermal and Fluid Science*, *45*, 203–212. https://doi.org/10.1016/j.expthermflusci.2012.11.006

Harband, J. (1976). Three dimensional flow over a submerged object. *Journal of Engineering Mathematics*, *10*(1), 1–21. https://doi.org/10.1007/BF01535423

Harrison, S. S., & Clayton, L. (1970). Effects of Ground-Water Seepage on Fluvial Processes. *Geological Society of America Bulletin*, *81*(4), 1217. https://doi.org/10.1130/0016-7606(1970)81[1217:EOGSOF]2.0.CO;2

Hausfather, Z., & Peters, G. P. (2020). Emissions – the 'business as usual' story is misleading. *Nature*, *577*(7792), 618–620. https://doi.org/10.1038/d41586-020-00177-3

Hester, E. T., Young, K. I., & Widdowson, M. A. (2013). Mixing of surface and groundwater induced by riverbed dunes: Implications for hyporheic zone definitions and pollutant reactions. *Water Resources Research*, *49*(9), 5221–5237. https://doi.org/10.1002/wrcr.20399

Hild, F., & Roux, S. (2012). Comparison of Local and Global Approaches to Digital Image Correlation. *Experimental Mechanics*, *52*(9), 1503–1519. https://doi.org/10.1007/s11340-012-9603-7

Hinze, J. O. (1987). *Turbulence* (2nd ed). McGraw-Hill.

Horn, B. K. (1977). Understanding image intensities. *Artificial Intelligence*, *8*(2), 201–231. https://doi.org/10.1016/0004-3702(77)90020-0

Horoshenkov, K. V., Nichols, A., Tait, S. J., & Maximov, G. A. (2013). The pattern of surface waves in a shallow free surface flow. *Journal of Geophysical Research: Earth Surface*, *118*(3), 1864–1876. https://doi.org/10.1002/jgrf.20117

Hughes, B., Grant, H., & Chappell, R. (1977). A fast response surface-wave slope meter and measured wind-wave moments. *Deep Sea Research*, *24*(12), 1211–1223. https://doi.org/10.1016/0146-6291(77)90524-0

Imamoto, H., & Ishigaki, T. (1985). Visualization of longitudinal eddies in an open channel flow. *Journal of the Flow Visualization Society of Japan*, *5*(18), 219–222. https://doi.org/10.3154/jvs1981.5.219

Intergovernmental Panel on Climate Change. (2023). Summary for policymakers. In *Climate change 2021 – the physical science basis: Working group i contribution to the sixth assessment report of the intergovernmental panel on climate change* (pp. 3–32). Cambridge University Press. https://doi.org/10.1017/9781009157896.001

Jackson, R. G. (1976). Sedimentological and fluid-dynamic implications of the turbulent bursting phenomenon in geophysical flows. *Journal of Fluid Mechanics*, *77*(3), 531–560. https://doi.org/10.1017/S0022112076002243

Jacobi, O. (1980). Photogrammetric tracking of a moving particle in running water.

Jähne, B., Klinke, J., & Waas, S. (1994). Imaging of short ocean wind waves: A critical theoretical review. *Journal of the Optical Society of America A*, *11*(8), 2197. https://doi.org/10.1364/JOSAA.11.002197

Jähne, B., & Waas, S. (1989). Optical Measuring Technique For Small Scale Water Surface Waves. In G. Duchossois, F. L. Herr, & R. J. Zander (Eds.). https://doi.org/10.1117/12.961496

Janssen, F., Cardenas, M. B., Sawyer, A. H., Dammrich, T., Krietsch, J., & De Beer, D. (2012). A comparative experimental and multiphysics computational fluid dynamics study of coupled surface–subsurface flow in bed forms. *Water Resources Research*, *48*(8), 2012WR011982. https://doi.org/10.1029/2012WR011982

Jin, G., Tang, H., Gibbes, B., Li, L., & Barry, D. (2010). Transport of nonsorbing solutes in a streambed with periodic bedforms. *Advances in Water Resources*, *33*(11), 1402–1416. https://doi.org/10.1016/j.advwatres.2010.09.003

Johnson, E. D., & Cowen, E. A. (2017). Estimating bed shear stress from remotely measured surface turbulent dissipation fields in open channel flows. *Water Resources Research*, *53*(3), 1982–1996. https://doi.org/10.1002/2016WR018898

Kähler, C. J., Scharnowski, S., & Cierpka, C. (2012). On the uncertainty of digital PIV and PTV near walls. *Experiments in Fluids*, *52*(6), 1641–1656. https://doi.org/10.1007/s00348-012-1307-3

Keeling, C. D., Piper, S. C., Bacastow, R. B., Wahlen, M., Whorf, T. P., Heimann, M., & Meijer, H. A. (2001). Exchanges of atmospheric co2 and 13co2 with the terrestrial biosphere and oceans from 1978 to 2000.

Kim, T., Blois, G., Best, J. L., & Christensen, K. T. (2018). Experimental study of turbulent flow over and within cubically packed walls of spheres: Effects of topography, permeability and wall thickness. *International Journal of Heat and Fluid Flow*, *73*, 16–29. https://doi.org/10.1016/j.ijheatfluidflow.2018.06.004

Kim, T., Blois, G., Best, J. L., & Christensen, K. T. (2020). PIV measurements of turbulent flow overlying large, cubic- and hexagonally-packed hemisphere arrays. *Journal of Hydraulic Research*, *58*(2), 363–383. https://doi.org/10.1080/00221686.2019.1581671

Kline, S. J., Reynolds, W. C., Schraub, F. A., & Runstadler, P. W. (1967). The structure of turbulent boundary layers. *Journal of Fluid Mechanics*, *30*(4), 741–773. https://doi.org/10.1017/S0022112067001740

Kobayashi, T., Saga, T., & Sekimoto, K. (1989). Velocity measurement of three-dimensional flow around rotating parallel disks by digital image processing. *Proceedings of Flow Visualization*.

Kohlschutter, E. (1906). Die Forschungsreise S. M. S. Planet. *Ann. Hydrographie*, *34*(219).

Koll, K. (2006). Parameterisation of the vertical velocity profile in the wall region over rough surfaces. In E. Alves, A. Cardoso, J. Leal, & R. Ferreira (Eds.), *River Flow 2006*. Taylor & Francis. https://doi.org/10.1201/9781439833865.ch15

Komori, S., Murakami, Y., & Ueda, H. (1989). The relationship between surface-renewal and bursting motions in an open-channel flow. *Journal of Fluid Mechanics*, *203*, 103–123. https://doi.org/10.1017/S0022112089001394

Kovats, S., & Brisley, R. (2021). Health, communities and the built environment. In R. Betts, A. Haward, & K. Pearson (Eds.), *The Third UK Climate Change Risk Assessment Technical Report* (pp. 1–284).

Krynkin, A., Horoshenkov, K. V., Nichols, A., & Tait, S. J. (2014). A non-invasive acoustical method to measure the mean roughness height of the free surface of a turbulent shallow water flow. *Review of Scientific Instruments*, *85*(11), 114902. https://doi.org/10.1063/1.4901932

Kumar, S., Gupta, R., & Banerjee, S. (1998). An experimental investigation of the characteristics of free-surface turbulence in channel flow. *Physics of Fluids*, *10*(2), 437–456. https://doi.org/10.1063/1.869573

Kwak, E., Detchev, I., Habib, A., El-Badry, M., & Hughes, C. (2013). Precise Photogrammetric Reconstruction Using Model-Based Image Fitting for 3D Beam Deformation Monitoring. *Journal of Surveying Engineering*, *139*(3), 143–155. https://doi.org/10.1061/(ASCE)SU.1943-5428.0000105

Laas, W. (1905). Photographische messung der meereswellen. *Z. Vereins Deutsch. Ingenieure*, *49*.

Lamb, H. (2005). *Hydrodynamics* (6th Edition). Dover Publ.

Lange, P. A., Jähne, B., Tschiersch, J., & Ilmberger, I. (1982). Comparison between an amplitude-measuring wire and a slope-measuring laser water wave gauge. *Review of Scientific Instruments*, *53*(5), 651–655. https://doi.org/10.1063/1.1137036

Lecompte, D., Smits, A., Bossuyt, S., Sol, H., Vantomme, J., Van Hemelrijck, D., & Habraken, A. (2006). Quality assessment of speckle patterns for digital image correlation. *Optics and Lasers in Engineering*, *44*(11), 1132–1145. https://doi.org/10.1016/j.optlaseng.2005.10.004

Legleiter, C. J., Mobley, C. D., & Overstreet, B. T. (2017). A framework for modeling connections between hydraulics, water surface roughness, and surface reflectance in open channel flows. *Journal of Geophysical Research: Earth Surface*, *122*(9), 1715–1741. https://doi.org/10.1002/2017JF004323

Liu, H.-T., Katsaros, K. B., & Weissman, M. A. (1982). Dynamic response of thin-wire wave gauges. *Journal of Geophysical Research: Oceans*, *87*(C8), 5686–5698. https://doi.org/10.1029/JC087iC08p05686

Liu, Y.-F., Cho, S., Spencer, B. F., & Fan, J.-S. (2016). Concrete Crack Assessment Using Digital Image Processing and 3D Scene Reconstruction. *Journal of Computing in Civil Engineering*, *30*(1), 04014124. https://doi.org/10.1061/(ASCE)CP.1943-5487.0000446

Lizarazo, I., Angulo, V., & Rodríguez, J. (2017). Automatic mapping of land surface elevation changes from UAV-based imagery. *International Journal of Remote Sensing*, *38*(8-10), 2603–2622. https://doi.org/10.1080/01431161.2016.1278313

Longfield, S., Lamb, R., & Manson, S. (2022). *Flood hydrology roadmap roadmap development and the action plan* (tech. rep.). Environment Agency.

Longo, S. (2010). Experiments on turbulence beneath a free surface in a stationary field generated by a Crump weir: Free-surface characteristics and the relevant scales. *Experiments in Fluids*, *49*(6), 1325–1338. https://doi.org/10.1007/s00348-010-0881-5

Lovera, F., & Kennedy, J. F. (1969). Friction-Factors for Flat-Bed Flows in Sand Channels. *Journal of the Hydraulics Division*, *95*(4), 1227–1234. https://doi.org/10.1061/JYCEAJ.0002122

Lu, H., & Cary, P. D. (2000). Deformation measurements by digital image correlation: Implementation of a second-order displacement gradient. *Experimental Mechanics*, *40*(4), 393–400. https://doi.org/10.1007/BF02326485

Lubard, S. C., Krimmel, J. E., Thebaud, L. R., Evans, D. D., & Shemdin, O. H. (1980). Optical image and laser slope meter intercomparisons of high-frequency waves. *Journal of Geophysical Research: Oceans*, *85*(C9), 4996–5002. https://doi.org/10.1029/JC085iC09p04996

Luo, P. F., Chao, Y. J., Sutton, M. A., & Peters, W. H. (1993). Accurate measurement of three-dimensional deformations in deformable and rigid bodies using computer vision. *Experimental Mechanics*, *33*(2), 123–132. https://doi.org/10.1007/BF02322488

Lüthi, B., Tsinober, A., & Kinzelbach, W. (2005). Lagrangian measurement of vorticity dynamics in turbulent flow. *Journal of Fluid Mechanics*, *528*, 87–118. https://doi.org/10.1017/S0022112004003283

Ma, Z., & Liu, S. (2018). A review of 3d reconstruction techniques in civil engineering and their applications. *Advanced Engineering Informatics*, *37*. https://doi.org/10.1016/j.aei.2018.05.005

Maas, H. G., Gruen, A., & Papantoniou, D. (1993). Particle tracking velocimetry in three-dimensional flows: Part 1. Photogrammetric determination of particle coordinates. *Experiments in Fluids*, *15*(2), 133–146. https://doi.org/10.1007/BF00190953

Manes, C., Pokrajac, D., Nikora, V. I., Ridolfi, L., & Poggi, D. (2011). Turbulent friction in flows over permeable walls. *Geophysical Research Letters*, *38*(3), n/a–n/a. https://doi.org/10.1029/2010GL045695

Manes, C., Ridolfi, L., & Katul, G. (2012). A phenomenological model to describe turbulent friction in permeable-wall flows. *Geophysical Research Letters*, *39*(14). https://doi.org/10.1029/2012GL052369

Manes, C., Pokrajac, D., Coceal, O., & McEwan, I. (2008). On the significance of form-induced stress in rough wall turbulent boundary layers. *Acta Geophysica*, *56*(3), 845–861. https://doi.org/10.2478/s11600-008-0021-2

Manes, C., Pokrajac, D., McEwan, I., & Nikora, V. (2009). Turbulence structure of open channel flows over permeable and impermeable beds: A comparative study. *Physics of Fluids*, *21*(12), 125109. https://doi.org/10.1063/1.3276292

Manes, C., Pokrajac, D., McEwan, I., Nikora, V., & Campbell, L. (2006). Application of UVP within Porous Beds. *Journal of Hydraulic Engineering*, *132*(9), 983–986. https://doi.org/10.1061/(ASCE)0733-9429(2006)132:9(983)

Marcus, W. A., & Fonstad, M. A. (2008). Optical remote mapping of rivers at sub-meter resolutions and watershed extents. *Earth Surface Processes and Landforms*, *33*(1), 4–24. https://doi.org/10.1002/esp.1637

Marcus, W. A., & Fonstad, M. A. (2010). Remote sensing of rivers: The emergence of a subdiscipline in the river sciences. *Earth Surface Processes and Landforms*, *35*(15), 1867–1872. https://doi.org/10.1002/esp.2094

Matthes, G. H. (1947). Macroturbulence in natural stream flow. *Eos, Transactions American Geophysical Union*, *28*(2), 255–265. https://doi.org/10.1029/TR028i002p00255

Mendoza, C., & Zhou, D. (1992). Effects of Porous Bed on Turbulent Stream Flow above Bed. *Journal of Hydraulic Engineering*, *118*(9), 1222–1240. https://doi.org/10.1061/(ASCE)0733-9429(1992)118:9(1222)

Mitsuyasu, H. (1977). Measurement of the High-Frequency Spectrum of Ocean Surface Waves. *Journal of Physical Oceanography*, *7*(6), 882–891. https://doi.org/10.1175/1520-0485(1977)007⟨0882:MOTHFS⟩2.0.CO;2

Moody, L. F. (1944). Friction Factors for Pipe Flow. *Journal of Fluids Engineering*, *66*(8), 671–678. https://doi.org/10.1115/1.4018140

Morland, L. C., Saffman, P. G., & Yuen, H. C. (1991). Waves generated by shear layer instabilities. *Proceedings of the Royal Society of London. Series A: Mathematical and Physical Sciences*, *433*(1888), 441–450. https://doi.org/10.1098/rspa.1991.0057

Munoz Goma, R. J., & Gelhar, L. W. (1968). *Turbulent Pipe Flow with Rough and Porous Walls* (tech. rep. No. 109). Massachusetts Institute of Technology. Department of Civil Engineering. Cambridge, Massachusetts.

Muraro, F., Dolcetti, G., Nichols, A., Tait, S. J., & Horoshenkov, K. V. (2021). Free-surface behaviour of shallow turbulent flows. *Journal of Hydraulic Research*, *59*(1), 1–20. https://doi.org/10.1080/00221686.2020.1870007

Muste, M., Fujita, I., & Hauet, A. (2008). Large-scale particle image velocimetry for measurements in riverine environments. *Water Resources Research*, *44*(4). https://doi.org/10.1029/2008WR006950

Nagaoka, H., & Ohgaki, S. (1990). Mass transfer mechanism in a porous riverbed. *Water Research*, *24*(4), 417–425. https://doi.org/10.1016/0043-1354(90)90223-S

Nakagawa, H., & Nezu, I. (1981). Structure of space-time correlations of bursting phenomena in an open-channel flow. *Journal of Fluid Mechanics*, *104*, 1–43. https://doi.org/10.1017/S0022112081002796

Nakamura, Y., & Stefan, H. G. (1994). Effect of Flow Velocity on Sediment Oxygen Demand: Theory. *Journal of Environmental Engineering*, *120*(5), 996–1016. https://doi.org/10.1061/(ASCE)0733-9372(1994)120:5(996)

Navaratnam, C., Aberle, J., Qin, J., & Henry, P.-Y. (2018). Influence of Gravel-Bed Porosity and Grain Orientation on Bulk Flow Resistance. *Water*, *10*(5), 561. https://doi.org/10.3390/w10050561

Nezu, I. (1977). *Turbulent structure in open-channel flows* [Doctoral dissertation, Kyoto University].

Nezu, I., Nakagawa, H., & Tominaga, A. (1985). Secondary Currents in a Straight Channel Flow and the Relation to Its Aspect Ratio. In L. J. S. Bradbury, F. Durst, B. E. Launder, F. W. Schmidt, & J. H. Whitelaw (Eds.), *Turbulent Shear Flows 4* (pp. 246–260). Springer Berlin Heidelberg. https://doi.org/10.1007/978-3-642-69996-2_20

Nezu, I., & Rodi, W. (1985). Experimental study on secondary currents in open channel flow. *Proceedings of the 21st IAHR Congress*, 115–119.

Nezu, I., & Nakagawa, H. (1993). *Turbulence in Open-Channel Flows* (H. Nakagawa, Ed.; 1st Edition). Routledge. https://doi.org/10.1201/9780203734902

Nezu, I., Tominaga, A., & Nakagawa, H. (1993). Field Measurements of Secondary Currents in Straight Rivers. *Journal of Hydraulic Engineering*, *119*(5), 598–614. https://doi.org/10.1061/(ASCE)0733-9429(1993)119:5(598)

Nichols, A. (2013). *Free surface dynamics in shallow turbulent flows* [Doctoral dissertation, University of Bradford].

Nichols, A., & Rubinato, M. (2016). Remote sensing of environmental processes via low-cost 3d free-surface mapping. *Sustainable Hydraulics in the Era of Global Change*, 186–192.

Nichols, A., Tait, S., Horoshenkov, K., & Shepherd, S. (2013). A non-invasive airborne wave monitor. *Flow Measurement and Instrumentation*, *34*, 118–126. https://doi.org/10.1016/j.flowmeasinst.2013.09.006

Nichols, A., Tait, S. J., & Horoshenkov, K. V. (2012). Characterization of shallow flows using novel acoustic instrumentation. *River Flow 2012*, *2*, 1285–1292.

Nichols, A., Rubinato, M., Cho, Y.-H., & Wu, J. (2020). Optimal Use of Titanium Dioxide Colourant to Enable Water Surfaces to Be Measured by Kinect Sensors. *Sensors*, *20*(12), 3507. https://doi.org/10.3390/s20123507

Nichols, A., Tait, S. J., Horoshenkov, K. V., & Shepherd, S. J. (2016). A model of the free surface dynamics of shallow turbulent flows. *Journal of Hydraulic Research*, *54*(5), 516–526. https://doi.org/10.1080/00221686.2016.1176607

Nikora, V., & Goring, D. (2000). Flow Turbulence over Fixed and Weakly Mobile Gravel Beds. *Journal of Hydraulic Engineering*, *126*(9), 679–690. https://doi.org/10.1061/(ASCE)0733-9429(2000)126:9(679)

Nikora, V., Goring, D., McEwan, I., & Griffiths, G. (2001). Spatially Averaged Open-Channel Flow over Rough Bed. *Journal of Hydraulic Engineering*, *127*(2), 123–133. https://doi.org/10.1061/(ASCE)0733-9429(2001)127:2(123)

Nikora, V., Koll, K., McEwan, I., McLean, S., & Dittrich, A. (2004). Velocity Distribution in the Roughness Layer of Rough-Bed Flows. *Journal of Hydraulic Engineering*, *130*(10), 1036–1042. https://doi.org/10.1061/(ASCE)0733-9429(2004)130:10(1036)

Nishino, K., & Kasagi, N. (1990). Turbulence statistics measurement in a two-dimensional turbulent channel flow with the aid of the three-dimensional particle tracking velocimeter. *Transactions of the Japan Society of Mechanical Engineers Series B*, *56*(525), 1338–1347. https://doi.org/10.1299/kikaib.56.1338

Noss, C., Koca, K., Zinke, P., Henry, P.-Y., Navaratnam, C. U., Aberle, J., & Lorke, A. (2020). A Lagrangian drifter for surveys of water surface roughness in streams. *Journal of Hydraulic Research*, *58*(3), 471–488. https://doi.org/10.1080/00221686.2019.1623930

Onitsuka, K., & Nezu, I. (2001). Generation Mechanism of Turbulence-Driven Secondary Currents in Open-Channel Flows. In R. Moreau, T. Kambe, T. Nakano, & T. Miyauchi (Eds.), *IUTAM Symposium on Geometry and Statistics of Turbulence* (pp. 345–350, Vol. 59). Springer Netherlands. https://doi.org/10.1007/978-94-015-9638-1_45

Orteu, J.-J. (2009). 3-D computer vision in experimental mechanics. *Optics and Lasers in Engineering*, *47*(3-4), 282–291. https://doi.org/10.1016/j.optlaseng.2007.11.009

Pan, B. (2011). Recent Progress in Digital Image Correlation. *Experimental Mechanics*, *51*(7), 1223–1235. https://doi.org/10.1007/s11340-010-9418-3

Pan, B. (2018). Digital image correlation for surface deformation measurement: Historical developments, recent advances and future goals. *Measurement Science and Technology*, *29*(8), 082001. https://doi.org/10.1088/1361-6501/aac55b

Pan, B., Qian, K., Xie, H., & Asundi, A. (2009). Two-dimensional digital image correlation for in-plane displacement and strain measurement: A review. *Measurement Science and Technology*, *20*(6), 062001. https://doi.org/10.1088/0957-0233/20/6/062001

Pan, Y., & Banerjee, S. (1995). A numerical study of free-surface turbulence in channel flow. *Physics of Fluids*, *7*(7), 1649–1664. https://doi.org/10.1063/1.868483

Papantoniou, D., & Dracos, T. (1989). Analyzing 3-d turbulent motions in open channel flow by use of stereoscopy and particle tracking. *Proceedings of the Second European Turbulence Conference*. https://doi.org/10.1007/978-3-642-83822-4

Pecora, C. (2018). *Particle Tracking Velocimetry: A Review* [Doctoral dissertation, University of Washington].

Pedras, M. H., & De Lemos, M. J. (2001). Macroscopic turbulence modeling for incompressible flow through undeformable porous media. *International Journal of Heat and Mass Transfer*, *44*(6), 1081–1093. https://doi.org/10.1016/S0017-9310(00)00202-7

Perry, A. E., & Li, J. D. (1990). Experimental support for the attached-eddy hypothesis in zero-pressure-gradient turbulent boundary layers. *Journal of Fluid Mechanics*, *218*(-1), 405. https://doi.org/10.1017/S0022112090001057

Peters, W. H., & Ranson, W. F. (1982). Digital Imaging Techniques In Experimental Stress Analysis. *Optical Engineering*, *21*(3). https://doi.org/10.1117/12.7972925

Peters, W. H., Ranson, W. F., Sutton, M. A., Chu, T. C., & Anderson, J. (1983). Application Of Digital Correlation Methods To Rigid Body Mechanics. *Optical Engineering*, *22*(6). https://doi.org/10.1117/12.7973231

Plant, W., Keller, W., & Hayes, K. (2005). Measurement of river surface currents with coherent microwave systems. *IEEE Transactions on Geoscience and Remote Sensing*, *43*(6), 1242–1257. https://doi.org/10.1109/TGRS.2005.845641

Pokrajac, D., Finnigan, J. J., Manes, C., McEwan, I., & Nikora, V. (2006). On the definition of the shear velocity in rough bed open channel flows. *Proceedings of the International Conference on Fluvial Hydraulics*.

Pokrajac, D., Manes, C., & McEwan, I. (2007). Peculiar mean velocity profiles within a porous bed of an open channel. *Physics of Fluids*, *19*(9), 098109. https://doi.org/10.1063/1.2780193

Pokrajac, D., & Manes, C. (2009). Velocity Measurements of a Free-Surface Turbulent Flow Penetrating a Porous Medium Composed of Uniform-Size Spheres. *Transport in Porous Media*, *78*(3), 367–383. https://doi.org/10.1007/s11242-009-9339-8

Prinos, P., Sofialidis, D., & Keramaris, E. (2003). Turbulent Flow Over and Within a Porous Bed. *Journal of Hydraulic Engineering*, *129*(9), 720–733. https://doi.org/10.1061/(ASCE)0733-9429(2003)129:9(720)

Raffel, M., Kähler, C. J., Kompenhans, J., Scarano, F., Wereley, S. T., & Willert, C. E. (2018). *Particle Image Velocimetry: A Practical Guide* (3rd ed. 2018). Springer International Publishing : Imprint: Springer. https://doi.org/10.1007/978-3-319-68852-7

Rao, K. N., Narasimha, R., & Narayanan, M. A. B. (1971). The ‘bursting’ phenomenon in a turbulent boundary layer. *Journal of Fluid Mechanics*, *48*(2), 339–352. https://doi.org/10.1017/S0022112071001605

Rashidi, M. (1997). Burst–interface interactions in free surface turbulent flows. *Physics of Fluids*, *9*(11), 3485–3501. https://doi.org/10.1063/1.869457

Raupach, M. R. (1981). Conditional statistics of Reynolds stress in rough-wall and smooth-wall turbulent boundary layers. *Journal of Fluid Mechanics*, *108*, 363–382. https://doi.org/10.1017/S0022112081002164

Raupach, M. R., Antonia, R. A., & Rajagopalan, S. (1991). Rough-Wall Turbulent Boundary Layers. *Applied Mechanics Reviews*, *44*(1), 1–25. https://doi.org/10.1115/1.3119492

Raupach, M. R., & Shaw, R. H. (1982). Averaging procedures for flow within vegetation canopies. *Boundary-Layer Meteorology*, *22*(1), 79–90. https://doi.org/10.1007/BF00128057

Rayleigh, L. (1883). The Form of Standing Waves on the Surface of Running Water. *Proceedings of the London Mathematical Society*, *s1-15*(1), 69–78. https://doi.org/10.1112/plms/s1-15.1.69

Remondino, F. (2011). Heritage Recording and 3D Modeling with Photogrammetry and 3D Scanning. *Remote Sensing*, *3*(6), 1104–1138. https://doi.org/10.3390/rs3061104

Reu, P. (2013). A Study of the Influence of Calibration Uncertainty on the Global Uncertainty for Digital Image Correlation Using a Monte Carlo Approach. *Experimental Mechanics*, *53*(9), 1661–1680. https://doi.org/10.1007/s11340-013-9746-1

Roy, A. G., Buffin-Blanger, T., Lamarre, H., & Kirkbride, A. D. (2004). Size, shape and dynamics of large-scale turbulent flow structures in a gravel-bed river. *Journal of Fluid Mechanics*, *500*, 1–27. https://doi.org/10.1017/S0022112003006396

Rudraiah, N. (1985). Coupled Parallel Flows in a Channel and a Bounding Porous Medium of Finite Thickness. *Journal of Fluids Engineering*, *107*(3), 322–329. https://doi.org/10.1115/1.3242486

Ruff, J. F., & Gelhar, L. W. (1970). *Porous Boundary Effects in Turbulent Shear Flow* (R No. 126). Massachusetts Institute of Technology. Department of Civil Engineering. Cambridge, Massachusetts.

Savelsberg, R., Holten, A., & Van De Water, W. (2006). Measurement of the gradient field of a turbulent free surface. *Experiments in Fluids*, *41*(4), 629–640. https://doi.org/10.1007/s00348-006-0186-x

Savelsberg, R., & Van De Water, W. (2008). Turbulence of a Free Surface. *Physical Review Letters*, *100*(3), 034501. https://doi.org/10.1103/PhysRevLett.100.034501

Savelsberg, R., & Van De Water, W. (2009). Experiments on free-surface turbulence. *Journal of Fluid Mechanics*, *619*, 95–125. https://doi.org/10.1017/S0022112008004369

Sayers, P. B., Horritt, M., Penning-Rowsell, E., & McKenzie, A. (2015). *Climate change risk assessment 2017: Projections of future flood risk in the UK.*

Scarano, F. (2013). Tomographic PIV: Principles and practice. *Measurement Science and Technology*, *24*(1), 012001. https://doi.org/10.1088/0957-0233/24/1/012001

Schanz, D., Gesemann, S., & Schröder, A. (2016). Shake-The-Box: Lagrangian particle tracking at high particle image densities. *Experiments in Fluids*, *57*(5), 70. https://doi.org/10.1007/s00348-016-2157-1

Schanz, D., Gesemann, S., Schröder, A., Wieneke, B., & Novara, M. (2013a). Non-uniform optical transfer functions in particle imaging: Calibration and application to tomographic reconstruction. *Measurement Science and Technology*, *24*(2), 024009. https://doi.org/10.1088/0957-0233/24/2/024009

Schanz, D., Schroder, A., Gesemann, S., Michaelis, D., & Wieneke, B. (2013b). 'Shake-The-Box ': A highly efficient and accurate tomographic particle tracking velocimetry (tomo-ptv) method using prediction of particle positions.

Schanz, D., Schroder, A., Gesemann, S., & Wieneke, B. (2015). 'Shake-The-Box': Lagrangian particle tracking in densely seeded flows at high spatial resolution.

Schreier, H. W. (2000). Systematic errors in digital image correlation caused by intensity interpolation. *Optical Engineering*, *39*(11), 2915. https://doi.org/10.1117/1.1314593

Shemdin, O. (1990). Measurement of Short Surface Waves with Stereophotography. *Conference Proceedings on Engineering in the Ocean Environment*, 568–571. https://doi.org/10.1109/OCEANS.1990.584829

Sheu, Y.-H., Chang, T., Tatterson, G., & Dickey, D. (1982). A three dimensional measurement technique for turbulent flows. *Chemical Engineering Communications*, *17*(1-6), 67–83. https://doi.org/10.1080/00986448208911615

Shrira, V. I. (1993). Surface waves on shear currents: Solution of the boundary-value problem. *Journal of Fluid Mechanics*, *252*, 565–584. https://doi.org/10.1017/S002211209300388X

Shvidchenko, A. B., & Pender, G. (2001). Macroturbulent structure of open-channel flow over gravel beds. *Water Resources Research*, *37*(3), 709–719. https://doi.org/10.1029/2000WR900280

Singh, K. M., Sandham, N. D., & Williams, J. J. R. (2007). Numerical Simulation of Flow over a Rough Bed. *Journal of Hydraulic Engineering*, *133*(4), 386–398. https://doi.org/10.1061/(ASCE)0733-9429(2007)133:4(386)

Slingo, J. (2021). Latest scientific evidence for observed and projected climate change. In R. Betts, A. Haward, & K. Pearson (Eds.), *The Third UK Climate Change Risk Assessment Technical Report* (pp. 1–107).

Smith, J. D., & McLean, S. R. (1977). Spatially averaged flow over a wavy surface. *Journal of Geophysical Research*, *82*(12), 1735–1746. https://doi.org/10.1029/JC082i012p01735

Smolentsev, S., & Miraghaie, R. (2005). Study of a free surface in open-channel water flows in the regime from “weak” to “strong” turbulence. *International Journal of Multiphase Flow*, *31*(8), 921–939. https://doi.org/10.1016/j.ijmultiphaseflow.2005.05.008

Stoesser, T., Frohlich, J., & Rodi, W. (2007). Turbulent open-channel flow over a permeable bed.

Stoesser, T., Fröhlich, J., & Rodi, W. (2006). Large eddy simulation of open-channel flow over and through two layers of spheres.

Strickler, A. (1924). Beiträge zur Frage der Geschwindigkeitsformel und der Rauigkeitszahlen für Ströme, Kanäle und geschlossene Leitungen. https://doi.org/10.5169/SEALS-82804

Stull, R. B. (2003). *An introduction to boundary layer meteorology*. Kluwer.

Suga, K., Matsumura, Y., Ashitaka, Y., Tominaga, S., & Kaneda, M. (2010). Effects of wall permeability on turbulence. *International Journal of Heat and Fluid Flow*, *31*(6), 974–984. https://doi.org/10.1016/j.ijheatfluidflow.2010.02.023

Sutton, M., Mingqi, C., Peters, W., Chao, Y., & McNeill, S. (1986). Application of an optimized digital correlation method to planar deformation analysis. *Image and Vision Computing*, *4*(3), 143–150. https://doi.org/10.1016/0262-8856(86)90057-0

Sutton, M., Wolters, W., Peters, W., Ranson, W., & McNeill, S. (1983). Determination of displacements using an improved digital correlation method. *Image and Vision Computing*, *1*(3), 133–139. https://doi.org/10.1016/0262-8856(83)90064-1

Svensson, U., & Rahm, L. (1991). Toward a mathematical model of oxygen transfer to and within bottom sediments. *Journal of Geophysical Research: Oceans*, *96*(C2), 2777–2783. https://doi.org/10.1029/90JC02209

Takeda, M., Ina, H., & Kobayashi, S. (1982). Fourier-transform method of fringe-pattern analysis for computer-based topography and interferometry. *Journal of the Optical Society of America*, *72*(1), 156. https://doi.org/10.1364/JOSA.72.000156

Tamburrino, A., & Gulliver, J. S. (2007). Free-surface visualization of streamwise vortices in a channel flow. *Water Resources Research*, *43*(11). https://doi.org/10.1029/2007WR005988

Tani, K., & Fujita, I. (2018). Wavenumber-frequency analysis of river surface texture to improve accuracy of image-based velocimetry (A. Paquier & N. Rivière, Eds.). *E3S Web of Conferences*, *40*, 06012. https://doi.org/10.1051/e3sconf/20184006012

Teixeira, M., & Belcher, S. (2006). On the initiation of surface waves by turbulent shear flow. *Dynamics of Atmospheres and Oceans*, *41*(1), 1–27. https://doi.org/10.1016/j.dynatmoce.2005.10.001

Teixeira, M. A. C. (2019). Wavelet spectral analysis of the free surface of turbulent flows By Giulio Dolcetti and Héctor García Nava. *Journal of Hydraulic Research*, *57*(4), 603–604. https://doi.org/10.1080/00221686.2018.1555560

Tong, W. (2005). An Evaluation of Digital Image Correlation Criteria for Strain Mapping Applications. *Strain*, *41*(4), 167–175. https://doi.org/10.1111/j.1475-1305.2005.00227.x

Townsend, A. A. (1999). *The structure of turbulent shear flow* (2nd Edition). Cambridge Univ. Pr.

Tropea, C., Yarin, A. L., & Foss, J. F. (Eds.). (2007). *Springer Handbook of Experimental Fluid Mechanics*. Springer Berlin Heidelberg. https://doi.org/10.1007/978-3-540-30299-5

Tsubaki, R., & Fujita, I. (2005). Stereoscopic measurement of a fluctuating free surface with discontinuities. *Measurement Science and Technology*, *16*(10), 1894–1902. https://doi.org/10.1088/0957-0233/16/10/003

Tsubaki, R., Fujita, I., & Tsutsumi, S. (2011). Measurement of the flood discharge of a small-sized river using an existing digital video recording system. *Journal of Hydro-environment Research*, *5*(4), 313–321. https://doi.org/10.1016/j.jher.2010.12.004

Turney, D. E., Anderer, A., & Banerjee, S. (2009). A method for three-dimensional interfacial particle image velocimetry (3D-IPIV) of an air–water interface. *Measurement Science and Technology*, *20*(4), 045403. https://doi.org/10.1088/0957-0233/20/4/045403

Vandenberghe, S., D'Asseler, Y., Van De Walle, R., Kauppinen, T., Koole, M., Bouwens, L., Van Laere, K., Lemahieu, I., & Dierckx, R. (2001). Iterative reconstruction algorithms in nuclear medicine. *Computerized Medical Imaging and Graphics*, *25*(2), 105–111. https://doi.org/10.1016/S0895-6111(00)00060-4

Vendroux, G., & Knauss, W. G. (1998). Submicron deformation field measurements: Part 2. Improved digital image correlation. *Experimental Mechanics*, *38*(2), 86–92. https://doi.org/10.1007/BF02321649

Waas, S., & Jähne, B. (1992). Combined slope-height measurements of short wind waves: First results from field and laboratory measurements. In L. Estep (Ed.). https://doi.org/10.1117/12.138858

Walsh, E. J., Hancock, D. W., Hines, D. E., Swift, R. N., & Scott, J. F. (1985). Directional Wave Spectra Measured with the Surface Contour Radar. *Journal of Physical Oceanography*, *15*(5), 566–592. https://doi.org/10.1175/1520-0485(1985)015⟨0566:DWSMWT⟩2.0.CO;2

Wang, Y., Mingotaud, C., & Patterson, L. K. (1991). Noncontact monitoring of liquid surface levels with a precision of 10 micrometers: A simple ultrasound device. *Review of Scientific Instruments*, *62*(6), 1640–1641. https://doi.org/10.1063/1.1142445

Wang, Z., Wang, C., & Chen, K. (2001). Two-phase flow and transport in the air cathode of proton exchange membrane fuel cells. *Journal of Power Sources*, *94*(1), 40–50. https://doi.org/10.1016/S0378-7753(00)00662-5

Weigand, A. (1996). Simultaneous mapping of the velocity and deformation field at a free surface. *Experiments in Fluids*, *20*(5), 358–364. https://doi.org/10.1007/BF00191017

Welber, M., Le Coz, J., Laronne, J. B., Zolezzi, G., Zamler, D., Dramais, G., Hauet, A., & Salvaro, M. (2016). Field assessment of noncontact stream gauging using portable surface velocity radars (SVR). *Water Resources Research*, *52*(2), 1108–1126. https://doi.org/10.1002/2015WR017906

Westerweel, J. (1993). Analysis of PIV interrogation with low-pixel resolution. In S. S. Cha & J. D. Trolinger (Eds.). https://doi.org/10.1117/12.163745

Whitaker, S. (1967). Diffusion and dispersion in porous media. *AIChE Journal*, *13*(3), 420–427. https://doi.org/10.1002/aic.690130308

Wieneke, B. (2008). Volume self-calibration for 3D particle image velocimetry. *Experiments in Fluids*, *45*(4), 549–556. https://doi.org/10.1007/s00348-008-0521-5

Wieneke, B. (2013). Iterative reconstruction of volumetric particle distribution. *Measurement Science and Technology*, *24*(2), 024008. https://doi.org/10.1088/0957-0233/24/2/024008

Wiener, N. (1949). *Extrapolation, Interpolation, and Smoothing of Stationary Time Series: With Engineering Applications*. The MIT Press. https://doi.org/10.7551/mitpress/2946.001.0001

Wilkinson, R. T., & Allison, S. (1989). Age and Simple Reaction Time: Decade Differences for 5,325 Subjects. *Journal of Gerontology*, *44*(2), P29–P35. https://doi.org/10.1093/geronj/44.2.P29

Willert, C. E., & Gharib, M. (1991). Digital particle image velocimetry. *Experiments in Fluids*, *10*(4), 181–193. https://doi.org/10.1007/BF00190388

Willneff, J. (2003). *A Spatio-Temporal Matching Algorithm for 3D Particle Tracking Velocimetry* [Doctoral dissertation, ETH Zurich].

Wilson, N. R., & Shaw, R. H. (1977). A Higher Order Closure Model for Canopy Flow. *Journal of Applied Meteorology*, *16*(11), 1197–1205. https://doi.org/10.1175/1520-0450(1977)016⟨1197:AHOCMF⟩2.0.CO;2

Woodget, A. S., Austrums, R., Maddock, I. P., & Habit, E. (2017). Drones and digital photogrammetry: From classifications to continuums for monitoring river habitat and hydromorphology. *WIREs Water*, *4*(4), e1222. https://doi.org/10.1002/wat2.1222

Wu, J., Nichols, A., Krynkin, A., & Croft, M. (2022). Digital Image Correlation for stereoscopic measurement of water surface dynamics in a partially filled pipe. *Acta Geophysica*, *70*(5), 2451–2467. https://doi.org/10.1007/s11600-022-00792-w

Yaofeng, S., & Pang, J. H. (2007). Study of optimal subset size in digital image correlation of speckle pattern images. *Optics and Lasers in Engineering*, *45*(9), 967–974. https://doi.org/10.1016/j.optlaseng.2007.01.012

Yih, C.-S. (1972). Surface waves in flowing water. *Journal of Fluid Mechanics*, *51*(2), 209–220. https://doi.org/10.1017/S002211207200117X

Yoneyama, S., Kitagawa, A., Kitamura, K., & Kikuta, H. (2006). In-Plane Displacement Measurement Using Digital Image Correlation with Lens Distortion Correction. *JSME International Journal Series A*, *49*(3), 458–467. https://doi.org/10.1299/jsmea.49.458

Yoshimura, H., & Fujita, I. (2020). Investigation of free-surface dynamics in an open-channel flow. *Journal of Hydraulic Research*, *58*(2), 231–247. https://doi.org/10.1080/00221686.2018.1561531

Young, I. (1994). On the measurement of directional wave spectra. *Applied Ocean Research*, *16*(5), 283–294. https://doi.org/10.1016/0141-1187(94)90017-5

Young, W. R., & Wolfe, C. L. (2014). Generation of surface waves by shear-flow instability. *Journal of Fluid Mechanics*, *739*, 276–307. https://doi.org/10.1017/jfm.2013.617

Zagni, A. F. E., & Smith, K. V. H. (1976). Channel Flow Over Permeable Beds of Graded Spheres. *Journal of the Hydraulics Division*, *102*(2), 207–222. https://doi.org/10.1061/JYCEAJ.0004482

Zakharov, V., & Shrira, V. (1990). Formation of the angular spectrum of wind waves. *Soviet physics, JETP*, *71*.

Zhang, C., Shen, L., & Yue, D. K. P. (1999). The mechanism of vortex connection at a free surface. *Journal of Fluid Mechanics*, *384*, 207–241. https://doi.org/10.1017/S0022112099004243

Zhang, X., & Cox, C. S. (1994). Measuring the two-dimensional structure of a wavy water surface optically: A surface gradient detector. *Experiments in Fluids*, *17*(4), 225–237. https://doi.org/10.1007/BF00203041

Zhang, Z. (2000). A flexible new technique for camera calibration. *IEEE Transactions on Pattern Analysis and Machine Intelligence*, *22*(11), 1330–1334. https://doi.org/10.1109/34.888718

Zippe, H. J., & Graf, W. H. (1983). Turbulent boundary layer flow over permeable and non-permeable rough surfaces. *Journal of Hydraulic Research*, *21*(1), 51–65. https://doi.org/10.1080/00221688309499450

Znamenskaya, N. S. (1963). Experimental study of the dune movement of sediment. *Soviet Hydrology*, 253–275.

Zoheidi, L. (2018). *Flow characterization of milk protein foam transport in inner geometries* [Doctoral dissertation].

Appendix

The results from the PTV and DIC are extensively presented in this Appendix. Following the structure used in the main part of the text, PTV results are shown before the DIC results. The format used for presenting the plots is kept the same.

For the PTV:
Figure A.1: streamwise and lateral frequency-wavenumber spectra of the streamwise turbulent velocity for Q1_H at different planes.
Figure A.2: streamwise and lateral frequency-wavenumber spectra of the vertical turbulent velocity for Q1_H at different planes.
Figure A.3: streamwise and lateral frequency-wavenumber spectra of the streamwise turbulent velocity for Q2_H at different planes.
Figure A.4: streamwise and lateral frequency-wavenumber spectra of the vertical turbulent velocity for Q2_H at different planes.
Figure A.5: streamwise and lateral frequency-wavenumber spectra of the streamwise turbulent velocity for Q3_H at different planes.
Figure A.6: streamwise and lateral frequency-wavenumber spectra of the vertical turbulent velocity for Q3_H at different planes.
Figure A.7: streamwise and lateral frequency-wavenumber spectra of the streamwise turbulent velocity for Q4_H at different planes.
Figure A.8: streamwise and lateral frequency-wavenumber spectra of the vertical turbulent velocity for Q4_H at different planes.
Figure A.9: streamwise and lateral frequency-wavenumber spectra of the streamwise turbulent velocity for Q5_H at different planes.
Figure A.10: streamwise and lateral frequency-wavenumber spectra of the vertical turbulent velocity for Q5_H at different planes.
Figure A.11: streamwise and lateral frequency-wavenumber spectra of the streamwise turbulent velocity for Q6_H at different planes.
Figure A.12: streamwise and lateral frequency-wavenumber spectra of the vertical turbulent velocity for Q6_H at different planes.
Figure A.13: streamwise and lateral frequency-wavenumber spectra of the streamwise turbulent velocity for M1_H at different planes.
Figure A.14: streamwise and lateral frequency-wavenumber spectra of the vertical turbulent velocity for M1_H at different planes.
Figure A.15: streamwise and lateral frequency-wavenumber spectra of the streamwise turbulent

velocity for M2_H at different planes.
Figure A.16: streamwise and lateral frequency-wavenumber spectra of the vertical turbulent velocity for M2_H at different planes.
Figure A.17: streamwise and lateral frequency-wavenumber spectra of the streamwise turbulent velocity for M3_H at different planes.
Figure A.18: streamwise and lateral frequency-wavenumber spectra of the vertical turbulent velocity for M3_H at different planes.
Figure A.19: streamwise and lateral frequency-wavenumber spectra of the streamwise turbulent velocity for M4_H at different planes.
Figure A.20: streamwise and lateral frequency-wavenumber spectra of the vertical turbulent velocity for M4_H at different planes.
Figure A.21: streamwise and lateral frequency-wavenumber spectra of the streamwise turbulent velocity for M5_H at different planes.
Figure A.22: streamwise and lateral frequency-wavenumber spectra of the vertical turbulent velocity for M5_H at different planes.
Figure A.23: streamwise and lateral frequency-wavenumber spectra of the streamwise turbulent velocity for M6_H at different planes.
Figure A.24: streamwise and lateral frequency-wavenumber spectra of the vertical turbulent velocity for M6_H at different planes.
Figure A.25: streamwise and lateral frequency-wavenumber spectra of the streamwise turbulent velocity for A2_H at different planes.
Figure A.26: streamwise and lateral frequency-wavenumber spectra of the vertical turbulent velocity for A2_H at different planes.
Figure A.27: streamwise and lateral frequency-wavenumber spectra of the streamwise turbulent velocity for A3_H at different planes.
Figure A.28: streamwise and lateral frequency-wavenumber spectra of the vertical turbulent velocity for A3_H at different planes.
Figure A.29: streamwise and lateral frequency-wavenumber spectra of the streamwise turbulent velocity for A5_H at different planes.
Figure A.30: streamwise and lateral frequency-wavenumber spectra of the vertical turbulent velocity for A5_H at different planes.
Figure A.31: streamwise and lateral frequency-wavenumber spectra of the streamwise turbulent velocity for A6_H at different planes.
Figure A.32: streamwise and lateral frequency-wavenumber spectra of the vertical turbulent velocity for A6_H at different planes.

For the DIC:
Figure A.33: streamwise and lateral frequency-wavenumber spectra of the free-surface elevation for Q3_S, Q5_S and Q6_S.
Figure A.34: streamwise and lateral frequency-wavenumber spectra of the free-surface elevation for M5_S and M6_S.
Figure A.35: streamwise and lateral frequency-wavenumber spectra of the free-surface elevation for A3_S, A5_S and A6_S.

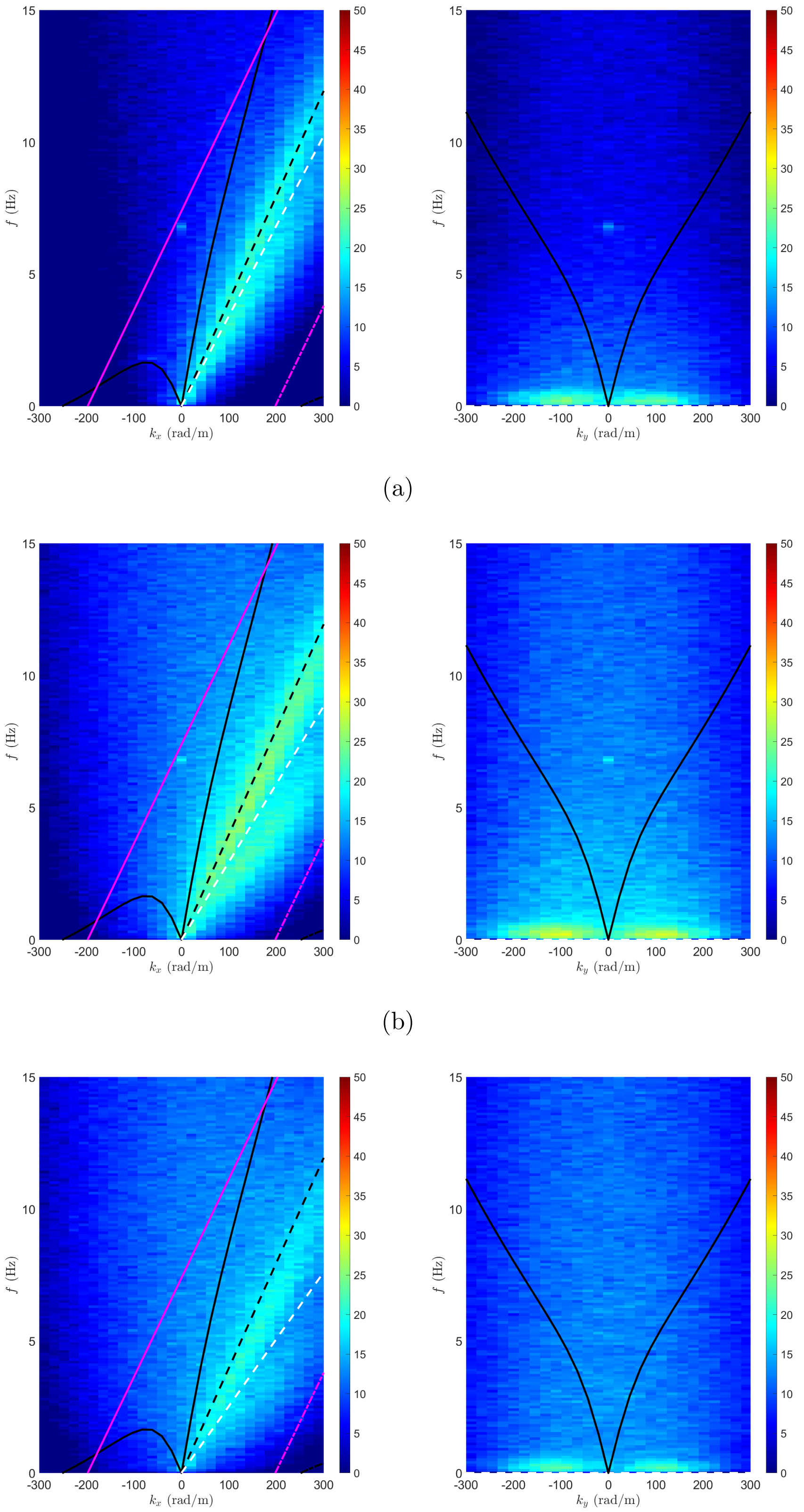

(a)

(b)

(c)

Figure A.1: Streamwise (left) and lateral (right) frequency-wavenumber spectra of the streamwise turbulent velocity for Q1_H at planes a) ”A”, b) ”C” and c) ”E”. Black lines: dashed is for non-dispersive structures advecting at U_S (Eq. 4.1), solid and dashed-dotted are positive and negative solutions for gravity-capillary waves (Eq. 4.2). White-dashed line: structures advecting at $\langle \bar{U} \rangle_{xz,plane_i}$. Magenta lines: solid and dashed-dotted are positive and negative solutions for gravity-capillary waves with $k = k_0$ (modified Eq. 4.2).

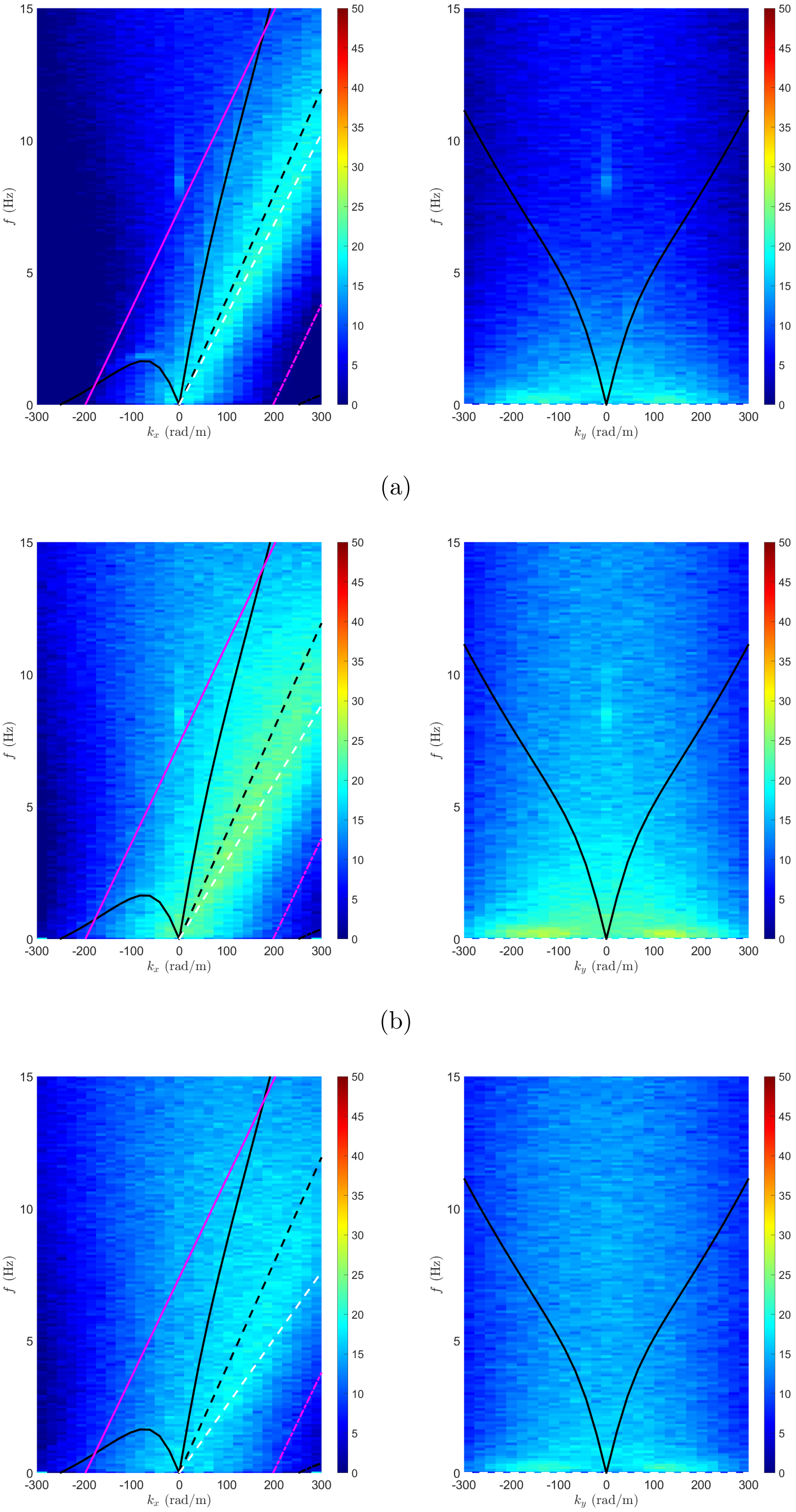

(a)

(b)

(c)

Figure A.2: Streamwise (left) and lateral (right) frequency-wavenumber spectra of the vertical turbulent velocity for Q1_H at planes a) "A", b) "C" and c) "E". Black lines: dashed is for non-dispersive structures advecting at U_S (Eq. 4.1), solid and dashed-dotted are positive and negative solutions for gravity-capillary waves (Eq. 4.2). White-dashed line: structures advecting at $\langle \bar{U} \rangle_{xz,plane_i}$. Magenta lines: solid and dashed-dotted are positive and negative solutions for gravity-capillary waves with $k = k_0$ (modified Eq. 4.2).

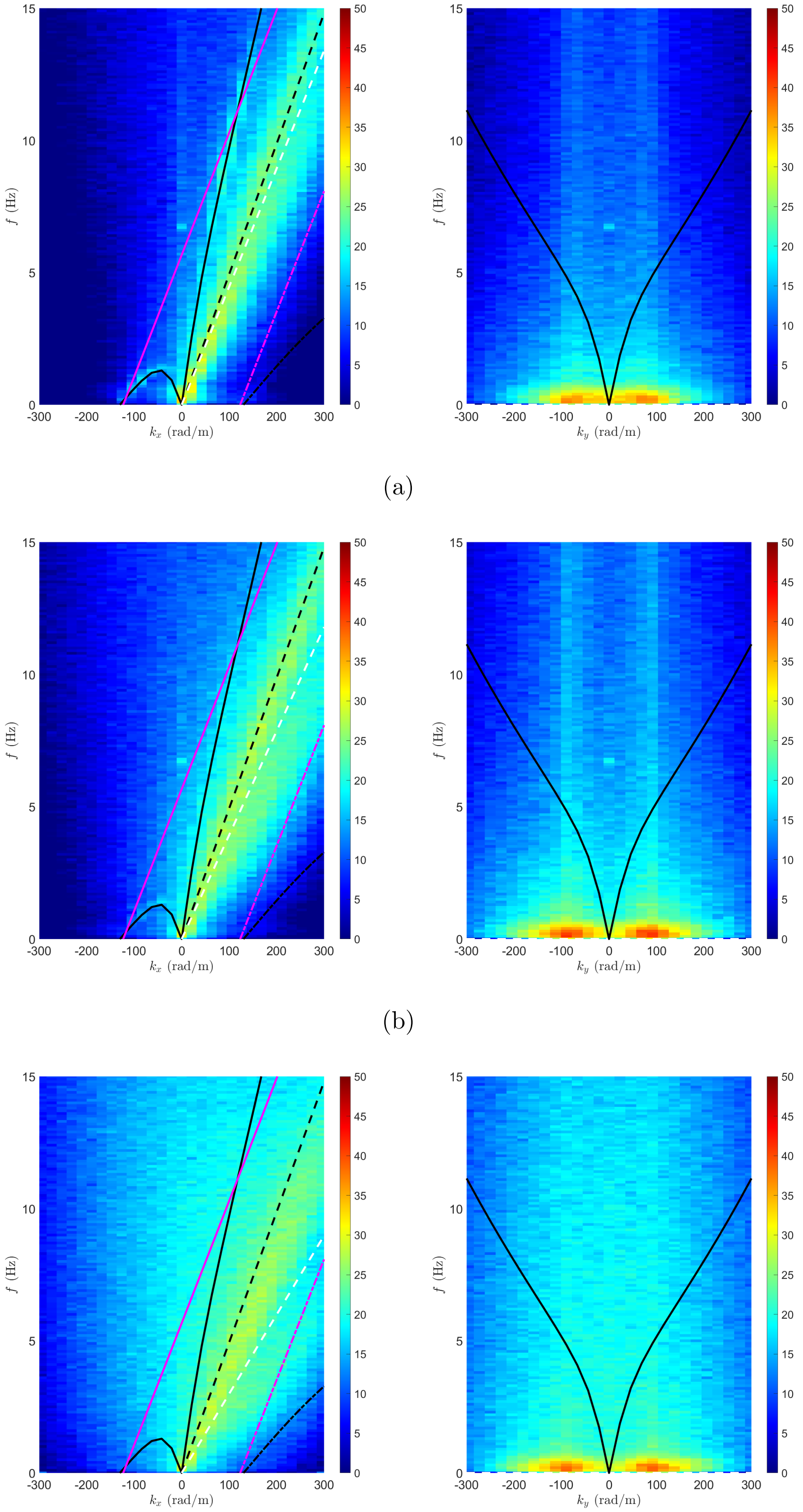

(a)

(b)

(c)

Figure A.3: Streamwise (left) and lateral (right) frequency-wavenumber spectra of the streamwise turbulent velocity for Q2_H at planes a) "A", b) "C" and c) "E". Black lines: dashed is for non-dispersive structures advecting at U_S (Eq. 4.1), solid and dashed-dotted are positive and negative solutions for gravity-capillary waves (Eq. 4.2). White-dashed line: structures advecting at $\langle \bar{U} \rangle_{xz,plane_i}$. Magenta lines: solid and dashed-dotted are positive and negative solutions for gravity-capillary waves with $k = k_0$ (modified Eq. 4.2).

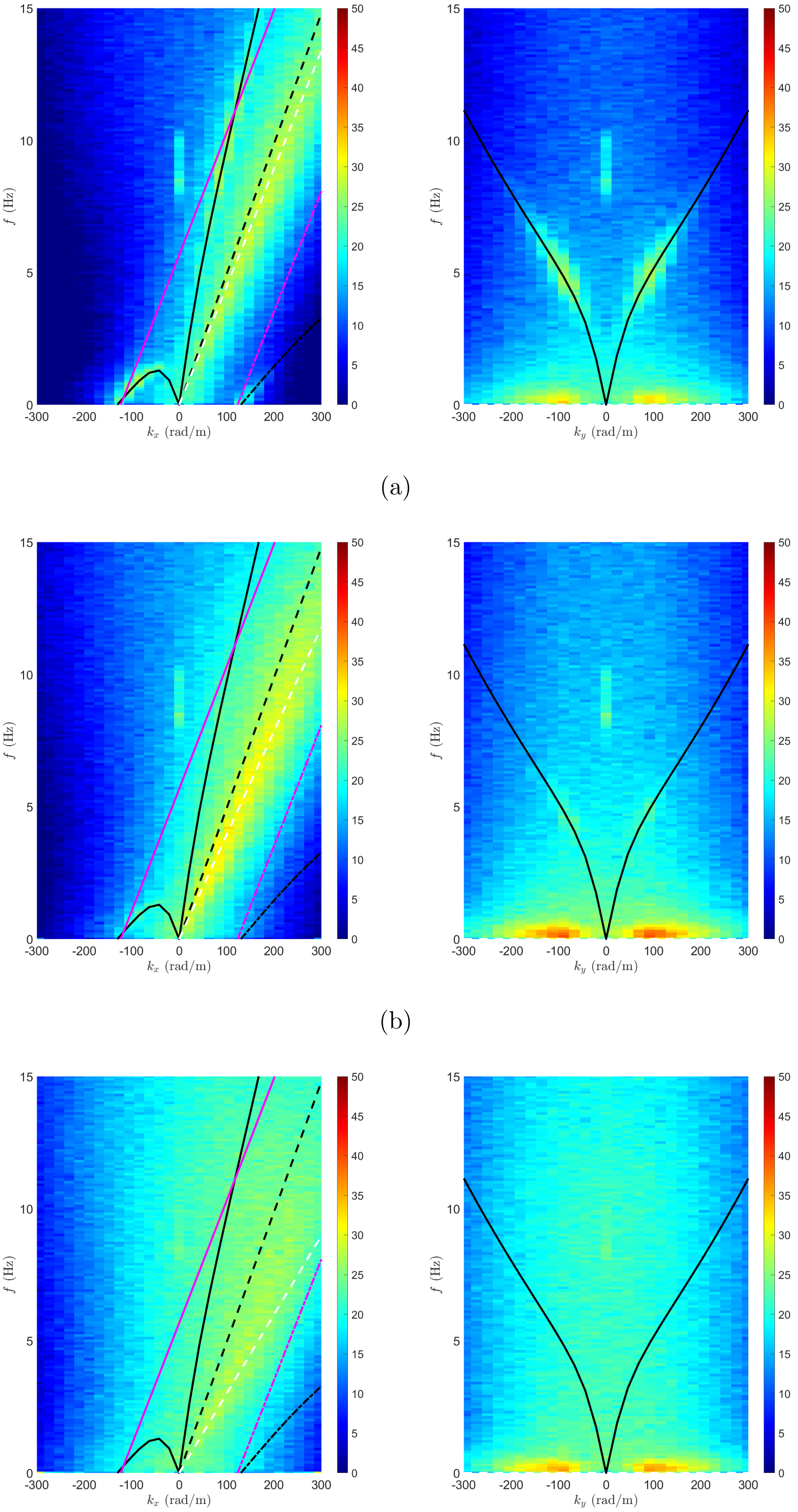

(a)

(b)

(c)

Figure A.4: Streamwise (left) and lateral (right) frequency-wavenumber spectra of the vertical turbulent velocity for Q2_H at planes a) "A", b) "C" and c) "E". Black lines: dashed is for non-dispersive structures advecting at U_S (Eq. 4.1), solid and dashed-dotted are positive and negative solutions for gravity-capillary waves (Eq. 4.2). White-dashed line: structures advecting at $\langle \bar{U} \rangle_{xz,plane_i}$. Magenta lines: solid and dashed-dotted are positive and negative solutions for gravity-capillary waves with $k = k_0$ (modified Eq. 4.2).

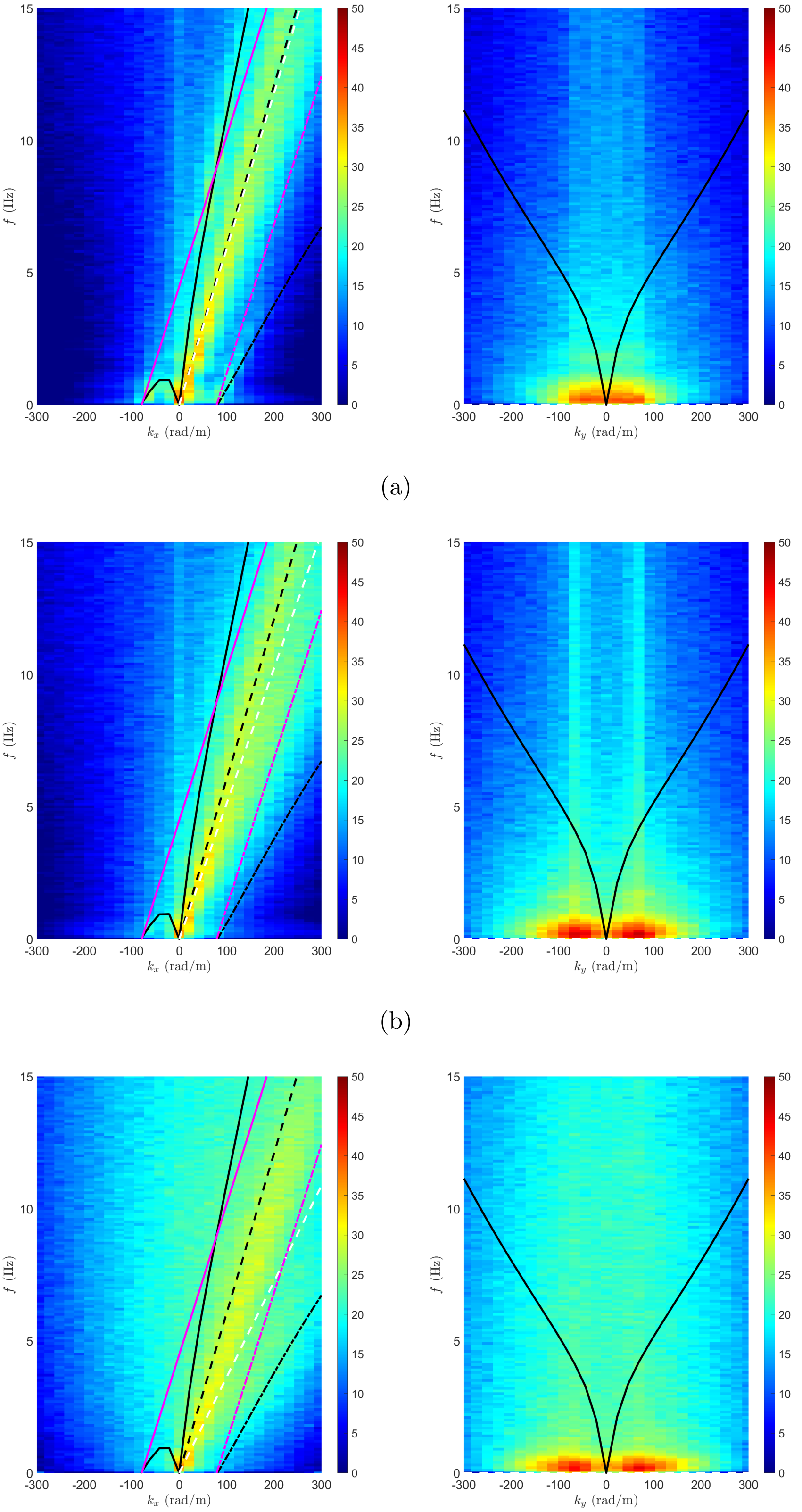

(a)

(b)

(c)

Figure A.5: Streamwise (left) and lateral (right) frequency-wavenumber spectra of the streamwise turbulent velocity for Q3_H at planes a) "A", b) "C" and c) "E". Black lines: dashed is for non-dispersive structures advecting at U_S (Eq. 4.1), solid and dashed-dotted are positive and negative solutions for gravity-capillary waves (Eq. 4.2). White-dashed line: structures advecting at $\langle \bar{U} \rangle_{xz,plane_i}$. Magenta lines: solid and dashed-dotted are positive and negative solutions for gravity-capillary waves with $k = k_0$ (modified Eq. 4.2).

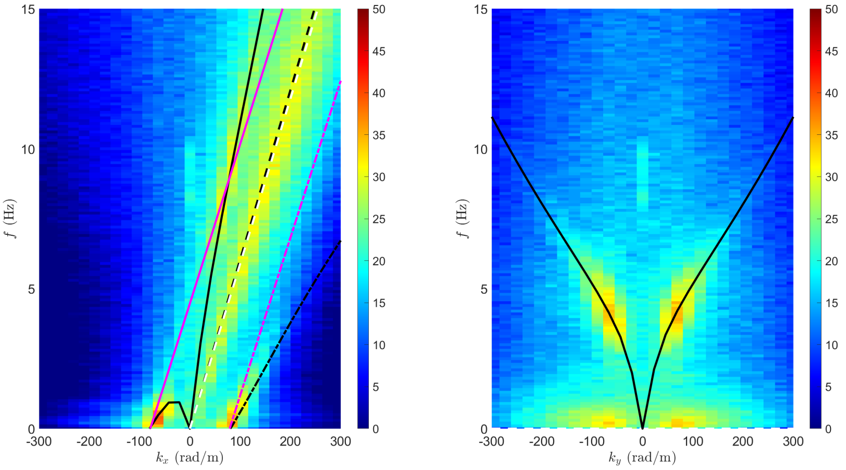

(a)

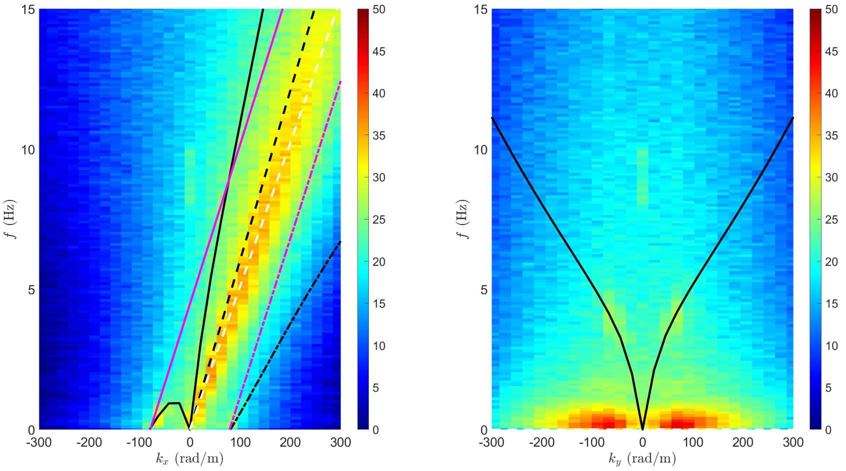

(b)

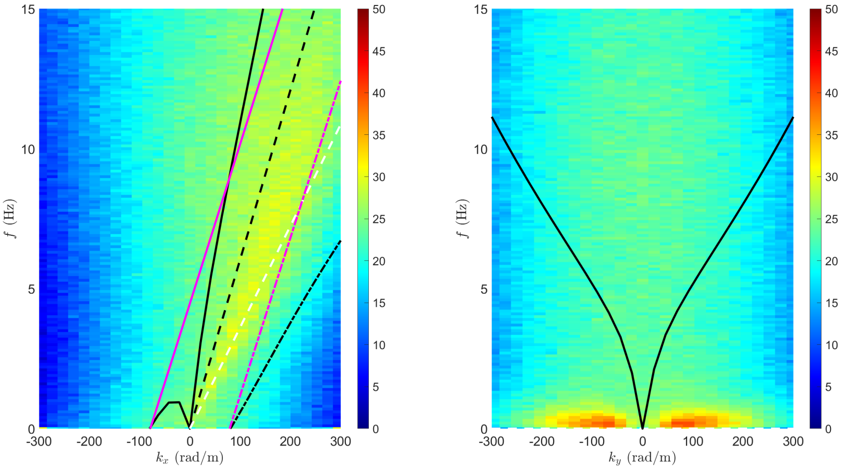

(c)

Figure A.6: Streamwise (left) and lateral (right) frequency-wavenumber spectra of the vertical turbulent velocity for Q3_H at planes a) "A", b) "C" and c) "E". Black lines: dashed is for non-dispersive structures advecting at U_S (Eq. 4.1), solid and dashed-dotted are positive and negative solutions for gravity-capillary waves (Eq. 4.2). White-dashed line: structures advecting at $\langle \bar{U} \rangle_{xz,plane_i}$. Magenta lines: solid and dashed-dotted are positive and negative solutions for gravity-capillary waves with $k = k_0$ (modified Eq. 4.2).

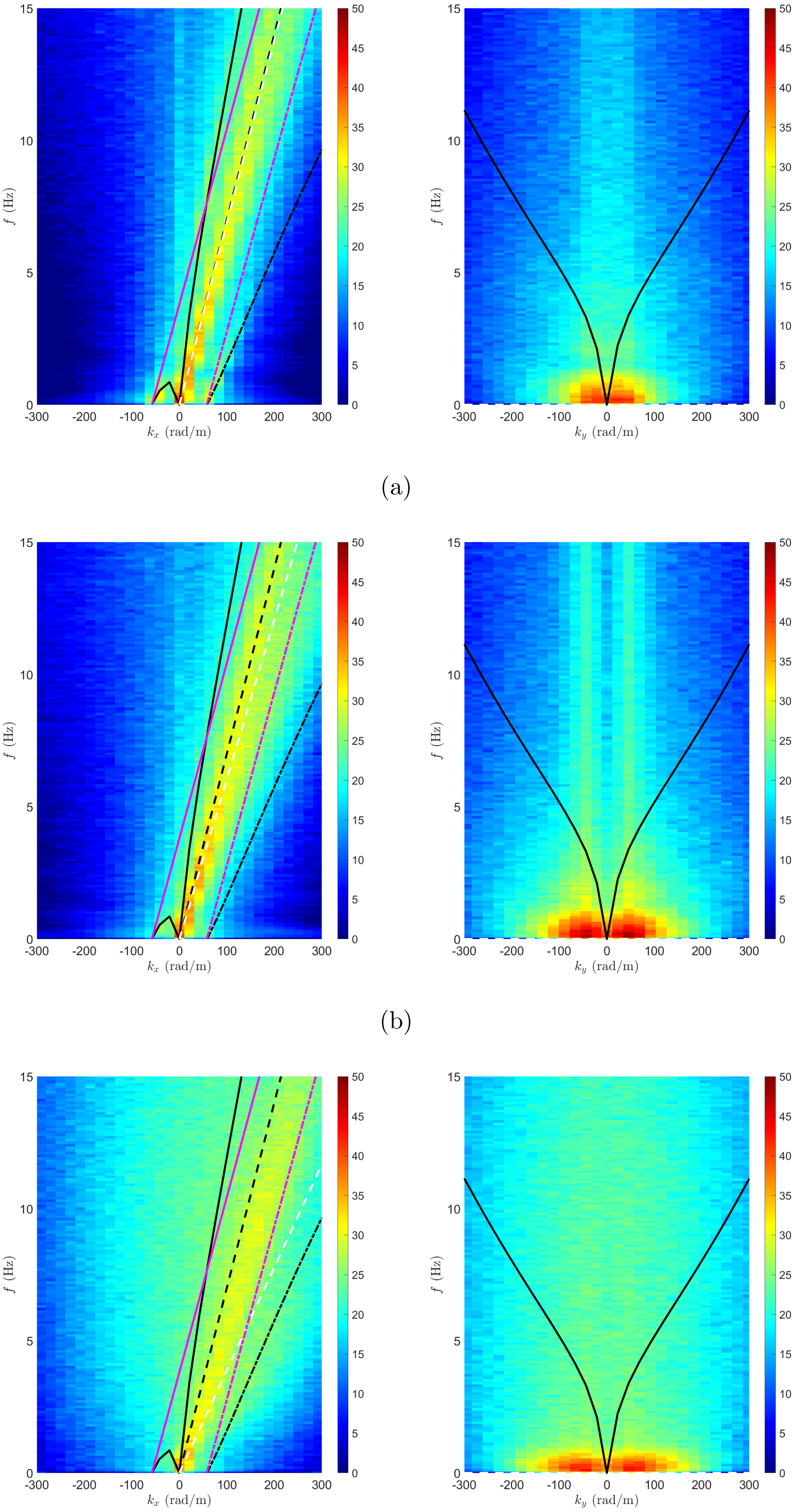

(a)

(b)

(c)

Figure A.7: Streamwise (left) and lateral (right) frequency-wavenumber spectra of the streamwise turbulent velocity for Q4_H at planes a) ”A”, b) ”C” and c) ”E”. Black lines: dashed is for non-dispersive structures advecting at U_S (Eq. 4.1), solid and dashed-dotted are positive and negative solutions for gravity-capillary waves (Eq. 4.2). White-dashed line: structures advecting at $\langle \bar{U} \rangle_{xz,plane_i}$. Magenta lines: solid and dashed-dotted are positive and negative solutions for gravity-capillary waves with $k = k_0$ (modified Eq. 4.2).

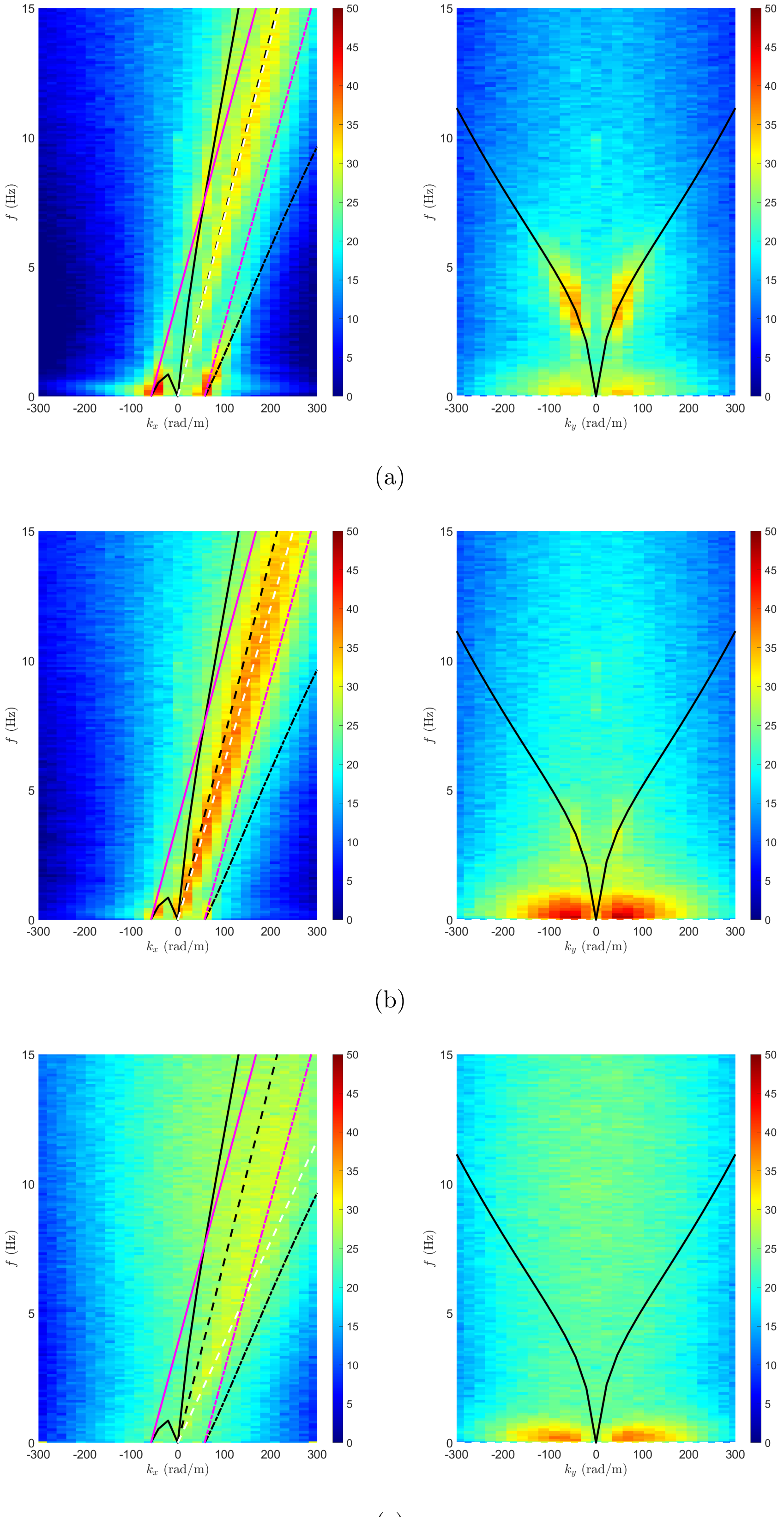

(a)

(b)

(c)

Figure A.8: Streamwise (left) and lateral (right) frequency-wavenumber spectra of the vertical turbulent velocity for Q4_H at planes a) ”A”, b) ”C” and c) ”E”. Black lines: dashed is for non-dispersive structures advecting at U_S (Eq. 4.1), solid and dashed-dotted are positive and negative solutions for gravity-capillary waves (Eq. 4.2). White-dashed line: structures advecting at $\langle \bar{U} \rangle_{xz,plane_i}$. Magenta lines: solid and dashed-dotted are positive and negative solutions for gravity-capillary waves with $k = k_0$ (modified Eq. 4.2).

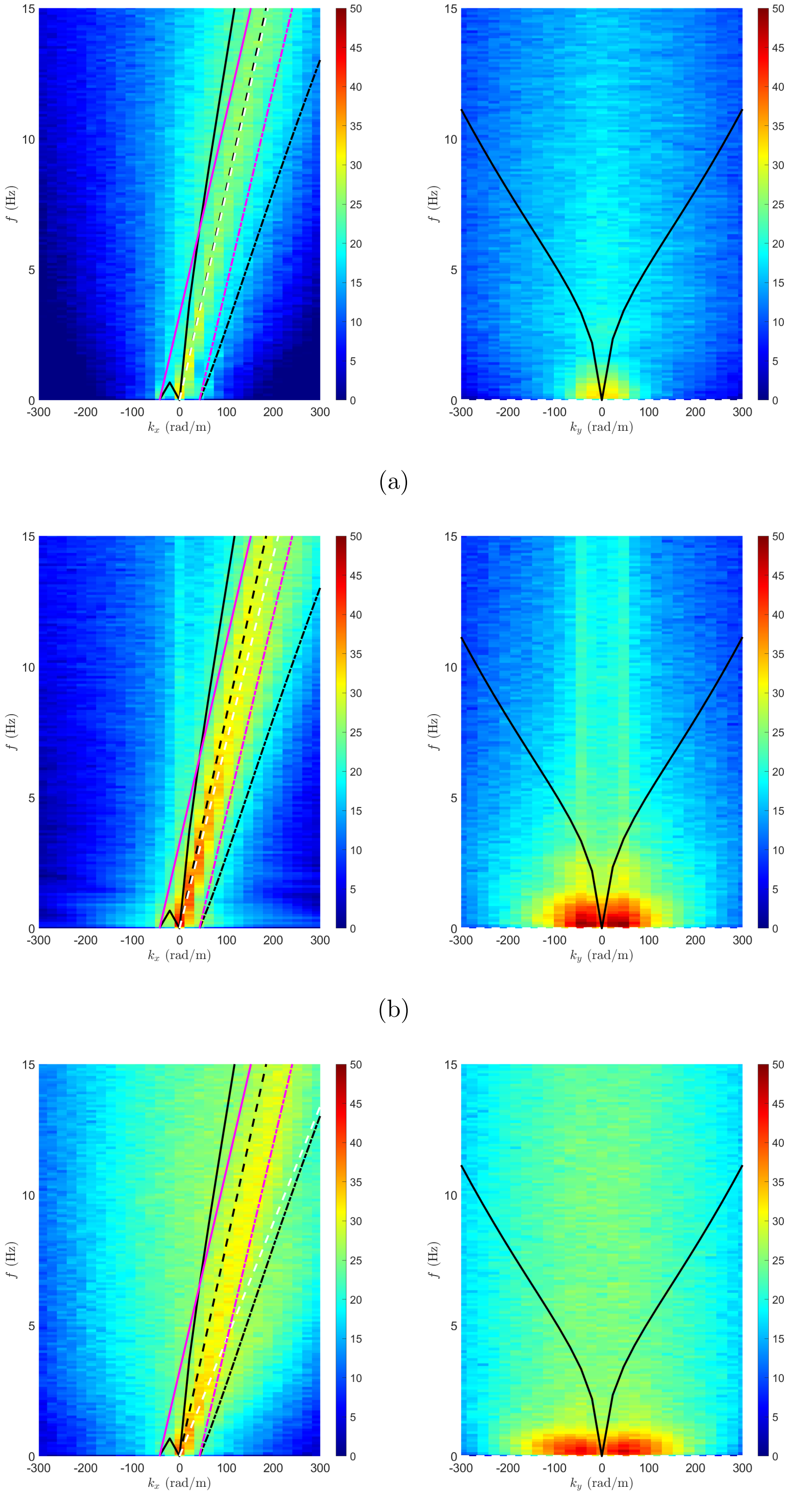

(a)

(b)

(c)

Figure A.9: Streamwise (left) and lateral (right) frequency-wavenumber spectra of the streamwise turbulent velocity for Q5_H at planes a) "A", b) "C" and c) "E". Black lines: dashed is for non-dispersive structures advecting at U_S (Eq. 4.1), solid and dashed-dotted are positive and negative solutions for gravity-capillary waves (Eq. 4.2). White-dashed line: structures advecting at $\langle \bar{U} \rangle_{xz,plane_i}$. Magenta lines: solid and dashed-dotted are positive and negative solutions for gravity-capillary waves with $k = k_0$ (modified Eq. 4.2).

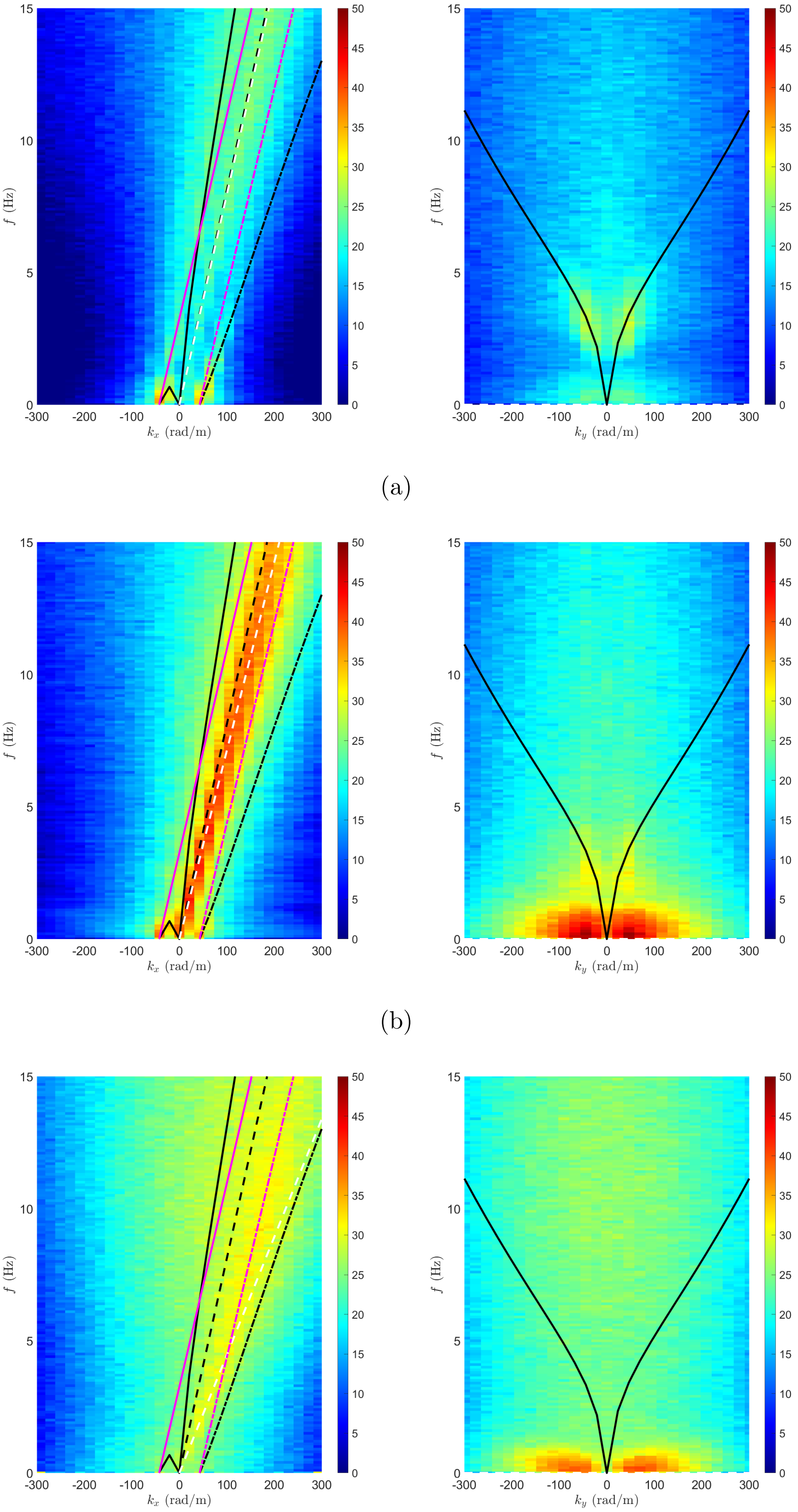

(a)

(b)

(c)

Figure A.10: Streamwise (left) and lateral (right) frequency-wavenumber spectra of the vertical turbulent velocity for Q5_H at planes a) "A", b) "C" and c) "E". Black lines: dashed is for non-dispersive structures advecting at U_S (Eq. 4.1), solid and dashed-dotted are positive and negative solutions for gravity-capillary waves (Eq. 4.2). White-dashed line: structures advecting at $\langle \bar{U} \rangle_{xz,plane_i}$. Magenta lines: solid and dashed-dotted are positive and negative solutions for gravity-capillary waves with $k = k_0$ (modified Eq. 4.2).

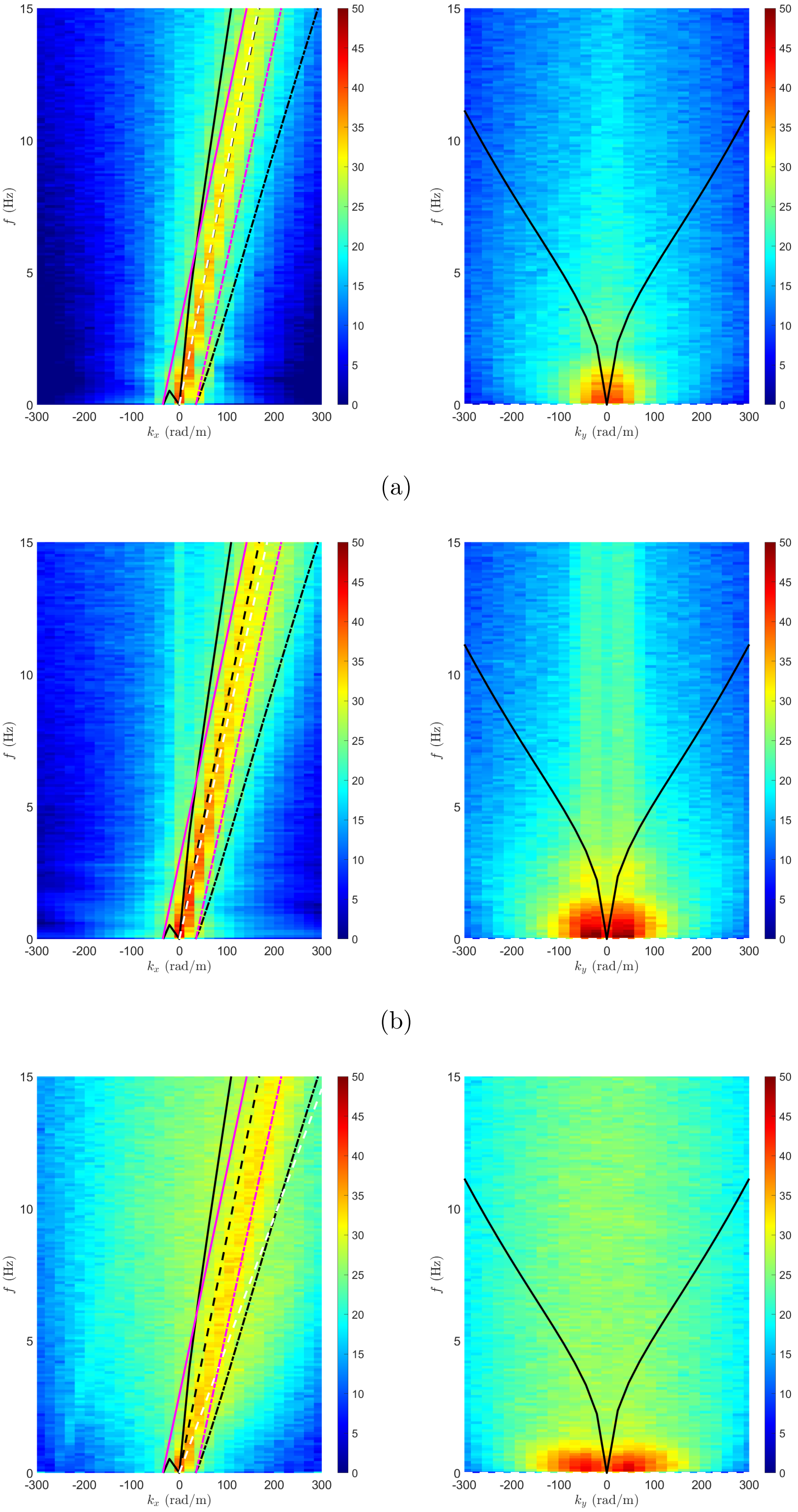

(a)

(b)

(c)

Figure A.11: Streamwise (left) and lateral (right) frequency-wavenumber spectra of the streamwise turbulent velocity for Q6_H at planes a) "A", b) "C" and c) "E". Black lines: dashed is for non-dispersive structures advecting at U_S (Eq. 4.1), solid and dashed-dotted are positive and negative solutions for gravity-capillary waves (Eq. 4.2). White-dashed line: structures advecting at $\langle \bar{U} \rangle_{xz,plane_i}$. Magenta lines: solid and dashed-dotted are positive and negative solutions for gravity-capillary waves with $k = k_0$ (modified Eq. 4.2).

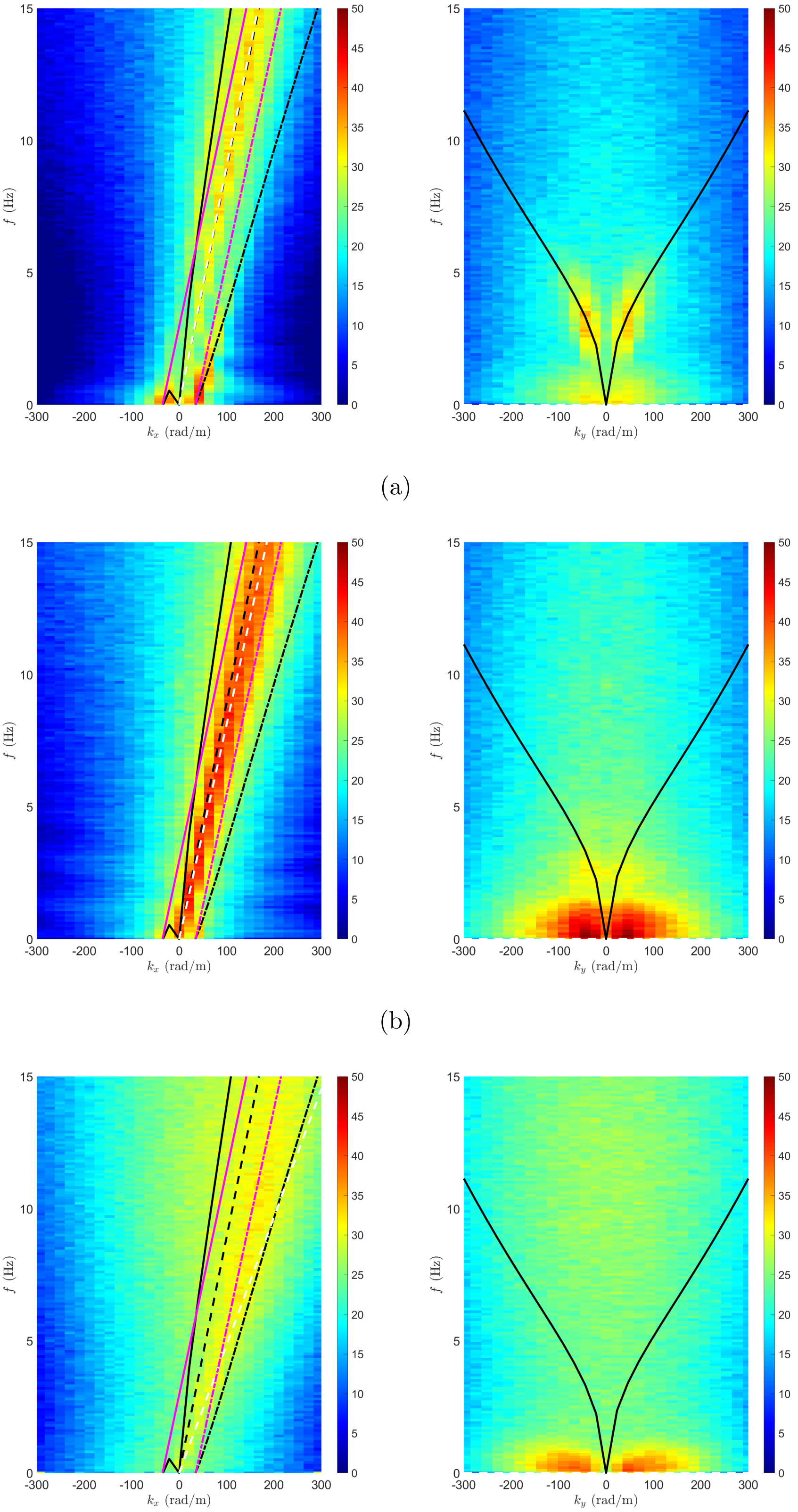

(a)

(b)

(c)

Figure A.12: Streamwise (left) and lateral (right) frequency-wavenumber spectra of the vertical turbulent velocity for Q6_H at planes a) ”A”, b) ”C” and c) ”E”. Black lines: dashed is for non-dispersive structures advecting at U_S (Eq. 4.1), solid and dashed-dotted are positive and negative solutions for gravity-capillary waves (Eq. 4.2). White-dashed line: structures advecting at $\langle \bar{U} \rangle_{xz,plane_i}$. Magenta lines: solid and dashed-dotted are positive and negative solutions for gravity-capillary waves with $k = k_0$ (modified Eq. 4.2).

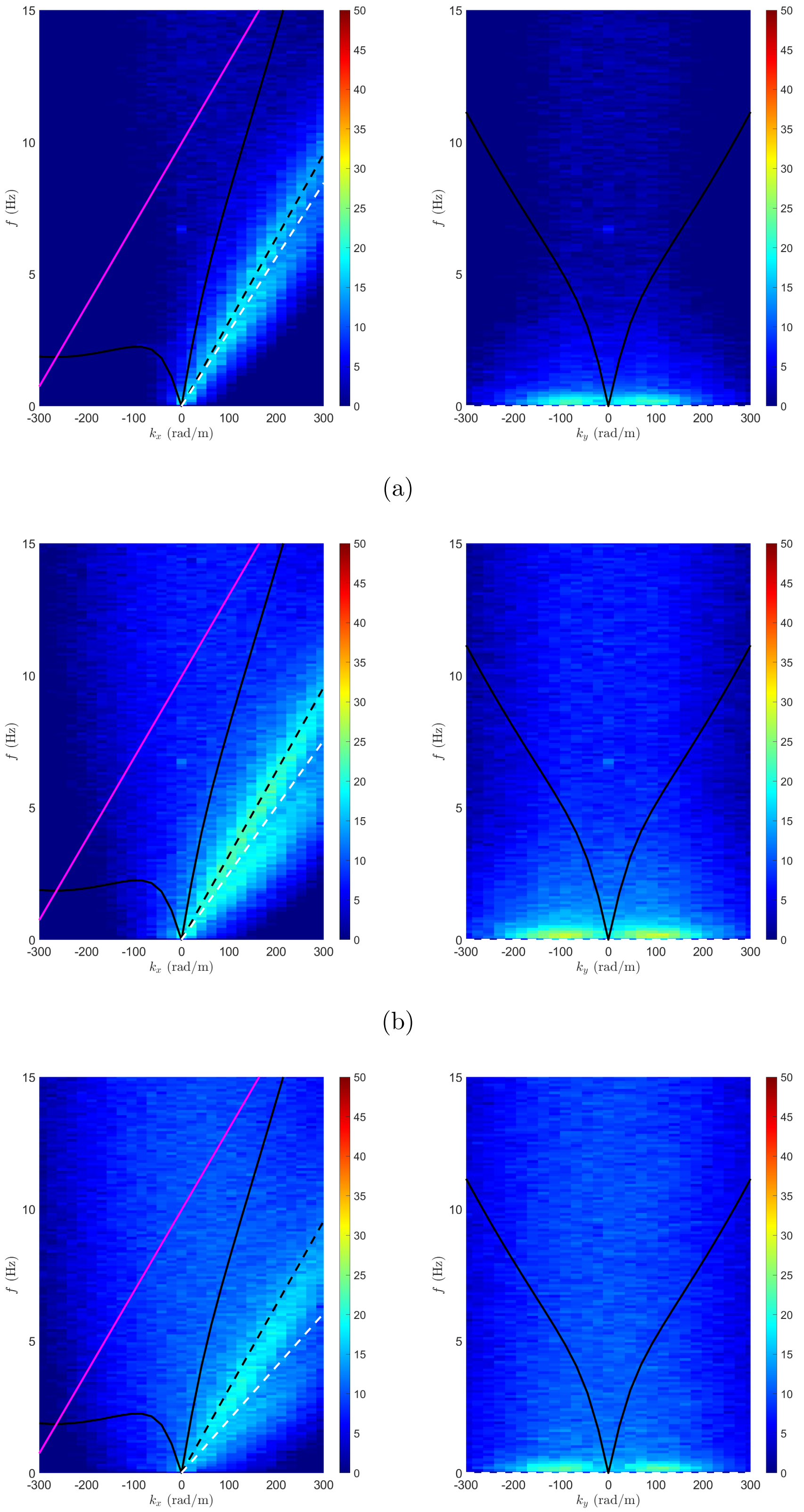

(a)

(b)

(c)

Figure A.13: Streamwise (left) and lateral (right) frequency-wavenumber spectra of the streamwise turbulent velocity for M1_H at planes a) "A", b) "C" and c) "E". Black lines: dashed is for non-dispersive structures advecting at U_S (Eq. 4.1), solid and dashed-dotted are positive and negative solutions for gravity-capillary waves (Eq. 4.2). White-dashed line: structures advecting at $\langle\bar{U}\rangle_{xz,plane_i}$. Magenta lines: solid and dashed-dotted are positive and negative solutions for gravity-capillary waves with $k = k_0$ (modified Eq. 4.2).

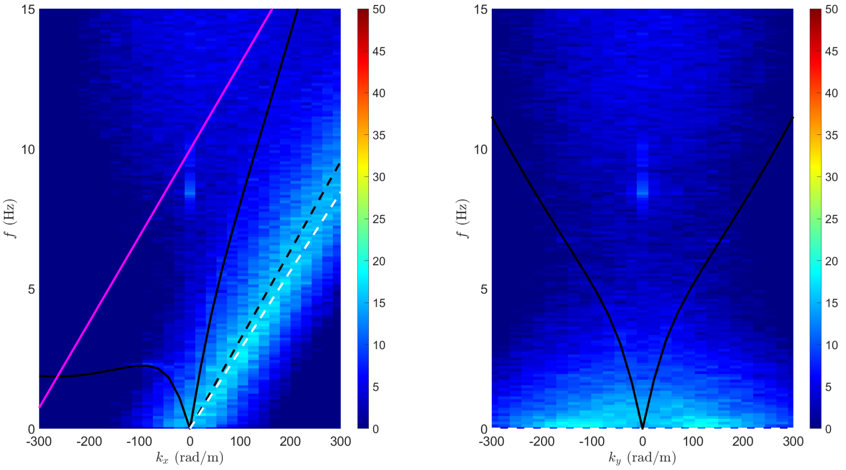

(a)

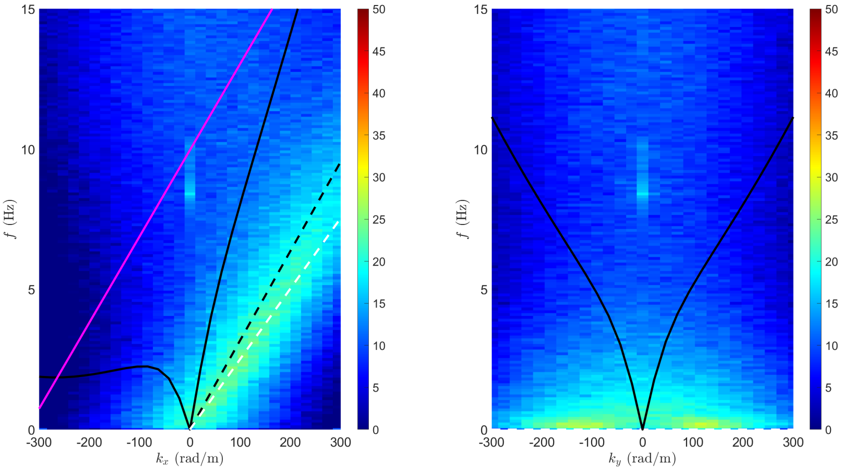

(b)

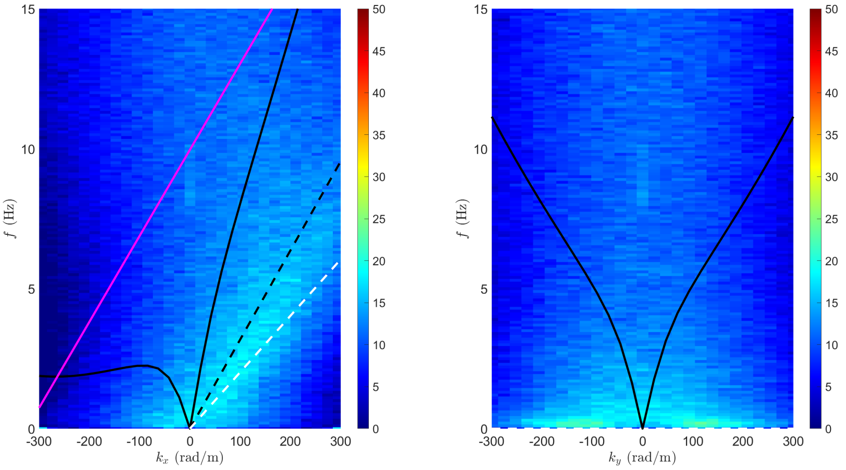

(c)

Figure A.14: Streamwise (left) and lateral (right) frequency-wavenumber spectra of the vertical turbulent velocity for M1_H at planes a) "A", b) "C" and c) "E". Black lines: dashed is for non-dispersive structures advecting at U_S (Eq. 4.1), solid and dashed-dotted are positive and negative solutions for gravity-capillary waves (Eq. 4.2). White-dashed line: structures advecting at $\langle \bar{U} \rangle_{xz,plane_i}$. Magenta lines: solid and dashed-dotted are positive and negative solutions for gravity-capillary waves with $k = k_0$ (modified Eq. 4.2).

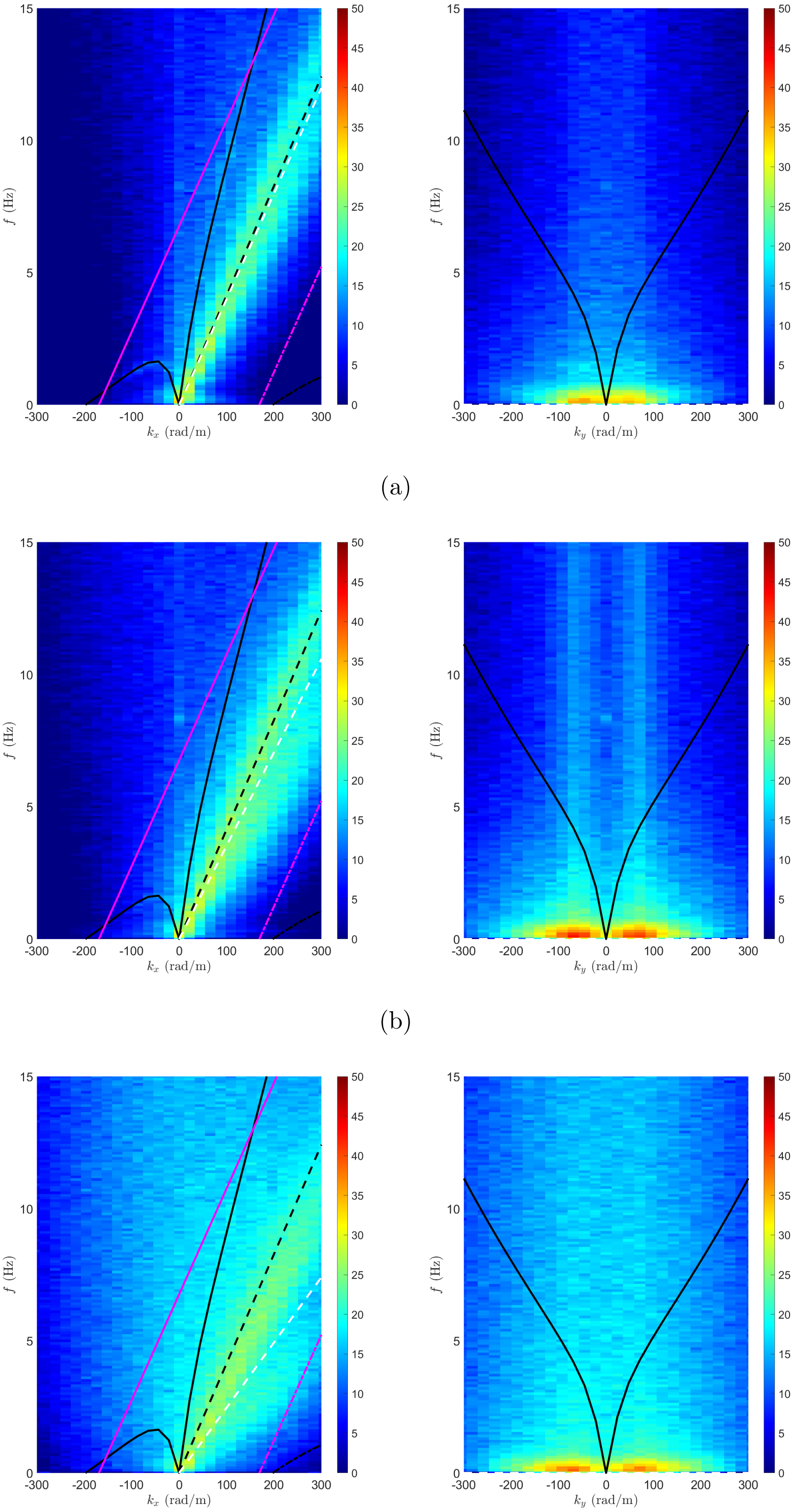

(a)

(b)

(c)

Figure A.15: Streamwise (left) and lateral (right) frequency-wavenumber spectra of the streamwise turbulent velocity for M2_H at planes a) "A", b) "C" and c) "E". Black lines: dashed is for non-dispersive structures advecting at U_S (Eq. 4.1), solid and dashed-dotted are positive and negative solutions for gravity-capillary waves (Eq. 4.2). White-dashed line: structures advecting at $\langle \bar{U} \rangle_{xz,plane_i}$. Magenta lines: solid and dashed-dotted are positive and negative solutions for gravity-capillary waves with $k = k_0$ (modified Eq. 4.2).

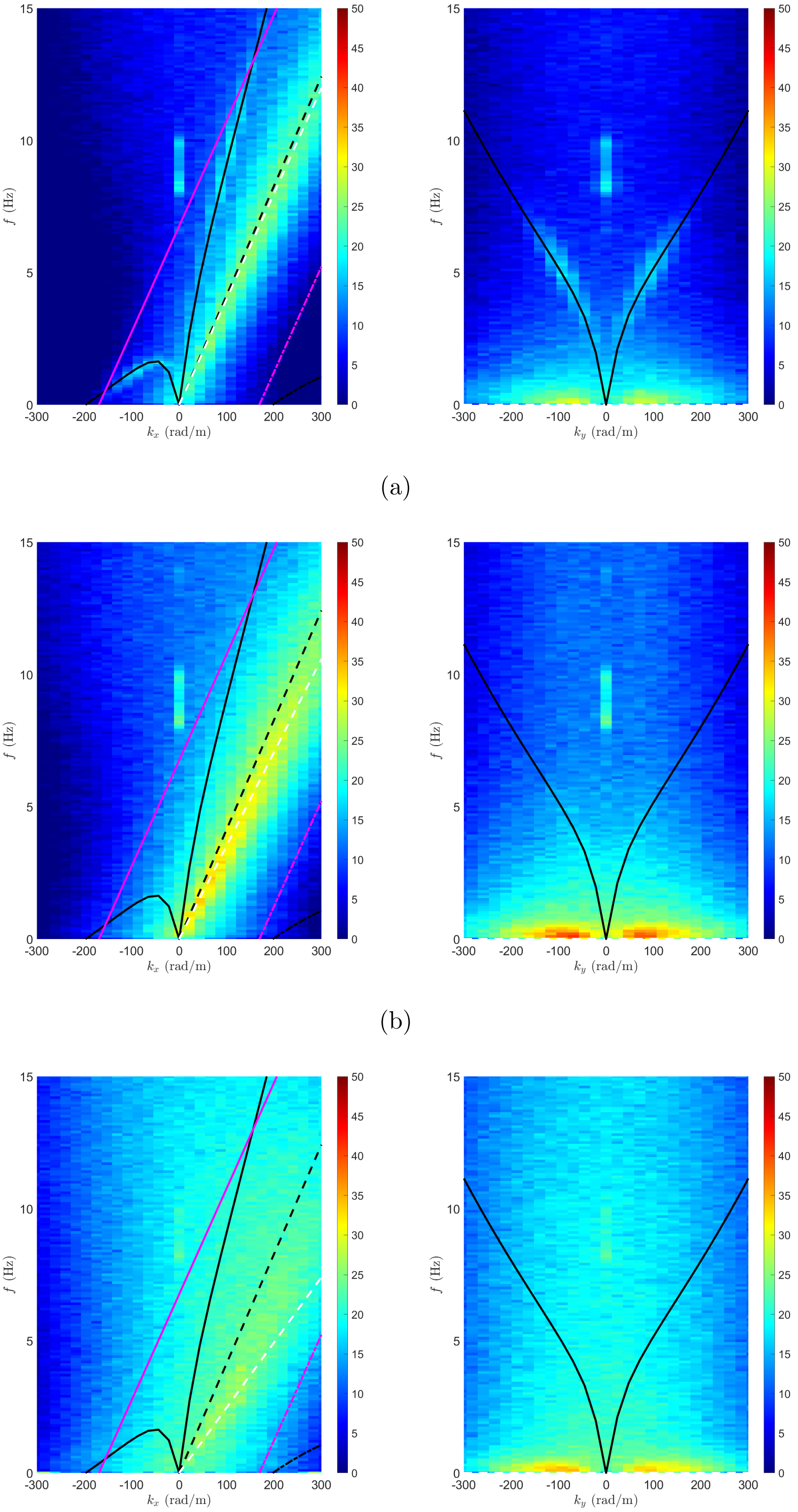

(a)

(b)

(c)

Figure A.16: Streamwise (left) and lateral (right) frequency-wavenumber spectra of the vertical turbulent velocity for M2_H at planes a) "A", b) "C" and c) "E". Black lines: dashed is for non-dispersive structures advecting at U_S (Eq. 4.1), solid and dashed-dotted are positive and negative solutions for gravity-capillary waves (Eq. 4.2). White-dashed line: structures advecting at $\langle \bar{U} \rangle_{xz,plane_i}$. Magenta lines: solid and dashed-dotted are positive and negative solutions for gravity-capillary waves with $k = k_0$ (modified Eq. 4.2).

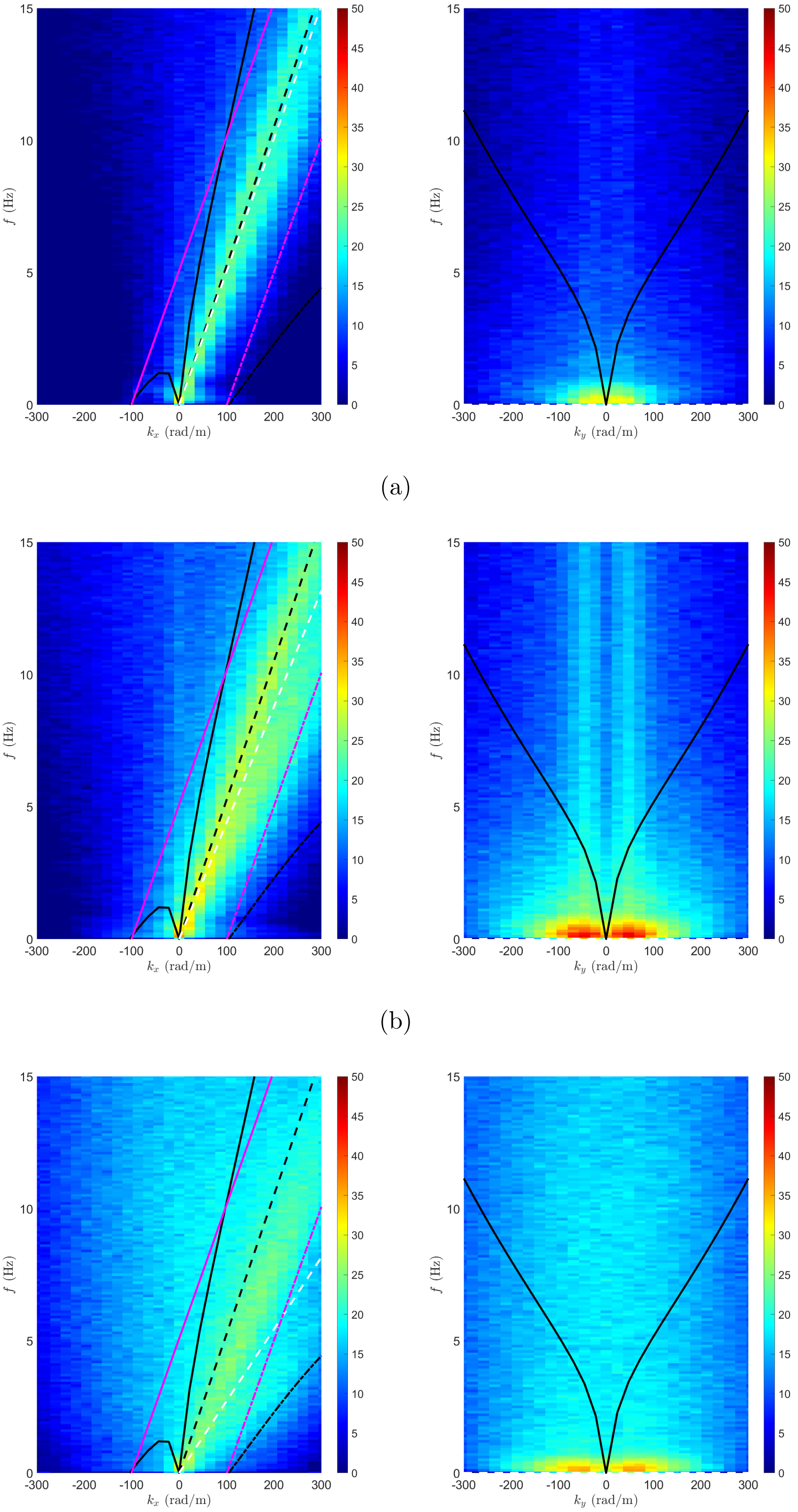

(a)

(b)

(c)

Figure A.17: Streamwise (left) and lateral (right) frequency-wavenumber spectra of the streamwise turbulent velocity for M3_H at planes a) "A", b) "C" and c) "E". Black lines: dashed is for non-dispersive structures advecting at U_S (Eq. 4.1), solid and dashed-dotted are positive and negative solutions for gravity-capillary waves (Eq. 4.2). White-dashed line: structures advecting at $\langle \bar{U} \rangle_{xz,plane_i}$. Magenta lines: solid and dashed-dotted are positive and negative solutions for gravity-capillary waves with $k = k_0$ (modified Eq. 4.2).

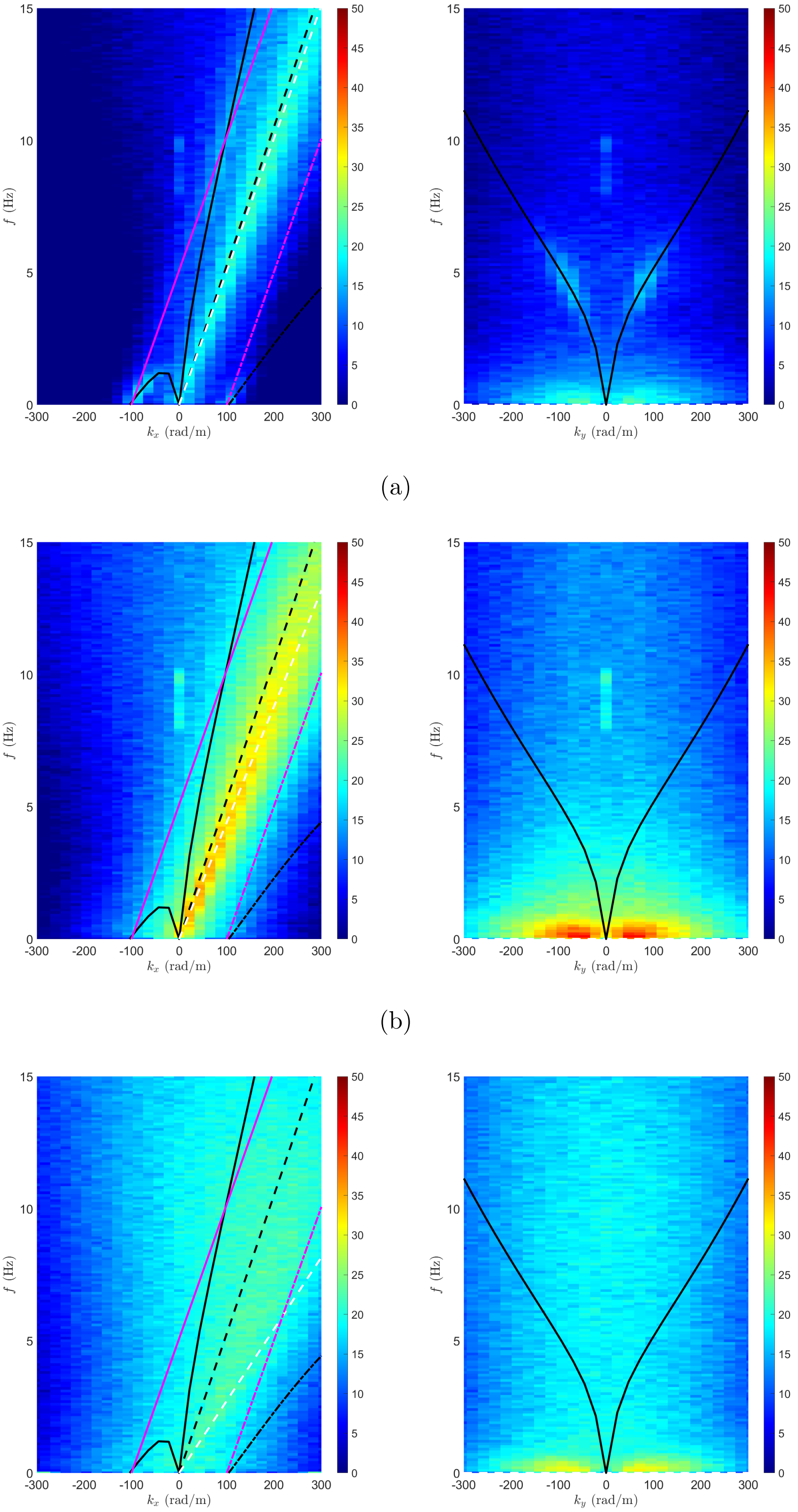

(a)

(b)

(c)

Figure A.18: Streamwise (left) and lateral (right) frequency-wavenumber spectra of the vertical turbulent velocity for M3_H at planes a) ”A”, b) ”C” and c) ”E”. Black lines: dashed is for non-dispersive structures advecting at U_S (Eq. 4.1), solid and dashed-dotted are positive and negative solutions for gravity-capillary waves (Eq. 4.2). White-dashed line: structures advecting at $\langle \bar{U} \rangle_{xz,plane_i}$. Magenta lines: solid and dashed-dotted are positive and negative solutions for gravity-capillary waves with $k = k_0$ (modified Eq. 4.2).

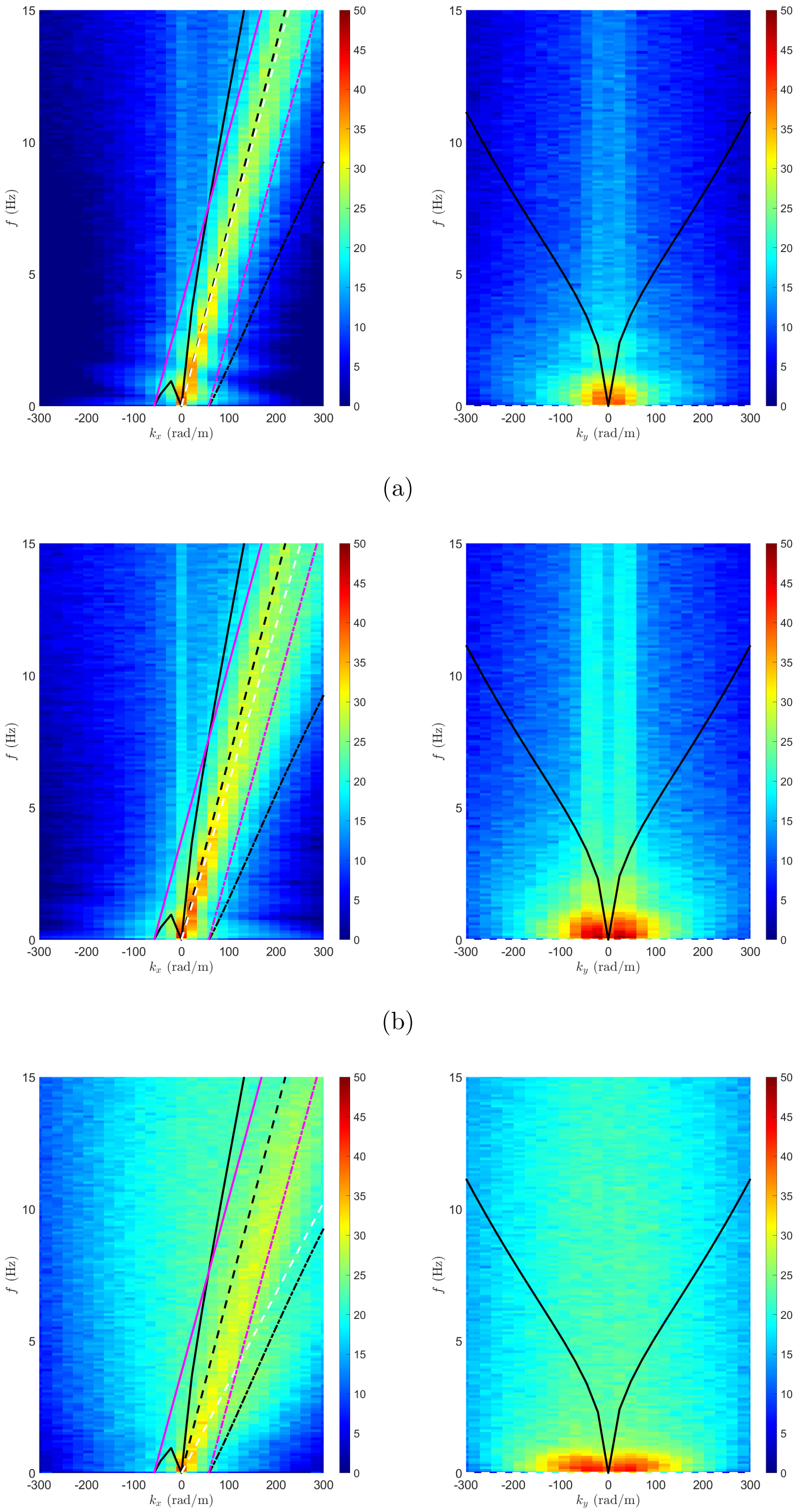

(a)

(b)

(c)

Figure A.19: Streamwise (left) and lateral (right) frequency-wavenumber spectra of the streamwise turbulent velocity for M4_H at planes a) "A", b) "C" and c) "E". Black lines: dashed is for non-dispersive structures advecting at U_S (Eq. 4.1), solid and dashed-dotted are positive and negative solutions for gravity-capillary waves (Eq. 4.2). White-dashed line: structures advecting at $\left\langle \bar{U} \right\rangle_{xz,plane_i}$. Magenta lines: solid and dashed-dotted are positive and negative solutions for gravity-capillary waves with $k = k_0$ (modified Eq. 4.2).

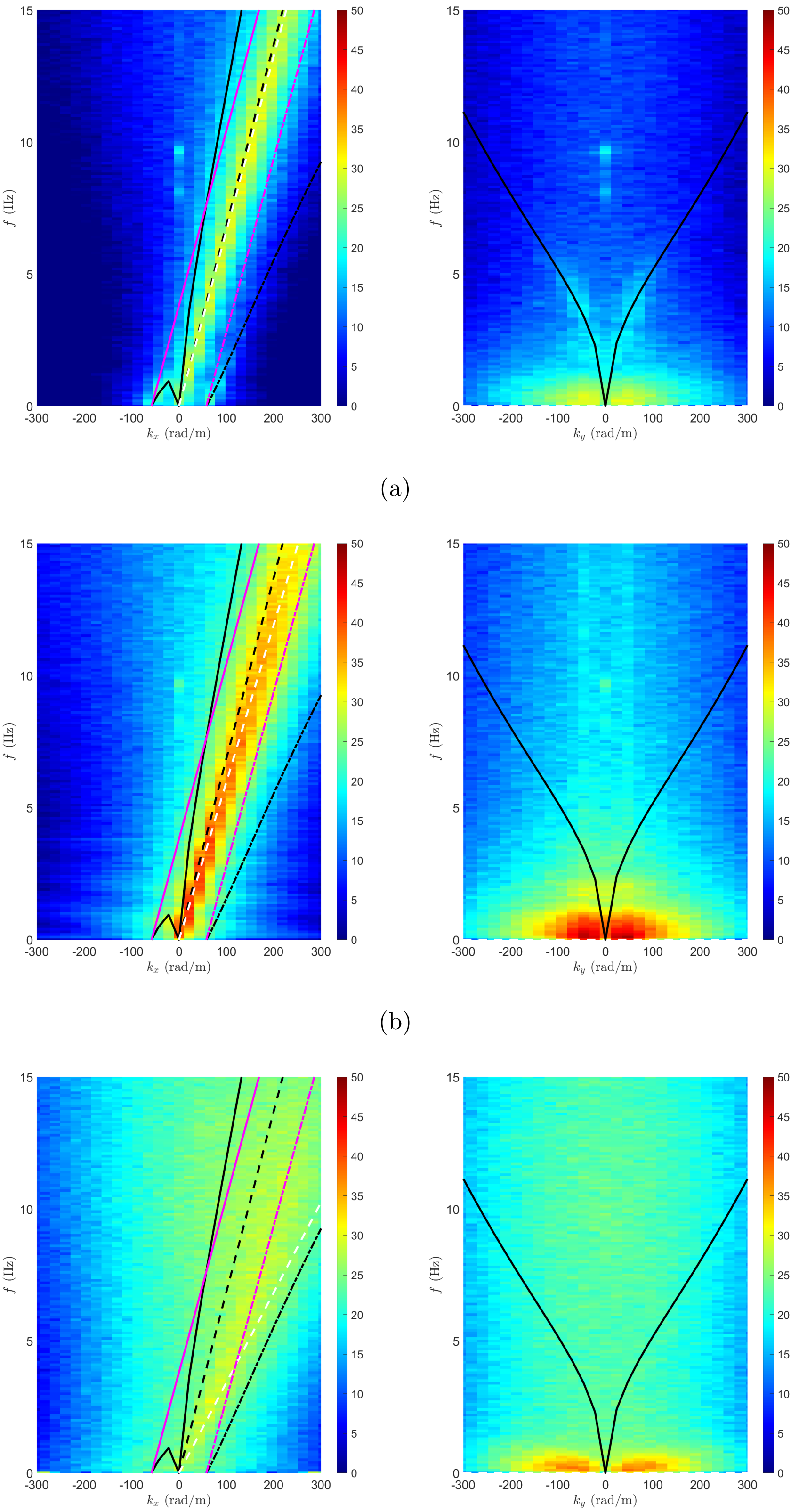

(a)

(b)

(c)

Figure A.20: Streamwise (left) and lateral (right) frequency-wavenumber spectra of the vertical turbulent velocity for M4_H at planes a) "A", b) "C" and c) "E". Black lines: dashed is for non-dispersive structures advecting at U_S (Eq. 4.1), solid and dashed-dotted are positive and negative solutions for gravity-capillary waves (Eq. 4.2). White-dashed line: structures advecting at $\langle \bar{U} \rangle_{xz,plane_i}$. Magenta lines: solid and dashed-dotted are positive and negative solutions for gravity-capillary waves with $k = k_0$ (modified Eq. 4.2).

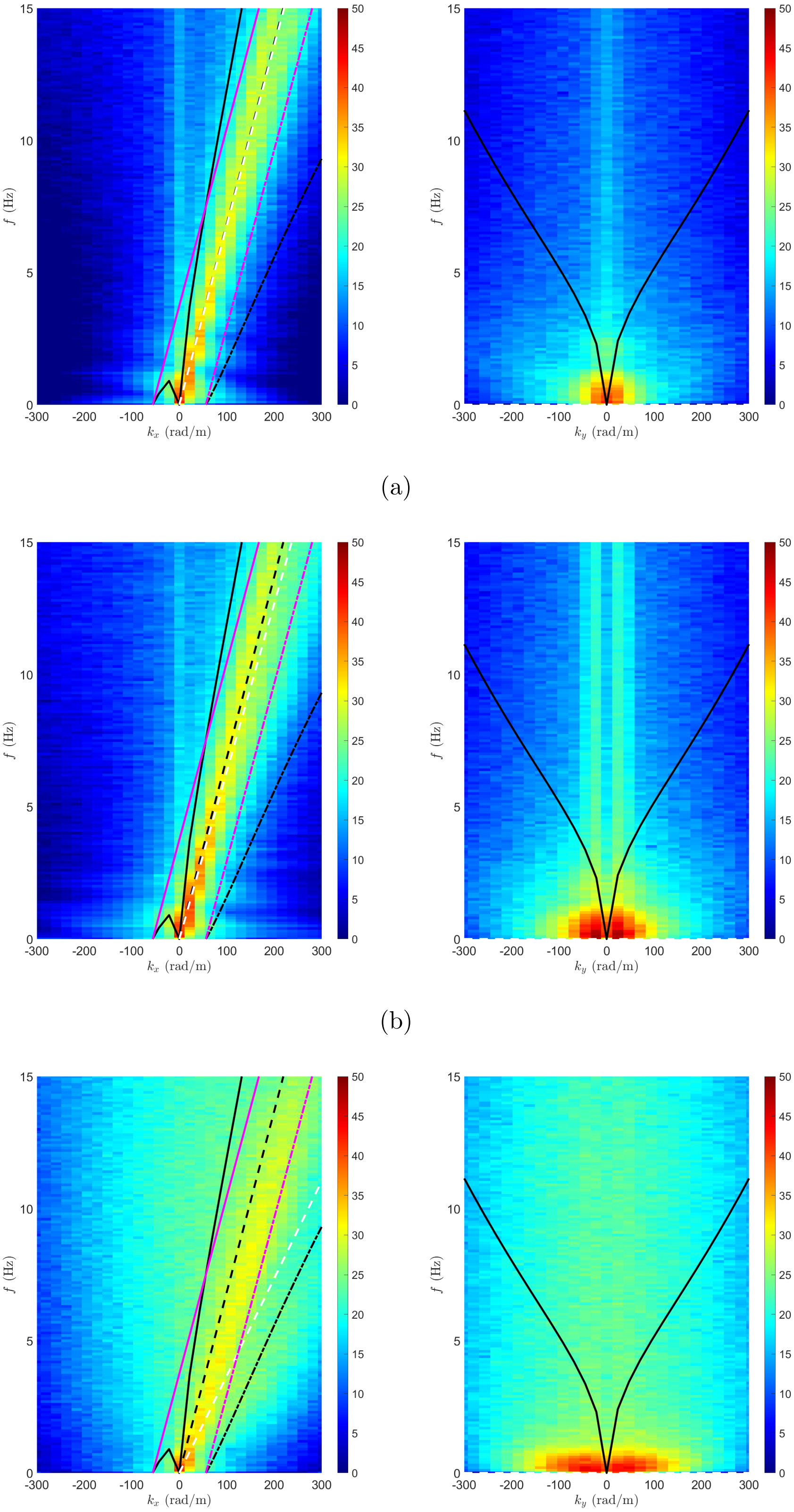

(a)

(b)

(c)

Figure A.21: Streamwise (left) and lateral (right) frequency-wavenumber spectra of the streamwise turbulent velocity for M5_H at planes a) "A", b) "C" and c) "E". Black lines: dashed is for non-dispersive structures advecting at U_S (Eq. 4.1), solid and dashed-dotted are positive and negative solutions for gravity-capillary waves (Eq. 4.2). White-dashed line: structures advecting at $\langle \bar{U} \rangle_{xz,plane_i}$. Magenta lines: solid and dashed-dotted are positive and negative solutions for gravity-capillary waves with $k = k_0$ (modified Eq. 4.2).

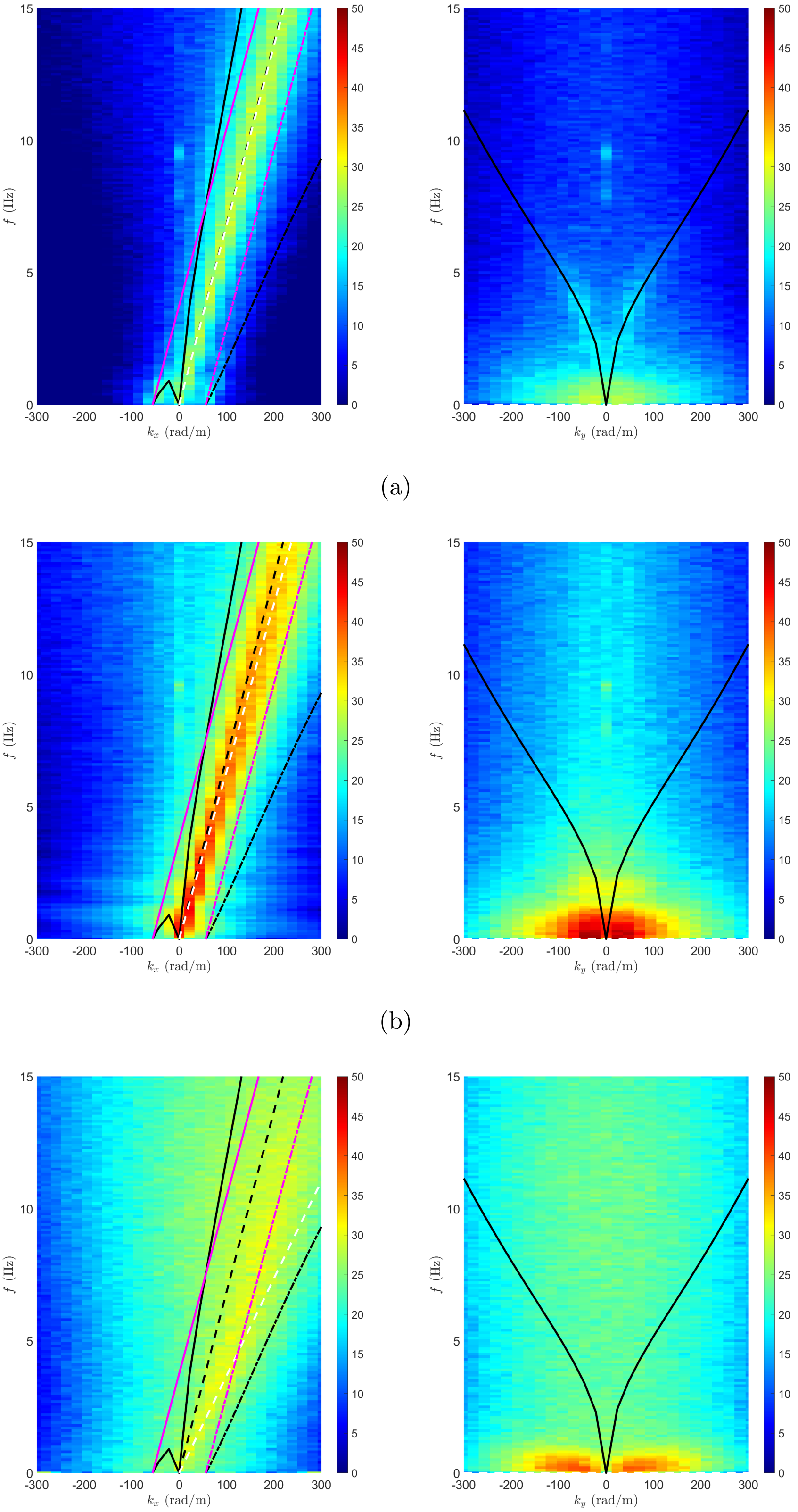

(a)

(b)

(c)

Figure A.22: Streamwise (left) and lateral (right) frequency-wavenumber spectra of the vertical turbulent velocity for M5_H at planes a) "A", b) "C" and c) "E". Black lines: dashed is for non-dispersive structures advecting at U_S (Eq. 4.1), solid and dashed-dotted are positive and negative solutions for gravity-capillary waves (Eq. 4.2). White-dashed line: structures advecting at $\langle \bar{U} \rangle_{xz,plane_i}$. Magenta lines: solid and dashed-dotted are positive and negative solutions for gravity-capillary waves with $k = k_0$ (modified Eq. 4.2).

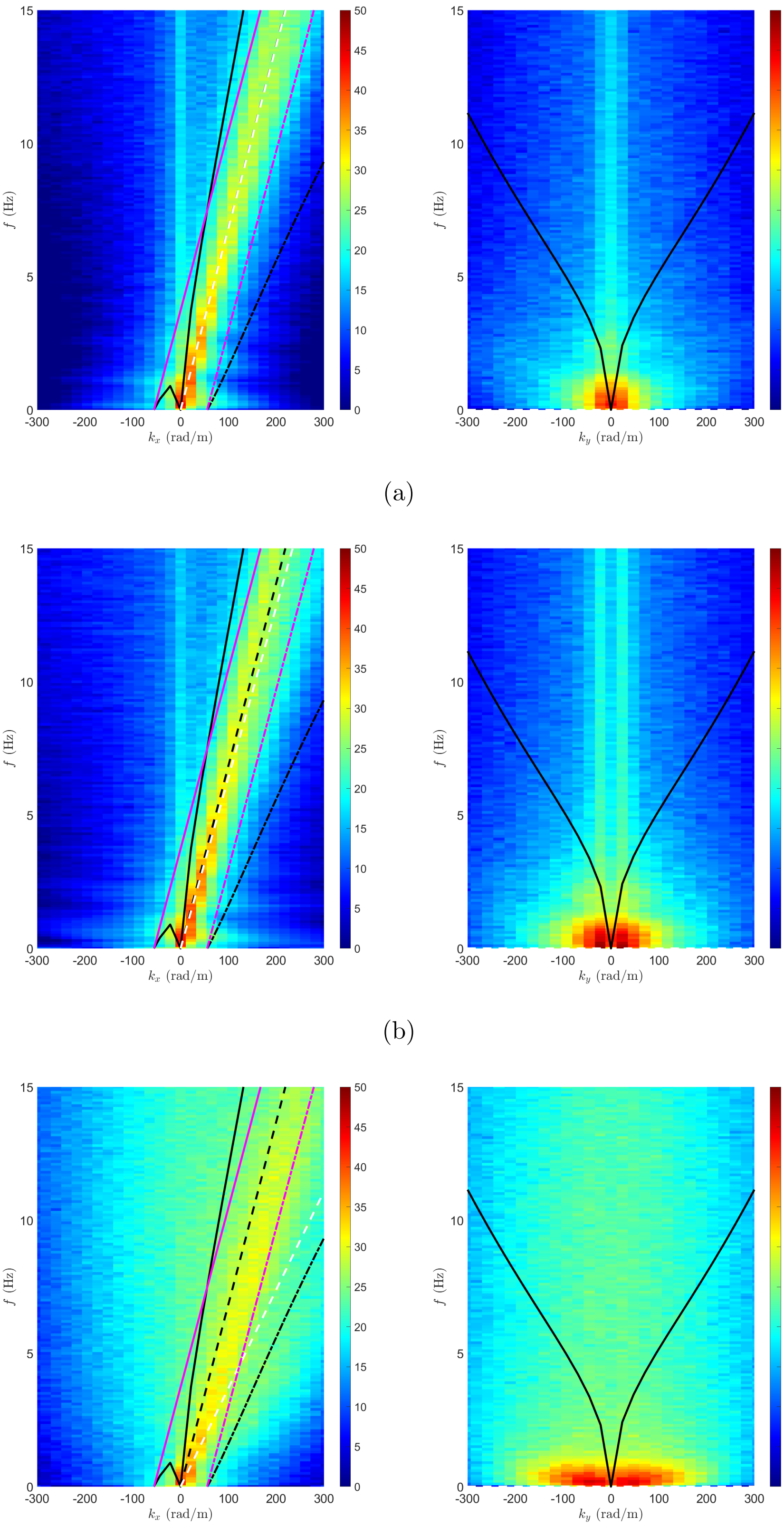

(a)

(b)

(c)

Figure A.23: Streamwise (left) and lateral (right) frequency-wavenumber spectra of the streamwise turbulent velocity for M6_H at planes a) "A", b) "C" and c) "E". Black lines: dashed is for non-dispersive structures advecting at U_S (Eq. 4.1), solid and dashed-dotted are positive and negative solutions for gravity-capillary waves (Eq. 4.2). White-dashed line: structures advecting at $\langle \bar{U} \rangle_{xz,plane_i}$. Magenta lines: solid and dashed-dotted are positive and negative solutions for gravity-capillary waves with $k = k_0$ (modified Eq. 4.2).

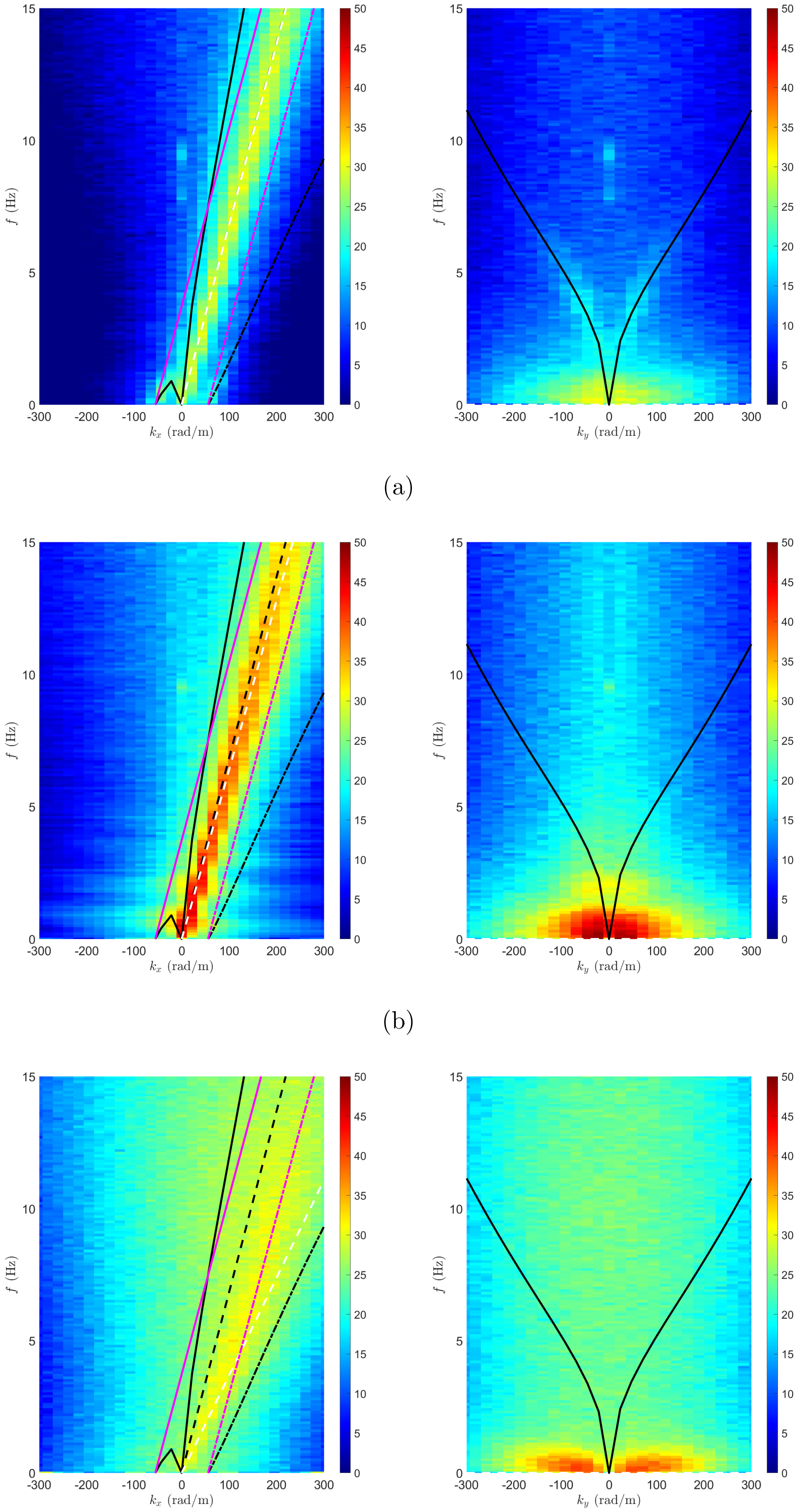

(a)

(b)

(c)

Figure A.24: Streamwise (left) and lateral (right) frequency-wavenumber spectra of the vertical turbulent velocity for M6_H at planes a) ”A”, b) ”C” and c) ”E”. Black lines: dashed is for non-dispersive structures advecting at U_S (Eq. 4.1), solid and dashed-dotted are positive and negative solutions for gravity-capillary waves (Eq. 4.2). White-dashed line: structures advecting at $\langle \bar{U} \rangle_{xz,plane_i}$. Magenta lines: solid and dashed-dotted are positive and negative solutions for gravity-capillary waves with $k = k_0$ (modified Eq. 4.2).

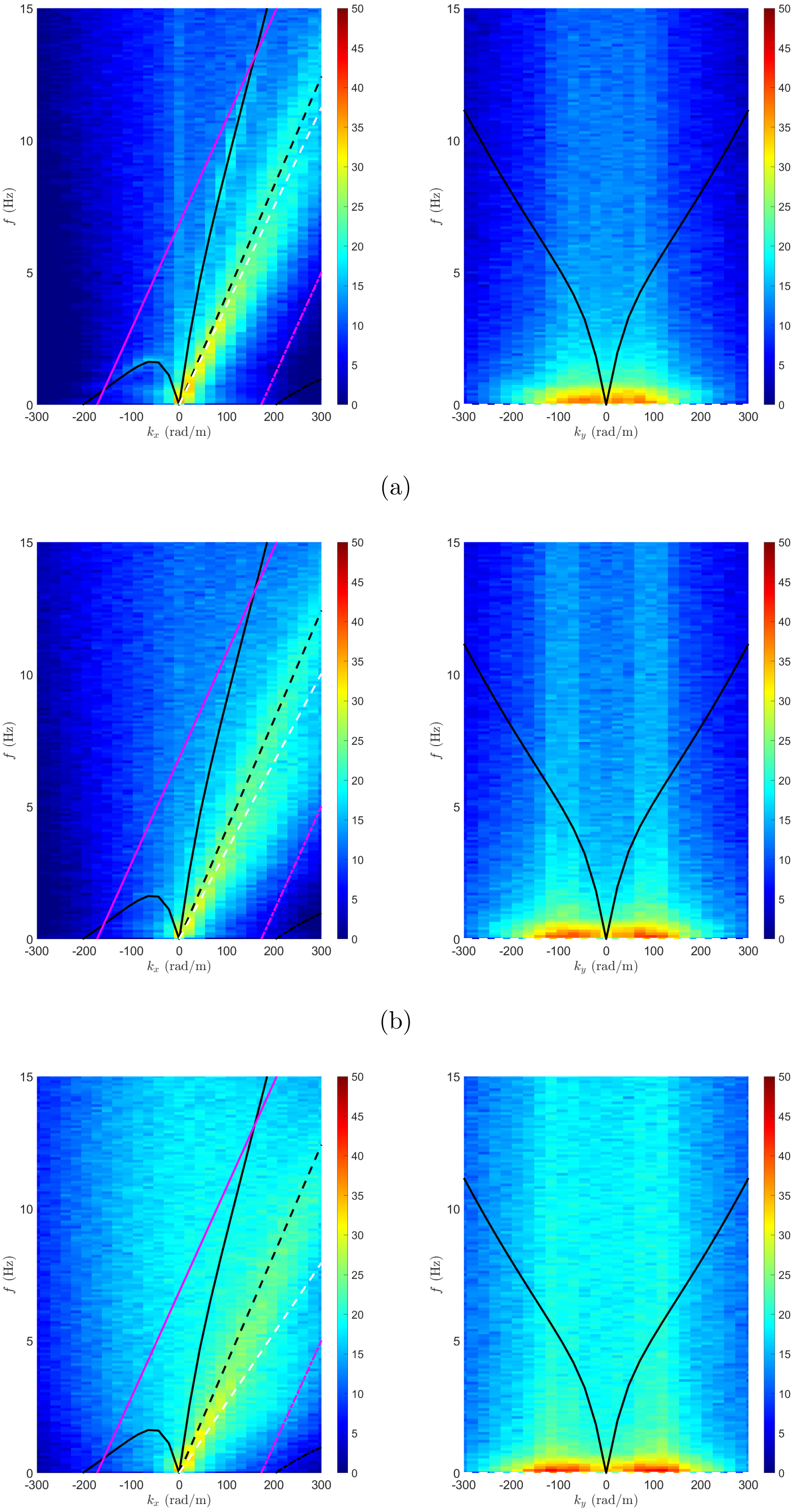

(a)

(b)

(c)

Figure A.25: Streamwise (left) and lateral (right) frequency-wavenumber spectra of the streamwise turbulent velocity for A2_H at planes a) "A", b) "C" and c) "E". Black lines: dashed is for non-dispersive structures advecting at U_S (Eq. 4.1), solid and dashed-dotted are positive and negative solutions for gravity-capillary waves (Eq. 4.2). White-dashed line: structures advecting at $\left\langle \bar{U} \right\rangle_{xz,plane_i}$. Magenta lines: solid and dashed-dotted are positive and negative solutions for gravity-capillary waves with $k = k_0$ (modified Eq. 4.2).

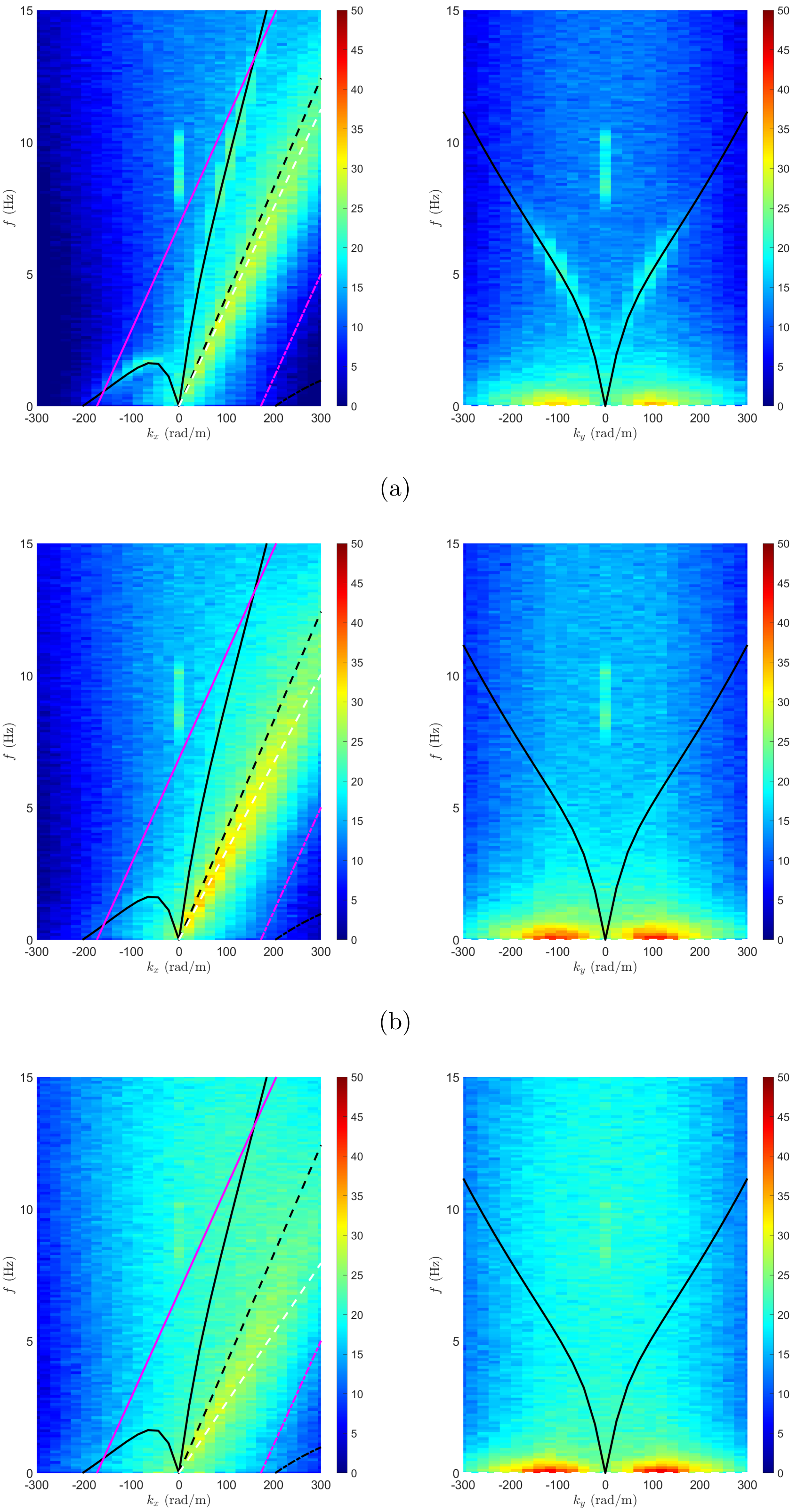

(a)

(b)

(c)

Figure A.26: Streamwise (left) and lateral (right) frequency-wavenumber spectra of the vertical turbulent velocity for A2_H at planes a) ”A”, b) ”C” and c) ”E”. Black lines: dashed is for non-dispersive structures advecting at U_S (Eq. 4.1), solid and dashed-dotted are positive and negative solutions for gravity-capillary waves (Eq. 4.2). White-dashed line: structures advecting at $\langle \bar{U} \rangle_{xz,plane_i}$. Magenta lines: solid and dashed-dotted are positive and negative solutions for gravity-capillary waves with $k = k_0$ (modified Eq. 4.2).

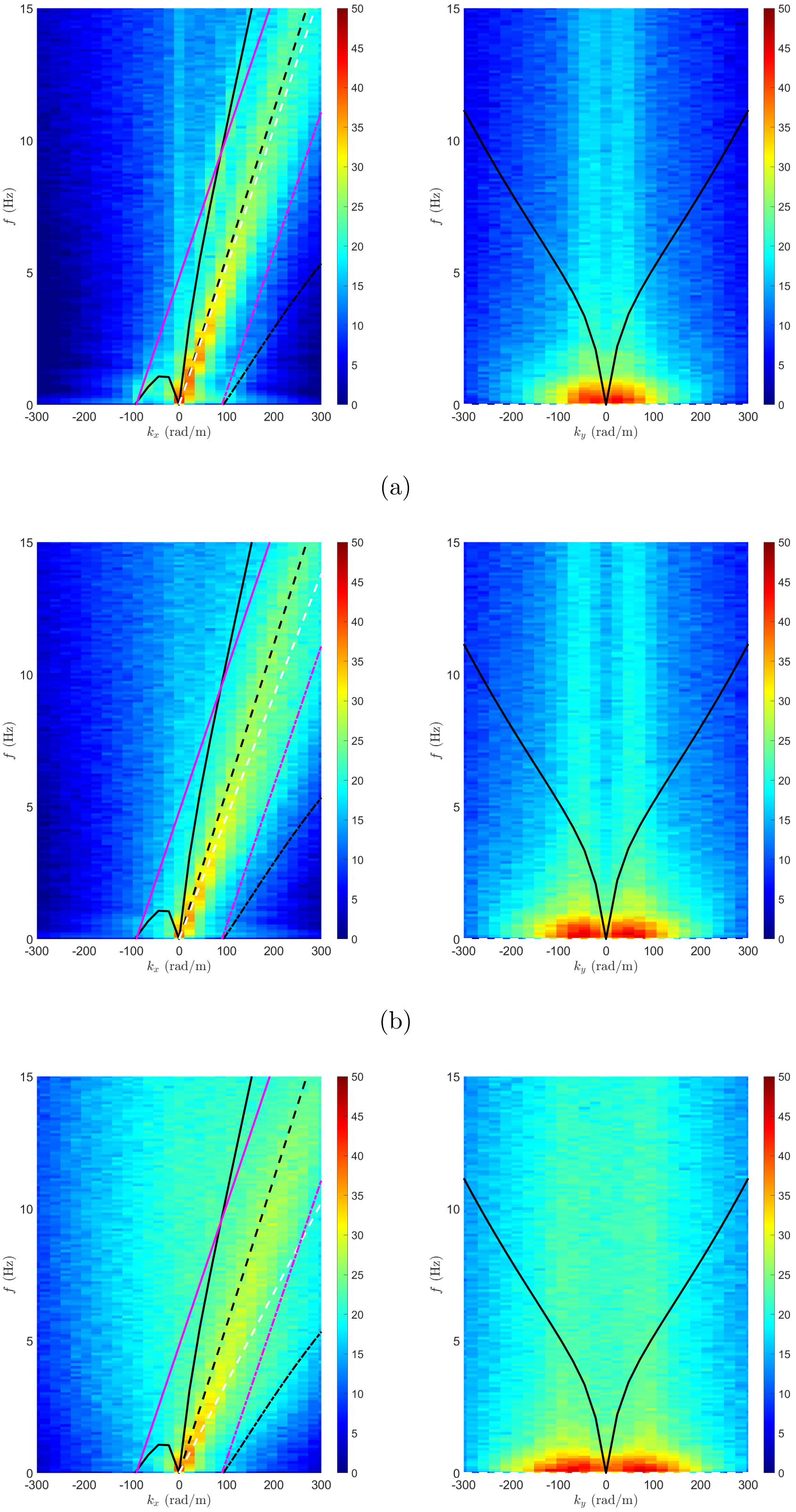

(a)

(b)

(c)

Figure A.27: Streamwise (left) and lateral (right) frequency-wavenumber spectra of the streamwise turbulent velocity for A3_H at planes a) ”A”, b) ”C” and c) ”E”. Black lines: dashed is for non-dispersive structures advecting at U_S (Eq. 4.1), solid and dashed-dotted are positive and negative solutions for gravity-capillary waves (Eq. 4.2). White-dashed line: structures advecting at $\langle \bar{U} \rangle_{xz,plane_i}$. Magenta lines: solid and dashed-dotted are positive and negative solutions for gravity-capillary waves with $k = k_0$ (modified Eq. 4.2).

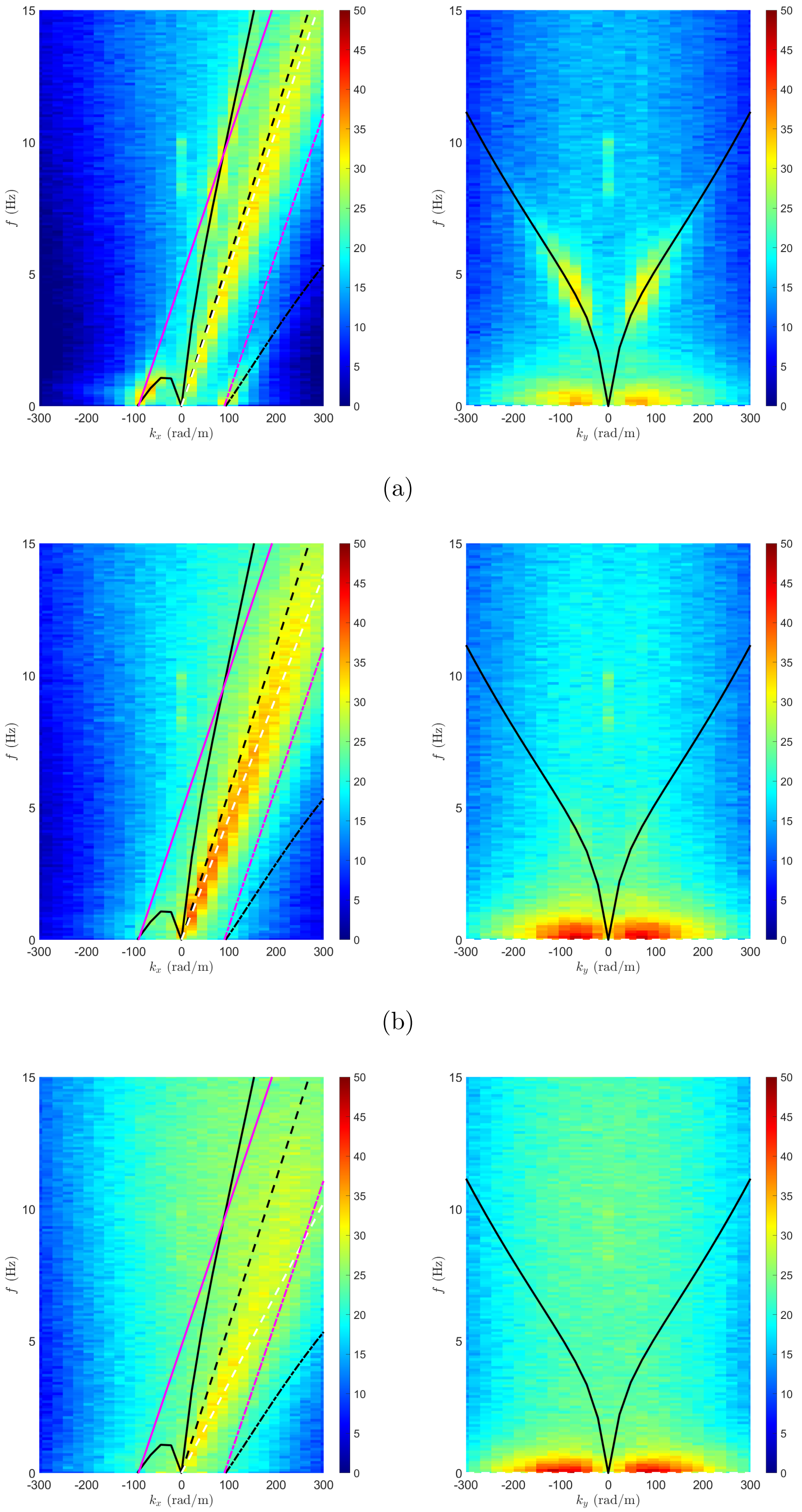

(a)

(b)

(c)

Figure A.28: Streamwise (left) and lateral (right) frequency-wavenumber spectra of the vertical turbulent velocity for A3_H at planes a) "A", b) "C" and c) "E". Black lines: dashed is for non-dispersive structures advecting at U_S (Eq. 4.1), solid and dashed-dotted are positive and negative solutions for gravity-capillary waves (Eq. 4.2). White-dashed line: structures advecting at $\langle \bar{U} \rangle_{xz,plane_i}$. Magenta lines: solid and dashed-dotted are positive and negative solutions for gravity-capillary waves with $k = k_0$ (modified Eq. 4.2).

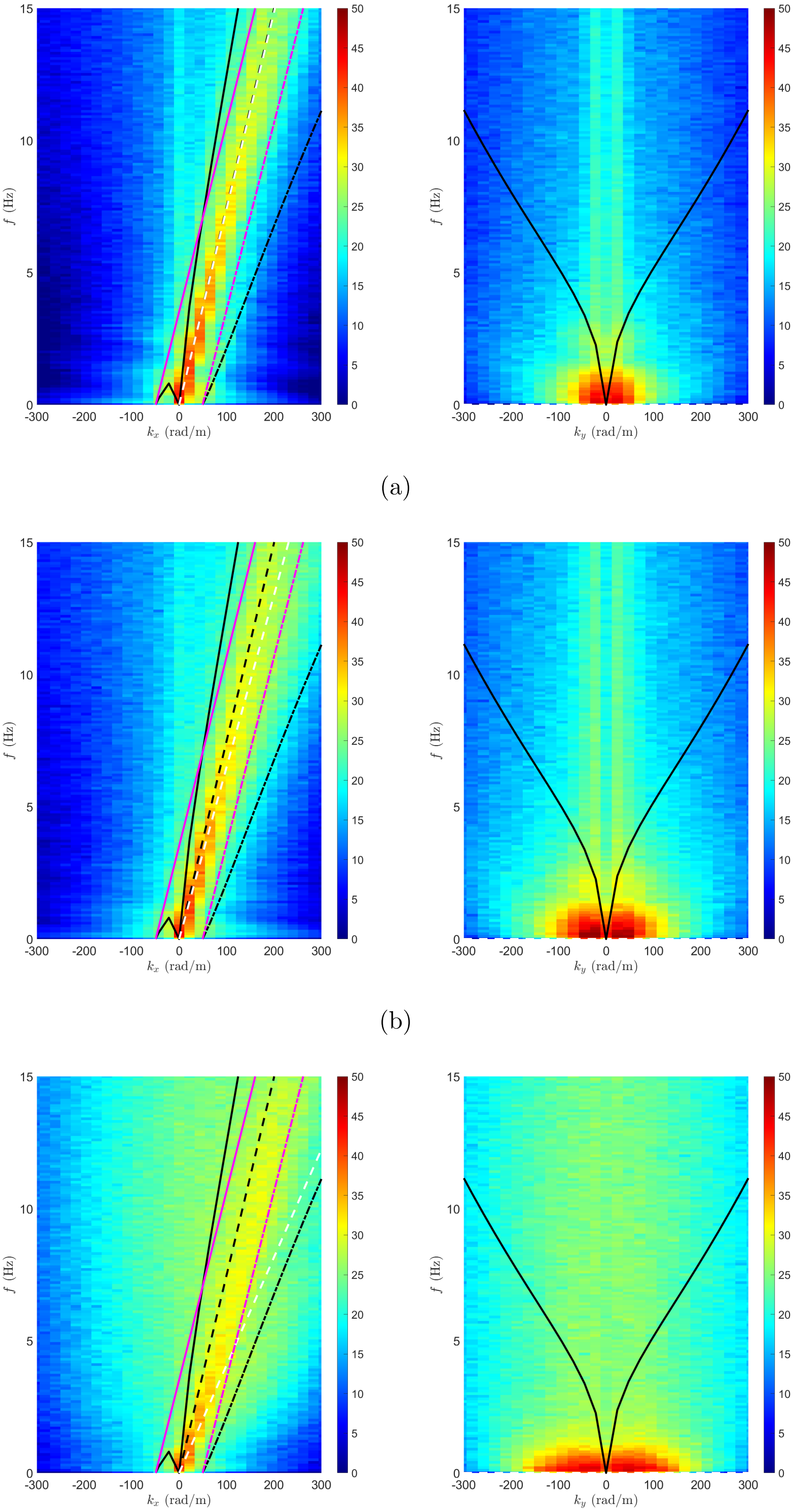

(a)

(b)

(c)

Figure A.29: Streamwise (left) and lateral (right) frequency-wavenumber spectra of the streamwise turbulent velocity for A5_H at planes a) "A", b) "C" and c) "E". Black lines: dashed is for non-dispersive structures advecting at U_S (Eq. 4.1), solid and dashed-dotted are positive and negative solutions for gravity-capillary waves (Eq. 4.2). White-dashed line: structures advecting at $\langle \bar{U} \rangle_{xz,plane_i}$. Magenta lines: solid and dashed-dotted are positive and negative solutions for gravity-capillary waves with $k = k_0$ (modified Eq. 4.2).

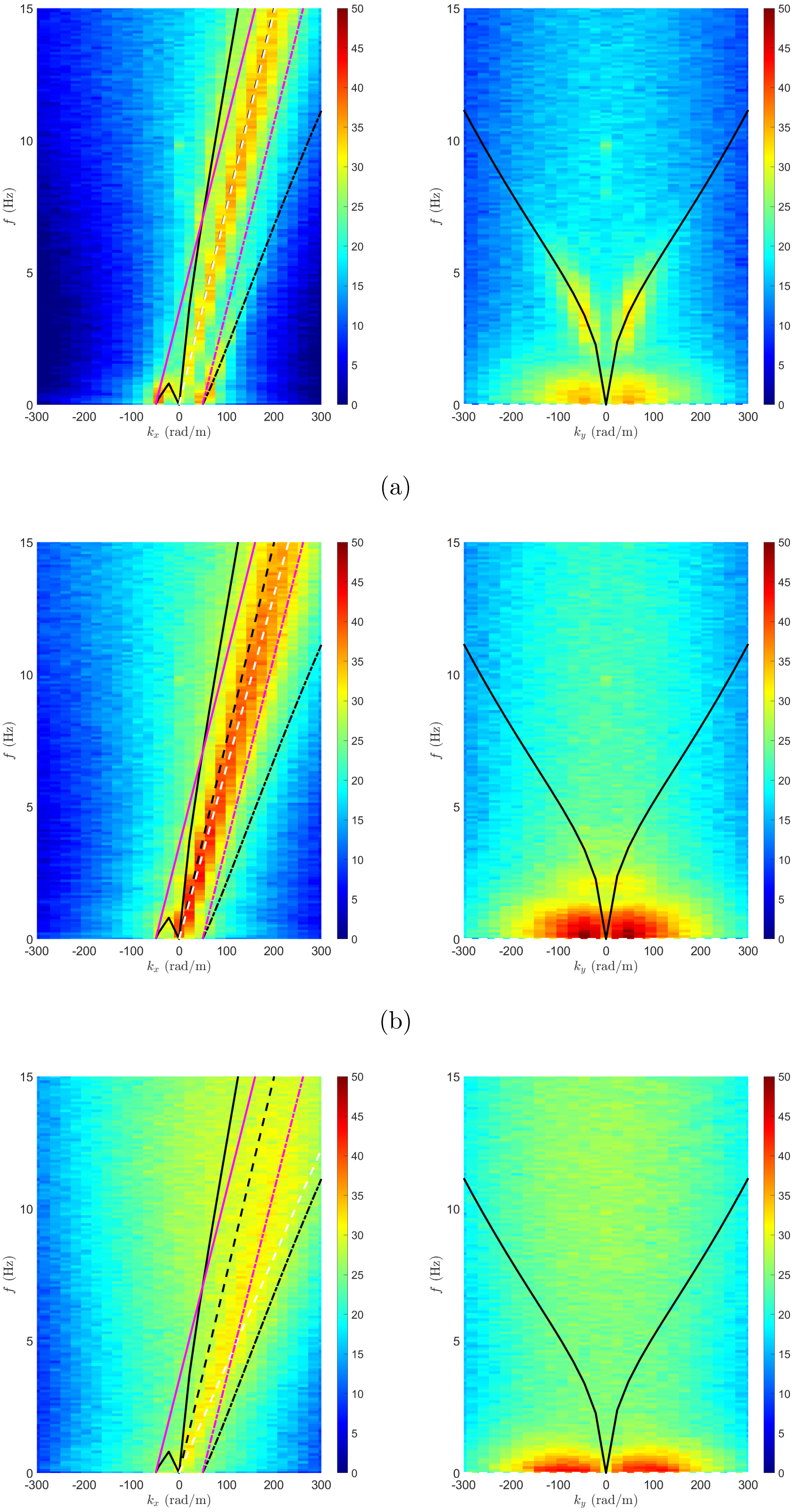

(a)

(b)

(c)

Figure A.30: Streamwise (left) and lateral (right) frequency-wavenumber spectra of the vertical turbulent velocity for A5_H at planes a) "A", b) "C" and c) "E". Black lines: dashed is for non-dispersive structures advecting at U_S (Eq. 4.1), solid and dashed-dotted are positive and negative solutions for gravity-capillary waves (Eq. 4.2). White-dashed line: structures advecting at $\langle \bar{U} \rangle_{xz,plane_i}$. Magenta lines: solid and dashed-dotted are positive and negative solutions for gravity-capillary waves with $k = k_0$ (modified Eq. 4.2).

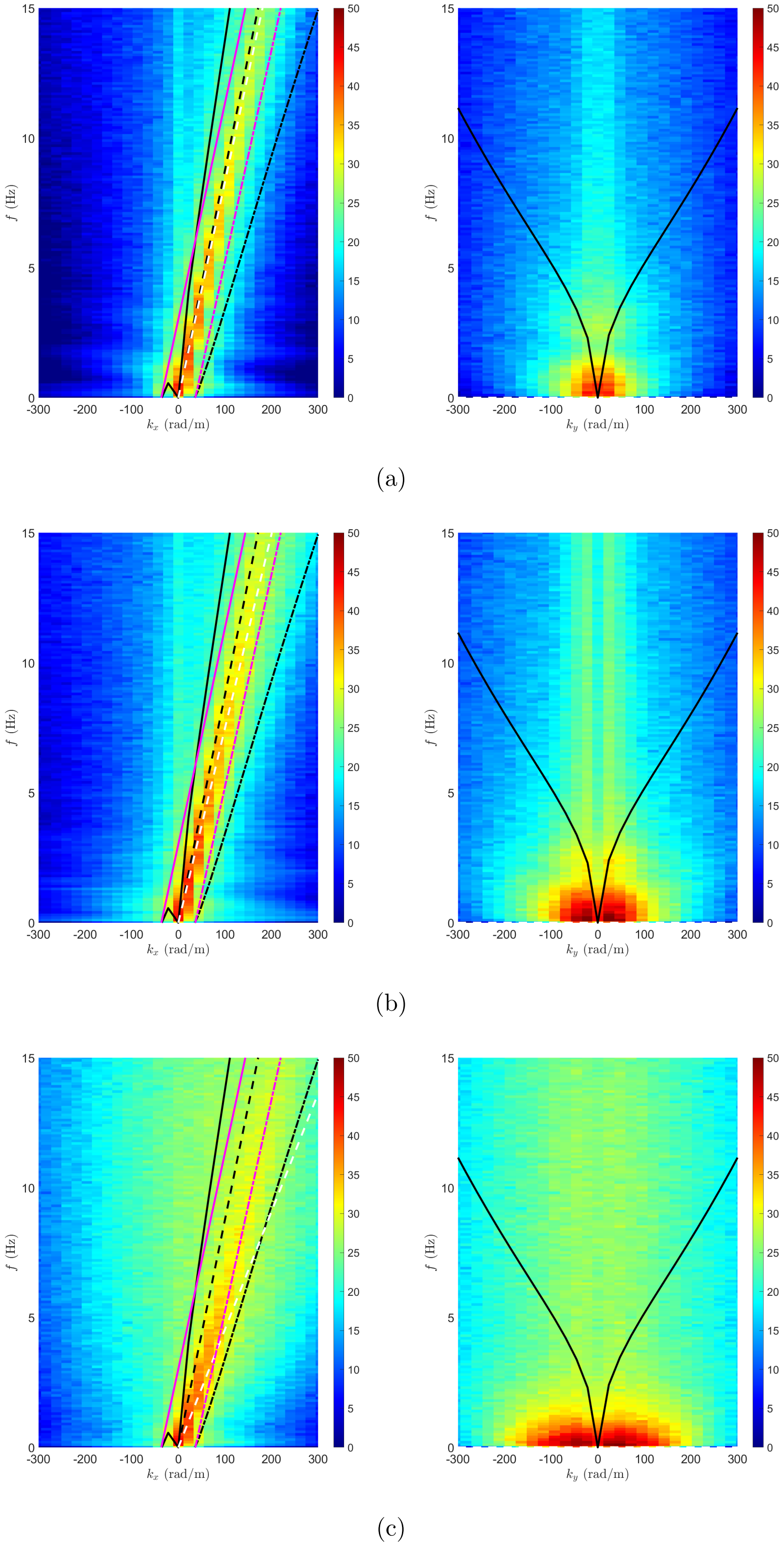

Figure A.31: Streamwise (left) and lateral (right) frequency-wavenumber spectra of the streamwise turbulent velocity for A6_H at planes a) "A", b) "C" and c) "E". Black lines: dashed is for non-dispersive structures advecting at U_S (Eq. 4.1), solid and dashed-dotted are positive and negative solutions for gravity-capillary waves (Eq. 4.2). White-dashed line: structures advecting at $\langle \bar{U} \rangle_{xz,plane_i}$. Magenta lines: solid and dashed-dotted are positive and negative solutions for gravity-capillary waves with $k = k_0$ (modified Eq. 4.2).

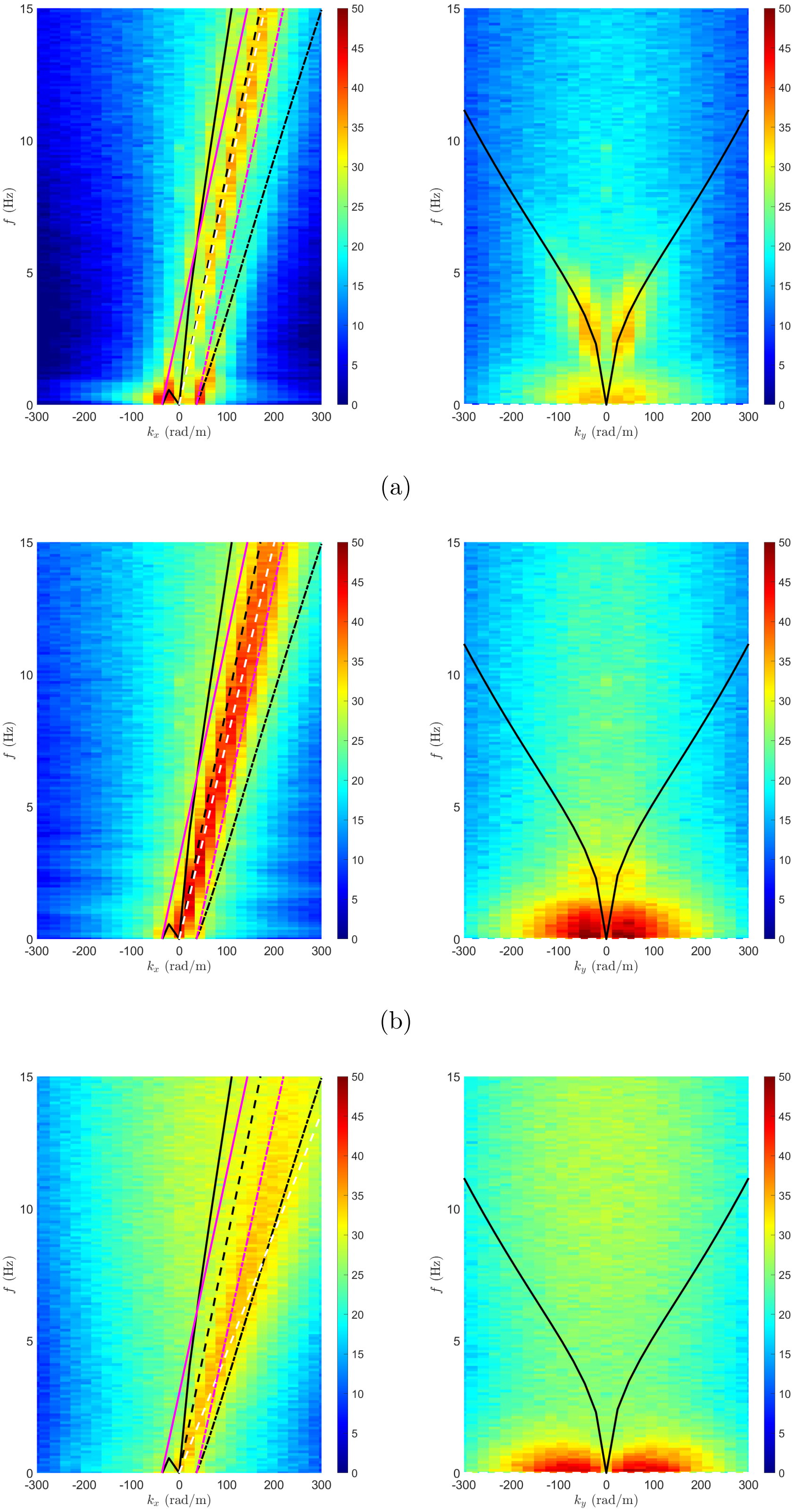

(a)

(b)

(c)

Figure A.32: Streamwise (left) and lateral (right) frequency-wavenumber spectra of the vertical turbulent velocity for A6_H at planes a) "A", b) "C" and c) "E". Black lines: dashed is for non-dispersive structures advecting at U_S (Eq. 4.1), solid and dashed-dotted are positive and negative solutions for gravity-capillary waves (Eq. 4.2). White-dashed line: structures advecting at $\langle \bar{U} \rangle_{xz,plane_i}$. Magenta lines: solid and dashed-dotted are positive and negative solutions for gravity-capillary waves with $k = k_0$ (modified Eq. 4.2).

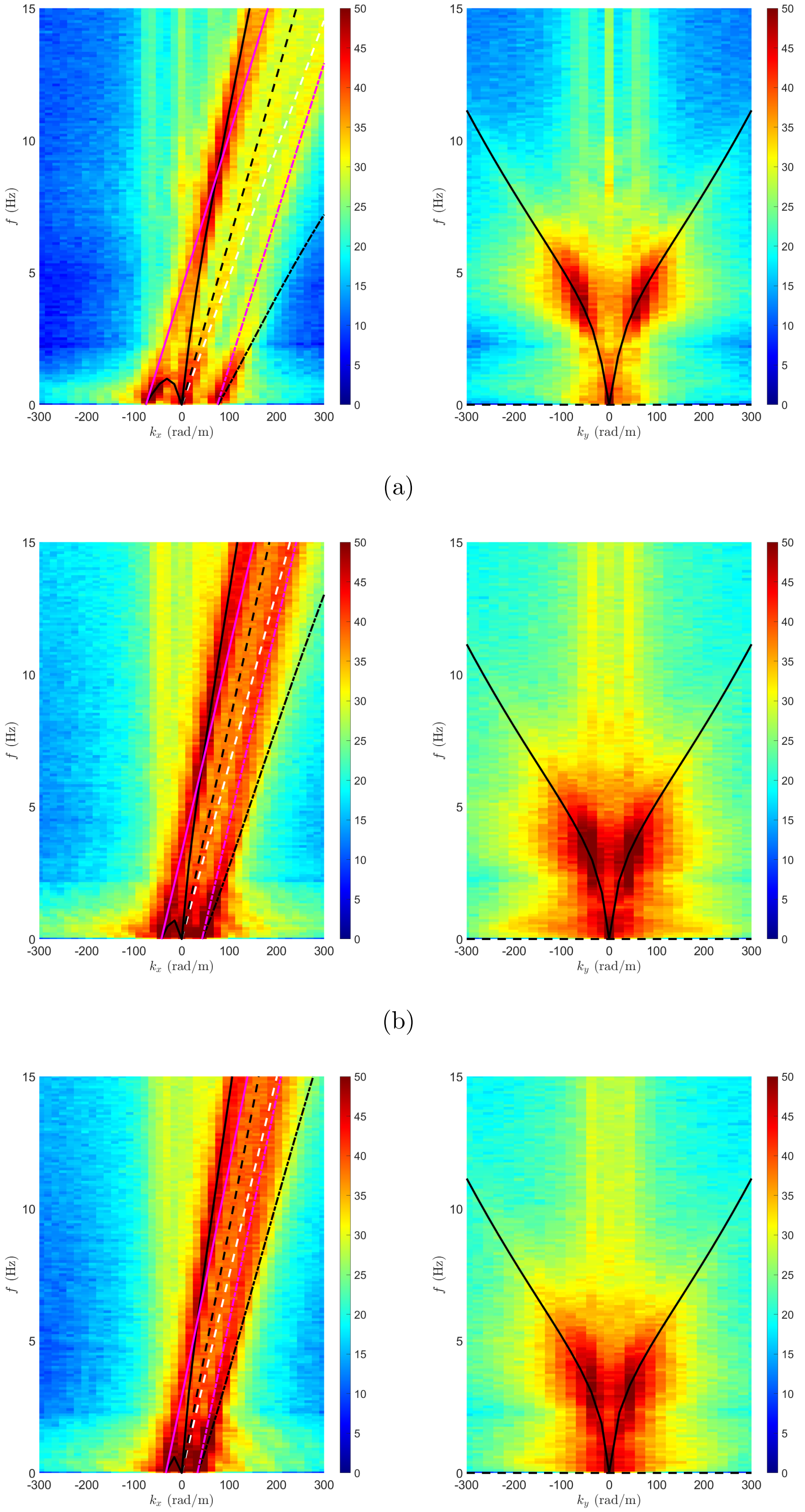

(a)

(b)

(c)

Figure A.33: Streamwise (left) and lateral (right) frequency-wavenumber spectra for tests of the "Q" series: a) Q3_S, b) Q5_S and c) Q6_S. Black lines: dashed is for non-dispersive patterns with U_S (Eq. 4.1), solid and dashed-dotted indicate the positive and negative solutions for gravity-capillary waves (Eq. 4.2). White-dashed line: non-dispersive patterns with $\bar{U}_B$ (Eq. 4.3). Magenta lines: solid and dashed-dotted are the positive and negative solutions for gravity-capillary waves with k_0 as wavenumber (modified Eq. 4.2).

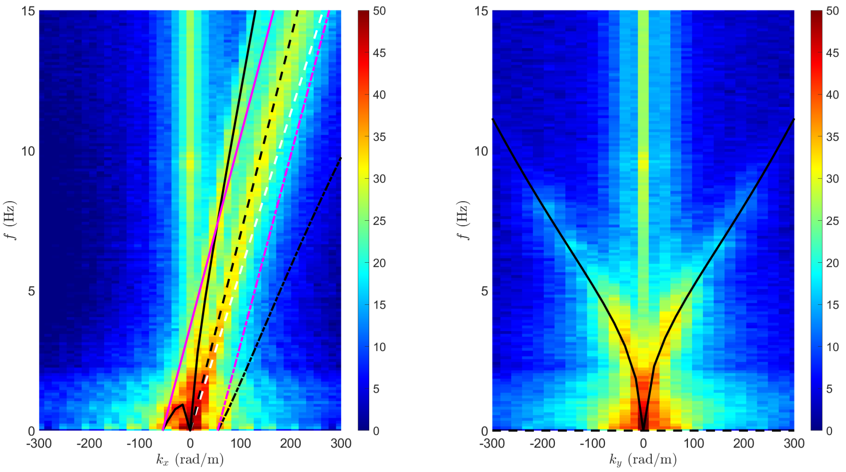

(a)

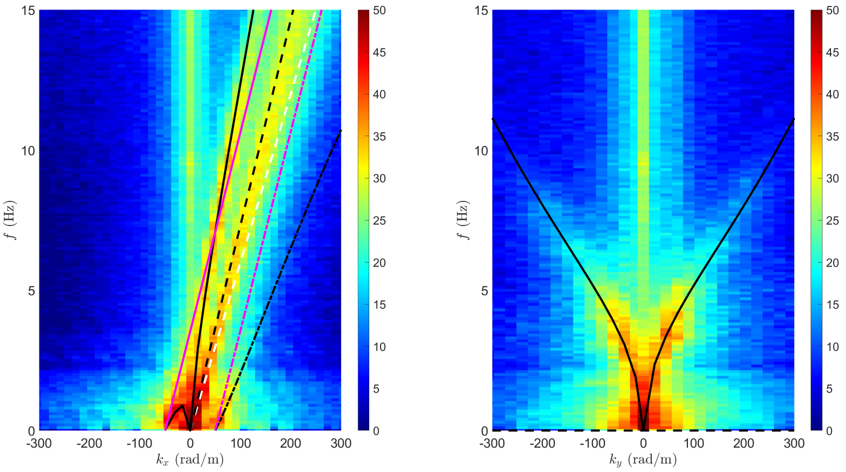

(b)

Figure A.34: Streamwise (left) and lateral (right) frequency-wavenumber spectra for tests of the "M" series: a) M5_S and b) M6_S. Black lines: dashed is for non-dispersive patterns with U_S (Eq. 4.1), solid and dashed-dotted indicate the positive and negative solutions for gravity-capillary waves (Eq. 4.2). White-dashed line: non-dispersive patterns with $\bar{U}_B$ (Eq. 4.3). Magenta lines: solid and dashed-dotted are the positive and negative solutions for gravity-capillary waves with k_0 as wavenumber (modified Eq. 4.2).

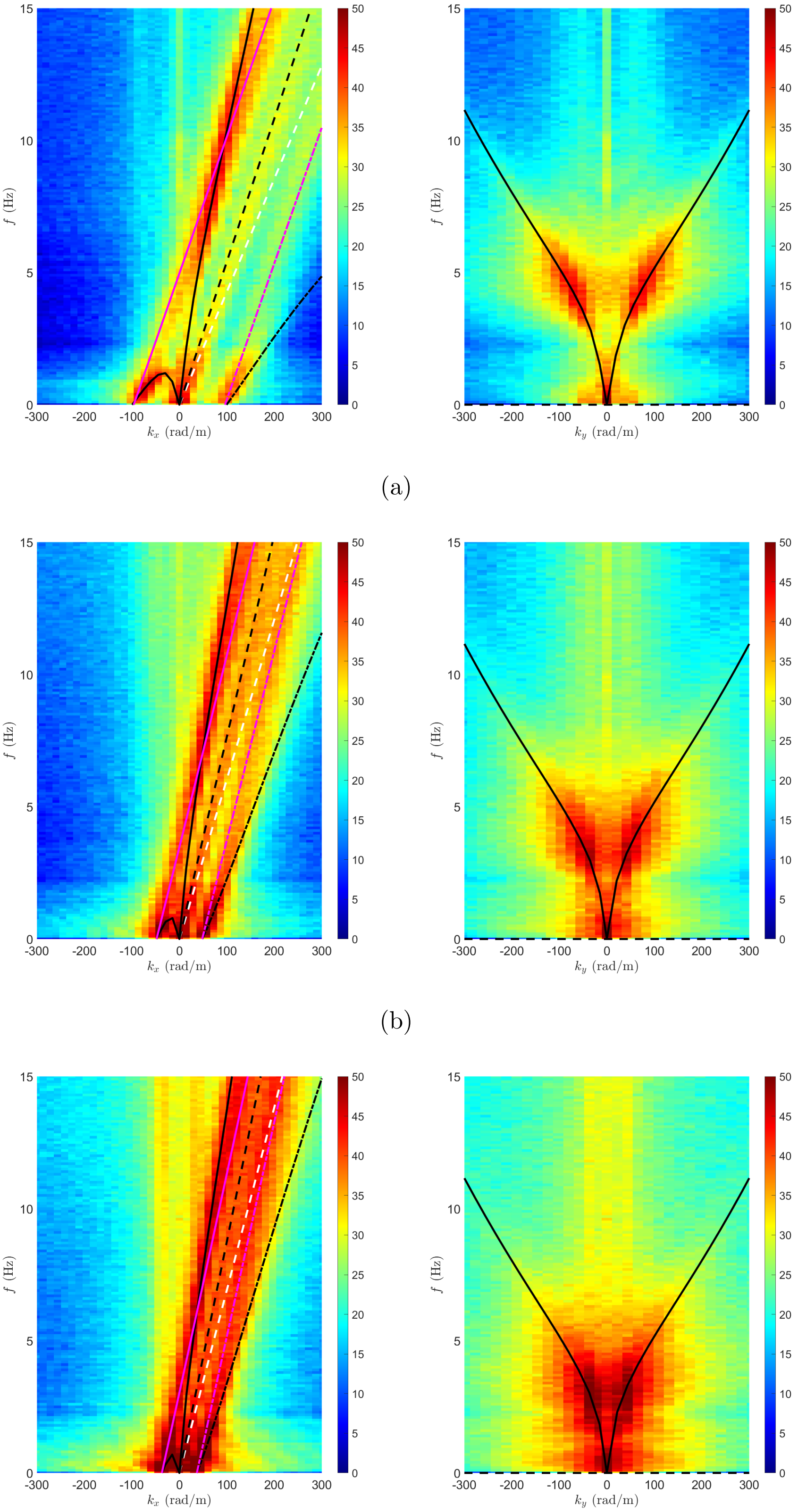

(a)

(b)

(c)

Figure A.35: Streamwise (left) and lateral (right) frequency-wavenumber spectra for tests of the "A" series: a) A3_S, b) A5_S and c) A6_S. Black lines: dashed is for non-dispersive patterns with U_S (Eq. 4.1), solid and dashed-dotted indicate the positive and negative solutions for gravity-capillary waves (Eq. 4.2). White-dashed line: non-dispersive patterns with $\bar{U}_B$ (Eq. 4.3). Magenta lines: solid and dashed-dotted are the positive and negative solutions for gravity-capillary waves with k_0 as wavenumber (modified Eq. 4.2).